

**STUDIES ON MECHANICAL PROPERTIES AND CORROSION
BEHAVIOR OF ZE41 MAGNESIUM ALLOY SUBJECTED TO EQUAL
CHANNEL ANGULAR PRESSING**

Thesis

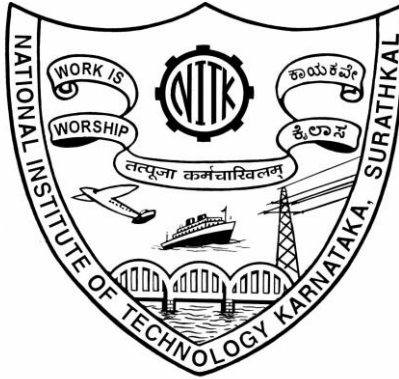
Submitted in partial fulfillment of the requirements for the degree of

DOCTOR OF PHILOSOPHY

by

PRITHIVIRAJAN SEKAR

(177066/177ME013)



DEPARTMENT OF MECHANICAL ENGINEERING

NATIONAL INSTITUTE OF TECHNOLOGY KARNATAKA, SURATHKAL,

MANGALORE -575025

JUNE - 2022

**STUDIES ON MECHANICAL PROPERTIES AND CORROSION
BEHAVIOR OF ZE41 MAGNESIUM ALLOY SUBJECTED TO EQUAL
CHANNEL ANGULAR PRESSING**

Thesis

Submitted in partial fulfillment of the requirements for the degree of

DOCTOR OF PHILOSOPHY

by

PRITHIVIRAJAN SEKAR

(177066/177ME013)

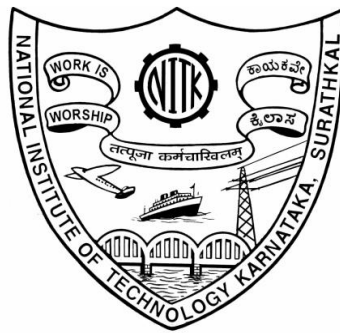
Under the guidance of

Dr. NARENDRANATH S

Professor

Dr. VIJAY DESAI

Professor



DEPARTMENT OF MECHANICAL ENGINEERING
NATIONAL INSTITUTE OF TECHNOLOGY KARNATAKA, SURATHKAL,
MANGALORE - 575025

JUNE - 2022

DECLARATION

I hereby declare that the Research Thesis entitled **STUDIES ON MECHANICAL PROPERTIES AND CORROSION BEHAVIOR OF ZE41 MAGNESIUM ALLOY SUBJECTED TO EQUAL CHANNEL ANGULAR PRESSING** which is being submitted to **National Institute of Technology Karnataka, Surathkal** in partial fulfilment of the requirements for the award of the degree of **Doctor of Philosophy** in Mechanical Engineering is a bonafide report of the research work carried out by me. The material contained in this Research Thesis has not been submitted to any other University or Institution for the award of any degree.



PRITHIVIRAJAN SEKAR

Register Number: **177066/ 177ME013**

Department of Mechanical Engineering

Place: NITK-Surathkal

Date: 29.06.2022

C E R T I F I C A T E

This is to certify that the Research Thesis entitled **STUDIES ON MECHANICAL PROPERTIES AND CORROSION BEHAVIOR OF ZE41 MAGNESIUM ALLOY SUBJECTED TO EQUAL CHANNEL ANGULAR PRESSING** submitted by **Mr. PRITHIVIRAJAN SEKAR (Reg. No: 177066-177ME013)** as the record of the research work carried out by him, is accepted as the Research Thesis submission in partial fulfilment of the requirements for the award of degree of **Doctor of Philosophy**.

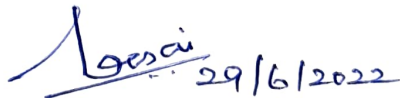
Research Guide(s)



Dr. NARENDRANATH S

Professor

Dept. of Mechanical Engineering



Dr. VIJAY DESAI

Professor

Dept. of Mechanical Engineering



Dr. Chairman - DRPC

Date: **30/6/2022**

ACKNOWLEDGMENT

I express my deep sense of gratitude and indebtedness to my supervisors **Dr. Narendranath S**, Professor, Department of Mechanical engineering, National Institute of Technology Karnataka, Surathkal and **Dr. Vijay Desai**, Professor, Department of Mechanical engineering, National Institute of Technology Karnataka, Surathkal for providing precious guidance, inspiring discussions and constant supervision throughout the course of this work. Their timely help, constructive criticism and continuous efforts made it possible to present the work contained in this thesis.

I express my sincere thanks to **Dr. Kulkarni S M**, Professor and Head of the Department and **Dr. Shrikantha S. Rao**, Professor and former Head of the Department, Department of Mechanical engineering, National Institute of Technology Karnataka, Surathkal.

I gratefully acknowledge the support from the **Naval Research Board (NRB)**, Government of India, under the project reference number **NRB/4003/PG/366-2015**.

I am grateful to the members of the Research Program Assessment Committee including **Dr. AC Hegde**, Professor, Department of Chemistry, **Dr. Ramesh MR**, Associate Professor, Department of Mechanical Engineering., for their unbiased and critical evaluation during the progress of my research.

I do thank **Dr. Gajanan M Naik**, Assistant Professor, Assistant Professor, RVITM, Bangalore, **Dr. Hargovind Soni**, Post Doctoral Fellow, University of Johnnesburg, **Dr. Sachin B C**, Assistant Professor, National Institute of Engineering, Mysore and **Dr. Abhinaba Roy**, Assistant Professor, National Institute of Engineering, Mysore for inspiring me through the course of my work.

I do thank **Mr. Gopal D Gote**, Research Scholar, Dept. of Mech. Engg. IIT-Bombay, Mumbai, **Mr. Aditya Prakash**, Research Scholar, Dept. of MEMS, IIT-Bombay, Mumbai, **Mr. Sandeep Sahu**, Research Scholar, Dept. of Materials Science and Engineering, IIT Kanpur, Kanpur for their help in EBSD characterization.

I express my sincere thanks to **Dr. M. Manjaiah**, Assistant Professor, NIT Warangal, **Dr. Muralidhar Avvari**, Assistant Professor, Bhair Dar University, Ethiopia, **Dr. Nithin**, Assistant Professor, Malnad College of Engineering, Hassan, **Dr. Gopi K R**, Assistant

Professor, Malnad College of Engineering, **Dr. Priyaranjan Sharma**, Assistant Professor, RVITM, Bangalore, **Dr. Gajanan anne**, Associate Professor, Shri Madhwa Vadiraja Institute of Technology, Udupi. **Dr. Mahesh D**, Professor, SCEM-Mangalore, **Dr. Sachin Kumar Patil, Associate Professor**, Reva University-Bengaluru, **Dr. Narendran**, Post-Doctoral Fellow, IIT Madras, Chennai. **Dr. Vinay Varghese**, Post-Doctoral Fellow, Dept. of Mech. Engg. IIT-Bombay, Mumbai.

I am grateful to all my research colleagues of Department of Mechanical Engineering **Mr. Manoj I V, Mr. Mayur, Mr. Praveen J, Mr. Vijay, Mr. Jagadeesh C, Mr Sandeep KV, Mr. Rakshith , Mr. Praveen J, Mr. Vijay, Mr. Praveen TR, Mr. Vijay G, Mr. Uzwal R, Mr. Jithendar Chaurasia, Mr. Rakesh, Mr. Kishan, Mrs. Snehal Chandurkar, Mrs. Pooja M Aithal, Mr. Bakshi, Mr. Chetan, Mr. Vinayak, Mr. Jagadeesh, Mr. Ramesh S, Mr. Suresh, Mr. Subba rao** and also the Teaching and Non-teaching staff members of the Department of Mechanical Engineering, NITK for their continuous help and support throughout the research work.

I express my sincere thanks to **Mr. Jaya Devadiga, Mr. C A Verghese, Mr. Pradeep, Mr. Aravind, Mrs Rashmi, Mr. Shailesh, Mr. Shashi and Mr. Harish**, Staff, NITK-Surathkal.

I am extremely grateful to my parents **Sri. Sekar V, Smt. Hemavathi M** and my family members who have been a motivating force throughout my life. It is a pleasure to thank my brother **Er. Pugazhendhi** for his support rendered during the study. I am also grateful to my uncle **Dr. Dhananchezian**, Associate Professor, Dept of Mechanical Engg, SSN College of engineering, Chennai for his guidance right from schooling to post graduate studies.

Finally, I wish to thank one and all who have helped me directly or indirectly during various phases of this research work. I THANK YOU ALL.....!

PRITHIVIRAJAN SEKAR

ABSTRACT

An exceptional combination of properties such as high specific strength, good damping capacity and abundant availability confirm magnesium alloys as a potential candidate for applications in automobile, biomedical, aerospace as well as electronics industries. However, the limited ductility of Magnesium and its alloys as well as their relatively lower corrosion resistance still remains a hindrance to extend their applications. Equal channel angular pressing (ECAP) has immense potential to attain remarkable grain refinement thereby improving mechanical properties such as yield strength, ultimate tensile strength and percentage of elongation of Mg alloys. In the present work, ZE41 Mg alloy is subjected to two step ECAP. The microstructure and mechanical properties of ZE41 Mg alloy before and after two step ECAP are investigated. Further, the corrosion and galvanic corrosion behaviour of ZE41 samples are evaluated in 0 M, 0.1 M and 1 M NaCl solutions to mimic conditions encountered in automobile applications. Two step equal channel angular pressing carried out on as received ZE41 Mg alloy resulted in a remarkable grain refinement. As compared to grain size of 46 μ m in as received sample, refinement upto 2.5 μ m is achieved after 8th pass equal channel angular pressing (ECAP). The combined effect of crystallographic orientation and grain refinement is investigated by analysing the mechanical properties and corrosion behaviour of ZE41 Mg alloy using electron back scattered diffraction (EBSD). The first stage comprises of 1st, 2nd, 3rd and 4th passes at a processing temperature of 300 °C while the 5th, 6th, 7th and 8th passes are ECAPed at 275 °C in second stage. The mechanical properties of ZE41 Mg alloy 158 MPa yield tensile strength (YTS), 230 MPa ultimate tensile strength (UTS) and 7 % elongation in as received condition is enhanced to 236 MPa YTS, 295 MPa UTS and 19.76% respectively after first stage ECAP. The yield tensile strength deteriorated due to the effect of texture predominating grain refinement during the second stage ECAP. The corrosion resistance of ZE41 Mg alloy is significantly enhanced by ECAP and is inferred from electrochemical impedance spectroscopy (EIS) and potentiodynamic polarisation results. The role of microstructure is minimal on corrosion behaviour of ZE41 Mg alloy due to extra resistance when tested in 0M NaCl. However, the influence of grain refinement greatly influenced the improvement in corrosion resistance of ZE41 Mg alloy rather than crystallographic

orientation observed from EBSD analysis. In contrast, the crystallographic orientation predominated the effect of grain refinement during ZE41 Mg alloy corrosion in chloride containing 0.1M and 1M NaCl solutions. From the observation of results it is found that equal channel angular pressing has the dual advantage of improving mechanical properties and corrosion resistance of ZE41 Mg alloy. Further, the galvanic corrosion behaviour of as received and ECAPed ZE41 Mg alloy coupled with Al7075 alloy is investigated using zero resistance ammeter (ZRA) in three different corrosive environments 0 M, 0.1 M and 1 M NaCl to mimic the conditions experienced in engineering applications. The mechanism of galvanic corrosion for ZE41 Mg alloy –Al7075 Aluminium alloy is explained. It is observed that a robust surface film containing composite layer of oxide/hydroxide of magnesium and aluminium is established in 0 M NaCl solution. However, only a single layer of magnesium oxide/ hydroxide is detected in chloride containing environments. ECAP improved the resistance to galvanic corrosion by 58% and 54% when compared with as received ZE41 Mg alloy in 0 M and 1 M NaCl solution respectively. In contrast, galvanic corrosion resistance decreased by 26% in 0.1 M NaCl after equal channel angular pressing while the as received samples evinced pits unfavourable to be used in engineering applications. ECAP is a promising method to combat galvanic corrosion encountered by ZE41 Magnesium alloy used in automobiles and components of military vehicles.

Keywords: *Corrosion, EBSD analysis, Equal Channel Angular Pressing, Galvanic corrosion, Grain Refinement, Magnesium Alloys, Mechanical Properties, Microstructure, Scanning Electron Microscope analysis, Texture analysis, Transmission Electron Microscope analysis, X-ray Diffraction analysis, X-ray Photo Electron Spectroscopy analysis and ZE41Mg alloy.*

CONTENTS

<i>Declaration</i>	
<i>Certificate</i>	
<i>Acknowledgement</i>	
<i>Abstract</i>	
<i>Contents</i>	<i>i</i>
<i>List of Figures</i>	<i>vi</i>
<i>List of Tables</i>	<i>xiv</i>
<i>List of Symbols and Abbreviations</i>	<i>xv</i>
CHAPTER-1 INTRODUCTION	1
1.1 BACKGROUND	1
1.2 MAGNESIUM ALLOYS IN AUTOMOBILE APPLICATION	2
1.3 STRENGTHENING MECHANISMS	5
1.3.1 Severe plastic deformation	6
1.3.2 Equal channel angular pressing	6
1.3.3 Microstructure of magnesium alloys before and after ECAP	7
1.3.4 Texture evolution during ECAP of magnesium alloys	9
1.3.5 Mechanical properties of Mg alloys processed by ECAP	11
1.4 CORROSION OF MAGNESIUM ALLOYS	13
1.4.1 Factors influencing the corrosion resistance of magnesium alloys	13
1.4.2 Corrosion of ZE41 magnesium alloy	14
1.4.3 Occurrence of galvanic corrosion in magnesium alloys	15
1.4.4 Corrosion thermodynamics and kinetics of magnesium	16
1.4.5 Effect of ECAP on corrosion behavior of magnesium alloys	18
1.5 SUMMARY	19
1.6 THESIS ORGANIZATION	19
CHAPTER-2 LITERATURE REVIEW	22
2.1 INTRODUCTION	22
2.2 CAST MAGNESIUM ALLOYS	22
2.3 STRENGTHENING MECHANISMS	23

2.3.1 Solid solution strengthening	23
2.3.2 Precipitation Strengthening	24
2.3.3 Grain boundary and texture strengthening	24
2.4 EQUAL CHANNEL ANGULAR PRESSING	25
2.4.1 Effect of microstructure on mechanical properties of Mg alloys after single step ECAP	25
2.4.2 Mechanical properties evaluation in magnesium alloys after two step and multi-step ECAP.	28
2.5 GRAIN BOUNDARY CHARACTERISTICS OF MAGNESIUM ALLOYS	31
2.6 EFFECT OF TEXTURE EVOLUTION ON MAGNESIUM ALLOYS PROCESSED BY ECAP	33
2.6.1 Macro texture of Mg alloys subject to ECAP	34
2.6.2 Role of micro-texture evolution on ECAPed Mg alloys obtained from EBSD	35
2.7 FRACTOGRAPHY OF MAGNESIUM ALLOYS BEFORE AND AFTER ECAP	37
2.8 CORROSION OF MAGNESIUM ALLOYS	41
2.8.1 Selecting corrosive medium for specific applications	41
2.9 INFLUENCE OF SECONDARY PHASE PARTICLES ON CORROSION BEHAVIOUR OF MAGNESIUM ALLOYS BEFORE AND AFTER ECAP	43
2.10 EFFECT OF CRYSTALLOGRAPHIC ORIENTATION ON CORROSION BEHAVIOUR OF MAGNESIUM ALLOYS	46
2.11 GALVANIC CORROSION OF MAGNESIUM ALLOYS	48
2.11.1 Galvanic corrosion measurement in magnesium alloy couple using scanning vibrating electrode technique (SVET).	48
2.11.2 Evaluation of corrosion rate in galvanic couples using zero resistance ammeter.	51
2.11.3 Surface film models proposed for Mg alloys.	53
2.12 CONCLUSION	54

2.13 RESEARCH GAPS	55
2.14 OBJECTIVES OF THE PROPOSED RESEARCH WORK	56
CHAPTER-3 EXPERIMENTAL WORK	57
3.1 INTRODUCTION	57
3.2 ZE41 MAGNESIUM ALLOY	57
3.3 EQUAL CHANNEL ANGULAR EXTRUSION	58
3.3.1 Selecting the processing temperature for two step ECAP	60
3.4 MICROSTRUCTURAL CHARACTERIZATION	62
3.4.1 Optical microscopy	62
3.4.2 Scanning Electron Microscopy	63
3.4.2 (a) Microstructural observation of ZE41 Mg and its secondary phases	63
3.4.2 (b) Electron Backscattered diffraction (EBSD)	63
3.5 MECHANICAL TESTING	65
3.5.1 Evaluation of mechanical properties using tensile test	65
3.5.2 Fractography of ZE41 Mg samples	66
3.6 CORROSION STUDIES	66
3.6.1 Electrochemical corrosion tests of ZE41 Mg	66
3.6.2 Galvanic corrosion experiments of ZE41 Mg- Al7075 Al couple.	67
3.7 PHASES AND SPECIES DETECTION	69
3.7.1 Identification of phases in ZE41 Mg alloy using X-ray Diffraction (XRD)	69
3.7.2 Revealing surface films models using X-ray photoelectron spectroscopy (XPS)	69
3.7.3 Corrosion morphology of ZE41 Mg	70
3.8 SUMMARY	71

CHAPTER 4. ANALYZING THE COMBINED EFFECT OF GRAIN REFINEMENT AND MICRO-TEXTURE ON MECHANICAL PROPERTIES OF ZE41 MAGNESIUM ALLOY SUBJECT TO TWO STEP ECAP.	73
4.1 INTRODUCTION	73
4.2 INFLUENCE OF ECAP ON MICROSTRUCTURE AND MECHANICAL PROPERTIES OF ZE41 MAGNESIUM ALLOY.	73
4.3 MICROSTRUCTURE OF ZE41 MAGNESIUM ALLOY	74
4.3.1 Microstructural evolution obtained as a result of ECAP	74
4.3.2 Grain refinement model of ZE41 Mg alloy	77
4.3.3 Grain boundary characteristics of ZE41 Mg alloy	78
4.4 MICRO-TEXTURE EVOLUTION OF ZE41 MAGNESIUM ALLOY	83
4.5 MECHANICAL PROPERTIES OF ZE41 MAGNESIUM ALLOY	86
4.5.1 Influence of micro-texture and grain refinement on yield strength of ZE41Mg	86
4.5.2 Modes of fractures and its effect on ductility of ZE41 Mg before and after ECAP	89
4.6 SUMMARY	92
CHAPTER 5: INFLUENCE OF GRAIN REFINEMENT AND CRYSTALLOGRAPHIC ORIENTATION ON CORROSION BEHAVIOUR OF ZE41 MAGNESIUM ALLOY.	95
5.1 CORROSION BEHAVIOUR OF ZE41 MAGNESIUM ALLOY	95
5.1.1 Open circuit potential (OCP) of ZE41 Mg alloy	95
5.1.2 Realizing the nature of surface film formed on ZE41 Mg using electrochemical impedance spectroscopy	97
5.1.3 Evaluating the corrosion rate of ZE41 Mg using Potentiodynamic Polarization plots.	106
5.2 COMBINED EFFECT OF GRAIN REFINEMENT AND CRYSTALLOGRAPHIC ORIENTATION ON ZE41 MAGNESIUM CORROSION.	109

5.3 MECHANISM OF CORROSION IN ZE41 MAGNESIUM ALLOY	115
5.4 SUMMARY	117
CHAPTER-6 ENHANCEMENT OF RESISTANCE TO GALVANIC CORROSION OF ZE41 MAGNESIUM ALLOY.	119
6.1 INTRODUCTION	119
6.2 MICROSTRUCTURAL EVOLUTION OF ZE41 MAGNESIUM ALLOY BEFORE AND AFTER ECAP	119
6.3 GALVANIC CORROSION BEHAVIOUR OF AS RECEIVED (ASR) AND EQUAL CHANNEL ANGULAR PRESSED ZE41 Mg-Al7075 COUPLE	121
6.3.1 Open circuit potential (OCP) of ZE41 Mg-Al7075 couple	121
6.3.2 Electrochemical impedance spectroscopy (EIS) of ZE41 Mg-Al7075 couple.	123
6.3.3 EDS and XRD analysis of ZE41 Magnesium alloy after galvanic corrosion.	126
6.3.4 Influence of microstructure on resistance to galvanic corrosion in three different environments.	127
6.3.5 Potentiodynamic polarization of galvanic couple	129
6.3.6 Corrosion morphology of ZE41 Magnesium alloy after galvanic corrosion in 0 M, 0.1 M and 1 M NaCl solution.	131
6.3.7 Mechanism of galvanic corrosion in ZE41 Mg–Al7075 galvanic couple.	132
6.4 COMPARISON OF CORROSION AND GALVANIC CORROSION BEHAVIOUR OF ZE41 MAGNESIUM ALLOY.	136
6.5 SUMMARY	143
CHAPTER 7: CONCLUSION	146
REFERENCES	151
LIST OF RESEARCH PAPERS PUBLISHED	
BIO-DATA	

LIST OF FIGURES

Figure No.	Description	Page No.
Figure 1.1	Automotive components made of Mg and the obtained weight reduction. (Kuleckci.2008).	3
Figure 1.2	Application of ZE41 Mg in automobile (a) Automobile wheel (b) transmission casing (c) door frame (d) seat (Kuleckci, 2008).	5
Figure 1.3	Schematic representation of ECAP process. (Azushima et al. 2008)	6
Figure 1.4	Grain refinement model of Mg alloys processed by ECAP (a), (d), (g), (j) initial grain size, (b), (e), (h), (k) grain size after 1 st pass, (c), (f), (i) grain size after multiple passes. (Figueiredo and Langdon, 2010)	8
Figure 1.5	Schematic of (a) extrusion and (b) ECAP process showing the orientation of basal planes (T Mukai et al, 2001).	9
Figure 1.6	Electron back scattered micrographs of LAE442 Mg alloy in (a) extruded and (b) ECAPed condition. (Minarik et al, 2015)	10
Figure 1.7	Pole figures of ZK60 Mg (a) Extruded (b) 8 th pass (c) 12 th pass (d) 20 th pass. (Mostaed et al, 2014)	10
Figure 1.8	Evolution of yield tensile strength (YTS) on the increasing number of ECAP passes of all three investigated alloys (Minarik et al, 2016).	12
Figure 1.9	Orientation of crystal after (a) extrusion and (b) ECAP process (Lin et al, 2005).	12
Figure 1.10	Open-circuit potential of AZ31 and JDBM alloy as a function of immersion time.(Zong et al, 2012).	16
Figure 1.11	Typical Nyquist plots of Mg alloys (King et al. 2014)	17

Figure 1.12	Potentiodynamic polarization curves of ZE41 magnesium alloy (a) variation in pH (b) variation in Cl^- concentration (Zhao et al. 2008)	18
Figure 2.1	Evolution of (a) the mean grain size in logarithmic scale, (b) the fraction of HAGBs with increasing number of ECAP passes (N) and (c) inverse pole figure maps of the samples after 8 th pass (Krajňák et al., 2019).	27
Figure 2.2	EBSD image orientation maps and corresponding grain size distribution of (a and b) extruded, (c and d) 4 th pass at 200 ° C (e and f) 4 th pass at 200 ° C + 4 th pass at 150 ° C (Mostaed et al., 2015).	29
Figure 2.3	Stress strain curve of AZ31 for different ECAP processing conditions. (Jin et.al 2005).	29
Figure 2.4	Stress Strain curves of AZ91 at single and two step ECAP (Chen et.al 2008).	30
Figure 2.5	a) ECAP deformed sample and schematic representation of different zones, b) unprocessed, c) shearing zone and d) ECAPed zone (Victoria-Hernández et al., 2016)	32
Figure 2.6	Grain boundary character distribution for the initial and the ECAE-processed samples (Biswas et.al, 2010)	32
Figure 2.7	Texture evolution of ZM21 Mg (a) extruded, (b) 4 th pass at 200 ° C (c) 4 th pass at 200 ° C + 4 th pass at 150 ° C (Mostaed et al., 2015)	36
Figure 2.8	Fractured surface of AZ80 Mg alloys (a) as-received, (b) homogenized at 400 °C, (c) 2P-90°, (d) 4P-90°, (e) 2P-110°, (f) 4P-110° (Naik et.al, 2019)	38
Figure 2.9	SEM micrographs of fractures surface (a) as received (b) 12 th pass (c) macrographs of tensile fracture. (Mostaed et al, 2014)	38

Figure 2.10	Distribution of Schmid factors for basal slip (a) extruded, (b) 4 th pass at 200 °C and (c) 4 th pass at 200 °C + 4 th pass at 150 °C samples of ZM21 Mg (Mostaed et.al, 2015)	39
Figure 2.11	Potentiodynamic polarisation plots of Pure Mg in different concentration of NaCl solution (a) as recorded (b) IR corrected. (King et al, 2014)	42
Figure 2.12	Cross-section of (a) AE21-0P, (b) AE21-8P, (c) AE42-0P and (d) AE42-8P (Minarik et.al, 2013)	44
Figure 2.13	General view of the corrosion surfaces of the materials immersed in PBS for 96 h: (a) extruded sample, (b) 12 th pass sample. (Mostaed et al, 2014)	45
Figure 2.14	Corrosion morphology: (a) ECAP-2P, (a1) 523 K for 12 h, (a2) 723 K for 12 h, (b) ECAP-4P, (b1) 523 K for 12 h, (b2) 723 K for 12 h (Naik et.al, 2019)	45
Figure 2.15	(a) EBSD grain distribution, and (b) schematic illustration of grain orientations of the Mg coupon (Song and Xu 2012)	47
Figure 2.16	(a) A photograph of the cross-sectional view of AE44 – mild steel (left) and AE44 – Al (right) couple after 3 days of immersion in the electrolyte solution. (b) The surface profile of the same couple obtained using image digitization technique. Deshpande (2010)	50
Figure 2.17	Configuration of the test panel and switchboard for the measurement of galvanic current. (Song et al. 2004)	52
Figure 2.18	CFRP/ Mg alloy couple showing (a) open circuit potential (OCP) (b) Galvanic corrosion current density in 3.5 Wt% NaCl. (Pan et al. 2015).	52
Figure 2.19	Typical multiplex XPS spectra for (a) C _{1s} ; (b) Mg _{2s} ; (c) Al _{2s} ; (d) Zn _{2p} and (e) O _{1s} . (G Song et.al, 1998).	66

Figure 2.20	Corrosion interfaces between solution and the following materials (a) AZ21, (b) AZ501 and (c) AZ91 (G Song et.al, 1998)	54
Figure 3.1	EDS of as received ZE41 Mg (a, b) SEM image and Wt % of constituent elements at grain (c, d) SEM image and Wt % of constituent elements at grain boundaries.	57
Figure 3.2	Equal channel angular pressing set up equipped with a temperature controller.	59
Figure 3.3	ECAP die having 90 ⁰ and 110 ⁰ channel angle and 30 ⁰ corner angle (Naik et al, 2019)	59
Figure 3.4	ZE41 Mg samples ECAPed at a) 250 °C and b) 275 °C.	60
Figure 3.5	Digital photographs of ZE41 Mg samples ECAPed during first and second step ECAP.	61
Figure 3.6	Zeiss optical microscope equipped with axio vision software	62
Figure 3.7	Scanning electron microscope attached with EDS detector.	63
Figure 3.8	FESEM equipped with EBSD detector.	64
Figure 3.9	ZE41 Mg sample mounted in SHIMADZU UTM	65
Figure 3.10	Tensile samples according to ASTM E8 standards	66
Figure 3.11	Corrosion equipment used a) Electrochemical corrosion analyser b) an expanded view showing electrical connection.	67
Figure 3.12	Experimental set up for galvanic corrosion	68
Figure 3.13	X-ray diffraction operated at 20 mA and 30 kV with Cu- α radiation	69
Figure 3.14	X-ray Photoelectron spectroscopy set up	70
Figure 4.1	EBSD Micrographs of ZE41 Mg alloy during first step ECAP (a) as received (b) 1 st pass (c) 2 nd pass (d) 3 rd pass (e) 4 th pass.	74
Figure 4.2	EBSD Micrographs of ZE41 Mg alloy during second step ECAP (a) as received (b) 5 th pass (c) 6 th pass (d) 7 th pass (e) 8 th pass	75

Figure 4.3	Grey scale micrographs and the corresponding grain boundary maps of ZE41 Mg alloy for first step ECAP samples (a, b) as received, (c, d) 1 st pass, (e, f) 2 nd pass, (g, h) 3 rd pass (i, j) 4 th pass	78
Figure 4.4	Grey scale micrographs and the corresponding grain boundary maps of ZE41 Mg ZE41 Mg alloy for second step ECAP samples (a, b) as received, (c, d) 5 th pass, (e, f) 6 th pass, (g, h) 7 th pass (i, j) 8 th pass	79
Figure 4.5	Grain boundary misorientation angles of ZE41 Mg as function of number of ECAP pass.	79
Figure 4.6	Representative kernel average maps of ZE41 Mg alloy during first step ECAP (a) as received (b) 1 st pass (c) 3 rd pass (d) 4 th pass.	80
Figure 4.7	Representative kernel average maps of ZE41 Mg alloy during first step ECAP (a) as received (b) 6 th pass (c) 7 th pass (d) 8 th pass.	81
Figure 4.8	X-ray diffraction patterns of ZE41 Mg alloy	82
Figure 4.9	Pole figures corresponding to (0001) plane of ZE41 Mg (a) as received (b) 1 st pass (c) 2 nd pass (d) 3 rd pass (e) 4 th pass	84
Figure 4.10	Pole figures corresponding to (0001) plane of ZE41 Mg (a) as received (b) 5 th pass (c) 6 th pass (d) 7 th pass (e) 8 th pass	85
Figure 4.11	Mechanical properties of ZE41 Mg alloy as function of number of ECAP passes	87
Figure 4.12	Schmid factor and corresponding number fraction of ZE41 Mg alloy in (a) as received (b) 1 st pass (c) 2 nd pass (d) 3 rd pass € 4 th pass.	89
Figure 4.13	Schmid factor and corresponding number fraction of ZE41 Mg alloy in (a) as received (b) 5 th pass (c) 6 th pass (d) 7 th pass (e) 8 th pass.	90
Figure 4.14	SEM fractured micrographs (a) as received (b) 2 nd pass (c) 4 th pass (d) 6 th pass (e) 8 th pass of ZE41 Mg alloy.	91

Figure 5.1	OCP curves of ZE41 Mg samples in (a) 0M NaCl (b) 0.1M NaCl (c) 1M NaCl	96
Figure 5.2	Nyquist Plot of ECAP samples processed at first step ECAP.	99
Figure 5.3	Nyquist Plot of ECAP samples processed at second step ECAP	100
Figure 5.4	corrosion parameters as a function of number of ECAP Passes (a) R_{ct} (b) R_s (c) C_{dl}	102
Figure 5.5	Bode Impedance plots of ECAP samples processed at first step.	103
Figure 5.6	Bode Impedance plots of ECAP samples processed at second step	104
Figure 5.7	Potentiodynamic Polarization plots of ECAP samples processed during first step	105
Figure 5.8	Potentiodynamic Polarization plots of ECAP samples processed during second step.	108
Figure 5.9	(a) Impedance (b) Corrosion rate as a function of number of ECAP Passes.	110
Figure 5.10	Inverse pole figures (contour) of ZE41 Mg alloys for different conditions (a) As Cast (b) 1P (c) 2P (d) 3P (e) 4P (f) 5P (g) 6P (h) 7P (i) 8P	113
Figure 5.11	SEM images of [(a) 0 M, (b) 0.1 M, (c) 1 M of as received] [(d) 0 M, (e) 0.1 M, (f) 1 M of 4 th pass] [(g) 0 M, (h) 0.1 M (i) 1M of 8 th pass] after corrosion.	114
Figure 5.12	Mechanism of corrosion in ZE41 Mg.	116
Figure 6.1	Optical images showing microstructural evolution (a) As Received (b) 2 nd Pass (c) 4 th Pass (d) 6 th Pass, SEM images of (e) As Received (f) 6 th Pass and TEM image (g) 6 th Pass	120
Figure 6.2	OCP curves of ZE41 Mg- Al7075 galvanic couple for ASR and ECAPed sample in three different concentration of	122

	NaCl (a) 0M NaCl solution (b) 0.1 M NaCl solution and (c) 1M NaCl solution.	
Figure 6.3	Nyquist plot for galvanic corrosion of ZE41 Mg- Al7075 galvanic couple for ASR and ECAPed sample in three different concentration of NaCl (a) 0M NaCl solution (b) 0.1 M NaCl solution and (c) 1M NaCl solution (d) Electrical Equivalent Circuit.	124
Figure 6.4	(a) Charge Transfer function (R_{ct}) and (b) Solution resistance (R_s) as a function of number ECAP passes in three different corrosive medium (c) Double layer capacitance C_{dl} as a function of number of ECAP passes.	125
Figure 6.5	(a) XRD plot of 4 th Pass ZE41 Mg alloy (b) selected area for EDS analysis on 4 th pass sample (c) EDS spectra 4 th Pass galvanic sample tested in 1M NaCl solution.	127
Figure 6.6	Bode impedance plot for galvanic corrosion of ZE41 Mg – Al7075 for three different concentration of NaCl solution (a) 0M NaCl (b) 0.1M NaCl (c) 1M NaCl.	128
Figure 6.7	Tafel plot for galvanic corrosion of ZE41 Mg – Al7075 in (a) 0M NaCl (b) 0.1M NaCl (c) 1M NaCl solution.	130
Figure 6.8	Corrosion morphology of ASR (a) (b) (c) and 4 th pass galvanic samples (d) (e) (f) in 0M NaCl, 0.1 M NaCl and 1M NaCl respectively.	132
Figure 6.9	XPS analysis of ZE41 Magnesium alloy after galvanic corrosion in 0M NaCl (a) Mg 1s (b) Al 2p and (c) O 1s spectra (d) XPS survey spectra for ZE41 Mg samples tested 0M,0.1M and 1M NaCl solution.	134
Figure 6.10	Schematic representation of ZE41 Magnesium alloy and Al7075 Aluminum alloy couple in interaction with corrosive medium.	134
Figure 6.11	surface film models developed on ZE41 Mg after galvanic corrosion.	135

Figure 6.12	Open Circuit potential of Al7075, ZE41 Mg and coupled ZE41 Mg-Al7075.	137
Figure 6.13	(a) Nyquist plot of Al7075, ZE41 Mg and coupled ZE41 Mg-Al7075 (b) Expanded view of Figure (a).	137
Figure 6.14	Potentiodynamic polarization curve of Al7075, ZE41 Mg and coupled ZE41 Mg-Al7075.	137
Figure 6.15	SEM images of (a) ZE41 Mg (b) corroded ZE41 Mg (c) corroded galvanic ZE41 Mg.	140
Figure 6.16	Comparing the corrosion rate obtained from ZE41 Mg corrosion and galvanic corrosion of ZE41 Mg- Al7075 couple.	140
Figure 6.17	Schematic of ZE41 Mg corrosion and galvanic corrosion of ZE41 Mg- Al7075 couple.	142

LIST OF TABLES

Table No.	Description	Page No.
Table 1.1	Comparison of selective properties of Mg, Al and Fe (Kuleckci.2008)	2
Table 1.2	Components produced from Mg alloys and its applications on car models (Kuleckci.2008).	4
Table 1.3	Grain refinement model of Mg alloys (Figueiredo and Langdon, (2010))	8
Table 2.1	Improvement in percentage elongation of Mg alloys before and after ECAP	40
Table 2.2	Corrosion rate of galvanic couples measured by using various techniques (Deshpande 2010b).	50
Table 3.1	Chemical composition of ZE41 Magnesium alloy in Wt%	58
Table 3.2	Two-step ECAP processing parameters	61
Table 4.1	Mechanical properties of ZE41 Mg alloy	88
Table 5.1	Corrosion parameters of ZE41 Mg alloy generated from Nyquist plot	101
Table 5.2	Impedance values and corrosion rate of ZE41 Mg alloy	109
Table 5.3	Atomic densities of planes in different crystallographic orientation	113
Table 6.1	Corrosion rate of galvanic couple in 0M NaCl, 0.1M NaCl and 1M NaCl solutions	131
Table 6.2	Atomic concentration from XPS analysis	135
Table 6.3	Corrosion rate obtained from ZE41 Mg and ZE41 Mg-Al7075 Al couple and the % change in corrosion rate after ECAP	141

LIST OF SYMBOLS AND ABBREVIATIONS

AE	: Auxiliary Electrode
AEXX	: Aluminum rare earth
AMXX	: Aluminum-Manganese
ALE	: Arbitrary Lagrangian Eulerian
AZ	: Aluminum-Zinc
AX	: Aluminum Calcium
ASTM	: American Society for Testing and Materials
ASR	: As received
BCC	: Body Centered Cubic
BM	: Base metal
BSE	: Backscattered Electron
C_{dl}	: Double layer capacitance
CR	: Corrosion Rate
'd'	: Initial grain size
'd _c '	: Critical grain size
DRX	: Dynamic Recrystallization
DMEM	: Dulbecco's modified eagle medium
EBSD	: Electron Back-Scatter Diffraction
EBSS	: Earle's balanced salt solution
ECAP	: Equal Channel Angular Pressing
E_{corr}	: Corrosion Potential
ED	: Extrusion direction
EDAX	: Energy Dispersive X-ray Spectroscopy
EIS	: Electrochemical Impedance Spectroscopy
% El	: percentage elongation
FCC	: Face Centered Cubic

FESEM	: Field emission scanning electron microscope
GBs	: Grain Boundaries
GBS	: Grain Boundary Strengthening
GS	: Grain size
HAGB	: High Angle Grain Boundaries
HBSS	: Hank's balanced salt solution
HDS	: Hot Die Steel
HCP	: Hexagonal Closed Pack
Hf	: High frequency
HPT	: High Pressure Torsion
I_{corr}	: Corrosion Current Density
IITB	: Indian institute of technology Bombay
KAM	: Kernel average misorientation
KBM	: Kirkland's bio-corrosion medium
LAEXXX	: Lithium Aluminum rare earth
LAGB	: Low Angle Grain Boundaries
LFID	: Low frequency inductive loop
LZXX	: Lithium Zinc
HAGB	: High Angle Grain Boundaries
LF	: Low frequency
LS	: Lateral surface
LP	: Linear Polarization
MPa	: Mega Pascal
MAF	: Multi-Axial Forging
MEMS	: Metallurgical engineering and material science
mf	: Medium frequency
MEM	: minimum essential medium
MH	: Microhardness
NPAR	: Neighbour pattern averaging and re-indexing

OCP	: Open Circuit Potential
OM	: Optical Microscopy
OIM	: Orientation imaging microscopy
P	: Pass
PBS	: phosphate buffered solution
PDP	: Potentiodynamic polarization
RE	: Rare Earth
RE	: Reference electrode
R_{ct}	: Charge Transfer Resistance
R_{sol}	: Solution resistance
RT	: Room Temperature
SCE	: Saturated Calomel Electrode
SKP	: Scanning kelvin probe
SEM	: Scanning Electron Microscopy
SPD	: Severe Plastic Deformation
SVE	: Scanning vibrating electrode
SCE	: Saturated calomel electrode
SZ	: Stir zone
TD	: Transverse direction
TEM	: Transmission electron microscope
TIFF	: Tag image file format
TS	: Transverse surface
UFG	: Ultrafine grain grains
UTM	: Universal Testing Machine
UTS	: Ultimate Tensile Strength
WE 1	: Working electrode 1
WE 2	: Working electrode 2
WEXX	: Yttrium rare earth
XRD	: X-ray Diffraction

YS	: Yield Strength
ZEXX	: Zinc rare earth
ZKXX	: Zinc-Zirconium
ZM	: Zinc- Manganese
ZRA	: zero resistance ammeter
XRD	: X-ray diffraction
XPS	: X-ray photoelectron spectroscopy
ϕ	: Channel Angle
ψ	: Corner Angle
γ	: Shear Strain
ε_{eq}	: Equivalent Strain

CHAPTER 1

INTRODUCTION

1.1 BACKGROUND

An exceptional combination of properties such as high specific strength, good damping capacity and abundant availability ensure magnesium alloys as a potential candidate for applications in automobile, aerospace, military vehicle, electronics as well as biomedical industries. The density of magnesium alloys is 1.75 g/cm^3 which is relatively less as compared to aluminium alloys possessing a density of 2.70 g/cm^3 . This property has resulted in magnesium alloys replacing the aluminium alloys in automobile and aerospace industries (Kulekci 2008). Magnesium alloys possessing hexagonal closed packed (HCP) crystal structure leading to limited number of slip systems which is detrimental to ductility. Recent findings by various researchers revealed that equal channel angular pressing (ECAP) is one of the promising methods of severe plastic deformation. In addition, ECAP has a great potential to achieve remarkable grain refinement. The mechanical properties such as yield strength, ultimate tensile strength and percentage of elongation of Mg alloys are improved due to grain boundary strengthening effect. Interestingly, sometimes the effect of grain refinement is predominated by the development of new texture element. This texture element aligns the basal plane approximately 45° to ECAP shearing plane resulting in lower yield strength even after grain refinement (Ding et al. 2010). Magnesium is the most active metal in the electromotive series. In addition, magnesium alloys are most active in galvanic series which makes them vulnerable to corrosion. Magnesium forms a partially protective oxide layer during interaction with the environment. The stability and nature of oxide film are dictated by the alloying elements and its distribution which also influences the corrosion resistance of magnesium alloys. The corrosion resistance also depends on the crystallographic orientation. Basal planes have lower theoretical dissolution rate when compared with non-basal planes. This is attributed to the better atomic co-ordination offered by basal planes. Better atomic coordination results in improved corrosion resistance (Liu et al. 2008). Magnesium alloys often encounter problems such as stress corrosion cracking, hydrogen embrittlement and galvanic corrosion when subjected to applications involving such environments. ECAP provides dual advantage of improving the mechanical

properties and corrosion resistance by grain refinement and homogeneous distribution of secondary phase particles respectively. Other metallurgical factors such as crystallographic orientation also affect the corrosion resistance of magnesium alloys. Hence, in the present research, effort has been made to explore the influence of ECAP on microstructure, mechanical properties, corrosion and galvanic corrosion of ZE41 Mg alloy.

1.2 MAGNESIUM ALLOYS IN AUTOMOBILE APPLICATION

The research and development work in the automobile industry highlights the importance of magnesium and its alloys. Magnesium being the lightest of all structural materials remarkably reduces the fuel consumption and CO₂ emissions. The low density of magnesium and its alloys also attracts the auto manufacturers to explore it as replacement for aluminium and steel components. It is well known that the major automotive components are made of magnesium, aluminium and steels.

Table 1.1 Comparison of selective properties of Mg, Al and Fe (Kulecki.2008).

Properties	Magnesium (Mg)	Aluminium (Al)	Iron (Fe)
Crystal Structure	Hexagonal Closed Pack	Face centred cubic	Body centred cubic
Density (g/cc)	1.74	2.70	7.86
Electrode Potential Vs Hydrogen electrode at 25 °C (Volts)	-2.363	-1.662	-0.440
Ductility	Low	High	Moderate

Table 1.1 depicts the selective properties of magnesium, aluminium and iron. It is evident from the table that magnesium, aluminium and iron have different crystal structures viz., hexagonal closed pack (HCP), face centred cubic (FCC) and body centred cubic (BCC) respectively. The crystal structures play an important role in dictating the mechanical properties of materials and in particular the ductility. Hence, the ductility of Mg, Al and Fe differs relatively and they are ranked as follows aluminium > iron > magnesium. Also, the

relatively lower corrosion resistance and limited ductility is still a hindrance while considering Mg and its alloys in automobile industry.

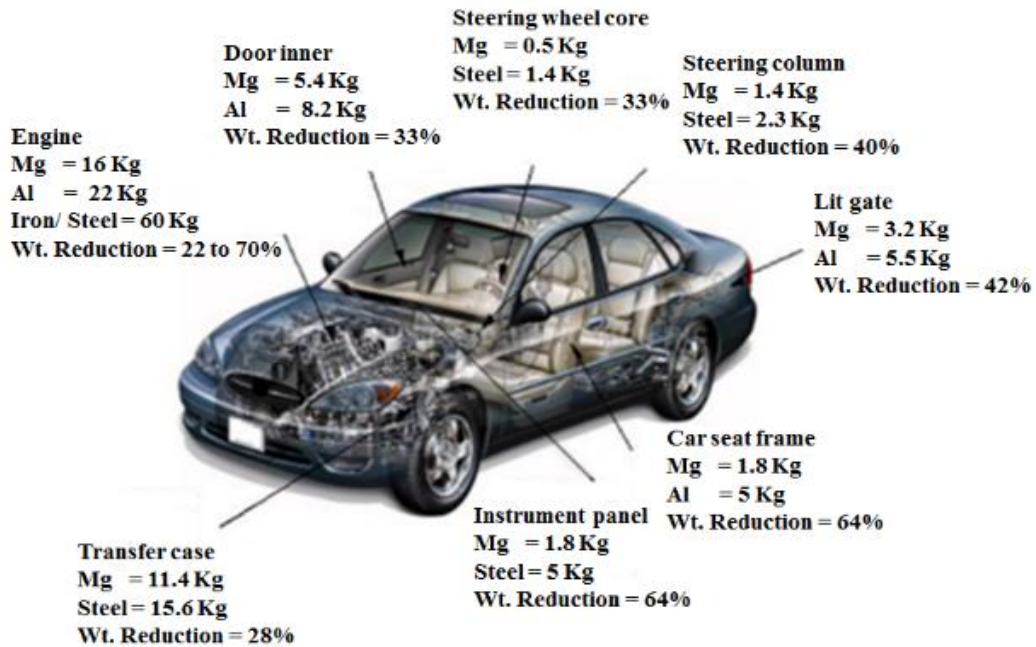


Fig 1.1 Automotive components made of Mg and the obtained weight reduction.

(Kuleckci.2008).

Figure 1.1 depicts automotive components made using magnesium alloys alongside the weight reduction after replacing steel and aluminium. The weight reduction was observed to be in the range of 22 to 70 % which is quite significant. In order to define the specific applications of Mg alloys, the components made from Mg and its corresponding auto manufacturers are listed in the table 1.2. It is very evident that the majority of important automotive components such as engine block, transmission case, wheel rims etc., are made of Mg and its alloys. However, they exhibit relatively less ductility and corrosion resistance due to their inherent properties. To extend the application of Mg alloys further there is pressing need to improve their ductility and corrosion resistance. The appropriate selection of alloying elements and processing routes are very essential to improve the mechanical properties i.e ductility in particular and also corrosion resistance. Hence, in the present study ECAP, a severe plastic deformation method is chosen to simultaneously improve both mechanical properties and corrosion behaviour of ZE41 Mg alloy.

Table 1.2 Components produced from Mg alloys and its applications on car models
(Kuleckci.2008).

Component	Automobile manufacturer
Engine block	Bayerische Motoren Werke (BMW)
Steering wheel frame	Ford, Chrysler, Toyota, BMW and Lexus
Seat frame	GM, Mercedes-Benz and Lexus.
Instrument panel	GM, Chrysler, Ford, Audi and Toyota
Wheel rims	Toyota, Alfa Romeo and Porsche AG.
Cylinder head	Dodge, Honda Motor, Alfa Romeo, AutoZAZ-Daewoo, Honda, BMW, Ford, Isuzu, Volvo Motors and Chrysler
Clutch case	AutoZAZ-Daewoo, Volvo Motors, Alfa Romeo.
Transmission case	AutoZAZ-Daewoo, Volvo Motors, Porsche AG, Volkswagen, Audi and Mercedes-Benz
Lower crankcase	Chrysler, Alfa Romeo, GM and McLaren Motors
Cylinder block	General Motors (GM)
Intake manifold	GM
Air intake system	BMW
Steering link bracing	GM
Oil pump body	McLaren Motors
Camshaft drive chain case	Porsche AG
Gear controls housing	AutoZAZ-Daewoo
Brackets for air comfort system compressor, steering booster pump and generator	Chrysler and Volkswagen.

The chemical composition of ZE41 magnesium alloy consists of 94.44% Magnesium, 3.90% Zinc, 1.10 % rare earth elements and 0.56 % Zirconium. The specific application of ZE41 Mg is represented in the figure 1.2. ZE41 Mg alloy is used in aircraft gear box casing, generator housing of military helicopters, wheels of champion racing cars and vibration testing equipment. The mechanical and corrosion properties of magnesium alloys are influenced by alloying elements and its distribution.

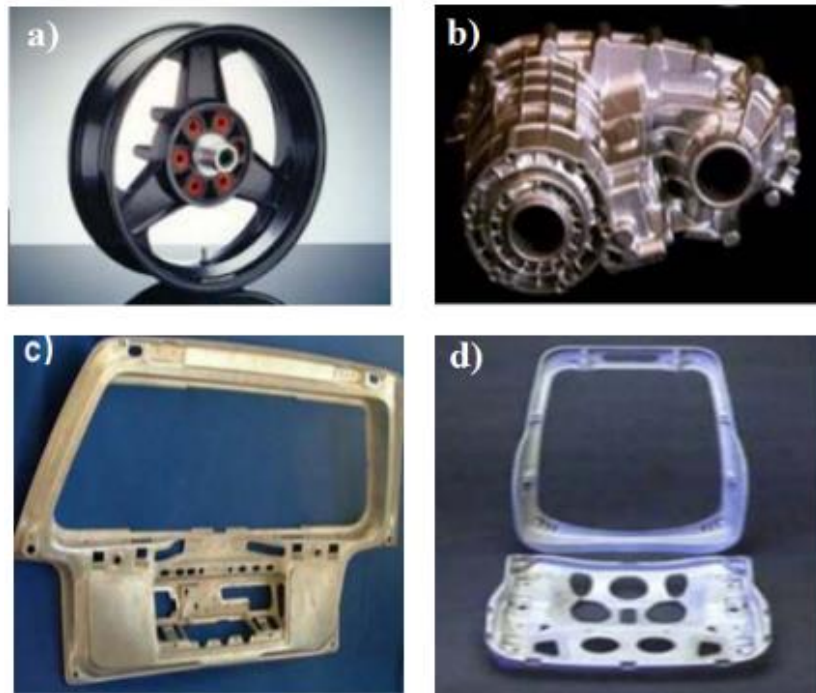


Fig 1.2 Application of ZE41 Mg in automobile (a) Automobile wheel (b) transmission casing (c) door frame (d) seat (Kuleckci, 2008).

Alloying elements such as Zn, Zr, RE (Ce,La,Gd), Al, Si, Sc and Ca are chosen to improve the desired physical, chemical and mechanical properties. Zirconium acts as a grain refiner in magnesium alloys. Rare earth containing magnesium alloys offer higher creep resistance and increases the working temperature up to 200 °C. When magnesium alloys are subjected to approximately 40% yield strength in the presence of a corrosive environment stress corrosion cracking occurs (Atrens et al. 2011). In automobile industry and military helicopters, magnesium alloys establish both electrical and physical contact with aluminium alloys and steel. ZE41 magnesium alloy suffers from galvanic corrosion when it is coupled with aluminium and steel (Mcadam et al, 2005).

1.3 STRENGTHENING MECHANISMS

The mechanical properties of metallic materials are enhanced using various strengthening techniques. Among the techniques, solid solution strengthening or alloying is the most commonly used technique. However, alloying might result only in relative improvement of mechanical properties. In contrast to alloying, significant enhancement in mechanical properties is achieved using grain boundary strengthening.

1.3.1 Severe plastic deformation

Severe plastic deformation improves the mechanical properties of metallic materials due to the effect of grain refinement. There are different types of severe plastic deformation processes; equal channel angular pressing, multi direction forging, repetitive corrugation and straightening and accumulative roll bonding. Among these severe plastic deformation processes, ECAP provides remarkable improvement in mechanical properties without changing the dimensions of the metallic materials. It also has dual advantage of improving mechanical properties as well as corrosion resistance.

1.3.2 Equal channel angular pressing

Equal channel angular pressing is one of the severe plastic deformation techniques that brings about remarkable improvement in mechanical properties such as yield strength, ultimate strength and percentage of elongation. Figure 1.3 shows the schematic representation of ECAP. Φ is the angle between two equal channels and Ψ is the corner

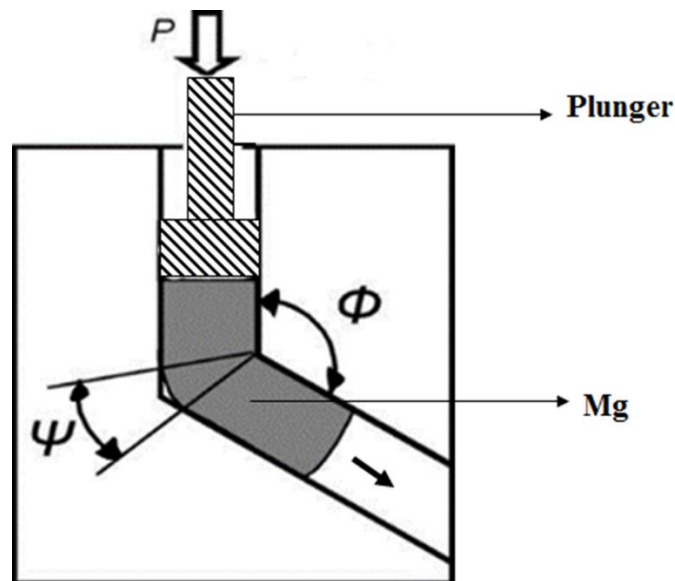


Fig 1.3 Schematic representation of ECAP process.

(Azushima et al. 2008)

angle or angle of curvature. The metallic material is placed inside the channel, heated to desired temperature and then equal channel angular pressed by using plunger in a robust universal testing machine (UTM). Based on the processing temperature, ECAP is classified into single, two step and multistep ECAP process. In single step or single stage ECAP all

the passes are carried out at same temperature. In contrast, during two step ECAP the initial passes are carried out at higher temperature followed by consecutive and final passes of ECAP at a relatively lower temperature. Recent findings have revealed that two step ECAP can result in better grain refinement than single step ECAP (Chen et al. 2008a; Jin et al. 2005; Mostaed et al. 2015). During ECAP, the grain refinement occurs due to simple shear deformation taking place at the intersection of two equal channels. The improvement in mechanical properties is correlated to grain refinement based on Hall Petch equation shown in the equation 1.1. According to Hall Petch equation the yield stress of a polycrystalline material should be improved to a greater extent by reducing the grain size (Avvari et al. 2015).

$$\sigma = \sigma_0 + k d^{-1/2} \quad \text{MPa} \quad (1.1)$$

Where “k” is strength coefficient of the metallic material, “ σ_0 ” is friction stress, “ σ ” yield stress and “d” is the grain size of the material. However, at times other metallurgical factors such as crystallographic orientation or texture affect the “k” value or strength coefficient of the material. Thus, the mechanical properties of Mg are influenced by grain refinement as well crystallographic texture. Hence, it is of prime importance to identify the individual role of grain refinement, texture and combined effect of grain refinement and texture to understand their impact on mechanical properties and corrosion behaviour of magnesium alloy.

1.3.3 Microstructure of magnesium alloys before and after ECAP.

Figueiredo and Langdon (2020) proposed grain refinement models for Mg alloys processed by ECAP. Figure 1.4 represents the schematic diagram of grain refinement model. It can be observed that the left most column viz., figure 1.4 (a), (d), (g) and (j) represent the initial microstructure of the Mg alloy. While (b), (e), (h), (k) depicts grain size after 1st pass and (c), (f), (i) shows the grain size after final ECAP passes. ‘d’ and ‘d_c’ are the initial and critical grain size of Mg alloys respectively. In the first case, the initial grain size is much higher than the critical grain size ($d \gg d_c$). After single pass of ECAP, bimodal grains were observed with the dynamic recrystallization occurring along the grain boundaries (GBs) as shown in figure 1.4 (b). The fine grains were arranged like a necklace along the GBs. Even after certain number of ECAP passes, uniform distribution of fine grains was not obtained

as seen in figure 1.4 (c). This phenomenon indicates that the Mg alloys with ($d \gg d_c$) condition required the highest number of passes to achieve uniform ultra-fine grains (UFG)

Table 1.3 Grain refinement model of Mg alloys (Figueiredo and Langdon, (2010))

Condition	Microstructure after 1 st pass	Microstructure after multi pass
$(d \gg d_c)$	Bi modal	Heterogeneous
$(d > d_c)$	Bi modal	Homogenous
$(d < d_c)$	Non bi-modal	Homogeneous

Note: 'd' – initial grain size and 'd_c' – critical grain size.

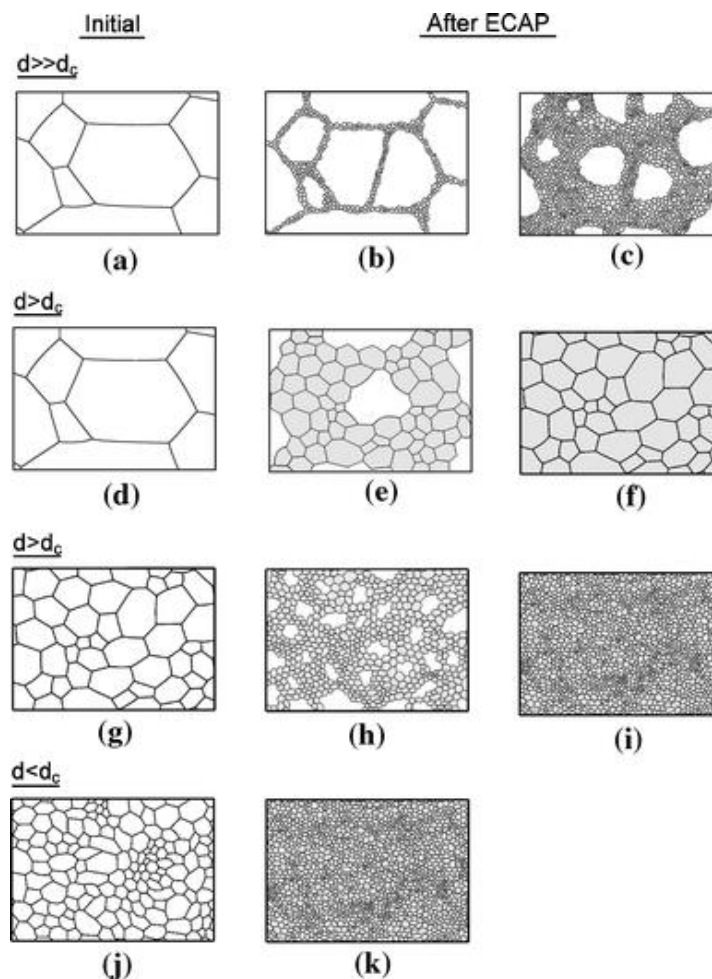


Fig 1.4 Grain refinement model of Mg alloys processed by ECAP (a), (d), (g), (j) initial grain size, (b), (e), (h), (k) grain size after 1st pass, (c), (f), (i) grain size after multiple passes. (Figueiredo and Langdon, 2010)

distribution. The grain parameters of second and third condition ($d > d_c$) were comparable in nature. But, processing history of starting material was different. As a result, after 1st pass of ECAP the area fraction of bi modal grain distribution varied as seen in figure 1.4 (e) and 1.4 (h) respectively. In contrast, in the final condition no bimodal grains are observed and uniform distribution of fine grains was achieved by the end of 1st pass. This is because initial grain size was relatively lesser than the critical grain size ($d < d_c$) (Figueiredo and Langdon , 2010). The significant findings of the grain refinement models proposed are tabulated in the table 1.3. From table 1.3 and figure 1.4 it is evident that grain refinement depends on history of initial material, initial grain size, critical grain size, processing temperature and number of ECAP passes. However, it is well established that in addition to grain refinement, texture also affects the mechanical properties and corrosion behaviour of Mg alloys. Hence, it is mandatory to evaluate the role of texture evolution occurring during ECAP of Mg alloys.

1.3.4 Texture evolution during ECAP of magnesium alloys

The grain refinement of Mg samples is generally examined from optical microscope (OM) and scanning electron micrographs (SEM) studies. However, the OM and SEM images do not give information about the crystallographic orientation or texture. Figure 1.5 shows that the orientation of basal planes changes before and after ECAP. In most of the cases, after

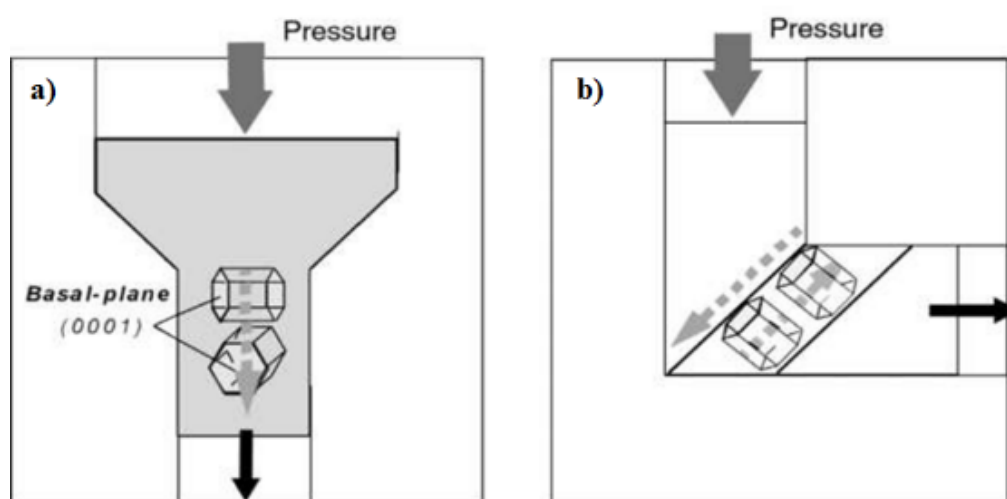


Fig 1.5 Schematic of (a) extrusion and (b) ECAP process showing the orientation of basal planes (Mukai et al, 2001).

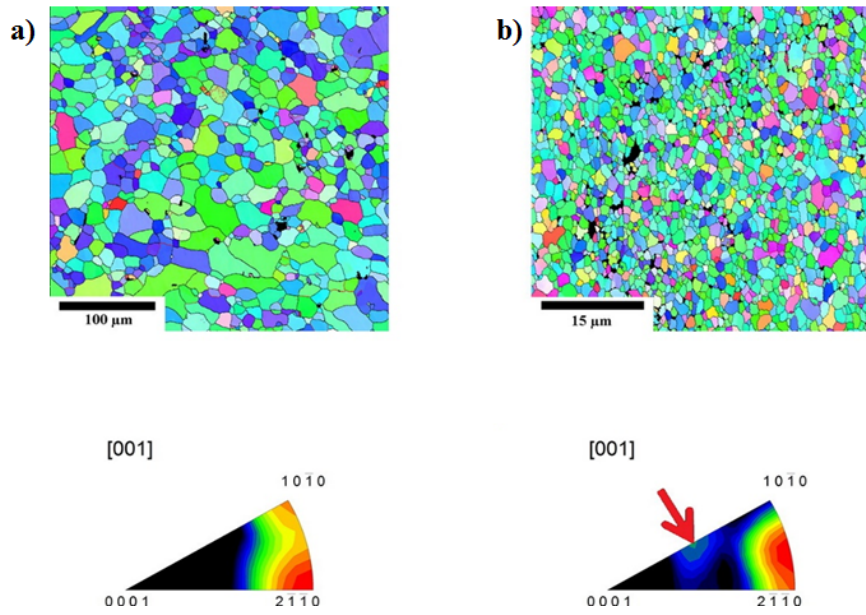


Fig 1.6 Electron back scattered micrographs of LAE442 Mg alloy in (a) extruded and (b) ECAPed condition. (Minarik et al, 2015)

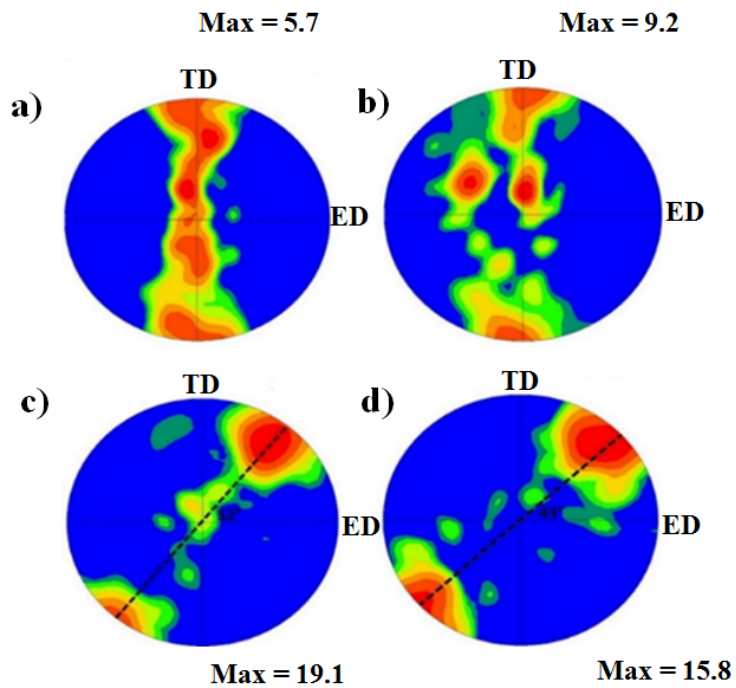


Fig 1.7 Pole figures of ZK60 Mg (a) Extruded (b) 8th pass (c) 12th pass (d) 20th pass.

(Mostaed et al, 2014)

ECAP the basal texture element gets aligned to approximately 45° with ECAP shearing plane (Agnew et al. 2004; Mukai et al. 2001). In order to detect the crystallographic orientation or texture of Mg alloys electron backscattered (EBSD) technique is used. For instance, the EBSD images of LAE442 Mg alloy in extruded and ECAPed condition is represented in the figure 1.6. From the figure 1.6, both the grain refinement details and crystallographic orientation of LAE442 Mg are revealed. In addition, grain boundary maps, texture evolution etc., can be generated from EBSD micrographs. Among various maps and plots obtained from EBSD, texture evolution plots have a greater influence on mechanical properties of Mg alloys. The pole figures generated from EBSD micrographs enlighten the texture evolution. Figure 1.7 depicts the pole figures of ZK60 Mg alloy in extruded and ECAPed conditions. The following chapters will enlighten the influence of texture on mechanical properties and corrosion behaviour of Mg alloys.

1.3.5 Mechanical properties of Mg alloys processed by ECAP.

In general, the mechanical properties viz., yield strength, ultimate tensile strength and % elongation of ECAPed Mg alloys are dependent on grain refinement and texture. In this section, the role of microstructural and texture evolution on specific mechanical property is enlightened. Figure 1.8 represents the yield strength of AE21, AE42 and LAE442 Mg alloys as a function of number of ECAP passes. Based on Hall Petch equation, the yield strength of these Mg alloys is expected to increase with increase in number of passes. Surprisingly, there is a decrease in yield strength noted even after grain refinement (Minarik et al, 2016). This is attributed to the fact that other metallurgical factors such as texture predominated the effect of grain refinement. The texture affects the “k” value in Hall Petch equation (Ding et al. 2010). The alignment of texture element after ECAP and extrusion with respect to tensile direction is shown in figure 1.9. This alignment of texture with respect to tensile direction favours the occurrence of basal slip which is detrimental to yield strength (Lin et al. 2005). This particular orientation of crystals in figure 1.9 was responsible for decrement in yield strength even after grain refinement as observed in figure 1.8. The cast Mg alloys evince random texture while rolling and extrusion of Mg alloys results in a fibre texture. The formation of such random and fibre texture is detrimental to ductility. In addition, it is previously discussed in section 1.2 that there is a need to improve the % elongation of Mg alloys to extend their application. . In contrast, ECAP disintegrates the initial random and fibre textures which leads to formation of a new texture.

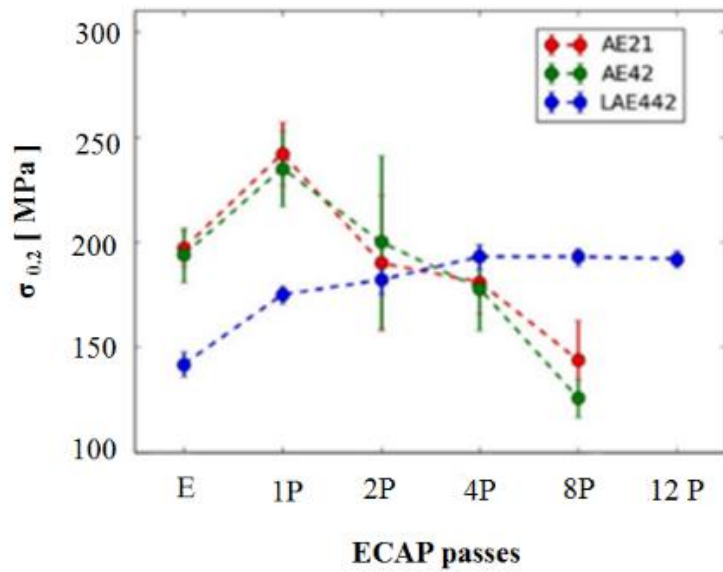


Fig 1.8 Evolution of yield tensile strength (YTS) on the increasing number of ECAP passes of all three investigated alloys (Minarik et al, 2016).

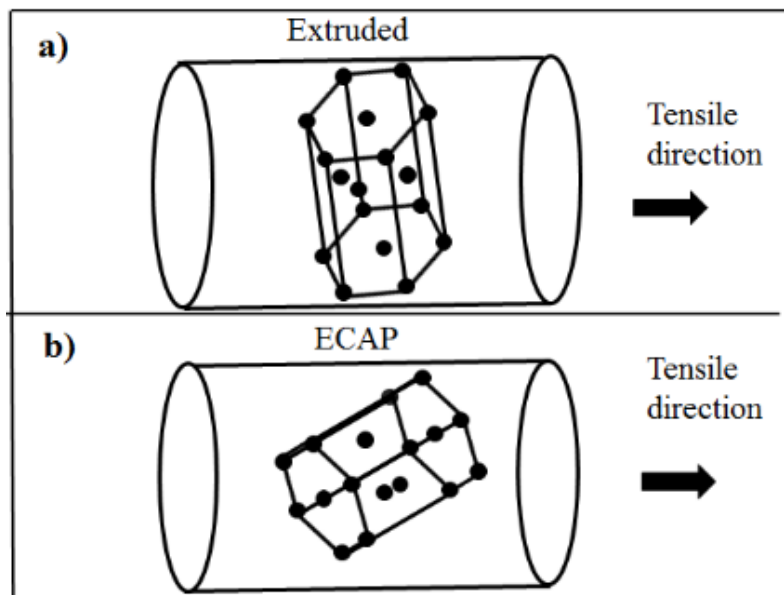


Fig 1.9 Orientation of crystal after (a) extrusion and (b) ECAP process (Lin et al, 2005).

Generally, this newly formed texture increases the % elongation of Mg alloys. Hence, it is reasonable to believe that the mechanical properties of Mg alloys is significantly enhanced by ECAP. However, enhancing only the mechanical properties of Mg alloys is not sufficient to widen their applications as relatively lower corrosion resistance of magnesium alloys and its alloys still remains a hindrance in extending applications of these alloys. In

order to improve the corrosion resistance of magnesium, it is necessary to analyse and understand the mechanism of corrosion and various factors influencing its behaviour.

1.4 CORROSION OF MAGNESIUM ALLOYS

Corrosion of magnesium and its alloys is very interesting because of the fact that there are good number of factors influencing its behaviour viz., microstructure, secondary phase and its distribution as well as crystallographic orientation. Magnesium and its alloys also deviate from standard corrosion process due to inherent anodic hydrogen evolution or negative difference effect. In addition, during corrosion of Mg alloys both chemical and electrochemical reactions take place when interacting with a corrosive medium. The above mentioned factors related to corrosion in Mg alloys highlights that there are several issues that needs attention in Mg corrosion. In addition, galvanic corrosion or bimetallic corrosion of Mg remains a major obstacle for its use in automobile and aerospace applications. This is because the self-corrosion or individual corrosion rate of AE44 Mg was reported to be ~ 0.5mm/year. In contrast, the corrosion rate of AE44 Mg- mild steel and AE44 Mg- Aluminum couple were measured to be ~197 and 42 mm/year (Deshpande, 2010a, 2010b).

1.4.1 Factors influencing the corrosion resistance of magnesium alloys

In general, Pure Mg exhibits relatively lower mechanical properties when compared to Mg alloys. This is due to the inherent HCP crystal structure of Mg (Yamashita et al, 2001). Researchers explored the role of alloying additions such as Al, Mn, Zn, Li, RE, Sr, Ca etc., or a combination of two or more elements (Bazhenov et al., 2020). The microstructure of alloyed Mg alloys contains Mg phase and its secondary phases generally distributed along the grain boundaries. In most of the cases, relative improvement in mechanical properties were noted due to the presence of secondary phases. However, the corrosion resistance decreased relatively due to formation of micro galvanic cells between bulk Mg and secondary phases formed. In order to overcome the shortcomings of alloying, coatings were used to improve the corrosion resistance of magnesium alloys. Even though coatings offered better corrosion resistance than bare Mg alloys during initial stages, the formation of macro galvanic cells between coatings and bare Mg accelerated the corrosion rate. Recent research on magnesium corrosion revealed that the grain character influences the corrosion. Some researchers claimed that the fine grains and fine distribution of secondary

phases improves the corrosion resistance and repassivation tendency (Jiang et al. 2009; Naik et al. 2019; Qiang et al. 2014; Zhang et al. 2013). In contrast, others proposed that fine grains achieved by severe plastic deformation process deteriorate the corrosion resistance (Minárik et al. 2013; Song et al. 2011a). This is because during SPD process, dislocations and grain boundaries increases significantly (Birbilis et al, 2010). In addition to grain refinement, crystallographic orientation or texture evolution influences the corrosion resistance of magnesium alloys. This is attributed to different dissolution rate possessed by basal and non-basal planes. The basal plane has more atomic density and therefore more atomic coordination when compared to the non-basal planes. Therefore basal planes have better corrosion resistance than non-basal plane (Liu et al. 2008). In order to thoroughly understand the corrosion mechanism of magnesium alloys the abovementioned factors should be taken into consideration.

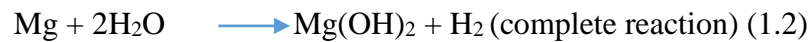
1.4.2 Corrosion of ZE41 magnesium alloy

The previous section enlightened the factors influencing the corrosion resistance of magnesium alloys in general. The role of microstructural features viz., bulk Mg, T phase (Mg_7Zn_3RE), grain size and texture effects on corrosion behaviour of ZE41 Mg is presented in this section. The size and distribution of T phase (Mg_7Zn_3RE) decorated along grain boundary, Zr rich area and Zn-Zr intermetallic particle dictated the corrosion behaviour of ZE41 Mg alloy. Heat treatment of ZE41 magnesium alloy altered the microstructural features resulting in a fine distribution of second phase particles thereby improving corrosion resistance (Neil et al. 2009, 2011). The relative Volta potential difference between magnesium matrix and secondary micro-constituents in ZE41 magnesium alloys such as grain boundary, T phase and Zr- Zn rich area were - 80, 100 and 180 mV respectively (Coy et al. 2010). ZE41 magnesium alloy offers improved corrosion resistance when processed by equal channel angular pressing and is a suitable candidate for biodegradable implants (Jiang et al. 2009; Zhang et al. 2013). The corrosion resistance of ZE41 Mg alloy is enhanced by coatings, heat treatment and addition of inhibitors (Dinodi and Shetty 2014). It is apparent that previous studies highlighted on improving either mechanical properties or corrosion behaviour of Mg alloys. However, in the real time applications, Mg is coupled with aluminium and steel which forms a macro galvanic couple. The formation of galvanic couple accelerates the corrosion of Mg alloys. Hence, it

is of necessary to study the galvanic corrosion of magnesium alloys to get insights into corrosion occurring in real time applications.

1.4.3 Occurrence of galvanic corrosion in magnesium alloys.

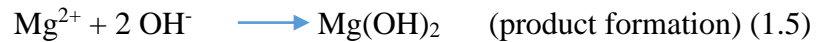
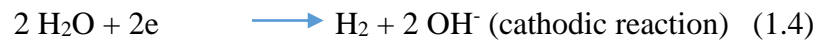
Galvanic corrosion occurs in magnesium when it is either in electrical or physical contact with other metals. This is inevitable since electrical and physical contact is needed to be established between magnesium and aluminium or steel in automobile and military vehicles. In general during galvanic corrosion magnesium becomes anode and the coupling metals viz., aluminium or steel becomes cathode. Various techniques such as zero resistance ammeter (ZRA), scanning vibrating electrode (SVE) technique and mixed potential theory are the used in measuring the corrosion rate of the galvanic couple. The corrosion reaction of magnesium including the corroded product formation is given in the below equations 1.2-1.5 (Song and Atrens, 1999).



The above reaction comprises anodic dissolution of magnesium



Hydrogen evolution occurs in cathodic reaction



In general, the term self-corrosion is referred to corrosion of single material and galvanic corrosion refers to the corrosion occurring in a galvanic couple. For instance, Mg- Al and Mg-Steel are most commonly used galvanic couple in automobile applications. The self-corrosion is always lesser than the galvanic corrosion. This is because in case of self-corrosion micro cathodes are involved. In contrast, during galvanic corrosion, coupling material acts as macro cathode. From equation 1.4 it is clear that larger cathode area results in hydrogen evolution. This higher hydrogen evolution in turn results in accelerating the dissolution of magnesium as represented in equation 1.2. The galvanic corrosion behaviour of Mg-steel, Zinc and aluminium, AE44- mild steel and AE44- Al couple was reported (Deshpande, 2010a). However, very few studies have explored the ways to combat the occurrence of galvanic corrosion (Pan et al, 2015). Electrochemical corrosion tests give

insights into understanding corrosion and galvanic corrosion mechanism of magnesium alloys.

1.4.4 Corrosion thermodynamics and kinetics of magnesium.

It is well established that the corrosion process involves material under study i.e magnesium and the environment. The corrosive medium mimic the environment and is chosen based on the intended application. In general, a surface film is formed between magnesium and corrosive environment. The properties and nature of surface films plays an important role in dictating the corrosion resistance of magnesium alloys. The properties of the surface film is understood by analysing the trend of open circuit potential curves.

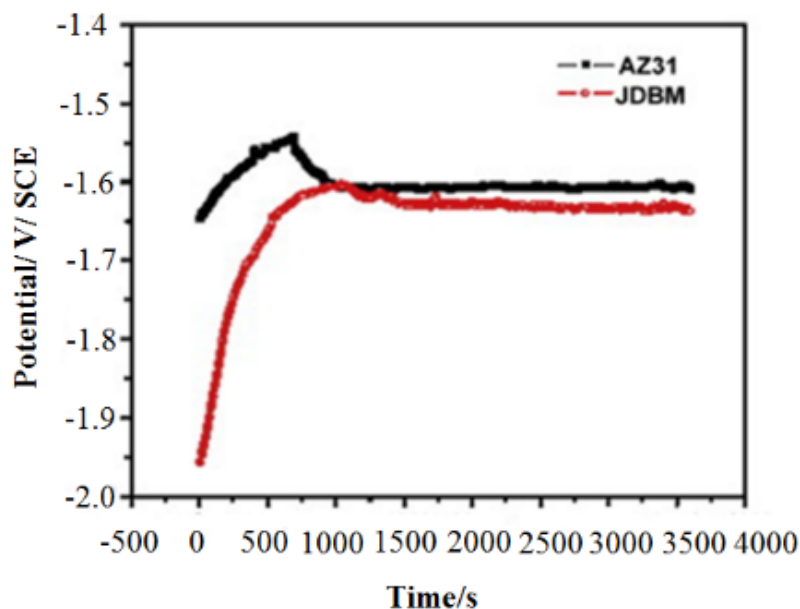


Fig 1.10 Open-circuit potential of AZ31 and JDBM alloy as a function of immersion time. (Zong et al, 2012).

The open circuit potential (OCP) curve of AZ31 and Mg–Nd–Zn–Zr (JDBM) alloy is shown in the figure 1.10. Based on the trend of OCP curves they speculated that pitting occurred in AZ31 Mg whereas no pitting evinced in JDBM (Zong et al, 2012). However, from OCP curves only the thermodynamic nature i.e stability and nature of surface film can be understood. OCP does not quantify the corrosion rate of material under investigation.

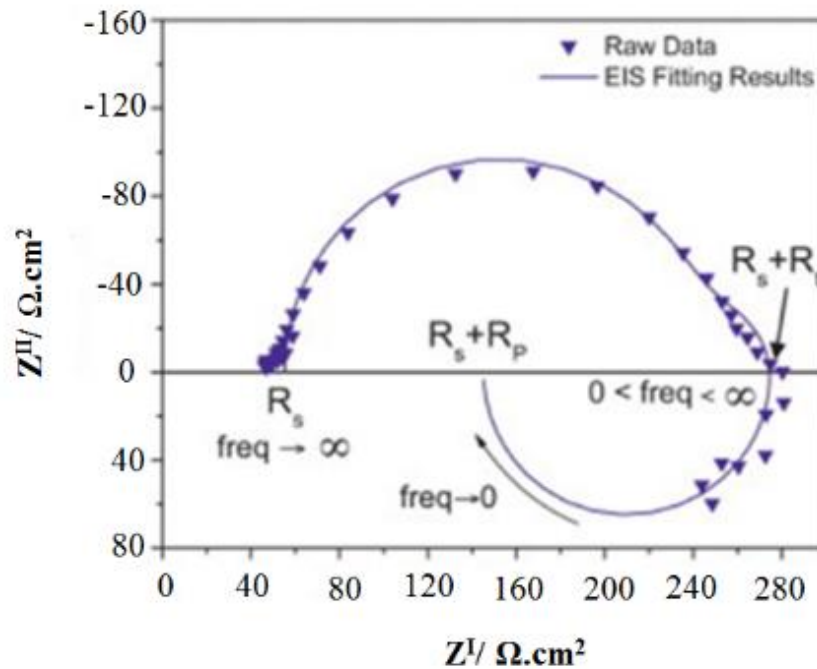


Fig 1.11 Typical Nyquist plots of Mg alloys (King et al. 2014)

The corrosion kinetics overcomes the limitations of corrosion thermodynamics. In general, the corrosion rate is quantified by using Nyquist plots and potentiodynamic polarization plots. Nyquist plots are obtained using electrochemical impedance spectroscopy (EIS) tests. This technique is non-destructive in nature and quantifies the corrosion rate based on the robustness of surface film formed between material under investigation and corrosive medium. The corrosion behaviour of pure Mg was evaluated in 0.1 M, 1 M and 5 M NaCl solution. Nyquist plots of pure Mg samples exhibited capacitive and inductive loops related to charge transfer resistance and absorption of species respectively. A typical Nyquist plot of Mg alloys is shown in figure 1.11. In contrast, the potentiodynamic polarisation technique is destructive in nature (King et al. 2014). In this case, corrosion rate is obtained from anodic and cathodic curves of Tafel plots. For instance, potentiodynamic polarization curve of ZE41 magnesium alloy with varying pH and concentration of NaCl is shown in figure 1.12. The effect of ECAP on corrosion behaviour is generally analysed from the Nyquist plots and potentiodynamic polarization curves. This in-turn gives insights into understanding the mechanism of corrosion. Also, occurrence of passivation can be detected from the anodic branch of polarization curve. In general, Magnesium and its alloys deviate from standard Tafel behaviour due to the occurrence of anodic hydrogen evolution or negative difference effect. Hence, the corrosion rate is evaluated from slope of cathodic

polarization curve (Zhao et al. 2008). Recent advancements in instrumentation enable us to analyse the galvanic behaviour of material. Zero resistance ammeter (ZRA) is integrated with the potentiostat, Galvanostat, frequency analyser and sweep generator in the electrochemical analyser (Deshpande, 2010a).

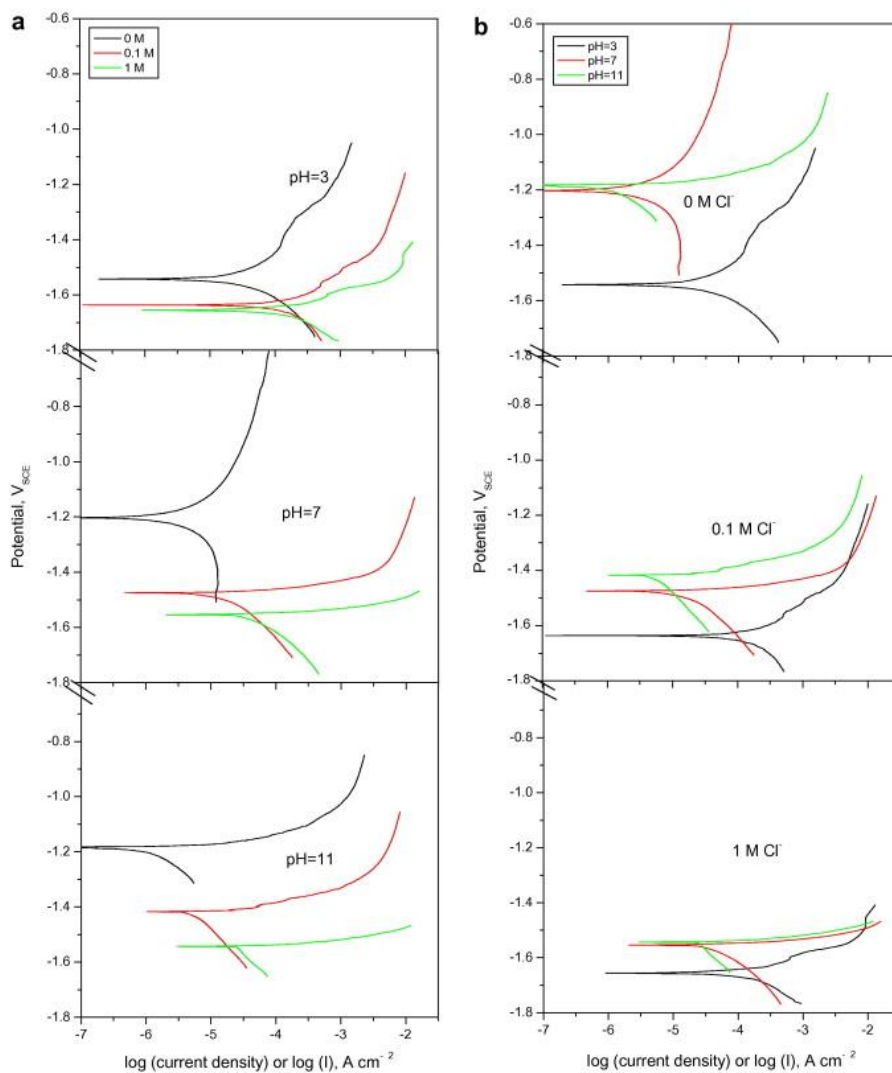


Fig 1.12 Potentiodynamic polarization curves of ZE41 magnesium alloy (a) variation in pH (b) variation in Cl⁻ concentration (Zhao et al. 2008)

1.4.5 Effect of ECAP on corrosion behaviour of Magnesium alloys

Mg alloys such as ZE41, ZM21, AE42 and AZ80 Mg subjected to ECAP improved the corrosion resistance of alloys due to fine distribution of secondary phase particles and better repassivation tendency (Jiang et al. 2009; Naik et al. 2019; Qiang et al. 2014; Zhang et al.

2013). In contrast, the adverse effects were observed in pure Mg, AZ91D and AE21 due to introduction of crystalline defects such as dislocation density and generation of high angle grain boundaries (HAGBs) after ECAP (Minárik et al. 2013; Song et al. 2011a). However, the recent research suggests that crystallographic orientation has a greater influence on corrosion behaviour (Song et al. 2010; Wang et al. 2016; Xin et al. 2011). Hence, it is of prime importance to evaluate the role of secondary phase, crystalline defects, and crystallographic orientation of Mg alloys to thoroughly understand the corrosion mechanism. The corrosion and galvanic corrosion behaviour of ZE41 Mg alloy due to altered microstructure after equal channel angular pressing and will be explained in detail in the results and discussion chapter.

1.5 SUMMARY

Research and development in the automobile, aerospace and defence sector have enlightened the importance of magnesium and its alloys. Magnesium and its alloys exhibit relatively lower ductility and higher susceptibility to corrosion. These inherent properties of magnesium alloys hinder wider usage in the automobile applications. This creates a necessity to process magnesium alloy by techniques that have potential to enhance the mechanical properties as well as corrosion resistance. ECAP is one of the severe plastic deformation techniques that significantly improves the mechanical properties as well as corrosion resistance of magnesium alloy. The mechanical properties and corrosion behaviour of ECAPed magnesium alloys are influenced by grain refinement and crystallographic orientation or texture. EBSD is a versatile technique that enlightens both the grain refinement and texture evolution. Hence, in the present research the mechanical properties and corrosion behaviour of ZE41 Mg alloy is correlated to microstructures obtained as a result of ECAP. They are observed using optical microscope (OM), scanning electron microscope (SEM) and electron back scattered diffraction (EBSD). In addition, an attempt is made to explore the galvanic corrosion behaviour of ZE41Mg – Al7075 couple in 0 M, 0.1 M and 1 M NaCl solution.

1.6 THESIS ORGANISATION

This thesis details enlightens the microstructure, mechanical properties and corrosion behaviour of ZE41 Mg alloy subject to two step ECAP. Also, the mechanism of corrosion

and galvanic corrosion occurring in ZE41 Mg alloy and ZE41 Mg – Al7075 Al couple is proposed. The thesis is presented as per the following chapters.

CHAPTER 1

Introduction chapter covers the importance of Mg alloys and its applications especially in the field of automobile applications. The limitations of Mg alloys that limits their use in to certain applications only is also discussed. In addition, the role of equal channel angular pressing in improving the mechanical properties and corrosion resistance of Mg alloys are explained in brief.

CHAPTER 2

The microstructure, mechanical properties and corrosion behaviour of Mg alloys before and after equal channel angular pressing from previous studies is critically reviewed. The strengthening mechanisms viz., solid solution, precipitate, grain boundary and texture strengthening that dictates mechanical properties of ECAP samples is enlightened. The factors influencing the corrosion mechanism of Mg alloys is also discussed. Based on literature review a strong foundation is established to decide the objectives for the current study.

CHAPTER 3

The experimental work highlights the composition of ZE41 Mg. It also elucidates on selecting the processing temperature for carrying out two step ECAP on ZE41 Mg. In addition, it summarizes the equipment used for investigating the microstructural, mechanical characterization and electrochemical testing of ZE41 Mg alloy before and after ECAP. The research methodology adapted to achieve the objectives of the present study is also highlighted.

CHAPTER 4

The microstructures of ZE41 Mg samples before and after ECAP generated using EBSD are revealed in this chapter. The mechanical properties of ZE41 Mg samples were correlated to grain refinement, distribution of secondary phases and texture effects. In addition, the chapter enlightens the strengthening mechanisms that affects the mechanical properties of ZE41 Mg.

CHAPTER 5

The corrosion behaviour of ZE41 Mg is discussed in detail. The combined effect of grain refinement, crystallographic orientation and role of secondary phases in ZE41 Mg alloys is enlightened. The possible mechanism of corrosion occurring in ZE41 Mg prior to ECAP and after processing is compared and highlighted.

CHAPTER 6

This chapter discusses the corrosion behaviour of ZE41 Mg alloy – Al7075 Al alloy couple in three varying concentration of 0M, 0.1M and 1M NaCl which in turn mimic automobile service environment. In addition, the mechanism of galvanic corrosion is proposed in this chapter based on results obtained from microstructural characterization, x-ray diffraction (XRD) and x-ray photoelectron spectroscopy (XPS). The role of fine grains and secondary phases obtained from ECAP that assisted in combating galvanic corrosion is also specified in this chapter.

CHAPTER 7

This chapter includes conclusion on the role of equal channel angular pressing in enhancing the mechanical properties, corrosion and galvanic corrosion behaviour of ZE41 Mg. The scope of future work is also proposed.

CHAPTER 2

LITERATURE REVIEW

2.1 INTRODUCTION

This chapter presents the literature review on microstructure, mechanical properties, texture evolution, corrosion and galvanic behaviour of magnesium alloys processed by ECAP. The combined effect of grain refinement, texture evolution on mechanical properties and corrosion behaviour of Mg alloys is enlightened. Also, the various processing and environmental factors affecting mechanical properties, corrosion and galvanic corrosion of magnesium alloys has been reviewed and presented. Based on the literature review, research gaps and objectives for the present research work have been derived.

2.2 CAST MAGNESIUM ALLOYS

It is noteworthy to mention that, at present, 90% of magnesium based products are produced by casting process. Commercially available cast Mg is generally alloyed with aluminium and rare earths elements forming Mg-Al and Mg-RE alloying systems respectively. However, Mg-Al alloys are not recommended to be used at a temperature above 120 °C due to their relatively lower creep resistance (Yang et al., 2005). In contrast, rare earth containing Mg alloys (Mg-RE) offer higher creep resistance and increase working temperature upto 200 °C (Dargusch et al., 2020). Pan et al (2016) reported that cast Mg alloys exhibit relatively better economic advantage than wrought Mg alloys. This is because cast magnesium alloys have following advantages such as (i) processed in shorter time (ii) assembled at low cost (iii) easier for mass production. Zheng et al. (2014) reported that in general the mechanical properties of Mg alloys based on the processing history followed the trend cast Mg < wrought Mg < SPD Mg. Cast magnesium alloys typically evince relatively lower % elongation. In contrast, wrought Mg alloys processed by rolling, extrusion and forging process undergo change in dimensions and hence not suitable for structural applications (Azushima et al., 2008). It is well established that Mg alloys exhibit relatively lower corrosion resistance. Alloying leads to formation of secondary phases which forms micro galvanic cells and accelerates corrosion. In contrast, during rolling and extrusion of magnesium alloys formation of twins deteriorate the corrosion resistance. The

conventional techniques viz., alloying, rolling, extrusion and forging do not enhance the mechanical properties of Mg alloys significantly. In addition, they deteriorate the corrosion resistance due formation of micro galvanic cells and twins (Hou et al., 2019; Song et al., 2003). This necessitate the design and development of Mg alloys exhibiting superior mechanical properties as well as improved corrosion resistance. The research communities across the globe are still exploring several ways to significantly enhance the mechanical properties as well as corrosion resistance of Mg alloys. Mostaed et al. (2014) reported that ECAP enhanced the mechanical properties and corrosion resistance of ZK60 Mg alloy. Krajňák et al., (2019) proved that better grain refinement of 1.4 μm was obtained in as cast AX41 Mg compared to the extruded alloy with G.S of 2.4 μm after 8th pass of ECAP. Hence, in the present study, as cast ZE41 Mg alloy was subject to ECAP to simultaneously enhance mechanical properties as well as corrosion behaviour. The improvement in mechanical properties of Mg alloys is attributed to strengthening mechanism.

2.3 STRENGTHENING MECHANISMS

In the recent years, achieving high strength and better ductility in Mg alloys has gained immense research interest. However, achieving such desirable properties in Mg alloys is challenging till date. It is also well known that the casting of Mg alloys leads to formation of defect such as porosity, shrinkage and inclusion that has negative effect on strength and ductility of Mg alloys (Yuan et al, 2013). In addition, wrought Mg alloys processed by rolling and extrusion evince a strong basal texture that deteriorate the ductility of Mg alloys (Minárik et al, 2016). On the contrary, simultaneous improvement in strength and ductility was achieved in Mg alloys processed by ECAP (Minárik et al. 2013, Minárik et al. 2016a). Also, it is well established that the mechanical properties of Mg alloys are governed by the strengthening mechanisms. The strengthening mechanisms viz., solid solution strengthening, precipitate strengthening, grain boundary and texture strengthening were reported in Mg alloys and are discussed in detail.

2.3.1 Solid solution strengthening.

Zhou et al (2020) reported that the ultimate tensile strength (UTS) and % elongation of AZ61 Mg were 295 MPa and 18 %. Upon addition of 2% Calcium, the UTS increased relatively to 312 MPa and % elongation was 17.5%. Bazhenov et al., (2020) stated that the mechanical properties of MgZnSiCa alloy developed by sand casting technique reported

yield strength (YS): 57 MPa, UTS: 133 MPa and % El: 4.5 %. The mechanical properties of MgZnSiCa increased significantly YS: 117 MPa, UTS: 215 MPa and % El: 12 % as a result of high pressure die casting. Zhou et al., (2020) evaluated the mechanical properties of Mg-1 Zn alloy after 0.5 % of Sn addition. The YS of Mg- 1 Zn enhanced relatively from 110 MPa to 115 MPa in Mg-1 Zn- 0.5 Sn. Wang et al. (2020) investigated the mechanical properties of Mg-4Zn micro alloyed with 0, 0.5, 1 and 2 Wt% addition of Gadolinium. The YS of Mg-4 Zn enhanced from 240 MPa to 286, 351 and 369 MPa for 0, 0.5, 1 and 2 Wt% Gd addition respectively. However, the % El of Mg-4 Zn decreased from 24.5 % to 15.3, 10.7 and 7.8 % for Gd addition of 0, 0.5, 1 and 2 Wt% respectively. In summary, it is reasonable to conclude that the solid solution strengthening or alloying results only in relative improvement of mechanical properties of Mg alloys. Therefore, an additional technique is required to further enhance the mechanical properties of Mg alloys in order to extend its applications.

2.3.2 Precipitate strengthening

Minarik et al. (2017) reported that precipitation strengthening occurred in WE43 Mg alloy due to ultra-fine Mg₅RE precipitates of ~150 nm achieved by multi step ECAP. Yuan et al.(2016) carried out thermo-mechanical process such as pre solution heat treatment, ECAP and low temperature aging treatment on ZK60 Mg. MgZn₂ precipitates in the form of spherical and rod shaped of about sub microns to nano level were responsible for precipitation strengthening effect. The grain boundary strengthening effect along with precipitation strengthening led to increase in work hardening of ZK60 Mg. Zhang et al. (2015) reported that the MgZnRE and REH₂ phase were responsible for precipitation strengthening that occurred in Mg-Gd-Nd-Zn-Zr alloy. Surprisingly, mechanical properties increased linearly with increase in ECAP passes. They claimed that such chronological increase was attributed to combination of grain refinement, precipitate strengthening and texture evolution. Based on the above mentioned research on precipitation strengthening of Mg alloys it is evident that precipitate strengthening generally occurred in rare earth containing Mg alloys.

2.3.3 Grain boundary and texture strengthening

It is well known that the mechanical properties of Mg alloys are altered by tailoring the microstructure. By reducing the grain size of metallic materials in the range of ~1 to 10 μm

or several nanometres, yield strength is expected to increase according to Hall Petch relation. This phenomenon is corroborated to grain boundary strengthening (Yuan et al, 2013). Researchers observed that the Mg alloys processed by ECAP deviated from classical Hall Petch relationship (Kim et al, 2002; Krajňák et al. 2017). The reason for such deviation was not known until the invention of advanced material characterization techniques. These techniques revealed that the mechanical properties of Mg alloys were also influenced by texture strengthening. This was evident from macro and micro texture plots generated from X ray pole figures and EBSD (Minárik et al. 2013, Minárik et al. 2016a). The yield strength of Mg alloys was not increased chronologically with increase in number of ECAP passes. This was attributed to the fact that basal planes were aligned ~ 45 to 55° to theoretical shear plane of ECAP that requires less stress for yielding. As a result, the effect of texture predominated the influence of grain boundary strengthening during ECAP (Agnew et al. 2004; Mukai et al. 2001).

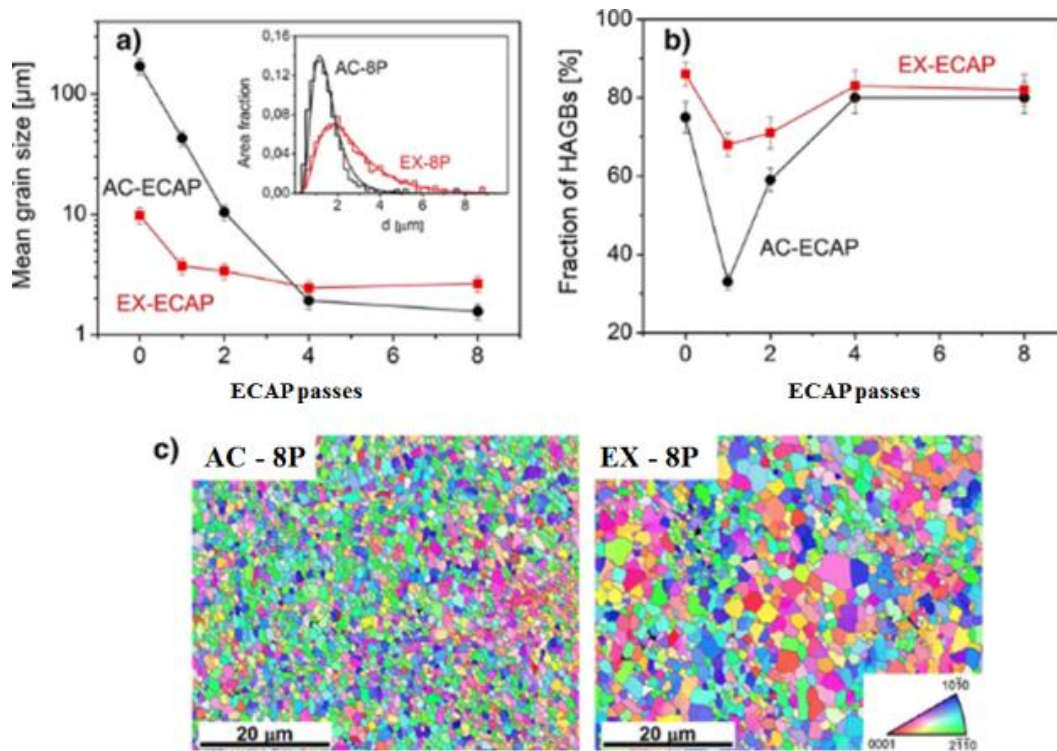
2.4 EQUAL CHANNEL ANGULAR PRESSING

Avvari et al., (2015) reported that the die geometry, processing routes, ram speed, application of back pressure and processing temperature are the various factors involved in ECAP. Among them, ECAP processing routes and temperature are the most important factors affecting microstructure and mechanical properties of magnesium alloys. In addition, it is well established that among processing routes, significant grain refinement is achieved using route Bc. Based on the processing temperatures, ECAP is classified into single step, two step and multi-step ECAP process (Naik et al., 2019). In single step ECAP process, each and every pass is carried out at the same temperature. In contrast, during two step and multi-step ECAP process the sample is processed using two different and more than two temperatures respectively.

2.4.1 Effect of microstructure on mechanical properties of Mg alloys after single step ECAP

Mukai et al, (2001) examined the microstructure and mechanical properties of extruded and ECAP + annealed AZ31 Mg alloy. The grain size of extruded, ECAPed and ECAP + annealed samples were measured to be 15 μm , 1 μm and 14 μm respectively. They observed that the grain size of extruded and ECAP + annealed samples were similar. However, the yield strength of ECAPed AZ31 Mg was ~ 220 MPa which was significantly higher than

that obtained in the extruded condition ~120 MPa. In contrast, the ECAP + annealed sample exhibited a ductility of 47% that is two times higher than that exhibited by 22 % in extruded sample. Hence, they concluded the role of grain refinement was dominated by texture effects. Kim et al. (2002) performed 8 passes of ECAP on extruded AZ61 Mg alloy at a temperature of 275° C. The grain size of extruded, 1st pass and 8th pass sample were measured to be 24 μm, 16 μm and 8.3 μm respectively. The yield strength of extruded, 1st pass and 8th pass samples were found to be 261 MPa, 249 MPa and 232 MPa. They proved that the decrease in yield strength even after grain refinement was attributed to development of new texture elements as a result of ECAP. Agnew et al. (2004) evaluated the microstructure and mechanical properties of AZ31B Mg alloy. The extruded Mg alloy having grain size of 49 μm reduced to fine grains of 6 μm. The yield strength of extruded sample reduced from ~200 MPa to ~100 MPa after 8th pass of ECAP. They reported that basal texture aligned in preferred orientation was favourable for slip which in turn required lower stress for yielding. This texture strengthening was the reason for the drop in yield strength which was in line with previous research findings (Mukai et al, 2001). To confirm the occurrence of texture strengthening in Mg alloys they evaluated the mechanical properties of ECAPed samples with six different orientations. They observed that the all the six ECAPed samples with various orientations exhibited a yield strength that is relatively lower than extruded AZ31 Mg. Lin et al. (2005) examined the microstructure and mechanical properties of extruded and ECAPed AZ31 Mg alloy. The average grain size of as extruded AZ31 Mg reduced from 2.5 μm to 0.7 μm after 8th pass of ECAP. Surprisingly, the yield strength of ECAPed sample was measured to be 217 MPa which is relatively less when compared to 265 MPa exhibited by extruded sample. Dumitru et al. (2014) performed ECAP on extruded ZK60 Mg alloy with average grain size of 37μm. A relative increase in grain size from 3rd pass condition to 4th pass ECAP was observed due to less stable nature of fine grains. However, even after 4th pass of ECAP, heterogeneous grains of size 2.4 μm and 10.9 μm were observed. The yield strength decreased from 221 MPa in extruded alloy to 148 MPa by the end of 4th pass. Rather than showing evidence for decrease in yield strength, the authors claimed that this phenomenon was observed by various researchers (Mukai et al, 2001; Agnew et al. 2004). Avvari et al. (2015) performed ECAP on AZ80 Mg alloy at different processing temperatures of 275 °C, 300 °C and 350 °C. The yield strength of the as cast and ECAPed samples was in the range of 120 to 160 MPa. This is attributed to the relatively larger grains size of 7 μm, 10 μm and 11 μm that were observed even after



Note: AC – as cast, EX – extruded, 8P – 8th pass of ECAP

Fig 2.1 Evolution of (a) the mean grain size in logarithmic scale, (b) the fraction of HAGBs with increasing number of ECAP passes (N) and (c) inverse pole figure maps of the samples after 8th pass (Krajňák et al., 2019).

4th pass ECAP. Gopi et al., (2016) subjected cast AM70 Mg alloy of 45 μm grain size to ECAP at a temperature of 275 °C. A grain refinement of 1 μm was achieved by the end of 4th pass ECAP. The Yield strength of all ECAPed samples were greater than as cast sample. However, the 2nd pass ECAPed sample evinced the highest yield strength of 170 MPa among all samples. The authors reported that this deviation from Hall Petch relation was attributed to texture components. However, they did not provide conclusive evidence of such texture evolution with respect to each ECAP passes. Naik et al., (2019) carried out ECAP on cast AZ80 Mg having average grain size of 50 μm . They achieved a grain refinement of ~6.35 μm by the end of 4th pass processed at 325°C. This resulted in increased yield strength from 400 MPa for as cast alloy to 489 MPa by 4th pass ECAP. Krajňák et al., (2019) investigated the microstructure of as cast and extruded AX41 Mg after ECAP. The mean grain size, fraction of high angle grain boundaries (HAGBs) and inverse pole figures of AX41 Mg samples are represented in the figure 2.1. A final grain size of 1.4 and 2.4 μm

was achieved after 8th pass in as cast and extruded Mg alloy respectively. They reported that polygonization of dynamic recovery and dynamic recrystallization and were responsible for grain refinement that occurred in as cast and extruded condition. Ding et al. (2010) reported that after 6th pass ECAP the yield strength and percentage of elongation of ZE41 Mg increased from 160 MPa and 8% to 230 MPa and 20% respectively. They also concluded that the 1st pass, 2nd pass and 6th pass samples exhibited comparable value of yield strength even after significant grain refinement. Similar trends in yield strength of Mg alloys were reported after single step ECAP. This is attributed to the fact that texture affecting strength co-efficient in Hall Petch relationship. In order to further enhance the mechanical properties of ZE41 Mg two step ECAP was adapted in the present study.

2.4.2 Mechanical properties evaluation in magnesium alloys after two step and multi-step ECAP.

Mostaed et al., (2015) carried out two step ECAP (200° C & 150° C) on extruded ZM21 Mg alloy. The EBSD micrographs of ZM21 Mg alloys are depicted in the figure 2.2. The extruded, single step and two step ZM21 Mg samples exhibited grains of diameter 16 µm, 0.7 µm and 0.9 µm. Despite the significant grain refinement, the tensile strength of extruded ZM21 Mg sample increased relatively from 172 MPa to 212 MPa during first stage ECAP. During second stage, the yield strength dropped to 110 MPa. The % elongation of extruded and first step ECAPed samples were 22 % and 24 % respectively. In contrast, the % elongation of second stage ECAP sample was increased to 40 % which is significantly higher than extruded and single step ECAP sample. Based on the results they concluded that the grain refinement dominated during first step of ECAP. Whereas, in the second step ECAP, texture effects predominated the role of grain refinement. AZ31 Mg alloy was processed using single-step and two-step ECAP. The stress strain curves of AZ31 Mg after single step and two step ECAP is shown in the figure 2.3. After single step ECAP at 225°C, the yield strength of ECAPed sample was comparable to as received sample. Surprisingly, the % elongation improved from 20% in as received condition to 33% after 5th pass ECAP. In contrast, during two step ECAP, the significant enhancement of yield strength from 150 MPa in as received sample to 276 MPa was observed. In addition, the two step ECAPed sample evinced elongation of 29% (Jin et.al, 2005).

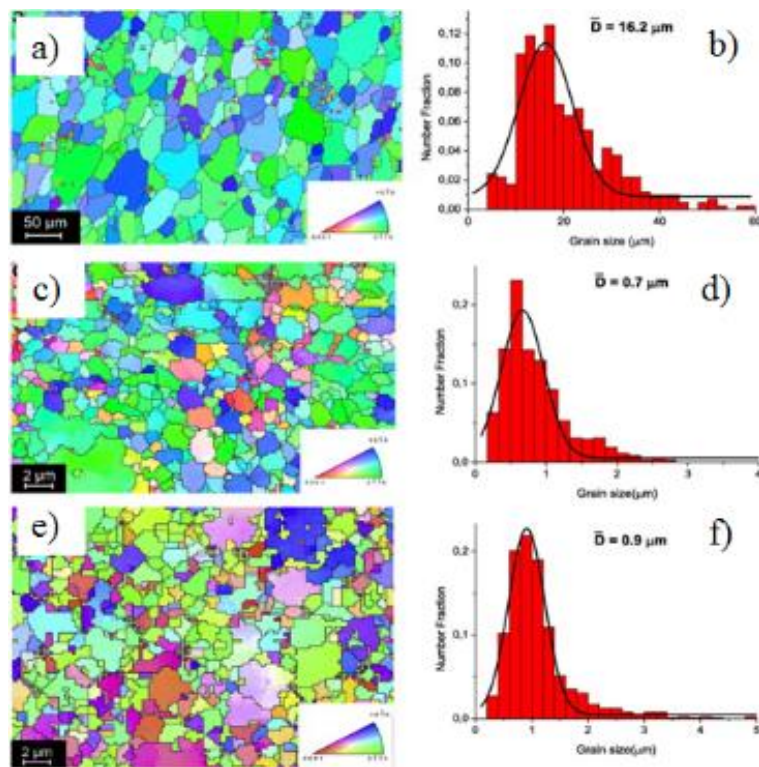


Fig. 2.2 EBSD image orientation maps and corresponding grain size distribution of (a and b) extruded, (c and d) 4th pass at 200 ° C (e and f) 4th pass at 200 ° C + 4th pass at 150 ° C (Mostaed et al., 2015).

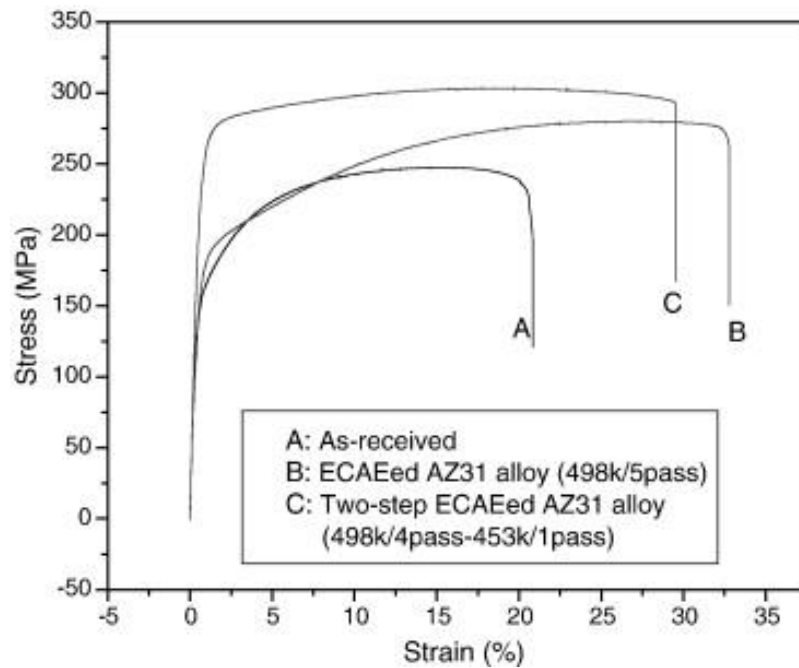


Fig 2.3 Stress strain curve of AZ31 for different ECAP processing conditions.

(Jin et.al 2005)

Chen and co-workers also carried out similar work on AZ91 Mg alloy. They reported that yield strength increased after ECAP but ductility decreased when the sample was 4th pass at 225 °C (single step ECAP). This deterioration in ductility was attributed to the presence of undissolved Mg₁₇Al₁₂ precipitates. When 4th pass sample was additionally ECAPed for another 2 passes at 180 °C i.e two step ECAP the ductility was recovered. The stress strain curve of AZ91 Mg for different ECAP processing conditions is depicted in figure 2.4.

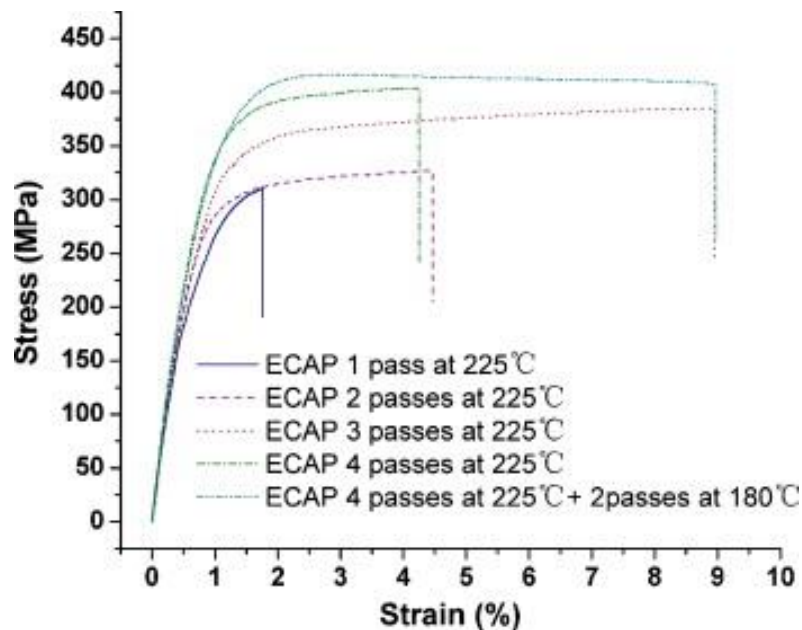


Fig 2.4 Stress Strain curves of AZ91 at single and two step ECAP (Chen et.al 2008).

Qiang et al. (2014) carried out ECAP on pure Mg and ZM21 Mg to evaluate their biodegradable properties. Pure Mg was ECAPed at a temperature of 275°C in the first step upto 2 passes. During the second step, the samples were subjected to additional passes at 250°C. The grain refinement of only ~40 µm was achieved in pure Mg even after two step ECAP due to initial higher grain size of ~100 µm in Mg. In contrast, when as cast ZM21 Mg having a grain size of ~15 µm was subjected to two step ECAP, a grain refinement of 500 nm was achieved. Minarik et al. (2017) achieved a grain refinement of 350 nm by subjecting as cast WE43 of grain size ~110 µm using multistep ECAP. The compression yield strength of as cast alloy increased from 125 MPa to 318 MPa and 427 MPa after 4th pass and 8th pass respectively. They claimed that the significant increase in compression yield strength was related to the combination of grain boundary strengthening and precipitation strengthening effect. Yuan et al. (2016) evaluated the mechanical properties

of ZK60 after single step ECAP at 300 °C and multistep at temperatures of 250°C, 200°C, 150°C ECAP. The mechanical properties of single step ECAPed samples were observed as yield strength (YS): 193 MPa and percentage elongation of 19%. In contrast, the yield strength of multi-step ECAP was measured to be 260 MPa but the % El was relatively lower % El: 18.5% compared to single step ECAP. They reported that grain boundary and precipitate strengthening assisted in simultaneously improvement of strength and ductility. The stress strain graphs of ZK60 Mg after single step and two step revealed that the tensile strength was dependent on grain size as well as texture. The texture developed during single-step and two-step ECAP was similar but the finer grain size obtained in two step ECAP contributed to improved mechanical properties when compared with single step ECAP (He et al. 2010). The effect of ECAP processing temperature of 250 °C and 220 °C on microstructure, texture and mechanical properties of AX41 Mg alloy was investigated. When processing ECAP at lower temperature higher number of passes was required to attain equiaxed homogenous microstructure. But, the grain refinement after 8th pass at 220 °C, 250 °C was found to be 2.7 µm and 4µm respectively. This behaviour of grain refinement in 8th pass at 220 °C was attributed to the higher density of dislocations and specific texture attained in ECAP processing (Krajňák et al. 2017). The multi-step ECAP strategy was adapted to obtain grain refinement in AE21, AE42 and LAE442 Mg alloys. The initial grain sizes of only AE containing alloys (AE21 and AE42) were comparable. Hence, both AE21 and AE42 resulted in a fine grains of ~ 1µm by the end of 8th pass ECAP. In contrast, there is pronounced difference in grain sizes of Li containing (LAE442) and non- Li containing (AE21 and AE42) Mg alloys. The fine grains of ~ 1µm was also achieved in LAE442 Mg alloy at relatively higher number of pass i.e 12th pass ECAP (Minarik et.al, 2016). Based on the observation from the above mentioned studies, it is reasonable to believe that by carrying out two step ECAP, simultaneous improvement in both yield strength and ductility can be obtained. Hence, two step and multistep ECAP strategy has great potential in obtaining fine grains with desirable mechanical properties.

2.5 GRAIN BOUNDARY CHARACTERISTICS OF MAGNESIUM ALLOYS

Grain boundary (GBs) characteristics are important to understand the microstructural evolution of Mg alloys after ECAP. From, EBSD micrographs a wide variety of grain boundary related maps can be generated. Victoria-Hernández et al. (2016) revealed the stored strain energy in unprocessed, shearing zone and ECAPed zone of AZ31 Mg sheet as

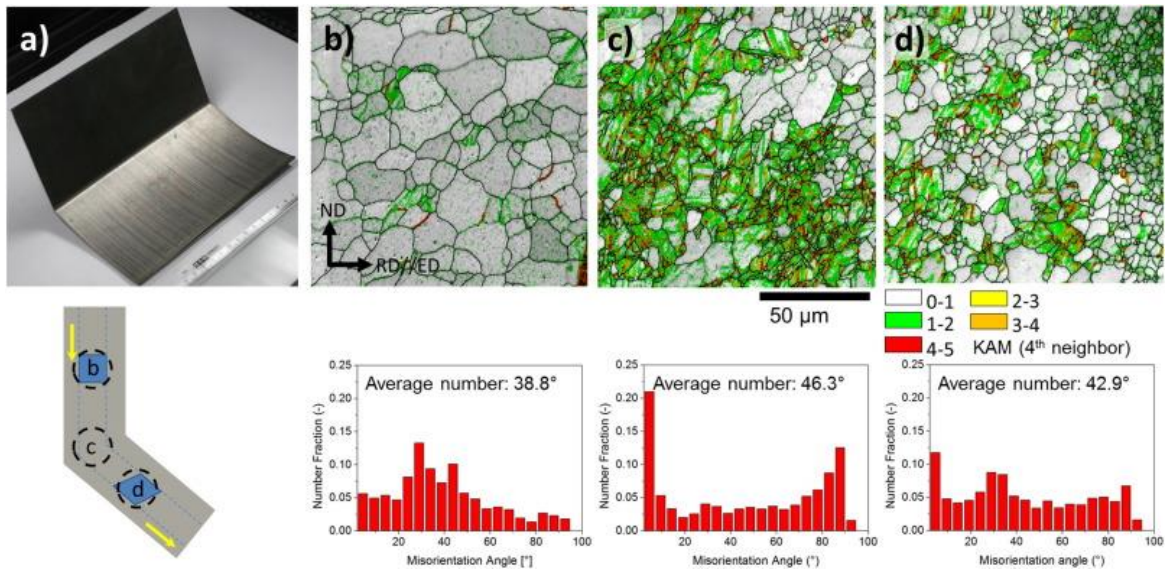


Fig 2.5 a) ECAP deformed sample and schematic representation of different zones, b) unprocessed, c) shearing zone and d) ECAPed zone (Victoria-Hernández et al., 2016)

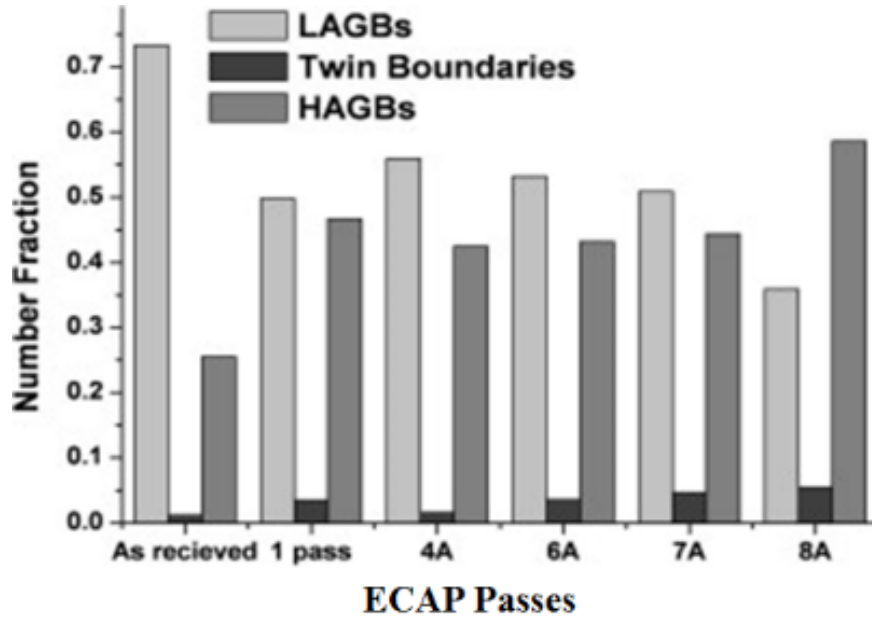


Fig 2.6 Grain boundary character distribution for the initial and the ECAE-processed samples (Biswas et.al, 2010)

shown in figure 2.5. The area fraction of strain increased significantly from unprocessed to shearing zone but decreased relatively at ECAPed zone. The average number fraction of grain boundaries was also found to be 38.8, 46.3 and 42.9 for unprocessed, shearing zone and ECAPed zone of AZ31 Mg sheet respectively. The trend of stored strain in their study was in accordance with formation of HAGBs. Suh et al., (2015) carried out ECAP on rolled AZ31 Mg sheets. The yield strength of as rolled AZ31 Mg decreased from 190 MPa to 130 MPa, 137 MPa and 146 MPa due to increased tensile twins when ECAPed at 175 °C, 200 °C and 225 °C respectively. The same research group extended the work and studied the anisotropic properties of rolled, 1st pass and route D ECAPed conditions in AZ31Mg. The route D ECAPed sample exhibited better isotropy when compared to rolled and 1st pass ECAP sample. They also reported that the ductility of ECAPed samples increased from 13.4 % to 18.4% because of increase in Schmid factor values (Suh et al., 2016). LAE442 Mg alloy was processed by ECAP. With increase in number of ECAP passes, the length fraction of LAGBs decreased with simultaneous increase in HAGBs. (Minarik et.al, 2016). In another study, the pure Mg alloy in as cast condition was ECAPed upto 7th pass using multi step technique. Interestingly, the final pass of ECAP was carried out at room temperature and grain size of 0.25 µm was achieved. Their study also indicated that with increase in number of ECAP passes the number fraction of HAGBs increased with simultaneous decrement in LAGBs as seen in figure 2.6. In addition, the twin boundaries number fraction also increased with increase in ECAP pass number (Biswas et.al, 2010). ZX11 Mg evinced twins as a result of rolling. The strain energy stored in the rolled sample were also revealed using kernel average misorientation (KAM) maps. After annealing treatment the twins disappeared and the stored strain energy also reduced significantly (Hou et.al, 2019). 80% volume fraction of HAGBs was observed in both as cast and extruded AX41 Mg after 8th pass of ECAP (Krajňák et al., 2019). From the above mentioned studies, it is very apparent that GB maps generated from EBSD helps to better understand the mechanical properties of Mg alloys subject to rolling, extrusion and equal channel angular pressing.

2.6 EFFECT OF TEXTURE EVOLUTION ON MAGNESIUM ALLOYS PROCESSED BY ECAP

The mechanical properties of Mg and its alloys are dictated by combined effect of grain refinement and texture or crystallographic orientation of material. The grain refinement of

Mg samples is generally evident from OM and SEM images. To detect the texture of Mg alloys EBSD detector and XRD are used. The micro texture is generated from EBSD images using TSL OIM software. In contrast, macro texture is obtained from bulk Mg samples using XRD and Schultz reflection method.

2.6.1 Macro texture of Mg alloys subject to ECAP

Kim et al (2003) examined the texture evolution in extruded, 1st pass to 4th pass and 8th pass ECAPed AZ61 Mg using Schultz reflection method. The extruded sample evinced a fibre texture with a maximum intensity of 7.0. Upon 1st pass ECAP, the fibre texture tilted 10° towards normal direction and the intensity decreased relatively to a value of 5.6. During 2nd and 3rd ECAP passes the initial fibre texture disappeared with further relative decrease in intensity of 2.8 and 3.7 respectively. By the end of 4th and 8th pass a new texture element was developed with intensities of 2.7 and 4.5 respectively. Lin et al. (2005) subjected extruded AZ31 Mg alloy upto 8th pass of ECAP. They reported that the extruded and ECAPed AZ31 Mg evinced different textures which was confirmed by EBSD and X-ray pole figures. In addition, in extruded and ECAPed condition the basal planes lie parallel and tilted at an angle 45° and 55° respectively. This led to reduction in yield strength of extruded alloy from 265 MPa to 217 MPa by the end of 8th pass ECAP. Zhang et al, (2015) subjected as cast Mg-Gd-Nd-Zn-Zr alloy upto 8th pass of ECAP at a temperature of 375 °C. The maximum texture intensity of basal pole figures increased from 53 for 1st pass ECAP to 125 by the end of 4th pass ECAP. In contrast, the texture intensity of 8th pass ECAP decreased relatively to a value of 115. The mechanical properties of as cast alloy YS: 78 MPa; %El: 12.3 % increased to a final value of YS: 231 MPa; %El: 20.3 % after 8th pass respectively. They claimed that the linear increase in mechanical properties was corroborated to the combination of grain boundary, precipitates and texture strengthening. In contrast to other Mg alloys, prismatic and pyramidal i.e (non-basal) slips were activated when WE43 Mg alloy was subject to ECAP (Minarik et al., 2017). However, the micrographs generated from EBSD technique assist in direct correlation of texture or crystallographic orientation with corrosion behaviour Mg samples. Hence, to understand the mechanical properties and corrosion behaviour of Mg alloys EBSD is a better tool when compared to XRD.

2.6.2 Role of micro-texture evolution on ECAPed Mg alloys obtained from EBSD

Kim et al (2002) evaluated the texture development in extruded, 1st pass and 8th pass ECAPed AZ61 Mg alloy. They reported that basal plane of extruded sample evinced most of the grain oriented parallel to extrusion direction(ED). After 1st pass ECAP, a portion of the grains with basal plane orientation moved away from ED with a relative increase in pole intensity. By the end of 8th pass, the basal planes were located in between ED and transverse direction (TD). They concluded that the variation in pole intensity and shifting of basal planes were due to the rotation of ECAP sample in route Bc. Janecek et al. (2010) studied the texture heterogeneity of all grains and grains less than 3 μ m in extruded and ECAPed AZ31. A typical basal fibre texture was observed in the extruded AZ31 Mg sample. The 1st pass and 2nd pass samples evinced bimodal grains of size more and less than 3 μ m. The texture intensity of 1st pass sample were 13.9 and 4.3 when all grains and grain of 3 μ m were taken into consideration for EBSD measurements. In contrast, after 4th pass ECAP, the maximum texture intensities were measured to be 12.6 and 11.0 for all grains and grain less than 3 μ m respectively. Hence, they concluded that the texture intensity also depends on the grain size of Mg alloys. Mostaed et al. (2014a) reported that extruded ZK60 Mg exhibited a fibre texture of intensity 5.7. After 8th pass of ECAP the texture was almost comparable to initial fibre texture but the intensity increased relatively to 9.2. Upon 12th and 26th ECAP passes the maximum texture intensity of basal plane aligned to 52° and 43° between extruded direction (ED) and transverse direction (TD). Mostaed et al. (2014b) examined the texture evolution of extruded ZM21 Mg after ECAP. The extruded ZM21 Mg evinced a texture in which basal plane were parallel to ED. This typical fibre texture exhibited a maximum intensity of 8.0. After 4 passes of ECAP, texture intensity increased relatively to 13.9 but the strong components of fibre texture remained unchanged. In contrast, by the end of 8th pass ECAP a new texture element with maximum intensity of 9.7 was developed 53° between ED/TD evident from figure 2.7. Minarik et al, (2016a) carried out ECAP on extruded AE21, AE42 and LAE442 Mg alloys. The extruded Mg alloys evinced typical fibre texture in which the (0001) basal planes are parallel to extrusion direction (ED). After 8th pass ECAP, new texture element aligned ~55° from initial fibre texture in AE21 and AE42 Mg alloys. This is in accordance with previous texture evolution reported in Mg alloys. In contrast to other Mg alloys, LAE442 Mg alloy exhibited a four-fold symmetry texture. They reported that occurrence of such new texture was attributed to

the activation of prismatic, pyramidal and basal slip. In addition, the presence of Lithium was also responsible for four fold symmetry texture (Minarik et al, 2016b).

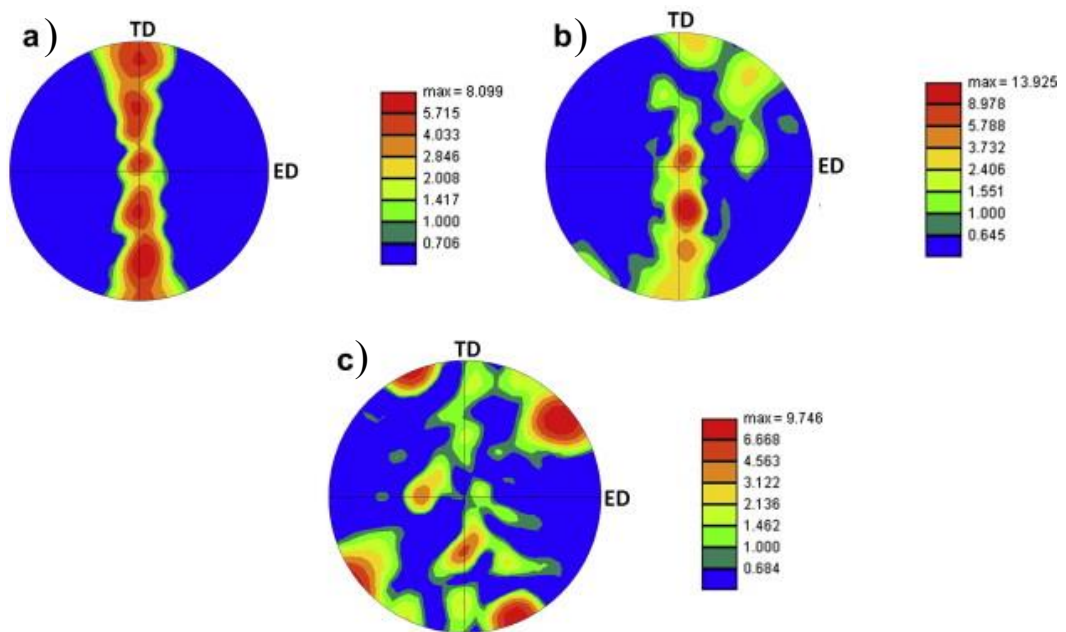


Fig. 2.7 Texture evolution of ZM21 Mg (a) extruded, (b) 4th pass at 200 ° C (c) 4th pass at 200 ° C + 4th pass at 150 ° C (Mostaed et al., 2015).

Krajňák et al. (2019) evaluated the texture evolution of as cast and extruded AX41 Mg. The cast AX41 Mg evinced a random texture in contrast to fibre texture of the extruded sample. Upon ECAP, the texture intensity of as cast AX41 increased from 14.7 to 24.8 after 1st pass ECAP. The texture intensity gradually decreased to a value of 7.5 after 8th pass. By contrast, the value of texture intensity increased chronologically from 5.0 in extruded condition to 7.4, 6.2, 8.8 and 10.0 after 1st, 2nd, 4th and 8th pass respectively. The yield strength of as cast AX41 Mg was significantly enhanced from 100 MPa to 200 MPa by 8th pass ECAP. While, yield strength of extruded AX41 alloy relatively improved from 160 MPa to 180 MPa. The % elongation of as cast and extruded Mg followed same trend. However, upon ECAP the % elongation of ~20 % was observed by end of 8th pass ECAP both in as cast and extruded condition. Recent research on ECAP of AE21, AE42 and LAE442 Mg alloys concluded that micro texture generated from EBSD and macro texture obtained from bulk Mg samples using XRD were in good agreement with each other (Minarik et.al, 2016). The cast Mg alloys evince random texture while rolling and extrusion of Mg alloys results in a

fibre texture. In contrast, ECAP disintegrates the initial random and fibre textures which leads to formation of a new texture. Hence, the mechanical properties are affected by texture in Mg alloys processed by ECAP. In summary, most of the researchers observed decrease in yield strength after ECAP. They attributed decrease to rotation of basal plane approximately 45° between extrusion and transverse direction. The development of such new texture after ECAP required less stress for yielding. (Kim et al., 2002, Janecek et al. 2010; Mostaed et al. 2014b). In order to get insights into % elongation of Mg alloys, investigating the fractured surface of Mg alloys after tensile testing is mandatory.

2.7 FRACTOGRAPHY OF MAGNESIUM ALLOYS BEFORE AND AFTER ECAP.

It is well established that the Mg and its alloys have relatively lower ductility due to their HCP crystal structure. Also, there is a necessity to improve their ductility to broaden the application of Mg alloys. In addition the fractography of Mg samples enlighten the mode of failure occurred during tensile, compressive and bending tests. In general, this mode of fractography is related to the brittle, ductile and mixed mode behaviour of samples under examination. Gopi et al. (2016) reported that tear ridges were observed in as cast and 1st pass AM60 Mg samples. In contrast, 2nd and 3rd pass samples evinced a combination of cleavages and dimples. While the 4th pass AM60 Mg exhibited fine and equiaxed dimples. The transition from tear ridges, cleavages to micro dimples resulted in enhancement of % elongation from 3.1% in cast AM60 Alloy to 20.7% in the 4th pass sample. Dumitru et al. (2014) also reported that ECAPed ZK60 Mg samples exhibited a transitional behaviour. The extruded sample exhibited elongation of 18% attributed to HCP crystal structure. With increase in number of ECAP passes, the dimples dominated the cleavage facets. This in turn increased % elongation of 4th pass ZK60 sample to ~28%. In another study, the fractured surface of as cast Mg-Gd-Nd-Zn-Zr alloy evinced large cleavage planes. These large cleavage planes were observed after 1st pass of ECAP but fracture occurred at the interface between Mg phase and MgZnRE phase. In the fractured surface of 4th pass ECAP sample cavities dominated the cleavage planes. Finally, by the end of 8th pass cavities of different shape and size increased. As a result, the % elongation of as cast Mg-Gd-Nd-Zn-Zr alloy increased from 11.3 to 20.3 % after ECAP (Zhang et al., 2015). Avvari et al. (2015) carried out ECAP on AZ80 Mg alloy at different processing temperatures of 275 °C, 300 °C and 350 °C. The as cast samples evinced deep hollow cracks which indicated brittle mode of failure. The samples exhibited quasi cleavage fractures even after homogenisation

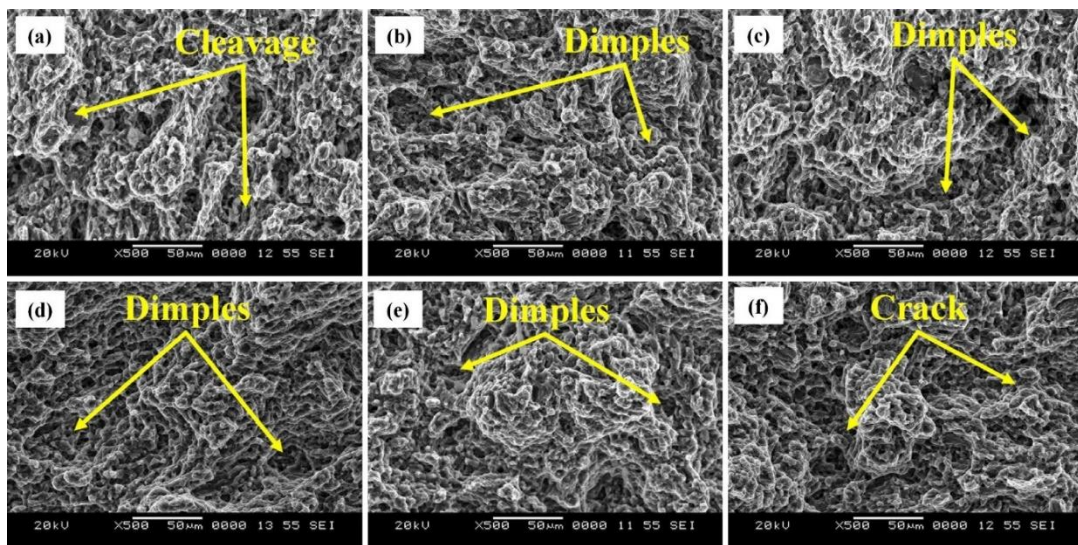


Fig 2.8 Fractured surface of AZ80 Mg alloys (a) as-received, (b) homogenized at 400 °C, (c) 2P-90°, (d) 4P-90°, (e) 2P-110°, (f) 4P-110° (Naik et.al, 2019)

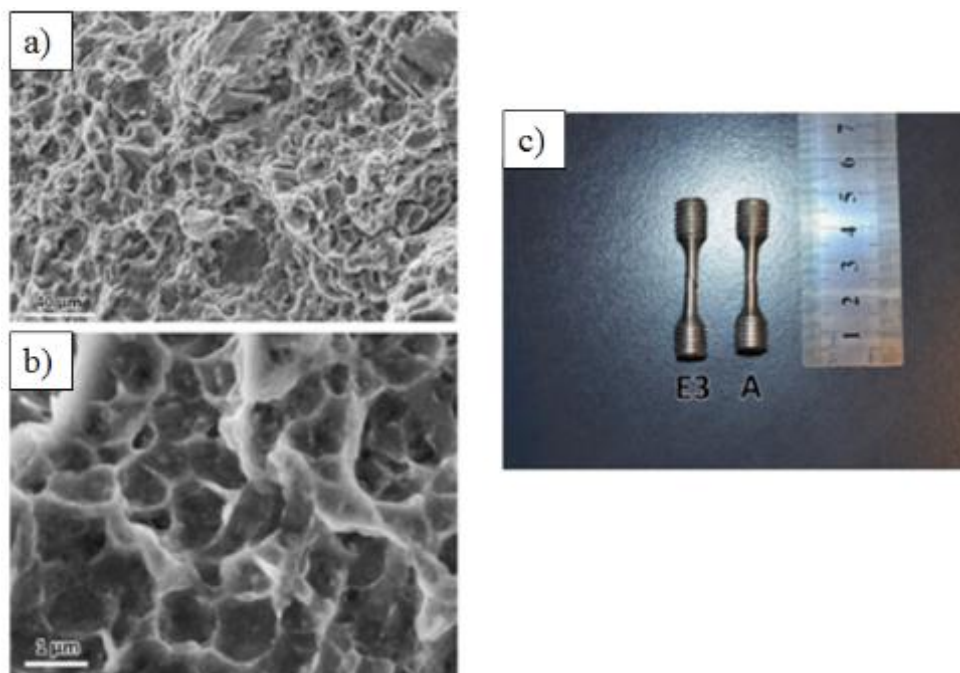


Fig 2.9 SEM micrographs of fractures surface (a) as received (b) 12th pass (c) macrographs of tensile fracture. (Mostaed et al, 2014)

but still failed in the brittle mode. In contrast, few dimples were observed on the fractured surfaces of 4th pass samples processed at 275 °C. The population of dimples increased further when temperature increased to 300 °C and 350 °C. Hence, the ductility of as cast AZ80 enhanced from 4.6 % to 7.4 %, 7.7 % and 8.1 % for 4th pass samples ECAPed at 275 °C, 300 °C and 350 °C respectively. Naik et al., (2019) revealed the fractured surface

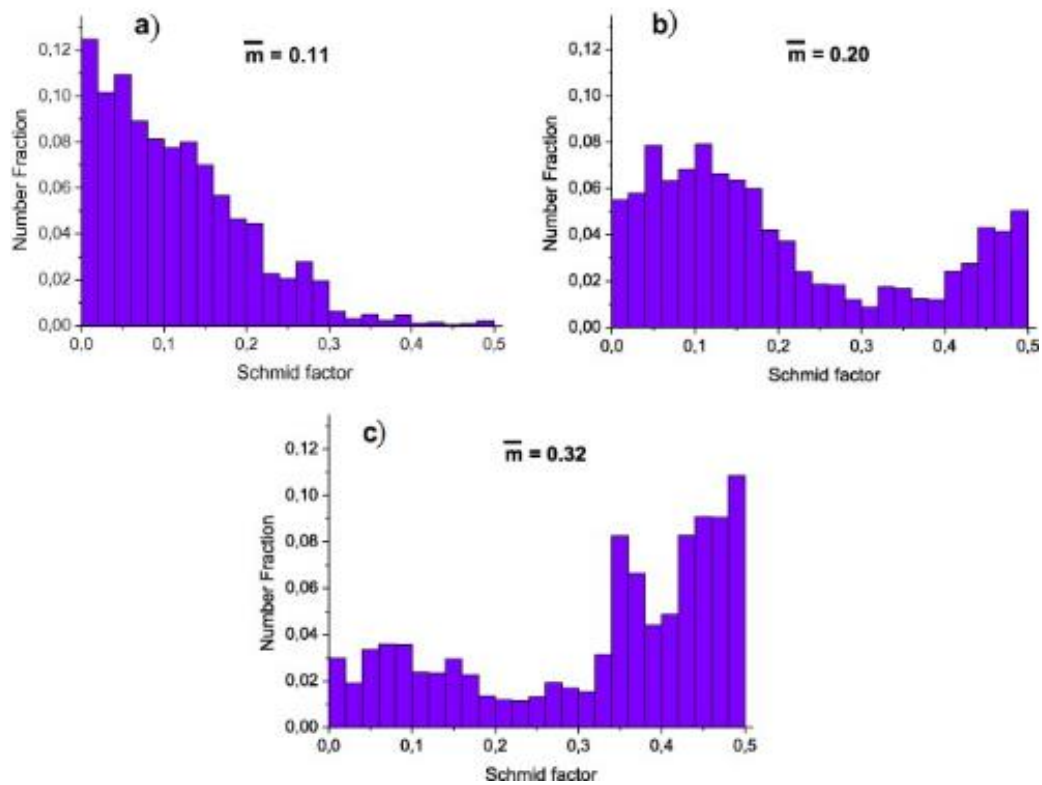


Fig 2.10 Schmid factors for basal slip (a) extruded, (b) 4th pass at 200 °C and (c) 4th pass at 200 °C + 4th pass at 150 °C samples of ZM21 Mg (Mostaed et.al, 2015).

morphology of AZ80 Mg alloys in as received, homogenized and ECAPed conditions. The fractured surface morphology of AZ80 Mg alloy is shown in the figure 2.8. The as received AZ80 Mg samples evinced cleavages which signifies brittle nature. In contrast, the 2nd and 4th pass AZ80 ECAP samples exhibited dimples indicating ductile modes of failure. In another work carried out by Mostaed et.al, (2014), extruded ZM21 Mg samples were subjected 12th pass ECAP. The SEM micrographs of ZM21 Mg in as received, 12th pass and their corresponding macrographs are represented in figure 2.9 (a-c) respectively. The extruded ZM21 Mg exhibited a brittle mode of failure characterized by the presence of cleavages on the fractured surface. In contrast, dimples were observed in the 12th pass ECAP sample. Dimples resulted in a ductile mode of failure after tensile testing. The digital image of fractured extruded and ECAPed ZM21 Mg also were in accordance with SEM micrographs (Mostaed et.al, 2014).

Table 2.1 Improvement in percentage elongation of Mg alloys before and after ECAP

Mg alloy	% Elongation		Reference
	Before ECAP	After ECAP	
AZ31	16	23	Avvari et al (2013)
AZ80	7.37	25.27	Naik et al (2019)
ZM21	22	39	Mostaed et al (2015)
ZK60	16	30	Mostaed et al (2014)
ZK60	18	28	Dumitru et.al (2014)
AZ91	3	8.45	Chen et.al (2008)
AZ31	22.5	33	Jin et.al (2005)
AX41	6.2	18.9	Krajňák et al (2019)
AX41	17.5	23	Krajňák et al (2019)
AM60	3.1	20.7	Gopi et al (2016)
Mg–Gd–Nd– Zn–Zr	11.3	20.3	Zhang et al (2015)

Table 2.1 represents the percentage elongation of various Mg alloys processed by ECAP. In general, the % elongation of Mg alloys depend on history of processing viz., cast, rolled and extruded condition. The rolled and extruded Mg alloy evince relatively lower ductility due to strong fibre texture. From table 2.1, it is evident that ECAP improved the % elongation of Mg alloys significantly. The schmid factor maps generated from EBSD micrographs enlighten this significant increase in % elongation of Mg alloys. The Schmid factor distribution of ZM21 Mg alloy for various ECAP conditions are shown in the figure 2.10. The % elongation of ZM21 Mg enhanced from 22% in extruded condition to 39% after 8th pass ECAP. The schmid factor values also increased from 0.11 in extruded condition to 0.32 by the end of 8th pass. The improvement in values of Schmid factor favours the occurrence of basal slip during tensile testing thereby significantly enhancing the ductility (Mostaed et al, 2015). Based on the literature, it is apparent that equal channel angular pressing has the potential to improve the % elongation of Mg alloys significantly. In addition, EBSD is a versatile characterization which enlightens the mechanism responsible for strengthening occurs in Mg alloys. Hence, in the present study EBSD characterization was performed on as received and ECAPed ZE41 Mg. The combined

effect of grain refinement and crystallographic orientation on mechanical properties of ZE41 Mg before and after ECAP were analysed. However, there is a need to enhance the corrosion resistance of Mg alloys to extend the longevity and application of Mg alloys. Therefore, it is of prime importance to understand the corrosion mechanism occurring in Mg alloys.

2.8 CORROSION OF MAGNESIUM ALLOYS

Magnesium corrosion is predominantly dictated by the alloying additions in Mg alloys. This is because the addition of alloying elements in Mg system leads to secondary phase formation. Generally, these secondary phases have higher or noble potential than primary Mg phase which leads to formation of micro-galvanic cells (Coy et al. 2010). These micro-galvanic cells are detrimental to corrosion resistance of Mg alloys. In contrast, sometimes the size and distribution of secondary phases might improve the corrosion resistance (Neil et al. 2009, 2011). Also, in addition to grain size and secondary phase particles, crystallographic orientation or texture also plays an important role in corrosion of Mg (Song and Xu 2012). It is well known that the Mg alloys are generally tested in various corrosive medium that mimic the intended application.

2.8.1 Selecting corrosive medium for specific applications

In recent days, magnesium research communities focus on extending the application of Mg in automobile and biomedical industries in particular. Song and Xu (2012) reported corrosion behaviour of pure Mg in 0.01 M NaCl solution. They stated that 0.01 M NaCl mimicked ocean fog and seawater splash conditions. Atrens and co-workers evaluated the corrosion behaviour of various Mg alloys in 3.5 Wt% NaCl. In a recent study, they reported that by testing Mg alloys in 0 M, 0.1 M and 1 M NaCl solution the automobile service environment is mimicked (Zhao et al, 2008). Walker et al., (2012) examined the corrosion of different Mg alloys in simulated body fluids such as Earle's balanced salt solution (EBSS), minimum essential medium (MEM), and minimum essential medium with bovine serum to evaluate the biodegradable nature. Mei et al., (2020) critically reviewed the advantages and disadvantages of using corrosive medium such as NaCl, phosphate buffered solution (PBS), HBSS, EBSS, SBF, MEM, DMEM in evaluating the biodegradable behaviour of Mg. King et al, (2014) studied the corrosion behaviour of pure Mg in varying concentration of NaCl viz., 0.1 M, 1 M and 5 M NaCl solution. They observed and recorded

potentiodynamic polarisation plot deviated from Tafel behaviour. This typical behaviour of Mg is due to anodic hydrogen evolution. However, IR corrected figure 2.11 (b) exhibited a relatively better Tafel behaviour than as recorded represented in figure 2.11 (a). From figure 2.11, they also observed that the corrosion rate of pure Mg obtained in 0.1 M NaCl was lower than that obtained in 1 M and 5 M NaCl solution. This phenomenon was corroborated to the destructive nature of chloride ions present in NaCl solution. The Bode plots of pure Mg were also in accordance with the Nyquist plots for different concentration of NaCl solution. The corrosion rate obtained by various methods viz., weight loss, hydrogen evolution and electrochemical impedance spectroscopy (EIS) were comparable (King et al, 2014). However, it should be borne in mind that the current study focusses on improving the corrosion resistance of ZE41 Mg for extending its application in automobile industries. Hence, the corrosive medium containing 0 M, 0.1 M and 1 M NaCl were chosen in the present study to examine the corrosion mechanism of ZE41 Mg before and after ECAP.

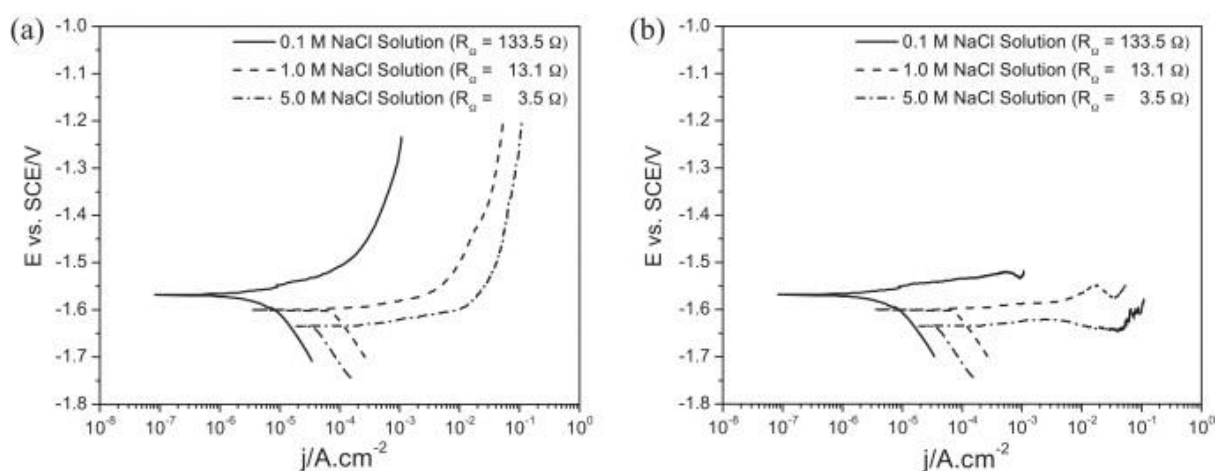


Fig. 2.11 Potentiodynamic polarisation plots of Pure Mg in different concentration of NaCl solution (a) as recorded (b) IR corrected. (King et al, 2014)

2.9 INFLUENCE OF SECONDARY PHASE PARTICLES ON CORROSION BEHAVIOUR OF MAGNESIUM ALLOYS BEFORE AND AFTER ECAP.

Birbilis et al (2010) made an attempt to establish a relationship between grain size and corrosion rate after subjecting pure Mg to 8th pass of ECAP. The grain size of as cast sample reduced from 125 μm to 2.6 μm . They found that the corrosion rate decreased with decrease in grain size when tested in 0.1 M NaCl solution. They speculated that by increasing the population of grain boundaries with higher misorientation angles robust passive film was developed. In contrast to speculation it is well known that grain boundaries are area of higher strain and corrosion tends to initiate at such active areas (Argade et al, 2012). Song et al. (2010) carried out ECAP on as cast pure Mg with average grain size of 800-1500 μm . They obtained grains of size 50-100 μm by the end of 6th pass ECAP. Electrochemical, immersion and in-situ corrosion studies using 3.5 Wt% NaCl revealed that the corrosion rate increased with increase in number of ECAP passes. This was attributed to increase in grain boundaries and dislocations. It can be seen that Birbilis et al (2010) and Song et al (2010) carried out ECAP on Pure Mg and made an attempt to establish relationship between grain size and corrosion rate. It is surprising to note that Birbilis et al (2010) claimed that ECAP improved the corrosion resistance of Mg while Song et al (2010) reported deterioration in corrosion resistance. This contrasting results on same material of Pure Mg might be corroborated to the difference in grain size of Mg and the different concentration of testing medium used. However, the influence of secondary phase particles on corrosion behaviour of Mg alloys cannot be understood from studying the corrosion of Pure Mg. Song et al. (2011) evaluated the factors involved in corrosion of AZ91 Mg alloy after ECAP. Grain size and $\text{Mg}_{17}\text{Al}_{12}$ secondary phases of size 5 μm and 1-2 μm were obtained after 12th pass of ECAP. Similar to ECAPed Pure Mg, AZ91D Mg also evinced increment in corrosion rate with increase in number of ECAP passes. This behaviour was attributed to the crystalline defects introduced during ECAP. In addition, the mode or regime of corrosion is also an important factor in deciding the application of Mg alloys. Recently, some researchers found that the corrosion resistance of Mg alloys increased or decreased after ECAP. For instance, the corrosion resistance of ECAPed AE21 Mg alloy decreased after 8th pass ECAP. In contrast, the 8th pass ECAPed AE42 Mg alloy exhibited a relatively increased corrosion resistance due to the fine distribution of Al_{11}RE secondary phases which is evident from figure 2.12 (Minarik et al, 2013). Irrespective of increase or decrease

in corrosion resistance of Mg alloys, ECAP converts the regime or mode of corrosion from pitting to uniform corrosion. The modes of corrosion occurring in ZK60 Mg before and after ECAP are shown in the figure 2.13 (Mostaed et al., 2014). This is attributed to the fragmentation and fine distribution of secondary phases after ECAP. The similar phenomenon was observed when ZK60 was ECAPed upto 12th pass and immersed in phosphate buffer solution (PBS) for 96 hours. Naik et al., (2019) reported that the corrosion resistance was enhanced relatively in ECAPed AZ80 Mg alloy after annealing and heat treatment. The corresponding SEM images of corroded samples shown in figure 2.14 were also in accordance with results obtained potentiodynamic polarization plots. Minarik et al., (2017) processed extruded LAE442 Mg with grain size of $\sim 21 \mu\text{m}$ alloy using ECAP. They obtained a grain size of $\sim 1.5 \mu\text{m}$ by the end of 12th pass ECAP. The corrosion rate of extruded and ECAPed LAE442 Mg were studied in 0.1 M NaCl, minimum essential medium (MEM) and Kirkland's bio-corrosion medium (KBM) solutions. The corrosion resistance of ECAPed LAE442 Mg was relatively higher than extruded counterpart in all tested mediums. They claimed that the fine grains contributed to better stability of corrosive film because they reduce the mismatch between matrix and surface film.

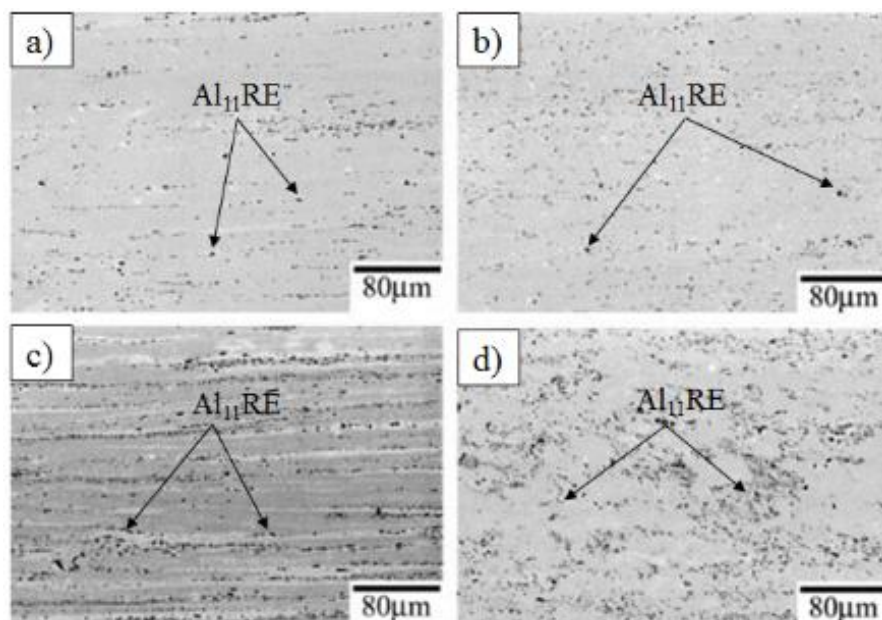


Fig 2.12 Cross-section of (a) AE21-0P, (b) AE21-8P, (c) AE42-0P and (d) AE42-8P (Minarik et.al, 2013)

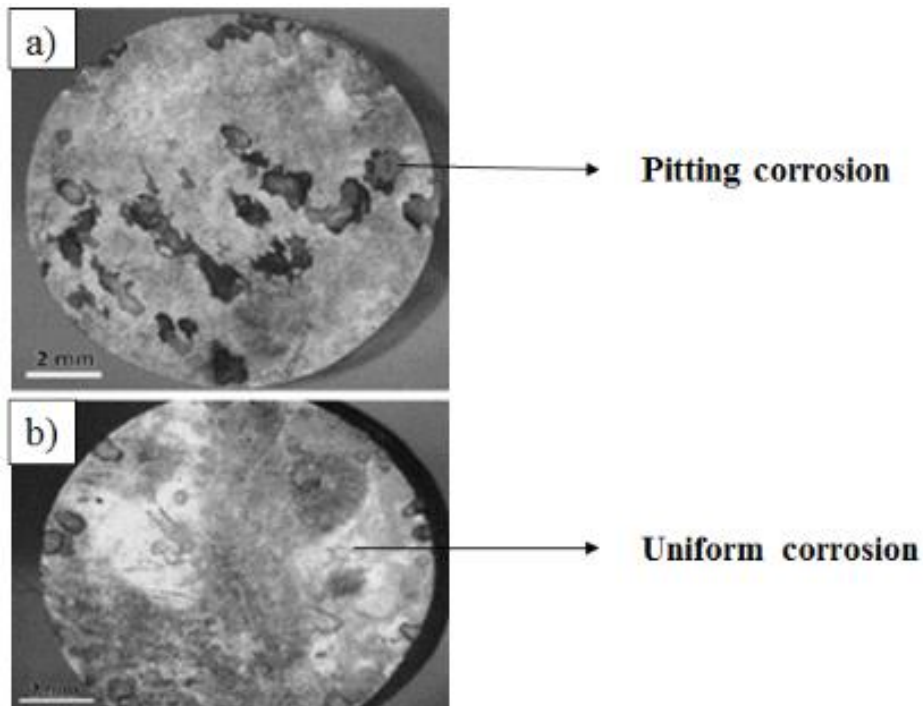


Fig 2.13 General view of the corrosion surfaces of the materials immersed in PBS for 96 h: (a) extruded sample, (b) 12th pass sample. (Mostaed et al, 2014).

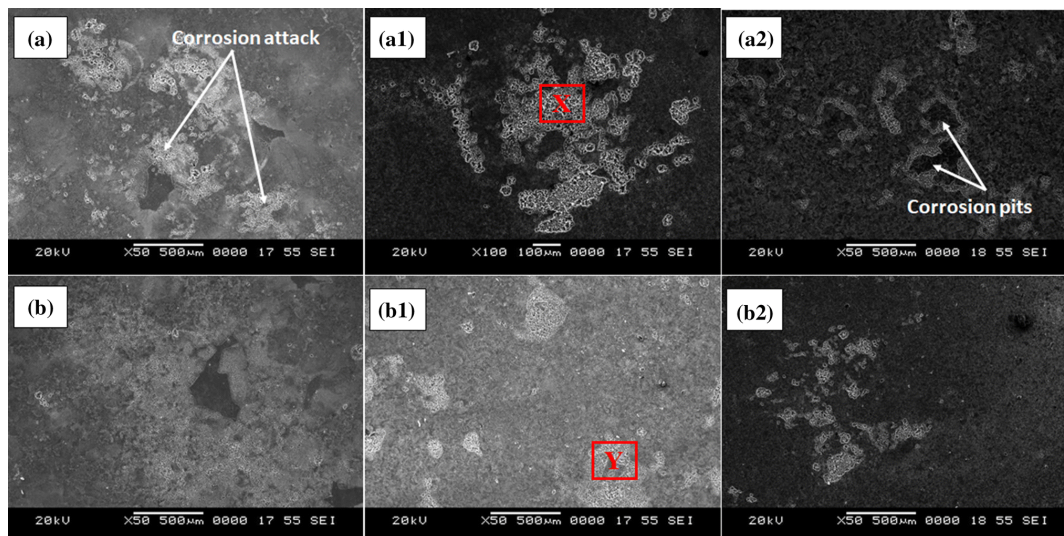


Fig 2.14 Corrosion morphology: (a) ECAP-2P, (a1) 523 K for 12 h, (a2) 723 K for 12 h, (b) ECAP-4P, (b1) 523 K for 12 h, (b2) 723 K for 12 h (Naik et.al, 2019)

However, there are additional factors such as crystallographic orientation or texture that influence the corrosion of Mg alloys (Mostaed et al, 2014a) These additional factors are discussed in the next section.

2.10 EFFECT OF CRYSTALLOGRAPHIC ORIENTATION ON CORROSION BEHAVIOUR OF MAGNESIUM ALLOYS.

Song and Xu (2012) reported the influence of corrosion behaviour on polycrystalline pure Mg in 0.01 M NaCl and saturated Mg(OH)₂ medium. The EBSD grain distribution and the schematic illustration of grain orientation are depicted in the figure 2.15. Scanning vibrating electrode (SVP) and scanning kelvin probe (SKP) maps revealed the current density and work function of grains with different crystal orientation of polycrystalline pure Mg. They concluded that the grains with basal orientation evinced better corrosion resistance than non-basal planes (prism and prismatic planes). This is because magnesium has basal planes (0001) and prism planes (10- 10) (11-20) which plays an important role in corrosion. Prism planes have a theoretical dissolution rate which is very higher i.e 20 percent more when compared to basal planes. Song et al. (2010) evaluated the effect of texture on corrosion properties of AZ31 magnesium alloy. Rolling surface (RS) of AZ31 Mg alloy exhibited most of the grains oriented towards the basal plane. In contrast, cross sectional surface (CS) showed grains oriented towards prism planes. From potentiodynamic polarization curve and Nyquist plot, it was apparent that rolling surface (RS) evinced better corrosion resistance than cross sectional surface (CS). Xin et al., (2011) evaluated the corrosion performance of AZ31 Mg alloy using 3.5 Wt% NaCl as testing medium. The samples were cut along 0°, 30°, 60° and 90° orientation from AZ31 Mg slab. Electron back scattered diffraction (EBSD) characterization showed that 0° sample had most of the grains oriented towards basal plane exhibiting more corrosion resistance. In contrast, 90° degrees samples evinced most of the grains oriented towards prism planes exhibiting relatively poor corrosion resistance. Hydrogen evolution test of AZ31 Mg samples revealed the order of increasing corrosion resistance 0°>30°>60°>90°. Savaguira et al. (2017) examined the influence of crystal orientation on AZ31B Mg alloy after friction stir spot welding. The rolled surface of base metal (BM) and stir zone (SZ) evinced strong basal texture. On the contrary, cross sectional surface of AZ31 Mg exhibited majority of grains oriented towards (-1, 2,-1, 0) and (0, 1,-1, 0) planes.

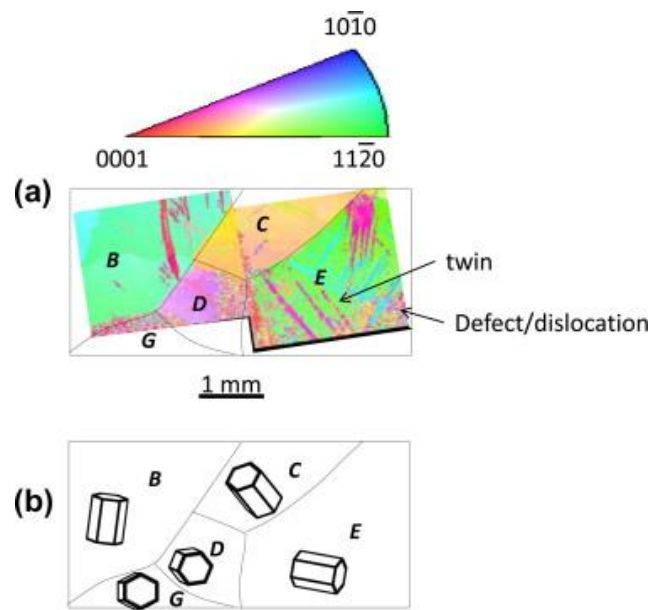


Fig 2.15 (a) EBSD grain distribution, and (b) schematic illustration of grain orientations of the Mg coupon (Song and Xu 2012).

The corrosion current density of BM was measured to $9.0 \mu\text{A}/\text{cm}^2$ and $16.0 \mu\text{A}/\text{cm}^2$ in rolled surface and cross sectional surface respectively. In contrast, the corrosion current density of rolled and cross sectional surface in SZ zone was calculated to be $2.2 \mu\text{A}/\text{cm}^2$ and $3.1 \mu\text{A}/\text{cm}^2$ respectively which is significantly lower than BM zone. They concluded that the basal orientation along with fine second phase were responsible for better corrosion resistance in SZ than BM. Wang et al, (2016) investigated the effect of crystallographic orientation on extruded AZ31 Mg in phosphate buffer solution (PBS). The transverse surface (TS) consisted of grains oriented in $\{10\text{-}10\}$ and $\{11\text{-}20\}$ prism planes. Strikingly, the lateral surface (LS) was composed of grains with combination of $\{0001\}$ basal and prism planes. The corrosion current density of TS sample corresponds to $43 \mu\text{A}/\text{cm}^2$ and $6 \mu\text{A}/\text{cm}^2$ after 10 minutes and 48 hours of immersion. In contrast, corrosion current density of $100 \mu\text{A}/\text{cm}^2$ and $912 \mu\text{A}/\text{cm}^2$ corresponded to 10 minutes and 48 hours of immersion respectively. The corrosion rate of LS sample was observed to be significantly higher than the TS sample for both the time durations. They reported that the combination of basal and prism planes in LS sample accelerated the corrosion due to formation of micro-galvanic cells. Wang et al. (2014) examined the combined influence of twinning and crystallographic orientation on extruded AZ31 Mg. The longitudinal surface (LS) exhibited grain orientation with combination of basal and prism planes. On the contrary, the transverse surface consist of grain orientation dominated only by prism planes. The

misorientation angle plots generated from EBSD revealed that TS surface evinced relatively higher density of twins than LS. They concluded that the prism planes combat the formation of micro galvanic cells between twinned and un-twinned areas in addition to those formed between grains of different crystal orientations. In summary, some researchers claimed that the basal plane orientation enhanced the corrosion resistance in Mg alloys (Song and Xu, 2012; Xin et al, 2011; Song et al., 2010). On the contrary, others stated that combination of basal and prism planes deteriorated corrosion resistance due to formation of micro-galvanic cells (Wang et al., 2014). In previous section 2.9 the role of secondary phases on corrosion resistance of Mg alloys subject to ECAP was outlined. ECAP improved the corrosion resistance of Mg alloys due to fine distribution of secondary phases (Minarik et al., 2017; Naik et al., 2019; Mostaed et al., 2014). On the contrary, adverse effects were observed in other Mg alloys due to crystalline defects (Argade et al. 2012). Therefore, in the present study XRD and SEM techniques were used to detect the secondary phases and its distribution in ZE41 Mg. While, crystallographic orientation of grains were generated from EBSD micrographs. In addition, the combined influence of secondary phases and crystallographic orientation on corrosion and galvanic corrosion of ZE41 Mg before and after ECAP processing was investigated.

2.11 GALVANIC CORROSION OF MAGNESIUM ALLOYS

Galvanic corrosion or bimetallic corrosion is one of the most serious and common problems reported in automobile, aerospace and military vehicles used in defence (Song et al. 2004). The corrosion rate of AE44 Mg was interpolated to be 0.5 mm/year from potentiodynamic polarization experiments. However, the corrosion rate of same AE44 Mg in AE44 Mg- mild steel couple was ~ 200 mm/year. This phenomenal increase in corrosion rate in galvanic couple should be thoroughly investigated (Deshpande, 2010a, 2010b).

2.11.1 Galvanic corrosion measurement in magnesium alloy couple using scanning vibrating electrode technique (SVET).

Deshpande (2010a) investigated the galvanic corrosion of AE44-mild steel and AE44-AA6063 couple using scanning vibrating electrode technique (SVET) and immersion technique in 1.6 Wt% NaCl. The corrosion rate of 197 mm/yr and 42 mm/yr were obtained using SVET for AE44 – mild steel and AE44 – AA6063 respectively. In contrast, the corrosion rate evaluated from immersion studies of AE44 – mild steel and AE44 – AA6063

were measured to be 243 mm/yr and 52 mm/year. The variation in corrosion rate was corroborated to the difference in exposure of couple to electrolyte solution in SVET and immersion studies. Figure 2.16 (a) and (b) on left hand side represents the photograph of the cross-sectional view of AE44 – mild steel couple after 3 days of immersion in the electrolyte solution and surface profile of the same couple obtained using image digitization technique. While, the photo and cross sectional profile of AE44- Al couple is shown in right hand side of figure 2.16 (a) and (b) respectively. The author reported that AE44 –Al couple exhibited better galvanic corrosion resistance than AE44- mild steel couple. The same author further extended above work by using numerical model and reported that results from the model were in good agreement with experiments (Deshpande 2010b). The corrosion rates of the two galvanic couples was calculated using mixed potential theory, predicted using the arbitrary langrangian Eulerian (ALE) method and estimated from the SVET and immersion techniques. The results of corrosion rate obtained from different techniques are tabulated in the table 2.2. They observed that corrosion rate predicted from ALE method were comparable with experimental results in case of AE44- mild steel couple. In contrast, ALE model under-predicted the corrosion rate of AE44- AA6063 couple. The reason for such under-prediction was not reported by the researchers. Sun et al. (2012) also anticipated the galvanic corrosion of AE44-mild steel in chloride containing solution using ALE method. In addition to corrosion rate they also predicted the role of corrosion product and its evolution. They validated their model by comparing their results those obtained from immersion experiments from previous studies (Deshpande 2010b). The maximum corrosion depth of 2mm appeared at the junction of AE44-mild steel couple. Deshpande's ALE model predicted a value of pit depth value of 1.6 mm. The maximum corrosion depth at junction predicted in the model of Sun et al (2012) was 1.71 mm. Wang et al (2021) also made an attempt to predict the galvanic corrosion behaviour of AE44- mild steel couple using multi-physics model. They obtained a maximum corrosion pit depth of 1.745 mm at the junction of AE44-mild steel couple. They claimed that the pit depth of 1.745mm obtained from their model was relatively precise to true value of 2mm than 1.6 mm and 1.71 mm predicted by Deshpande (2010b) and Sun et al (2012) respectively. In addition, the variation of galvanic corrosion behaviour when aluminium spacer from 0 to 5 mm thickness was placed between AE44- mild steel couple was investigated. The corrosion rate of galvanic couple was calculated using numerical model and scanning vibrating electrode technique (SVET).

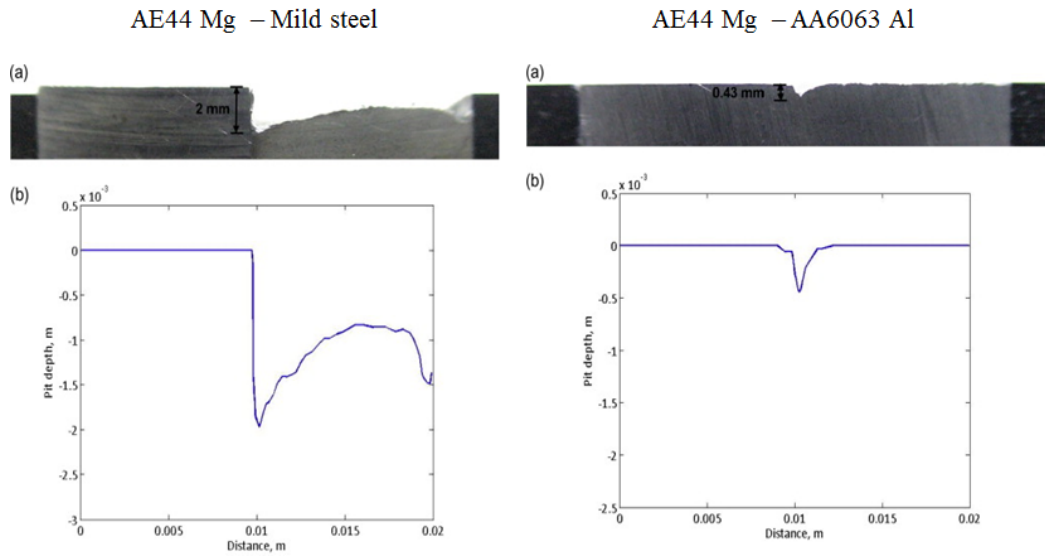


Fig 2.16 (a) A photograph of the cross-sectional view of AE44 – mild steel (left) and AE44 – Al (right) couple after 3 days of immersion in the electrolyte solution. (b) The surface profile of the same couple obtained using image digitization technique.

Deshpande (2010)

Table 2.2 Corrosion rate of galvanic couples measured by using various techniques (Deshpande 2010b).

Galvanic couples	Mixed potential theory	ALE Current density	ALE Depth prediction	SVET	Immersion (Experiment)
AE44- Mild steel	231	210	195	197	243
AE44- AA6063	26	29	28	42	52

The corrosion rate of no spacer (0 mm), 1 mm, 2 mm, 3 mm, 4 mm and 5 mm Al spacer was measured to be 211 mm/year, 184 mm/year, 173 mm/year, 165 mm/year, 160 mm/year and 157 mm/year respectively. They observed that the corrosion rate of galvanic couple decreased linearly with respect to increase in thickness of Al spacer (Deshpande, 2012). The current obtained from SVET experiments were bestowed with a numerical model developed based on Potentiodynamic polarization curves of AE44, Al spacer and mild steel. The above studies on prediction of galvanic corrosion using ALE and multi-physics

model resulted in under prediction or over prediction of galvanic corrosion rate. Hence other researchers believed that experimental techniques are viable option for evaluating the galvanic corrosion behaviour of Mg.

2.11.2 Evaluation of corrosion rate in galvanic couples using zero resistance ammeter

Song and co-workers studied the galvanic corrosion of AZ91D when coupled with three cathodes aluminium alloy, zinc and steel. Their experimental set up is shown in figure 2.17. The current density of AZ91D when coupled with Al, Zn and Steel obtained by the end of 30 hours salt spray testing was found to be $\sim 100 \mu\text{A}/\text{cm}^2$, $136 \mu\text{A}/\text{cm}^2$ and $290 \mu\text{A}/\text{cm}^2$ respectively. They reported that AZ91D- aluminium alloy galvanic couple exhibited lower corrosion rate when compared with zinc and steel couple. Various corrosion products formed due to three different Al, Zn and steel cathodes affected the corrosion process (Song et al. 2004). The role of galvanic corrosion of EW75 magnesium alloy- Ti6Al4V couple with and without Silane treatment was studied. The mass loss of Mg, Mg- Ti couple and Silane treated Mg-Ti couple were calculated to be 1.74 %, 2.87 % and 2.37 % respectively. Hence they concluded that Silane treatment reduced the galvanic corrosion by forming a protective film and converted the localized pitting into uniform corrosion (Ruanli et al. 2015). Banjade et al. (2016) investigated the role of self –corrosion in Mg- steel couple by varying the cathodic steel area. The average current density of Mg-steel couple with 8 mm^2 , 12 mm^2 and 16 mm^2 area were reported to be $2115 \text{ A}/\text{m}^2$, $2480 \text{ A}/\text{m}^2$ and $2510 \text{ A}/\text{m}^2$ respectively. The observation revealed that galvanic corrosion increased with increase in cathodic area due to the additional surface for hydrogen evolution but self- corrosion remained constant. Pan et al. (2015) reported the effect of micro arc oxidation coating on galvanic corrosion of carbon fibre reinforced polymers (CFRP, T300/648) AZ91, LZ91, and LZ141 Mg alloys. From the OCP measurements, figure 2.18 (a) it was identified that the carbon fibre reinforced polymer CFRP was nobler than the Mg alloys. The galvanic corrosion behaviour of CFRP/ Mg alloy couple were investigated using 3.5 Wt% NaCl as a corrosive medium and represented in figure 2.18 (b).The galvanic corrosion density was ranked in the following increasing order $\text{CFRP}/\text{AZ31} < \text{CFRP}/\text{LZ91} < \text{CFRP}/\text{LZ141}$.

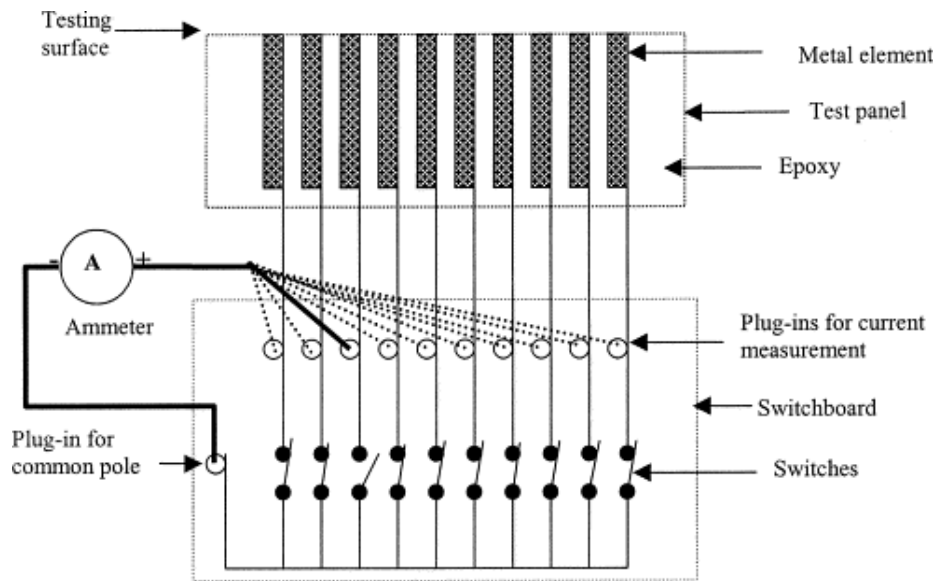


Fig 2.17 Configuration of the test panel and switchboard for the measurement of galvanic current. (Song et al. 2004)

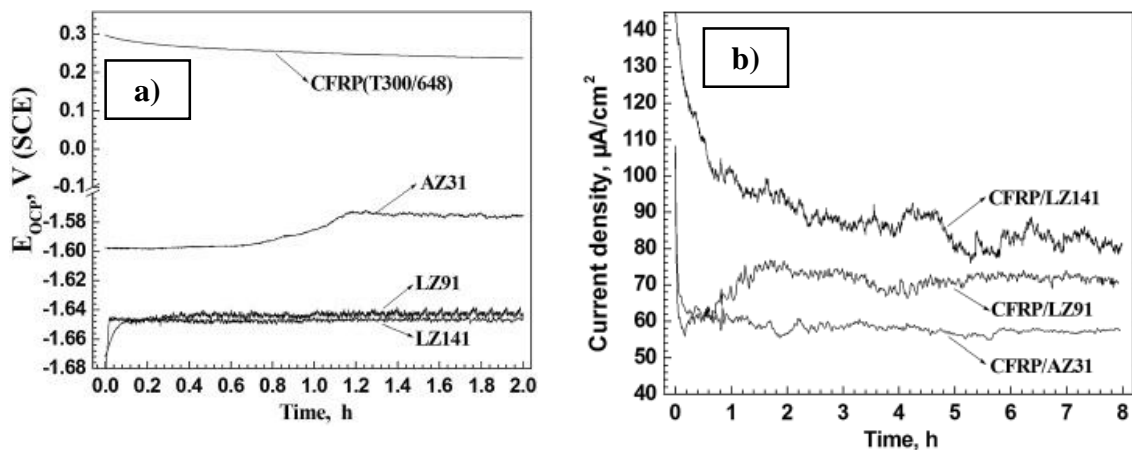


Fig 2.18 CFRP/ Mg alloy couple showing (a) open circuit potential (OCP) (b) Galvanic corrosion current density in 3.5 Wt% NaCl. (Pan et al. 2015).

In contrast, the presence of lithium did not offer any passivation to inhibit the galvanic corrosion. The increase in Li content in LZ alloys further increased the galvanic corrosion because of the formation of micro galvanic couples in larger area fractions. The lower galvanic corrosion rate of CFRP/AZ31 was due to the presence of Al^{3+} passive ions present in the AZ31 Mg alloy.

2.11.3 Surface film models proposed for Mg alloys.

It is well known that the corrosion behaviour of Mg alloys is influenced by microstructural features viz., size and volume of secondary phases as well as crystallographic orientation. In addition, the nature of ions present in the corrosive medium also play significant role during corrosion of Mg (Mei et al., 2020). In contrast, during galvanic corrosion scenario along with Mg additional materials such as steel and Aluminum are generally coupled. Hence, during the process of galvanic corrosion both Mg and coupled material undergo dissolution in the presence of corrosive medium (Deshpande, 2010a, 2010b).

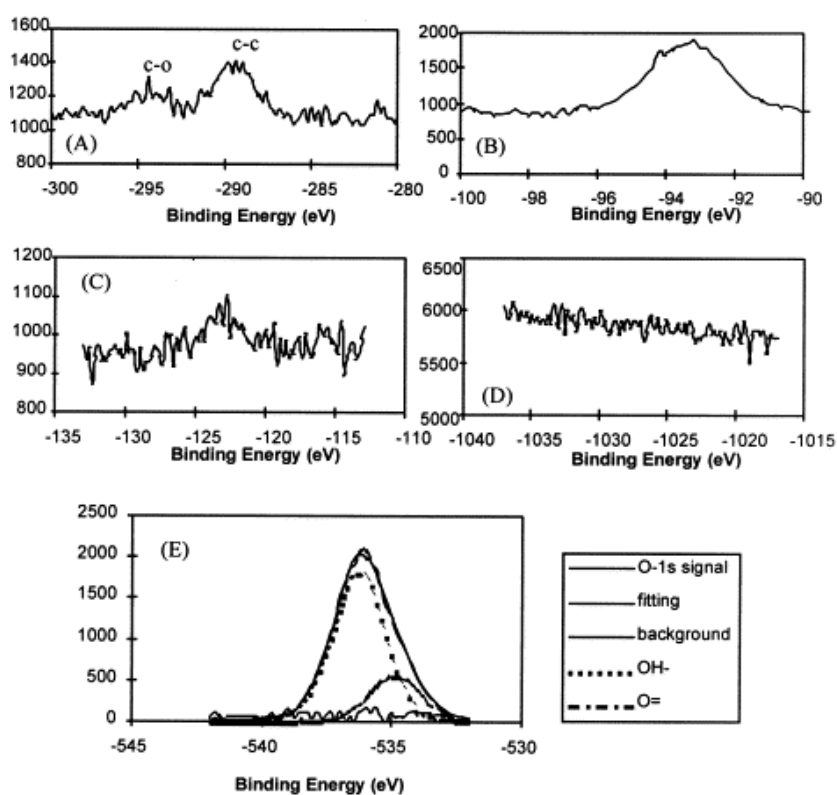


Fig 2.19 Typical multiplex XPS spectra for (a) C_{1s}; (b) Mg_{2s}; (c) Al_{2s}; (d) Zn_{2p} and (e) O_{1s}. (G Song et.al, 1998).

In order to get insights into the galvanic corrosion mechanism, it is very essential to identify the surface film developed. X ray photoelectron spectroscopy (XPS) is a very useful tool to predict surface film model using atomic concentration present in each spectra. G Song et.al, (1998) predicted and developed surface film models based on the binding energy values and the atomic concentration of corresponding Mg sample. The XPS spectra of carbon, magnesium, aluminium, zinc and oxygen are depicted in the figure 2.19. The

surface film models of AZ21, AZ501 and AZ91 are represented in the figure 2.20. The formation of MgO and Mg(OH)₂ layers is typically observed in Mg and its alloys

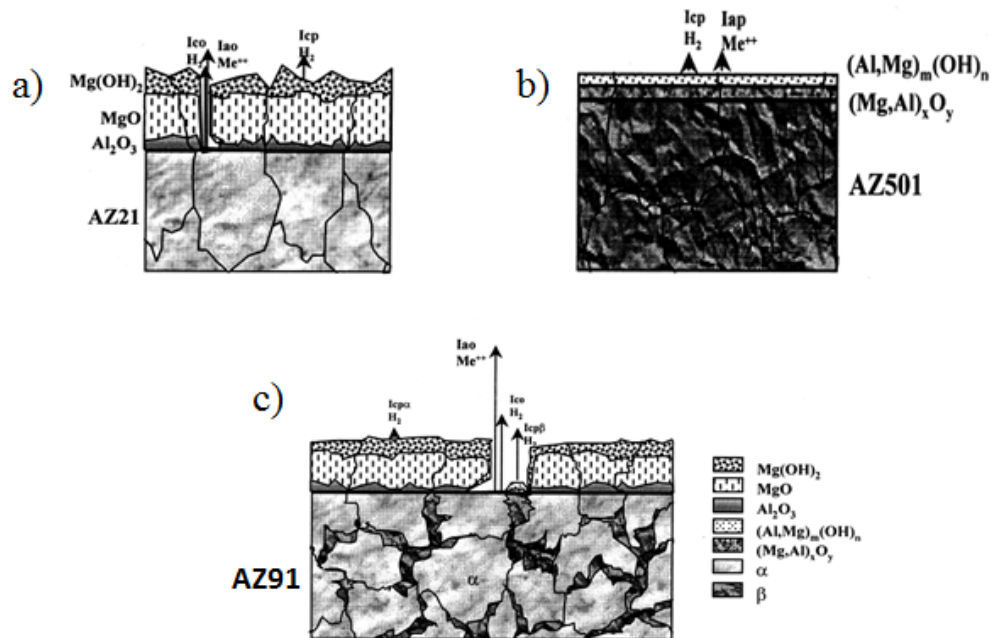


Fig. 2.20 Corrosion interfaces between solution and the following materials (a) AZ21, (b) AZ501 and (c) AZ91 (G Song et.al, 1998).

In contrast, the AZ21, AZ501 and AZ91 contains 1.33 Wt%, 51.04 Wt% and 8.73 Wt% of Aluminum respectively. Hence, they observed the formation of Al₂O₃, (Al, Mg)_m(OH)_n, (Mg,Al)_xO_y layers. The proposed surface models helped in better understanding the galvanic corrosion mechanism involved in AZ21, AZ501 and AZ91 Mg alloys. Hence, in the present study, XPS was carried out on ZE41 Mg – Al7075 Al couple after galvanic corrosion in 0 M, 0.1 M and 1 M NaCl to propose possible surface film model and its mechanism.

2.12 CONCLUSION

From the literature it is evident that the mechanical properties of various Mg alloys were improved by single step ECAP. However, grain refinement and % elongation are relatively better in two step when compared to single step ECAP. Very few studies explored the influence of two step ECAP on mechanical properties of Mg alloys. In the past decade, researchers observed that Mg and its alloys deviated from Hall Petch relation when subject to ECAP. However, the reason for this deviation was not revealed until the invention of

EBSD. Also, very few researchers focussed on evaluating the influence of crystallographic orientation or texture on mechanical properties. In addition, despite several research works carried out on corrosion behaviour of Mg alloys, the corrosion mechanism of Mg needs more understanding and clarification in different aspects. This is because Mg corrosion involves chemical, electrochemical reaction and undergoes anodic hydrogen evolution. In addition, the corrosion resistance of Mg is dictated by grain size, size and distribution of secondary phases and crystallographic orientation. The combination of all the above mentioned factors makes the corrosion mechanism of Mg complex in nature. It is also observed that limited studies on ZE41 Mg focussed on analysing the combined effect of grain refinement and crystallographic orientation on mechanical properties and corrosion behaviour. Most of the researchers studied the galvanic corrosion behaviour of magnesium alloys without reporting on methods to improve the same. Also, there is not much literature on the galvanic corrosion behaviour of magnesium alloys whose corrosion resistance is enhanced by ECAP. Keeping this in mind the following research gaps were identified for our research work.

2.13 RESEARCH GAPS

From the above literature, it was observed that mediocre efforts were made to extend the applications of Mg and its alloys possessing fine grain microstructure.

- ❖ Mg alloys deviate from classical Hall Petch relationship. Hence, there is a need to enlighten the combined effect of grain refinement, crystallographic orientation and the ECAP processing temperature on mechanical properties of Mg alloys.
- ❖ The corrosion behaviour of magnesium alloys in different corrosive medium pertaining to specific application is reported. However, mechanism of corrosion in Mg requires elucidation because various factors are involved.
- ❖ The galvanic corrosion is an inevitable threat involved in real time applications of magnesium alloys. Therefore, there is a necessity to combat galvanic corrosion.

2.14 OBJECTIVES OF THE PROPOSED RESEARCH WORK

Lightweight materials with high strength and ductility have immense potential in revolutionizing the automobile, aerospace, bio-medical and defence sector. Magnesium and its alloys are the candidates that are best suited for application in abovementioned sectors. However, achieving combination of properties such as high strength, good ductility and relatively better corrosion resistance in Mg alloys is still challenging. In the present study efforts have been made to enhance the mechanical properties, corrosion and galvanic corrosion resistance of ZE41 Mg using ECAP. The following objectives are broadly identified and focussed on the current research work.

- ❖ To study the combined effect of grain refinement and micro-texture on mechanical properties of two step ECAPed ZE41 Mg alloy using grain boundary maps and texture plots obtained from EBSD.
- ❖ Understanding the corrosion mechanism of ZE41 Mg by investigating the effect of grain size, secondary phase particles and crystallographic orientation before and after ECAP.
- ❖ Analyzing the galvanic corrosion behavior of as received and ECAPed ZE41 Mg alloy by studying the role of microstructure and species formed after corrosion. Proposing surface film models developed after galvanic corrosion by understanding mechanism of galvanic corrosion occurring in ZE41 Mg- Al7075 Al couple.

CHAPTER 3

EXPERIMENTAL WORK

3.1 INTRODUCTION

This chapter gives detailed description about the research methodology adapted to investigate the mechanical properties and corrosion behaviour of ZE41 Mg alloy. It also elaborates the details about equipment used for microstructural observation, mechanical characterization and electrochemical testing. These investigations are used in correlating microstructure, mechanical properties and corrosion behaviour of ZE41 Mg alloy before and after subjecting to ECAP.

3.2 ZE41 MAGNESIUM ALLOY

Commercially available ZE41 Magnesium alloy was procured in as cast condition from Exclusive Magnesium, Hyderabad, Telangana, India. The as received samples were of

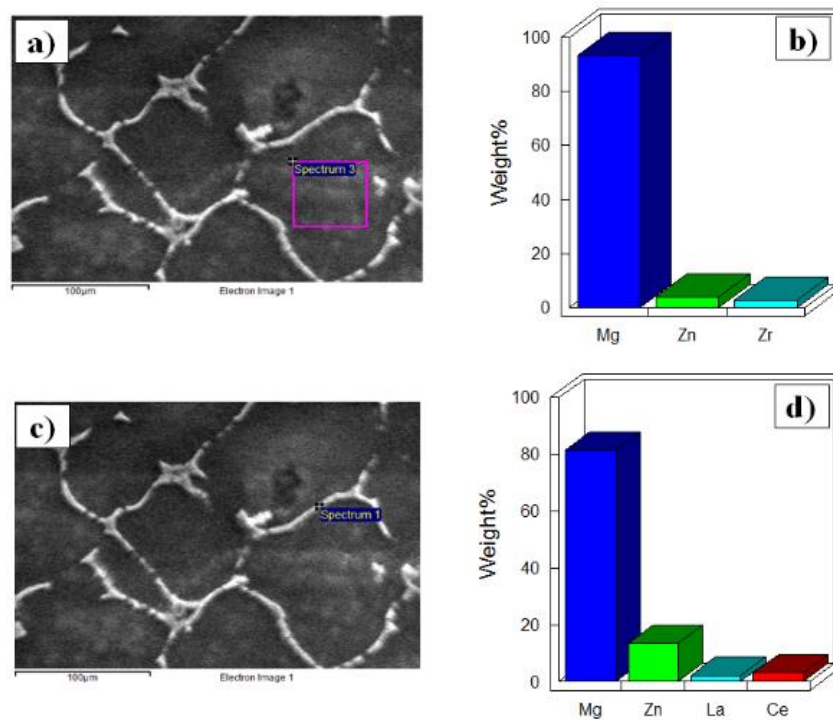


Fig 3.1 EDS of as received ZE41 Mg (a, b) SEM image and Wt % of constituent elements at grain (c, d) SEM image and Wt % of constituent elements at grain boundaries

16mm diameter and 200mm length. Figure 3.1 shows elemental dispersive spectroscopy (EDS) results of as received cast ZE41 Mg samples scanned particularly around the grain and the grain boundaries region. It is evident from figure 3.1 (a-b) that the grains are rich in magnesium with traces of Zn and Zr. The grain boundaries are also show large amount of Mg but traces of Ce and La elements were found along with Zn which is apparent from figure 3.1 (c-d). The chemical composition of ZE41 Mg alloy provided by manufacturer obtained from inductively coupled plasma atomic emission spectroscopy (ICP –AES) is tabulated in the table 3.1.

Table 3.1 Chemical composition of ZE41 Magnesium alloy in Wt%.

Zinc	Rare Earths	Zirconium	Magnesium
3.90	1.10	0.56	94.4(reminder)

3.3 EQUAL CHANNEL ANGULAR PRESSING

The as received ZE41 Mg samples were subjected to equal channel angular pressing to induce severe plastic deformation. Figure 3.2 represents the equal channel angular pressing set up equipped with temperature controller. Figure 3.3 depicts the details of the ECAP die used in the present study. ECAP die consists of two equal channels having a length of 100mm × diameter 16mm with channel angle and corner angle being 110° and 30° respectively. It is noteworthy to mention that this flipping type ECAP die was made in house and received a copyright from Government of India (Copyrights: Diary Number: 14668/2018-CO/L., Reg. No: L-79923/2018) (Naik et al, 2019). ECAP die has provision for heating as well as a thermocouple to measure the temperature. A temperature controller is used to monitor the temperature of ZE41 Mg sample placed inside the ECAP die. A robust universal testing machine (UTM) provided by Fuel instruments and engineers Pvt Ltd, Mumbai, Maharashtra, India was utilized to perform ECAP operation. It was used to press ZE41 Mg having a dimension of 15.5 mm diameter and 90 mm length after heating the sample to the desired temperature. The ram presses the sample through the equal channels at a strain rate of 5mm/min for every ECAP pass. After each pass, the ECAPed samples were machined again to dimension of 15.5 mm diameter. However, after successive ECAP passes the length of ZE41 Mg samples reduced relatively due to shear

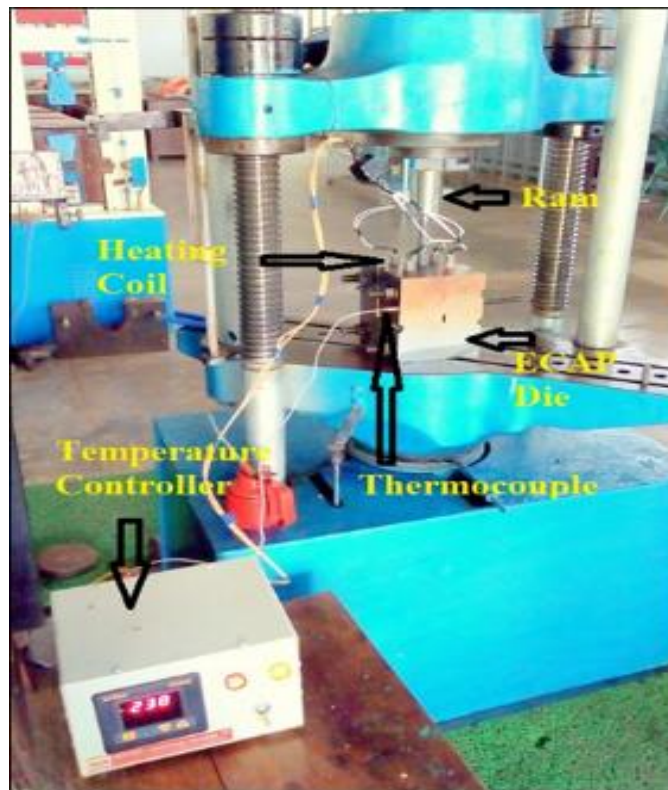


Fig 3.2 Equal channel angular pressing set up equipped with a temperature controller

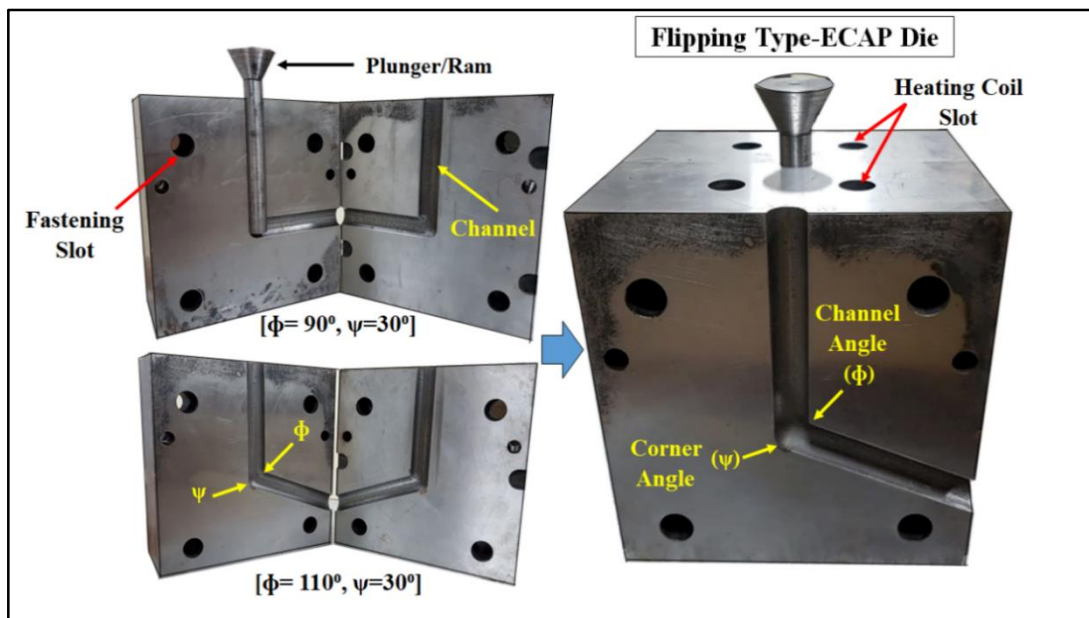


Figure 3.3 ECAP die having 90° and 110° channel angle and 30° corner angle

(Naik et al, 2019)

deformation. Then, the samples were rotated to 90° in a counter clock wise direction following the route Bc. Later, they were placed inside the die for next pass of ECAP operation. The process was repeated eight times and as a result, eight passes of ECAP were carried out on ZE41 Mg sample. Molybdenum disulphide was used as a lubricant during ECAP to reduce the friction between ZE41 Mg samples and die during pressing.

3.3.1 Selecting the processing temperature for two step ECAP

Conventionally, magnesium samples are ECAPed at single temperature which is termed as single step ECAP. A new strategy called two step ECAP came into application to overcome certain limitations of single step ECAP. In two step ECAP process, two temperatures are involved. Mg samples are pressed initially at a relatively higher temperature upto certain number of passes which is similar to single step ECAP. In addition, additional number of passes are carried at a relatively lower temperature. It is well known that the Mg alloys exhibit limited ductility owing to their inherent hexagonal closed pack (HCP) crystal structure. In addition, they possess only two slip systems for undergoing deformation. Hence, Mg and its alloys can be ECAPed successfully without surface cracks at temperature ranges of ~150 °C to 300 °C. In the present study, when ZE41 Mg samples were ECAPed at temperature below 250 °C surface cracks appeared on the specimen. This surface cracks are represented in the figure 3.4 (a). However, ZE41 Mg samples were ECAPed successfully at 275 °C without surface cracks as evident from figure 3.4 (b). Hence, during the first stage of ECAP, samples were pressed at a temperature of 300°C upto 4th pass while the second stage involved pressing of samples upto 8th pass at a temperature of 275°C.



Fig 3.4 ZE41 Mg samples ECAPed at a) 250 °C and b) 275 °C.

Table 3.2 Two-step ECAP processing parameters

	First step	Second step	
ECAP pass number	1 st , 2 nd , 3 rd , 4 th pass	1 st , 2 nd , 3 rd , 4 th pass	5 th , 6 th , 7 th , 8 th pass
ECAP temperature (°C)	300	300	275

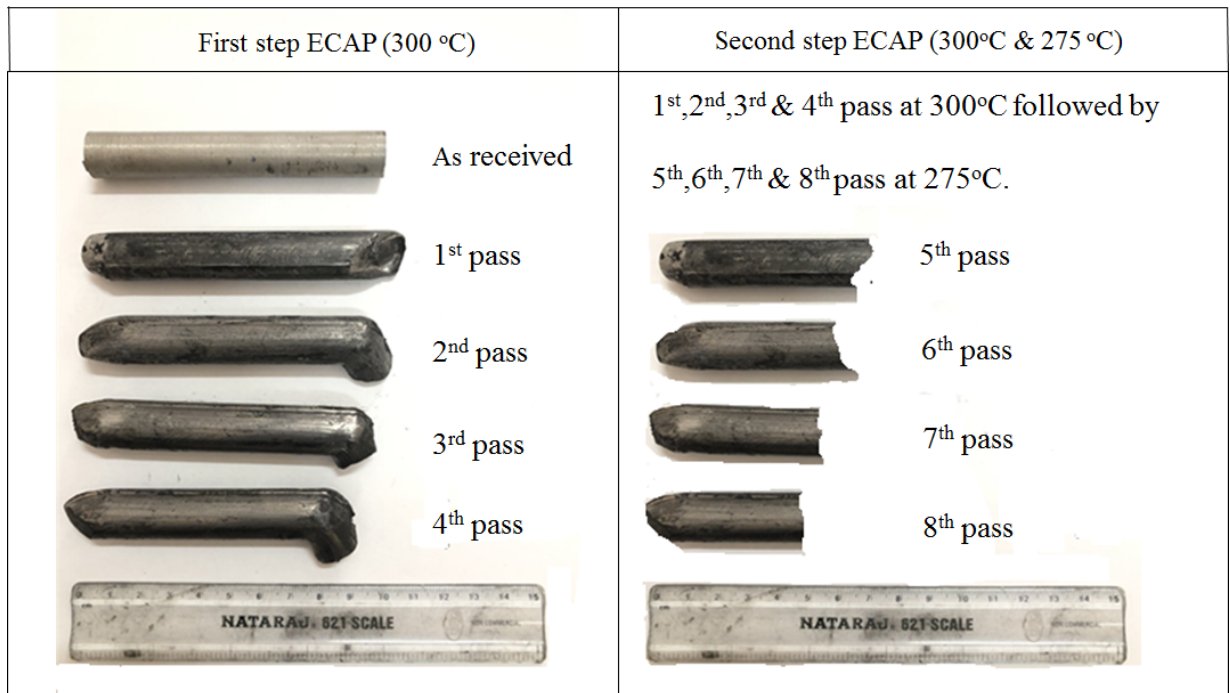


Fig. 3.5 Digital photographs of ZE41 Mg samples ECAPed during first and second step ECAP.

This process of carrying out ECAP at two different temperatures is termed as two step ECAP. Two step ECAP was carried out on ZE41 Mg alloy to eliminate the grain growth effect experienced in single step ECAP. The two step ECAP process parameters used in the present study are tabulated in the table 3.2. The digital photograph of ZE41 Mg samples ECAPed during single step and two step is shown in the figure 3.5. After successful completion of first and second step ECAP, microstructure, mechanical properties and corrosion behaviour of ZE41 Mg samples were investigated to analyse the impact of ECAP.

3.4 MICROSTRUCTURAL CHARACTERIZATION

The microstructural characterization is of prime importance to understand thoroughly the impact of ECAP on ZE41 Mg alloy. In general, OM and SEM techniques assist in realizing the microstructural evolution obtained as a result of ECAP. While, EBSD helps to envisage the crystallographic orientation or texture induced before and after ECAP. Indeed, the grain refinement and crystallographic orientation of ZE41 Mg alloy attained from microstructural studies are correlated to the mechanical properties, corrosion and galvanic corrosion behaviour.

3.4.1 Optical microscopy

The samples for microstructural studies were cut from as received and ECAPed samples along the extrusion direction. They underwent standard metallographic procedures and were etched by using 4% Nital solution. The grain boundaries of as received and ECAPed ZE41 Mg alloy was observed using Zeiss Axiolab microscope with Axio vision software for image capture. The optical microscope used in the study is shown in figure 3.6. Further insights on microstructural evolution after ECAP is studied.

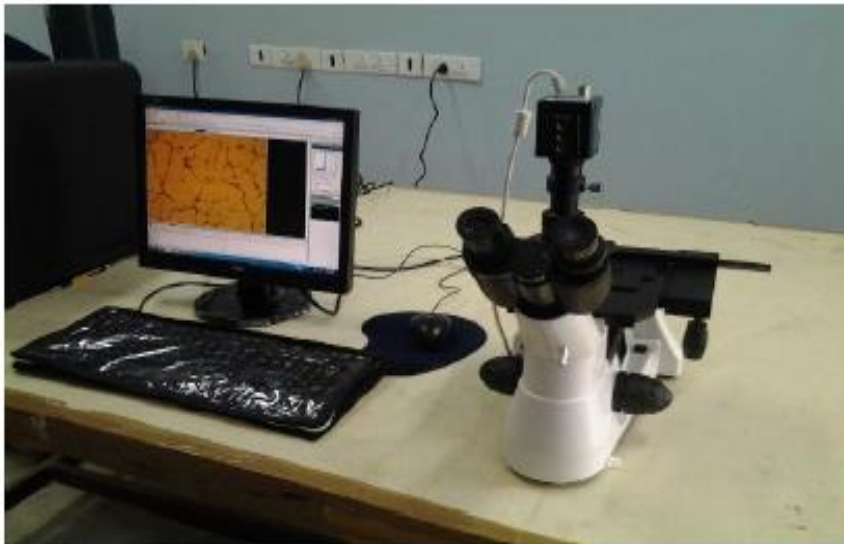


Fig 3.6 Zeiss optical microscope equipped with axio vision software.

3.4.2 Scanning electron microscopy

3.4.2 (a) Microstructural observation of ZE41 Mg and its secondary phases

After capturing images from optical microscope the same ZE41 Mg samples were further examined under SEM to study in depth about grain boundary evolution. Scanning Electron Microscopy Model: Jeol Jsm-6380la from Jeol, USA, operated at 30kV; Magnification range-3,00,000 x is depicted in figure 3.7. It is used to analyse the microstructural evolution after ECAP. It is well known that the secondary phase particles in Mg alloy undergo fragmentation after ECAP. Hence, SEM micrographs of ZE41 Mg alloy were obtained to correlate their role on mechanical properties and corrosion behaviour.

3.4.2 (b) Electron Backscattered diffraction (EBSD)

Recent studies revealed that mechanical properties and corrosion behaviour of Mg depends on both grain size and crystallographic orientation or texture. Hence, Fei Quanta 200 HV SEM equipped with EBSD detector shown in figure 3.8 was used to obtain electron backscattered micrographs. The equipment has a resolution of 3.0 nm at 30kV, 4-axis motorized stage for holding sample and image processor from which tag image file format (TIFF) image of 4096×3536 pixels can be obtained.



Fig 3.7 Scanning electron microscope attached with EDS detector.

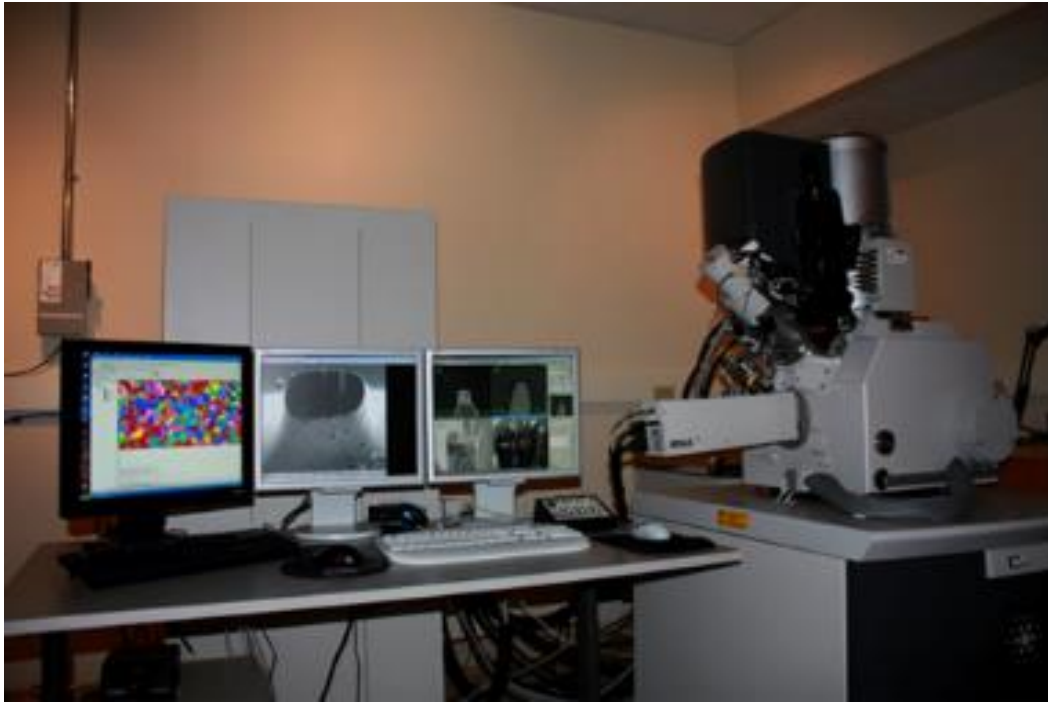


Fig 3.8 FESEM equipped with EBSD detector.

This equipment is housed under National facility of orientation imaging microscopy (OIM) and texture, OIM and texture lab, Metallurgical engineering and material science (MEMS) Department, Indian institute of technology Bombay (IITB), India. Prior to EBSD characterization ZE41 Mg samples were cut using Struers metallographic sample cutter along the extrusion direction. The samples were polished upto #5000 grit emery papers and mirror like finish was obtained by using 0.25 μ m diamond paste. This procedure is followed by electro polishing the sample with etchant containing 15mL perchloric acid, 41.5g sodium thiocyanate anhydrous, 75g citric acid, 800mL ethanol and 100mL propanol. After electro polishing, low angle ion milling was also carried out on the samples using precision ion polishing system (PIPS) Gatan Inc. USA, Model 591. After electro polishing and low angle ion milling ZE41 Mg samples were placed inside the sample stage of Fei Quanta 200 Nano SEM. The sample stage is tilted at angle of 70° to the horizontal surface. A beam of electrons were made to incident on ZE41 Mg alloy. These electrons after hitting the samples diverged in the form of cones and made to fall on phosphor screen in which the kikuchi patterns are formed. Neighbour pattern averaging and re-indexing (NPAR) was also done to enhance the quality of kikuchi pattern. This in turn improved the success rate of indexing. Later, Pole figures, inverse pole figures and schmid factor data was generated from EBSD micrographs using TSL OIM software (EDAX) version 8 for ZE41 Mg samples.

3.5 MECHANICAL TESTING

The improvement in mechanical properties of ZE41 magnesium alloy after ECAP was investigated from results obtained through tensile tests. The individual mechanical properties viz., yield strength, ultimate tensile strength and fractography before and after ECAP were correlated to the microstructure obtained from OM, SEM and EBSD. As a result, the strengthening mechanism responsible for enhancement in mechanical properties was revealed. The fractured surface morphology of ZE41 Mg samples were also observed using SEM in order to examine the role of ECAP on mode of fracture. Later, the mode of fracture is correlated to the ductility of ZE41 Mg samples.

3.5.1 Evaluation of mechanical properties using tensile test

The tensile tests of ZE41 Mg samples were conducted on tensile tester UTM-Shimadzu AG-X plus depicted in figure 3.9. It is equipped with 100 kN load cell and operated with a steady cross-head speed of 0.25 mm/min. The round tensile specimens were cut along extruded direction and machined according to ASTM E8M standard. These sample with a gauge diameter 4mm and gauge length 20mm and is represented in the figure 3.10. Triplicate tests were carried out to ensure reproducibility.



Fig 3.9 ZE41 Mg sample mounted in SHIMADZU UTM

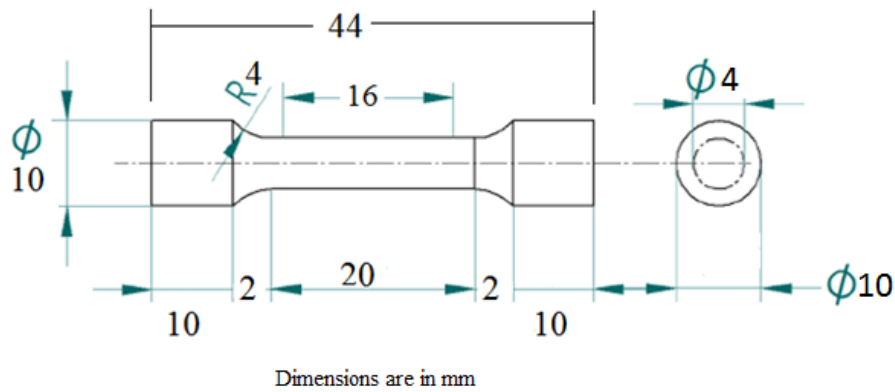


Fig 3.10 Tensile samples according to ASTM E8 standards.

3.5.2 Fractography of ZE41 Mg samples

The objective of this study is to enhance the mechanical properties of ZE41 Mg alloy in general and ductility in particular. Therefore, it is very essential to understand the type of fracture viz., brittle, ductile and mixed mode of fracture. Hence, post the tensile test, the fractured surfaces were also analysed using scanning electron microscope. Based on microstructural features such as cleavages, dimples and micro-cracks observed, the mode of failure is identified.

3.6 CORROSION STUDIES

Mg and its alloys exhibit relatively lower corrosion resistance. The current study aims to improve the corrosion resistance of ZE41 Mg alloy by ECAP. In addition, the combined effect of grain refinement, secondary phases and crystallographic orientation after ECAP is to be explored. In order to achieve the above mentioned objectives, the corrosion rate before and after ECAP is evaluated using electrochemical corrosion tests and galvanic corrosion tests.

3.6.1 Electrochemical corrosion tests of ZE41 Mg

Electrochemical corrosion analyser (make; Gill AC, ACM instruments, United Kingdom) was used to evaluate the corrosion behaviour of ZE41 Mg samples. The corrosion equipment used in the current study is shown in the figure 3.11. After obtaining mirror like surface finish the samples were inserted into corrosion kit with only 1cm² area of

ZE41 Mg expose to testing medium viz., 0 M, 0.1M and 1 M NaCl. Three types of tests were carried out and the chronological order of these tests were sequenced.

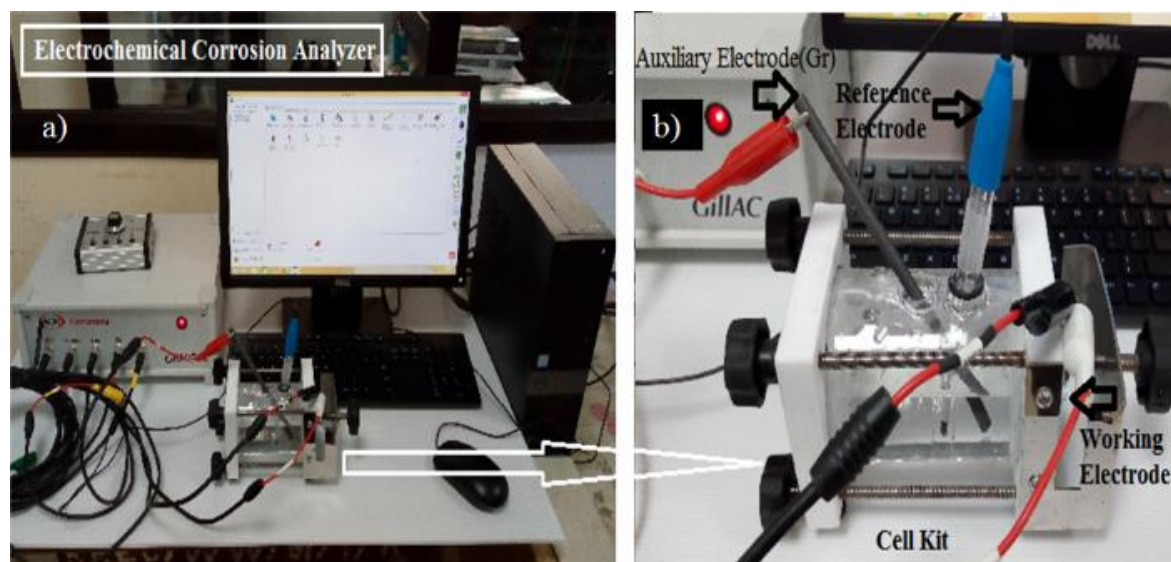


Fig 3.11 Corrosion equipment used a) Electrochemical corrosion analyser b) an expanded view showing electrical connection.

The thermodynamics of corrosion is given by open circuit potential (OCP). The OCP tests lasted for a duration of 20 minutes. The nature of surface film and its properties like charge transfer resistance (R_{ct}), double layer capacitance (C_{dl}) and solution resistance (R_s) were obtained from electrical impedance spectroscopy (EIS) test. The test started at a frequency of 10000Hz and ended at 0.001 Hz with amplitude of 10mV. The Nyquist plot obtained from EIS tests were fitted using V4 analysis software. Cyclic sweep tests were conducted by sweeping through a potential of -250 mV to +250mV with respect to rest potential. The corrosion rate of ZE41 Mg samples were calculated based on the cathodic slopes. The electrochemical corrosion tests were triplicated to gain confidence in measurements. All the experiments were carried out at room temperature.

3.6.2 Galvanic corrosion experiments of ZE41 Mg- Al7075 Al couple

The as received ZE41 Mg, ECAPed ZE41 Mg, aluminium alloy were mounted in an epoxy resin with electrical connections at the rear end of samples. All the samples were ground using standard metallographic procedures to obtain mirror polished surface eliminating the

effect of roughness on corrosion. The circuit connections for galvanic corrosion differ from electrochemical corrosion tests by addition of a secondary working electrode.

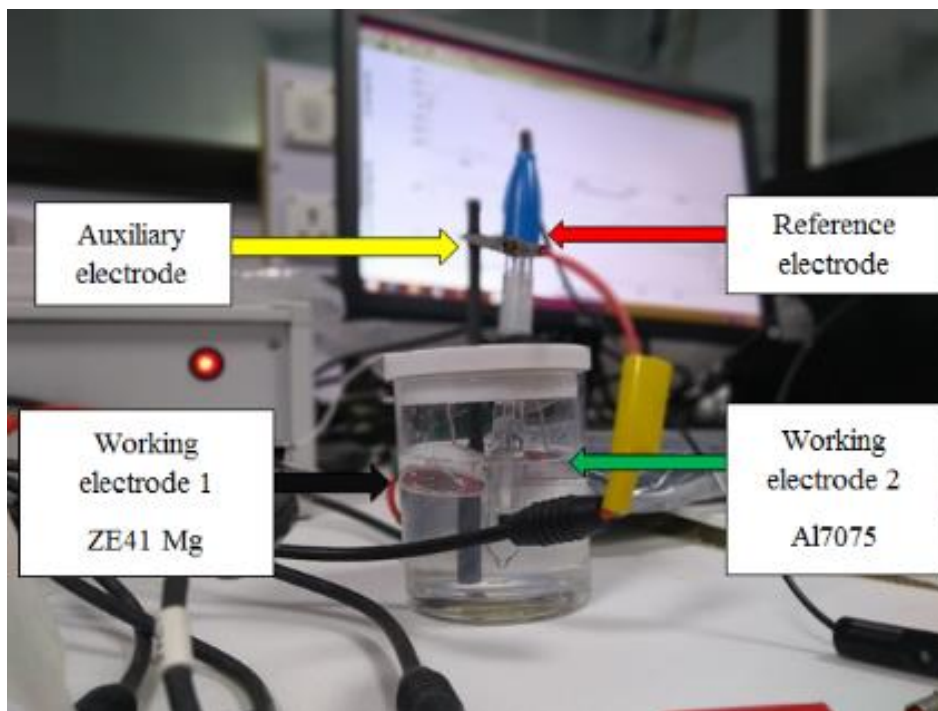


Figure 3.12 Experimental set up for galvanic corrosion.

ACM Gill AC potentiostat /Galvanostat integrated with zero resistance ammeter (ZRA) was used for carrying out the galvanic corrosion experiments. ZE41 Mg was connected to the working electrode 1 (WE1), aluminium alloy was connected to working electrode 2 (WE2), saturated calomel electrode (SCE) to reference electrode (RE) and graphite connected to auxiliary electrode (AE). The experimental set up for galvanic corrosion measurements is shown in figure 3.12. 0 M, 0.1M and 1M sodium chloride was used as an electrolyte. The distance between the galvanic couple and depth of electrolyte were maintained constant. The galvanic couple was established between ZE41 Mg- Al7075 Al alloy. ZRA measures the galvanic current between the galvanic couple. The corrosion rate and robustness of oxide film for galvanic experiments are obtained from potentiodynamic polarization plot and Nyquist plot respectively.

3.7 PHASES AND SPECIES DETECTION

3.7.1 Identification of phases in ZE41 Mg alloy using X-ray Diffraction (XRD)

Jeol X-ray diffractometer used in the present study is shown in the figure 3.13. It is equipped with Copper $K\alpha$ radiation as target, wavelength of 1.54056 \AA . 2 Theta range of 20° - 80° , a step size of 0.02 and a scan rate of $1^\circ/\text{min}$ was used for acquiring diffraction peaks. XRD was performed to ascertain the phases present in as received and ECAPed ZE41 Mg alloys. These XRD results are further related to the mechanical properties and corrosion behaviour of ZE41 Mg samples. In addition, they elucidate the possible strengthening mechanism responsible for variation in mechanical properties as a result of ECAP.

3.7.2 Revealing surface films models using X-ray photoelectron spectroscopy (XPS)

Figure 3.14 shows the XPS (make: Kratos Axis Ultra) having X ray source of high power Al monochromator and five axis sample stage. In addition, it is capable of detecting elemental composition of materials upto 0.1% and has a minimum scan area of $\sim 15 \mu\text{m}$ in diameter. This facility is housed at Amrita centre of Nano sciences, Kochi, Kerala, India. It was used for detecting species formed on ZE41 Mg samples after galvanic corrosion.



Fig 3.13 X-ray diffraction operated at 20 mA and 30 kV with Cu- $k\alpha$ radiation

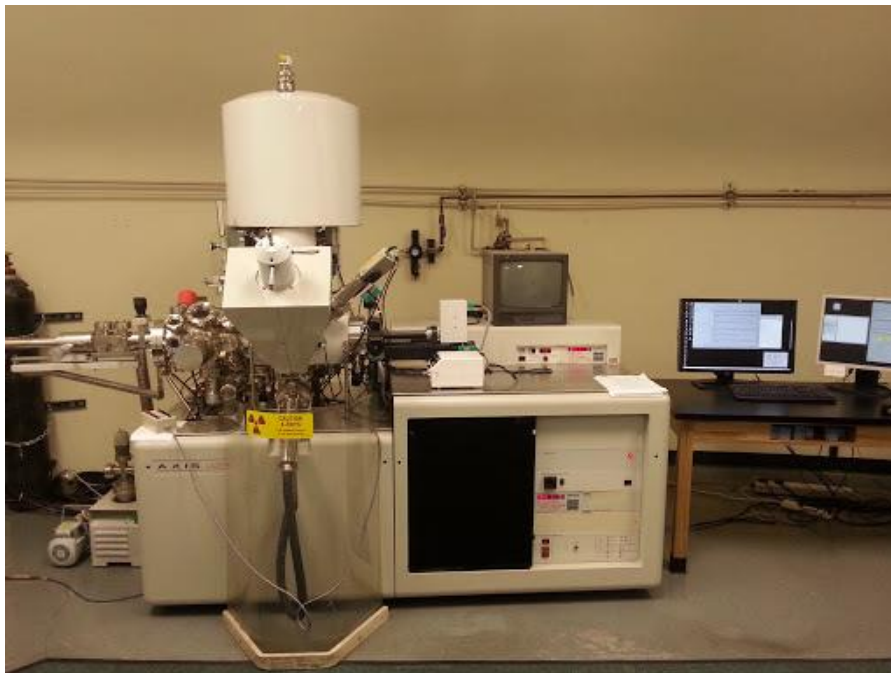


Fig 3.14 X-ray Photoelectron spectroscopy set up.

The corrosion product formed after Potentiodynamic polarization studies were also analysed initially using XRD. This analysis of corrosion product gives the detail about nature of oxide film formed on the surface of ZE41 Mg samples. The phases and adsorbed species after the occurrence of galvanic corrosion were detected by XRD and XPS respectively. The survey spectra generated from XPS gives information about the presence of elements and corresponding signals. Based on the binding energy of corresponding signal the species present on ZE41 Mg samples are revealed. In addition, the atomic concentration obtained from XPS analysis helped in realizing surface film models developed after galvanic corrosion.

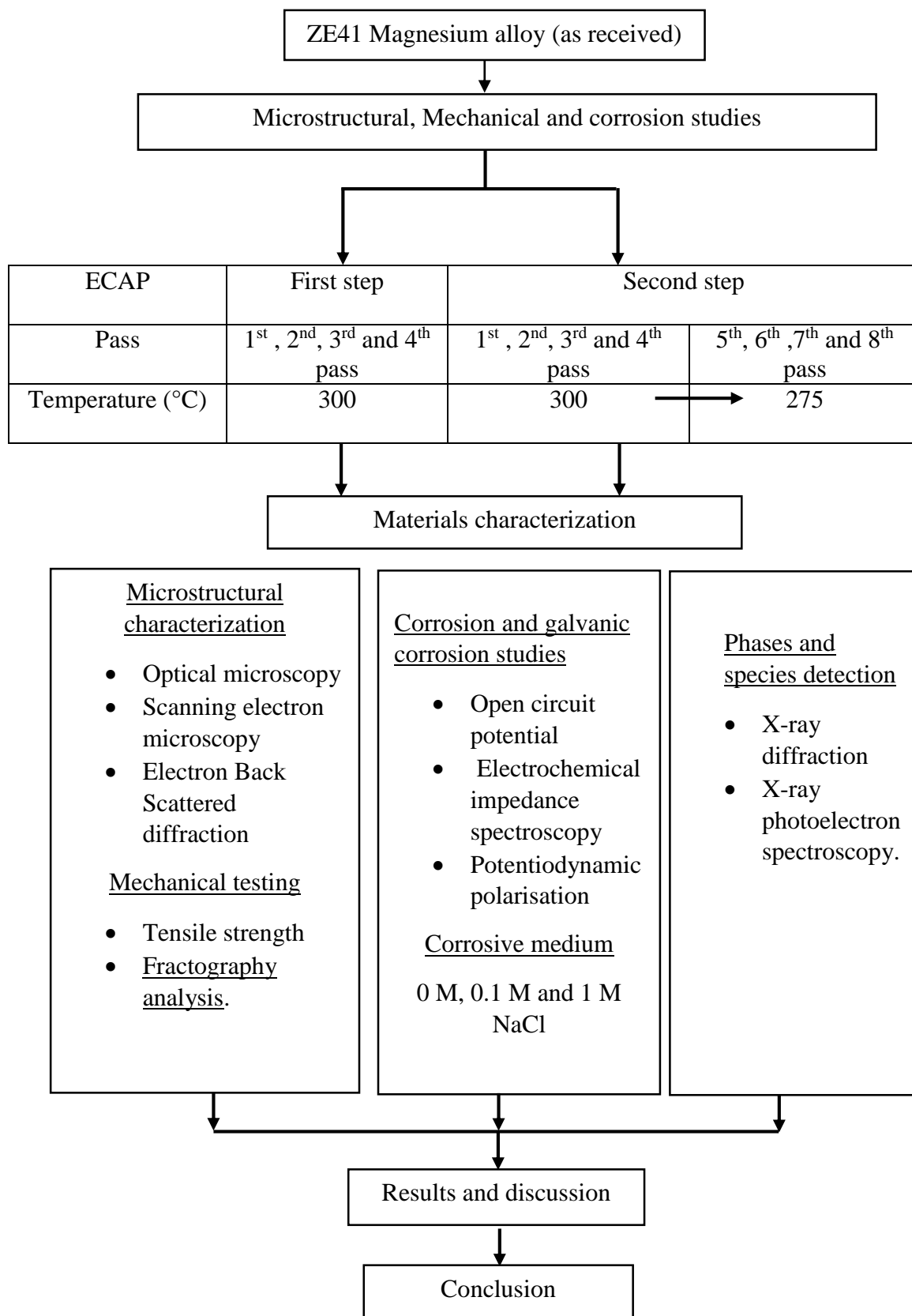
3.7.3 Corrosion morphology of ZE41 Mg

After completion of electrochemical tests, ZE41 Mg alloy subjected to corrosion and galvanic corrosion were removed from the set up. The corrosion products from corroded samples were removed by chromic acid. SEM was also used to characterize the corrosion morphology of ZE41 Mg samples obtained after corrosion and galvanic corrosion. The types of corrosion viz., filiform corrosion, pitting corrosion, uniform corrosion, micro-galvanic corrosion, trans-granular and inter-granular were revealed using corroded SEM

micrographs. Later, the corrosion rate of ZE41 Mg samples was correlated to their corrosion morphology.

3.8 SUMMARY

The as received ZE41 Mg samples were subjected to two step ECAP. The mechanical properties of as received and ECAPed ZE41 Mg alloy were investigated. Based on this investigation, the strengthening mechanism responsible for improvement or decrement in mechanical properties were identified. In addition, the corrosion and galvanic corrosion behaviour of ZE41 Mg samples were evaluated using electrochemical corrosion tests. The research methodology is sequenced chronologically to accomplish the objectives of the present work and is represented below in the form of a flow chart.



CHAPTER 4

ANALYZING THE COMBINED EFFECT OF GRAIN REFINEMENT AND MICRO-TEXTURE ON MECHANICAL PROPERTIES OF ZE41 MAGNESIUM ALLOY SUBJECTED TO TWO STEP ECAP.

4.1 INTRODUCTION

Two step equal channel angular pressing is carried out on as received ZE41 Mg alloy. The first step comprises of carrying out 1st, 2nd, 3rd and 4th passes of ECAP on as received ZE41 Mg sample at a processing temperature of 300°C. As a result of first step ECAP 1st pass, 2nd pass, 3rd pass and 4th pass ECAPed ZE41 Mg samples are obtained. The second step comprises of subjecting as received ZE41 Mg alloy to 1st, 2nd, 3rd and 4th passes of ECAP at a processing temperature of 300°C followed by 5th, 6th, 7th and 8th passes of ECAP at 275°C. After completion of second step ECAP 5th pass, 6th pass, 7th pass and 8th pass ECAPed ZE41 Mg samples are obtained. The as received and ECAPed ZE41 Mg samples are evaluated for combined effect of crystallographic orientation and grain refinement using electron back scattered diffraction (EBSD). In addition, the microstructure of as received and ECAPed ZE41 Mg samples is correlated to the mechanical properties.

4.2 INFLUENCE OF ECAP ON MICROSTRUCTURE AND MECHANICAL PROPERTIES OF ZE41 MAGNESIUM ALLOY.

Recent research observations point out that crystallographic orientation has a greater influence on mechanical properties of Mg alloys (Agnew et al. 2004; Mukai et al. 2001). However, from the literature, it is observed that not much attention has been given to analyse the combined effect of grain refinement, crystallographic orientation and the ECAP processing temperature on mechanical properties of ZE41 Mg alloy. Hence, in the current research work, an effort has been made to explore the influence of combined effect of grain refinement and crystallographic orientation on mechanical properties of ZE41 Mg alloy. Further, the effect of two step ECAP process on microstructure and mechanical properties of ZE41 Mg alloy is explored.

4.3 MICROSTRUCTURE OF ZE41 MAGNESIUM ALLOY

4.3.1 Microstructural evolution obtained as a result of ECAP

The electron backscattered micrographs of as received, 1st pass, 2nd pass, 3rd pass and 4th pass equal channel angular pressed ZE41 Mg samples generated from TSL OIM software are presented in figure 4.1 (a-e) respectively. The EBSD micrographs of 5th Pass, 6th Pass, 7th Pass and 8th Pass ZE41 Mg alloy are also presented in figure 4.2 (a-e) to enlighten the grain refinement phenomenon. The stereographic triangle in the lower left corner of

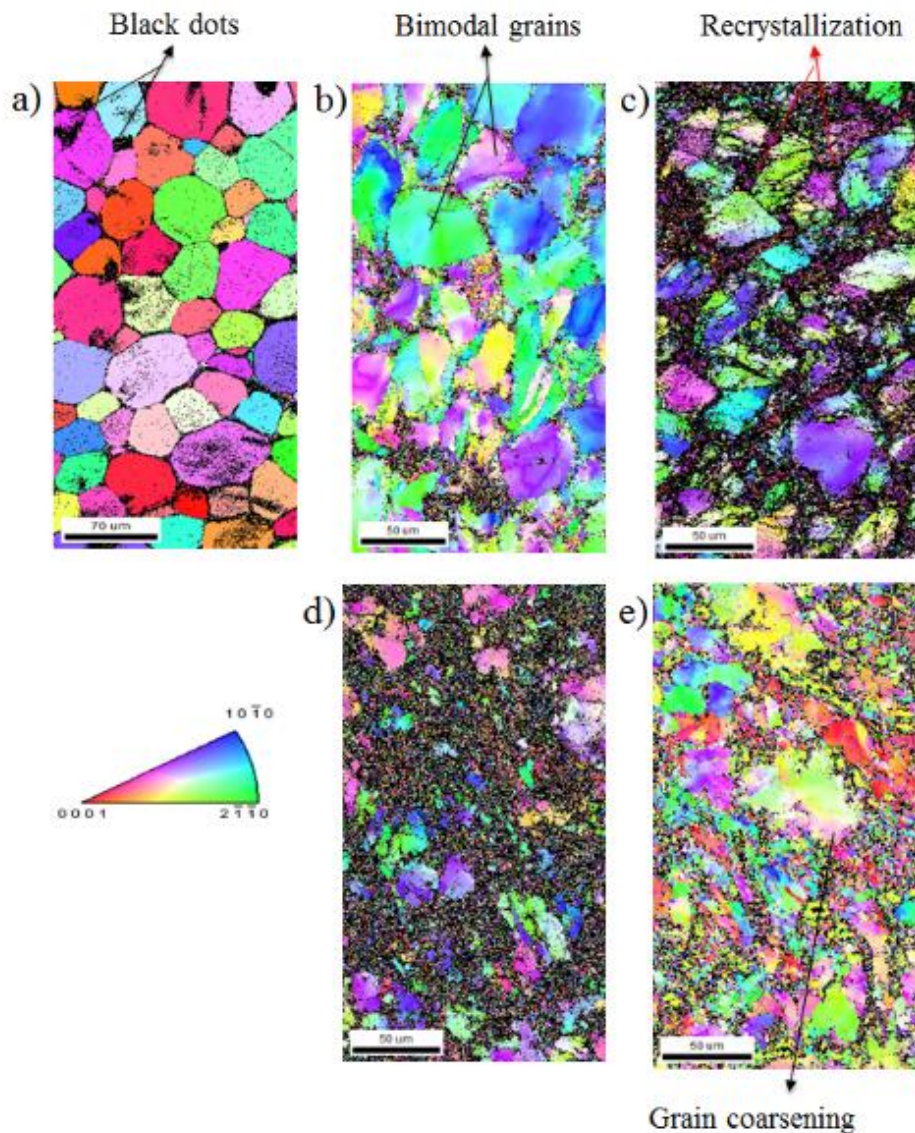


Fig 4.1 EBSD Micrographs of ZE41 Mg alloy during first step ECAP

(a) as received (b) 1st pass (c) 2nd pass (d) 3rd pass (e) 4th pass.

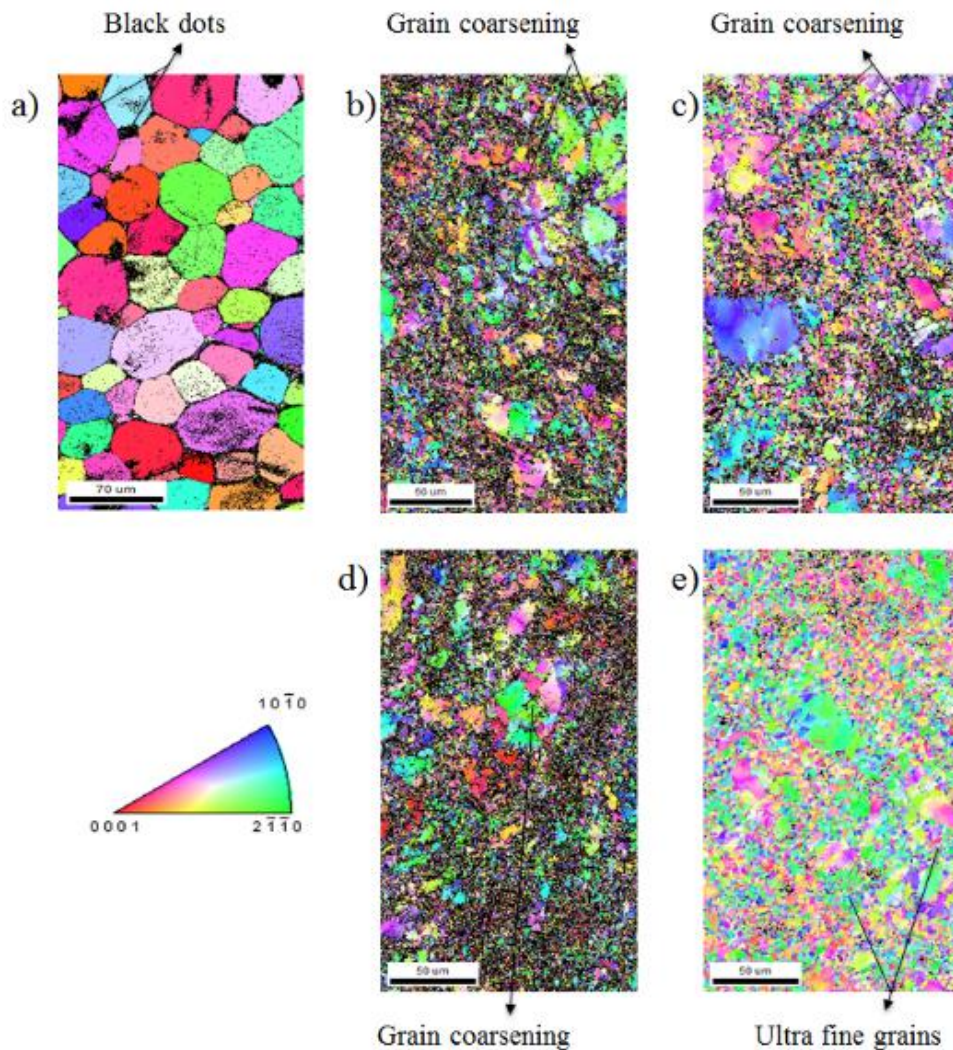


Fig 4.2 EBSD Micrographs of ZE41 Mg alloy during second step ECAP

(a) as received (b) 5th pass (c) 6th pass (d) 7th pass (e) 8th pass.

figures 4.1 and 4.2 represent the colour corresponding to the crystallographic orientation. As previously described, during the first step of ECAP the samples were pressed at a temperature of 300°C whilst the second step was carried out at 300°C and 275°C. The grain morphology of as received ZE41 Mg sample evinced heterogeneous grains with grain size varying from 35μm to 58μm as depicted in figure 4.1(a). However, the average grain size of as received sample is calculated to be 46μm. After 2nd pass of equal channel angular

pressing a bimodal grain morphology was observed with grain diameter of 25 μm and 12 μm having area fraction of 0.109 and 0.058 respectively. Also, recrystallization occurred only along the grain boundaries which is evident from figure 4.1(c). The average grain diameter of as received, 1st pass, 2nd pass, 3rd pass and 4th pass ECAP samples was measured to be ~46 μm , ~24 μm , ~13 μm , ~6 μm and ~10 μm respectively. Despite increasing the number of ECAP passes, grain coarsening was observed in 4th pass sample as shown in figure 4.1 (e). This grain growth during 4th pass is attributed to performing ECAP at same temperature of 300°C and inter pass time of 40 minutes that the sample spent during ECAP. Also, the grain boundaries of fine grain microstructure is less stable than the coarse grain microstructure (Dumitru et al. 2014, Mostaed et al. 2015a). Other researchers also observed similar phenomena and attributed this to fine grains possessing lower activation energy than the coarse grains. This leads to an increase in grain size to attain stable state during dynamic equilibrium (Mostaed et al. 2014b, Miao et al. 2010). The yield strength of ZE41 Mg alloy was 158 MPa in as received condition and gradually increased to 177 MPa, 190 MPa, 192 MPa and 236 MPa after 1st pass, 2nd pass, 3rd pass and 4th pass ECAP respectively. Indeed, the mechanical properties of ZE41 Mg alloy are discussed in detail in section 4.5. Previous studies on ECAP suggested that mechanical properties of Mg alloys can be further enhanced by two step ECAP (Mostaed et al. 2015a, Mostaed et al. 2014b). Hence, in this study, two-step ECAP process was chosen with an expectation that the mechanical properties of ZE41 Mg alloy will be improved further. During the second step of ECAP process the average grain diameter was calculated to be ~4.8 μm , ~7.14 μm , ~3.93 μm and ~2.5 μm after 5th Pass, 6th pass, 7th pass and 8th pass respectively. There is no remarkable change in grain size during two step ECAP at 275°C which is clearly observed from figure 4.2 (b-e). This minimal reduction in grain size during second step of ECAP was also observed by various researchers (Mostaed et al. 2015a, Mostaed et al. 2014b). From EBSD micrographs represented in the figures 4.1 (a-e) and 4.2 (a-e), it is observed that there is no evidence of secondary phases present in ZE41 Mg alloy. However, some black dots are observed in figure 4.1 (a) at the grain boundaries of as received samples. Minarik et al, (2016b) also witnessed such black areas in the EBSD micrographs of LAE442 Mg alloy. They postulated that those black area might correspond to secondary phases in LAE442 Mg alloy and occurred as a result of low confidence index values during cleaning raw data of EBSD. Mostaed et al. (2014a) also observed black area in EBSD micrographs of extruded ZK60 Mg alloy and reported them as secondary phase particles. Hence, the

presence of black areas in as received ZE41 Mg samples might correspond to secondary phase particles. However, after first step and second step ECAP of ZE41 Mg alloy the black areas appear at the grain boundaries and they are fine grains that evinced low confidence index. To enlighten the grain refinement phenomenon, the grain refinement model and grain boundary characteristics are further investigated.

4.3.2 Grain refinement model of ZE41 Mg alloy

Ding et al (2010) carried out single step ECAP on as cast ZE41 Mg alloy at a temperature of 320°C using ECAP die with channel angle of 90°. On the contrary, in the present study, ZE41 Mg samples were successfully ECAPed at relatively lower temperature of 300°C during first step ECAP. This is because the ECAP die used in the present study has a channel angle of 110°. As a result of using relatively higher channel angle of 110° the applied equivalent plastic strain is reduced and subsequently ZE41 Mg alloy is successfully ECAPed at 300°C. Indeed, during second step ECAP the samples were pressed at further lower temperature of 275°C. This was possible because the ductility of as received ZE41 Mg samples increased from 7 % to 19.76 % by the end of first step ECAP. The present study cannot be compared head to head with findings of Ding et al. (2010) because of the different ECAP processing parameters used. However, the initial grain size of as received ZE41 Mg and final grain size achieved after ECAP in the present study were comparable to that of Ding et al. (2010). Thus, it is evident that the channel angle of ECAP die and the ECAP processing temperature influence the grain refinement phenomenon. Figueiredo and Langdon (2010) proposed grain refinement models for magnesium and its alloys processed by ECAP. They proposed the concept of critical grain size (d_c) and its effect on number of ECAP passes required to achieve ultra-fine grains (UFG) in Mg. Whenever, the initial grain size (d) of Mg is larger ($d \gg d_c$) and relatively larger ($d > d_c$) than critical grain size more than one pass is required to achieve homogeneous ultra-fine grain microstructure. In contrast, if the critical grain size of Mg is relatively less than the initial grain size ($d < d_c$), homogeneous fine grain microstructure could possibly be achieved at only a single pass of ECAP. In this study, the initial grain size of as received ZE41 Mg alloy was $\sim 46 \mu\text{m}$ which is relatively higher than the critical grain size. Therefore, fine grains of $\sim 2.5 \mu\text{m}$ was achieved at 8th pass ECAP. Hence, in addition to channel angle of ECAP die and processing temperature, initial grain size, critical grain size and history of material processing prior to ECAP dictate the grain refinement phenomenon of magnesium and its alloys. So, it can be

concluded that the grain refinement obtained after ECAP is in good accordance with recent findings (Ding et al.2010, Sekar et al.2019, Praveen et al.2019) and proposed grain refinement models (Figueiredo and Langdon 2010).

4.3.3 Grain boundary characteristics of ZE41 Mg alloy

In order to elucidate the mechanism of grain refinement, the grain boundary maps of ZE41 Mg alloy after first step ECAP are represented in figure 4.3 (a-j). They are generated from field emission scanning electron microscope (FESEM) micrographs. The figure 4.3 (a, b, c, d, e) and (f, g, h, i, j) represents the grey FESEM images and grain boundary mapping of as received, 1st pass, 2nd pass, 3rd pass and 4th pass ZE41 Mg samples respectively. The EBSD micrographs of ZE41 Mg samples presented in the figures 4.1 and 4.2 did not completely represent the features present in the grain boundaries due to the low confidence index. In contrast, from the grain boundary maps of ZE41 Mg alloy, the zone with dynamically recrystallized (DRXed) grains are apparent from figure 4.3 (f, g, h, i, j).

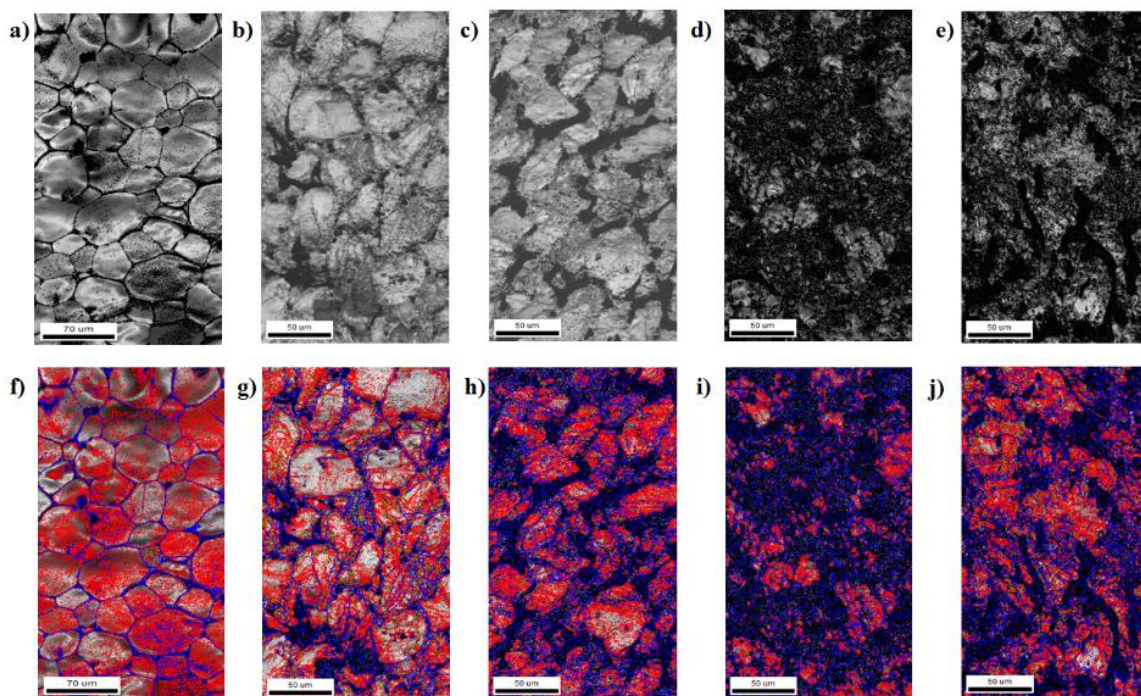


Fig 4.3 Grey scale micrographs of (a) as received, (b) 1st pass, (c) 2nd pass, (d) 3rd pass (e) 4th pass and grain boundary maps (f) as received, (g) 1st pass, (h) 2nd pass, (i) 3rd pass (j) 4th pass of ZE41 Mg alloy during first step ECAP.

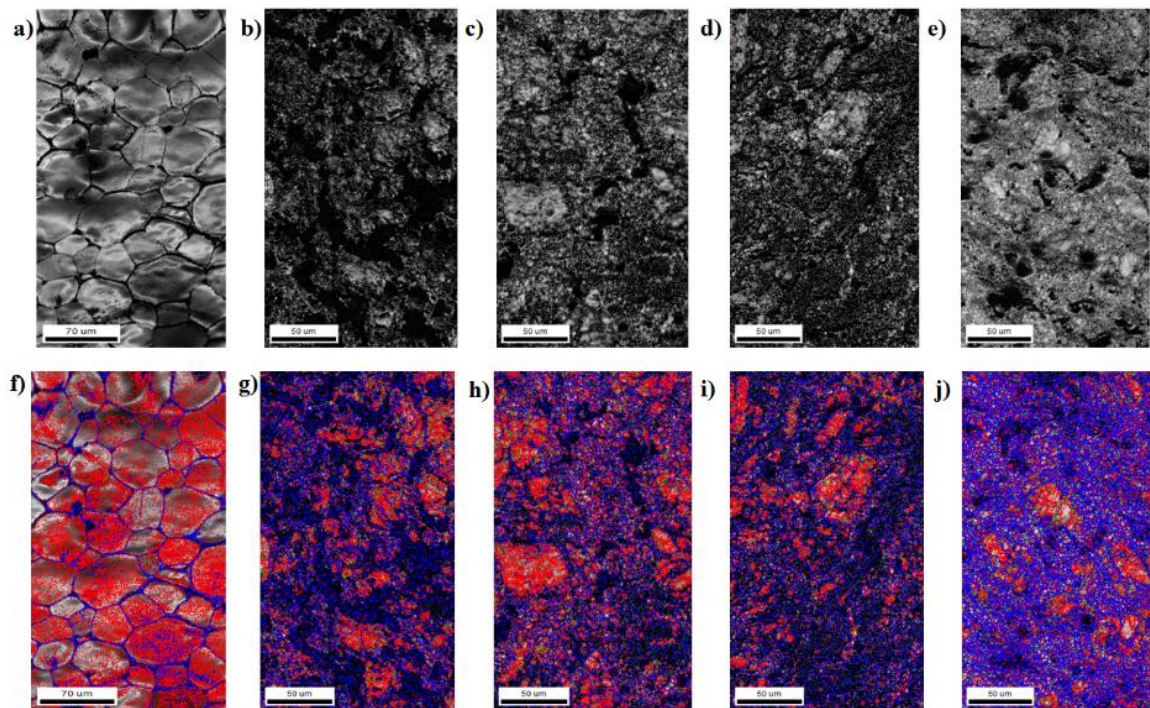


Fig 4.4 Grey scale micrographs of (a) as received, (b) 5th pass, (c) 6th pass, (d) 7th pass (e) 8th pass and grain boundary maps (f) as received, (g) 5th pass, (h) 6th pass, (i) 7th pass (j) 8th pass of ZE41 Mg alloy during second step ECAP.

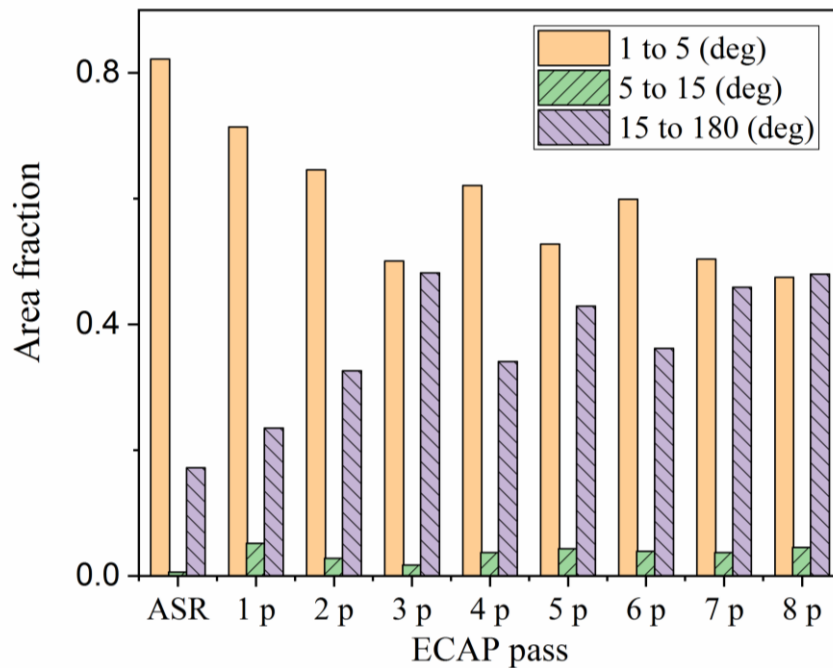


Fig 4.5 Grain boundary misorientation angles of ZE41 Mg as function of number of ECAP pass.

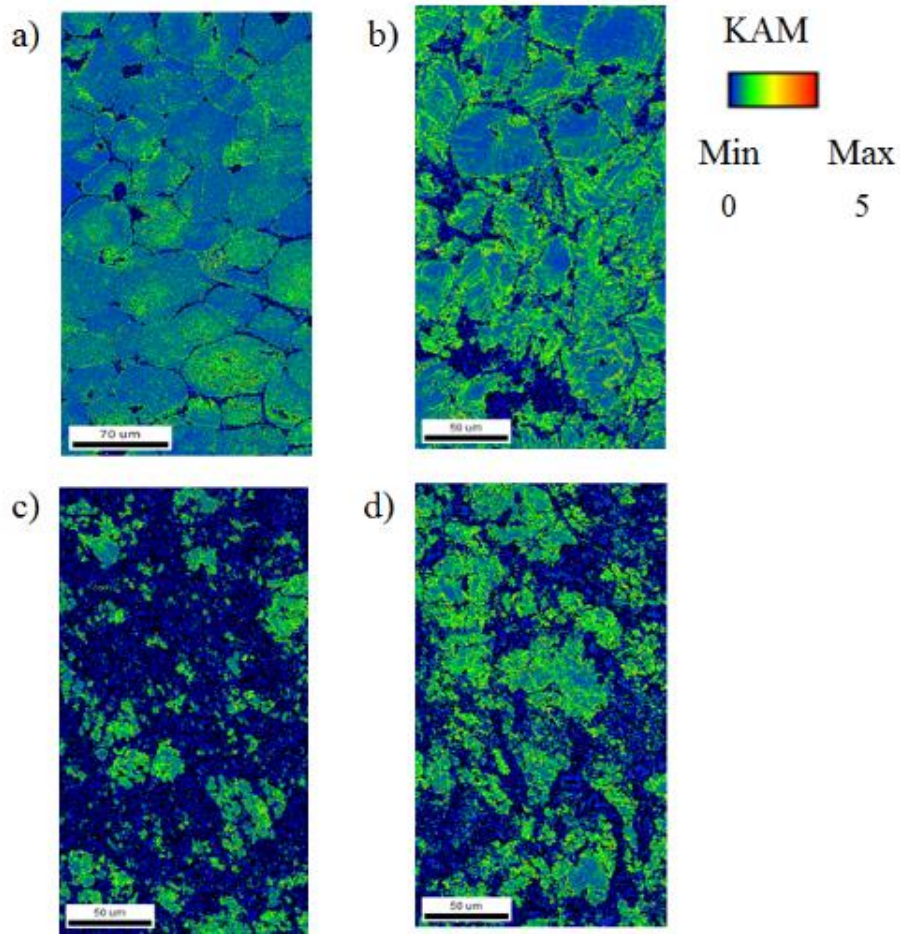


Fig 4.6 Representative kernel average maps of ZE41 Mg alloy during first step ECAP (a) as received (b) 1st pass (c) 3rd pass (d) 4th pass.

Figure 4.4 (a-j) depicts the grey scale micrographs and grain boundary maps of ZE41 Mg in as received, 5th, 6th, 7th and 8th pass condition. Also, the area fraction of low angle grain boundaries (LAGBs) and high angle grain boundaries (HAGBs) of ZE41 Mg samples are quantified in the figure 4.5. The grain boundaries with misorientation angle less than 15° and greater than 15° are classified as LAGBs (red in colour) and HAGBs (dark blue in colour) respectively. Interestingly, when compared to the grain boundary map of as received ZE41 Mg (figure 4.3 (f) and 4.4 (f)) the area fraction of DRXed grains increased steadily with increase in number of ECAP passes as seen from figure 4.3 (g, h, i, j) and 4.4 (g, h, i, j). From figures 4.3, 4.4 and 4.5 it is apparent that with increase in number of ECAP passes the area fraction of high angle grain boundaries (HAGBs) increases. During 1st and

2nd pass of ECAP, the area fraction of LAGBs are 70% and 50% greater than HAGBs. In contrast, the area fraction of LAGBs and HAGBs are comparable in 3rd, 4th, 5th, 6th and 7th passes. Even during the second step of ECAP, an increase in area fraction of DRXed grains and high angle grain boundaries (HAGBs) is noticed. However, the low angle grain boundaries (LAGBs) were not completely eliminated by the end of 8th pass ECAP. It is also interesting to observe that a relatively uniform microstructure is obtained in the 8th passes ECAP. Hence, it is reasonable to interpret that when the area fraction of LAGBs and HAGBs are comparable, it is possible to achieve a relatively uniform microstructure with

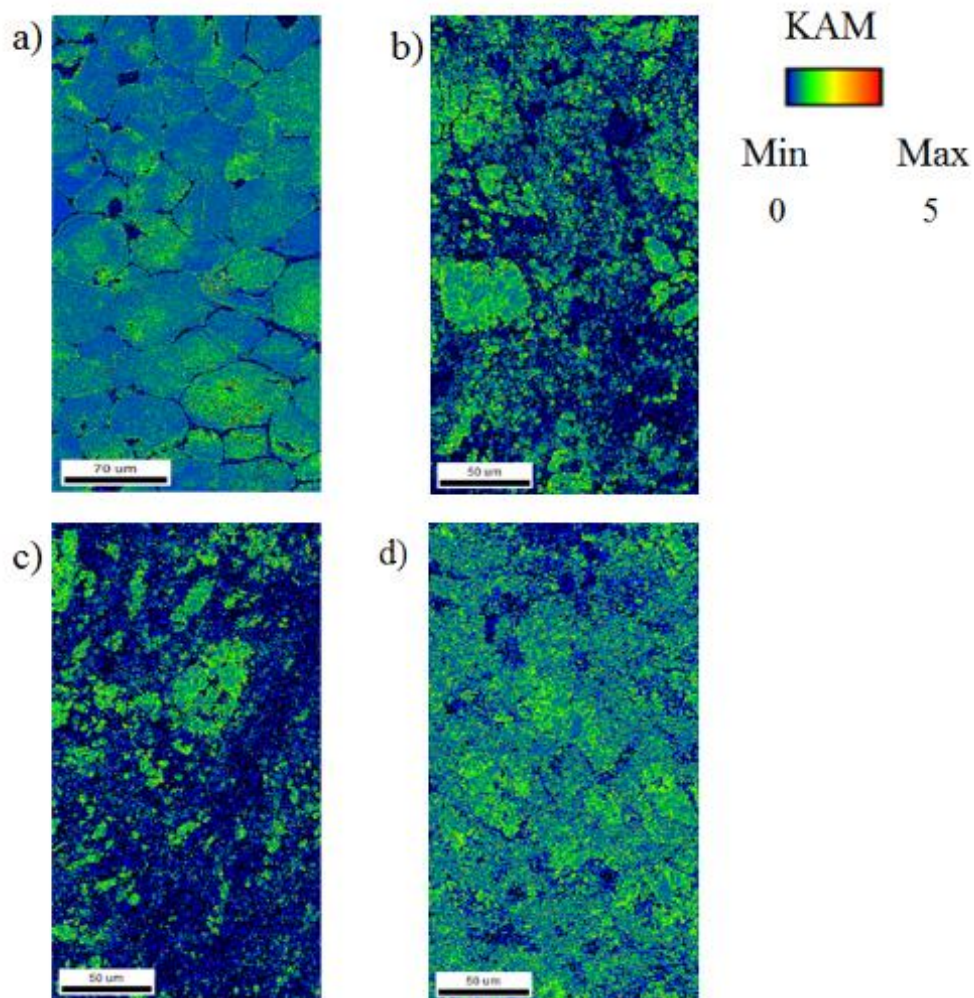


Fig 4.7 Representative kernel average maps of ZE41 Mg alloy during first step ECAP (a) as received (b) 6th pass (c) 7th pass (d) 8th pass.

ultra-fine grains. Janeček et al. 2017 also observed similar relative increase in HAGBs and relative decrease in LAGBs when LAE442 Mg alloy was subjected to ECAP. In another study, the pure Mg alloy in as cast condition was ECAPed upto 7th pass using multi step technique. The study also indicated that with increase in number of ECAP passes, the number fraction of HAGBs increased with simultaneous decrement in LAGBs (Biswas et al, 2010). Therefore, it can be concluded that the ECAP results in conversion of LAGBs to HAGBs. However, the population of LAGBs cannot be completely eliminated. The kernel average misorientation (KAM) maps of first step ECAPed ZE41 Mg samples are depicted in the figure 4.6 (a-d). They represent the local grain misorientation with an additional constraint considering only misorientation angle less than 5° to purposefully exclude the grain boundaries. The mean angle between crystallographic orientation with respect to nearest neighbours are denoted by colour coded pixels seen in right corner of figure 4.6 with minimum 0° to maximum 5°. It is observed from figure 4.6 (a) that the as received ZE41 Mg sample evinced minimum local grain orientation of 0° because it appears blue as per pixel coding.

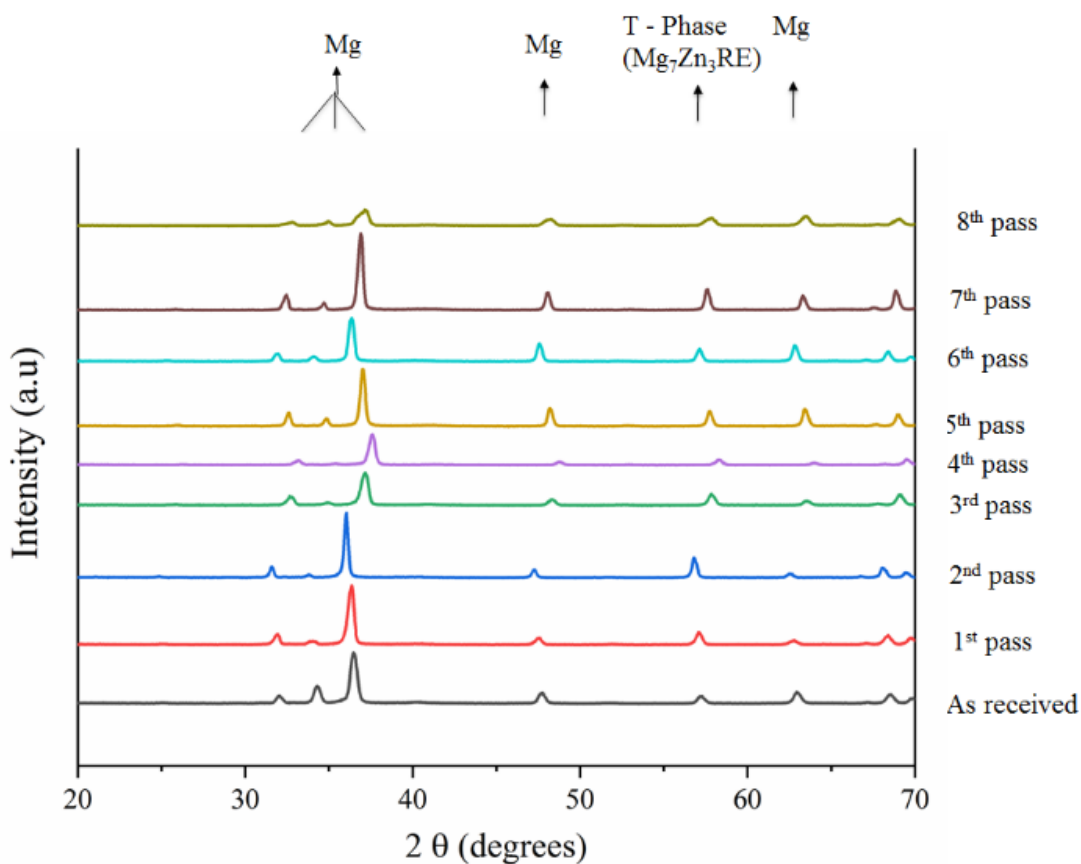


Fig 4.8 X-ray diffraction patterns of ZE41 Mg alloy.

On the contrary, for ECAPed samples in the first step green and yellow pixels were observed in figure 4.6 (b-d). This indicates that the ECAP resulted in local misorientation in the range of 0° to 3° . The kernel average misorientation (KAM) maps of second step ECAPed ZE41 Mg samples are depicted in the figure 4.7 (a-d). 6th pass and 7th pass ECAPed ZE41 Mg samples exhibited a combination of blue, green and yellow pixels, with area of blue pixel dominating among them. Interestingly, after 8th pass ECAP, the green pixel completely dominated the blue pixel indicating the maximum grain misorientation among ZE41 Mg samples. X-ray diffraction peaks of ZE41 Mg alloy for different passes is depicted in figure 4.8. It is observed that peaks corresponding to primary Mg Phase and T phase (Mg_7Zn_3RE) are clearly visible. One can observe the increase in relative intensity of peaks with respect to increase in number of pass. This is correlated to the variation in texture and fraction of secondary phases or precipitates (Janeček et al. 2017). ECAP is dynamic in nature where during extrusion process, heating of material coarsen the grain while simple shearing action at the intersection of equal channels contribute to grain refinement. The resulting microstructure after reaching dynamic equilibrium gives an insight into factors that dominated during each pass of ECAP.

4.4 MICRO-TEXTURE EVOLUTION OF ZE41 MAGNESIUM ALLOY.

The pole figures corresponding to (0001) plane for as received, 1st pass, 2nd pass, 3rd pass and 4th pass ECAPed ZE41 Mg samples constructed from EBSD plots are illustrated in figure 4.9 (a-e) respectively. The maximum texture intensity of as received, 1st pass, 2nd pass, 3rd pass and 4th pass samples are found to be 7.38, 13.77, 10.07, 8.07 and 9.66 respectively. The as received ZE41 Mg alloy exhibited a randomly distributed texture with a maximum texture intensity value of 7.38 as represented in the figure 4.9 (a). The intensity of texture increased to a maximum value of 13.77 and 10.07 after 1st and 2nd pass of ECAP respectively. This is due to formation of new grains during grain refinement which is apparent from figure 4.1 (b) and (c). Similar kind of increase in texture intensity and formation of new grains was also observed and reported when AZ61 Mg alloy was subject to ECAP (Kim et.al, 2002). The position of maximum texture also shifted to a new location away from extrusion direction (ED) and transverse direction (TD) after the completion of 2nd pass of ECAP as presented in figure 4.9 (c). Equal channel angular pressing resulted in variation of position, value of maximum texture intensity and formation of new texture elements which is attributed to rotation of ECAP billet by 90° after each pass following the

conventional route B_c. From figure 4.9 (e) it is clear that the 4th pass ECAP resulted in weakening of basal texture element with a slight decrease in intensity to a value of 9.6. The pole figures corresponding to (0001) plane of ZE41 Mg samples for as received, 5th pass, 6th pass, 7th pass and 8th pass samples are represented in figure 4.10 (a-e). The maximum texture intensity of 5th pass, 6th pass, 7th pass and 8th pass samples were reported to be 5.15, 9.23, 6.04 and 6.98 respectively. A decrease in maximum texture intensity of 5.15 during 5th pass and a relative increase in texture intensity of 9.23 and 6.9 was also observed after 6th and 8th pass respectively. This signifies the formation of new texture element.

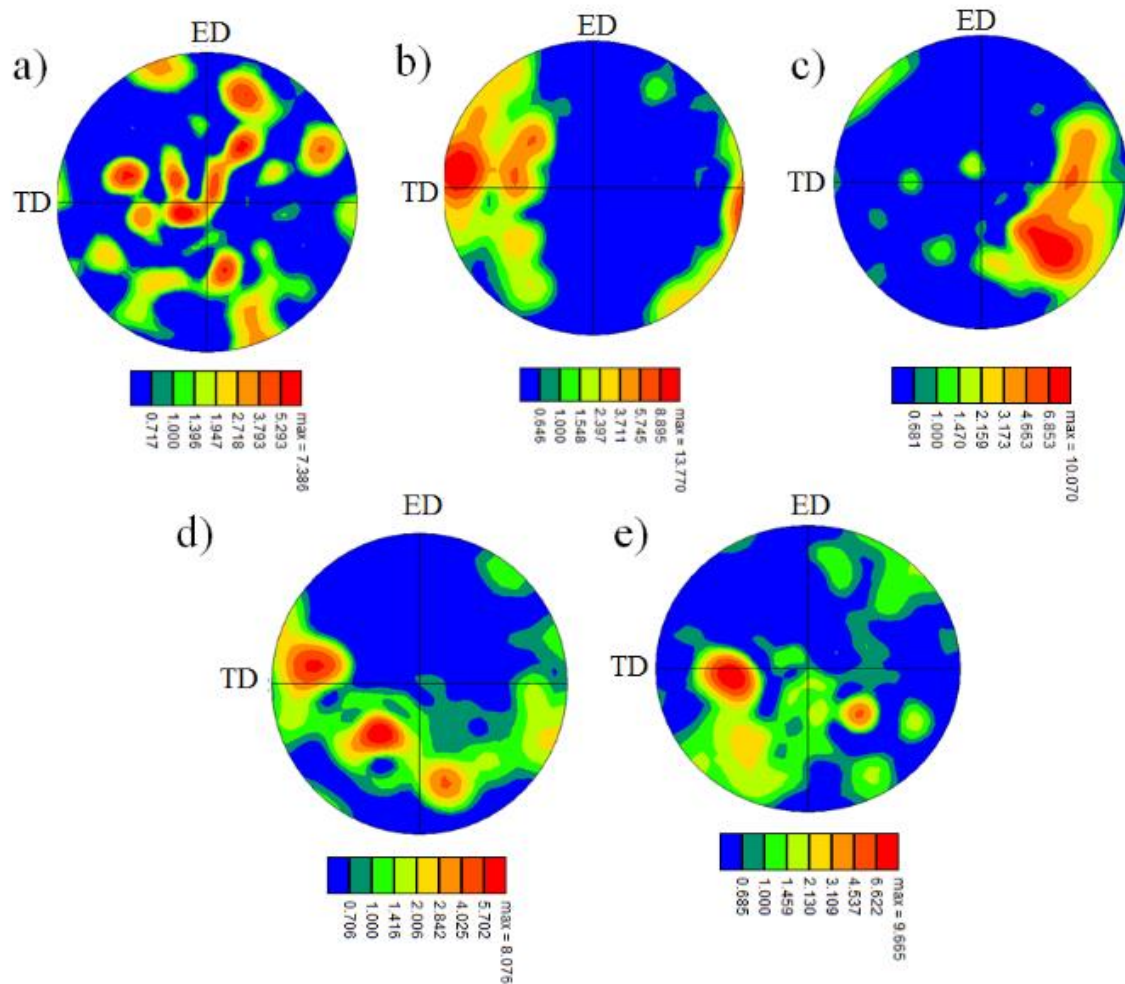


Fig 4.9 Pole figures corresponding to (0001) plane of ZE41 Mg (a) as received
 (b) 1st pass (c) 2nd pass (d) 3rd pass (e) 4th pass.

After completion of 6th pass and 8th pass the basal texture element aligned $\sim 65^\circ$ and $\sim 55^\circ$ to extrusion direction (ED) which is clearly indicated in figure 4.10 (c) and (e) respectively. This particular orientation of basal texture generally deteriorates yield strength of ZE41 Mg alloy and is also the reason for insignificant reduction in grain size after 6th pass and 8th pass ECAP as observed in figure 4.2 (b-e). Generally, it is observed that the extruded and cast Mg alloys evince fibre texture and random texture respectively. Upon ECAP, texture softening occurs and eventually the samples ends up in formation of new texture element with tilt angles of 40° to 55° between ED and TD. The texture modification (Kim et al.2002) and increase in texture intensity after first step followed by sharp decrease during the second step ECAP has been reported by various researchers during equal channel

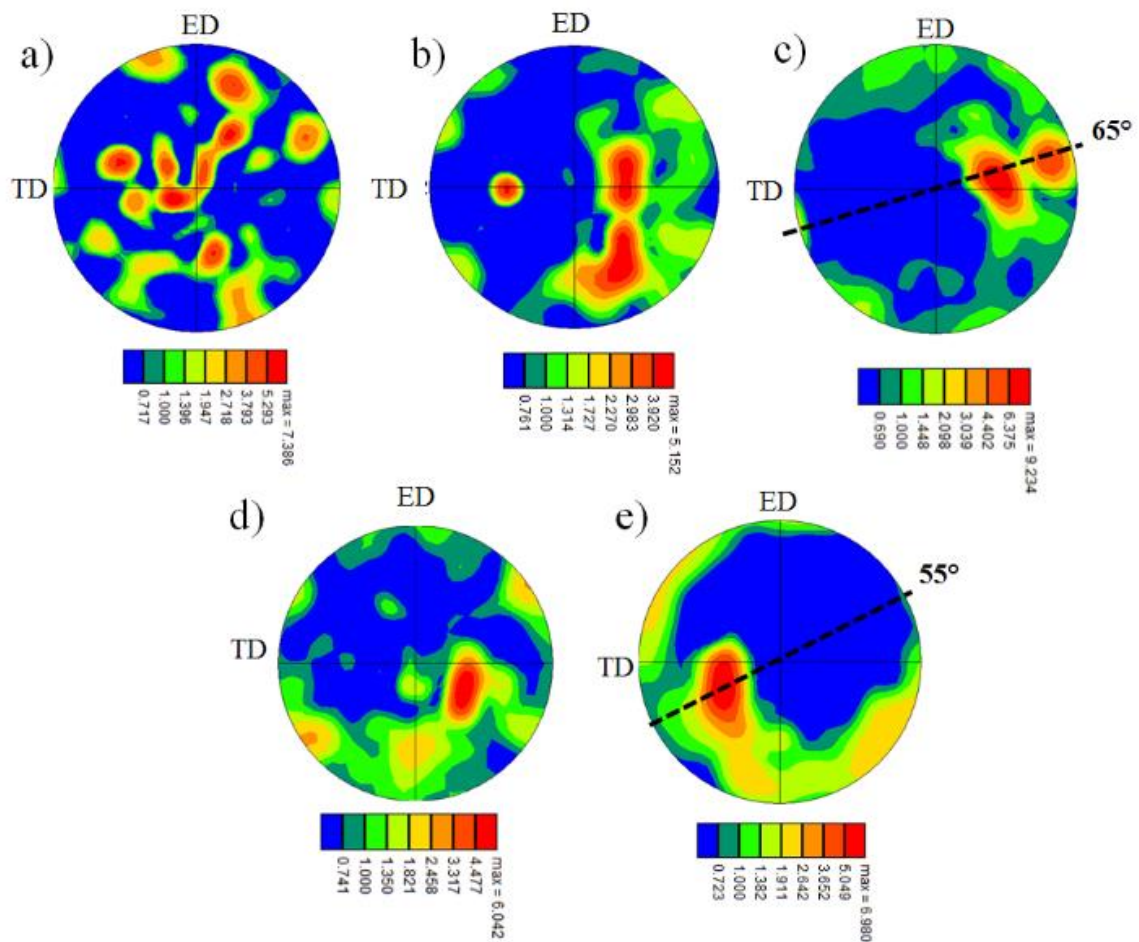


Fig 4.10 Pole figures corresponding to (0001) plane of ZE41 Mg (a) as received (b) 5th pass (c) 6th pass (d) 7th pass (e) 8th pass.

angular pressing of AE21, AE42, LAE442, ZK60 and ZM21 Mg alloys (Mostaed et al. 2015a, Mostaed et al. 2014b, Minárik et al. 2016). The as received AE21, AE42 and LAE442 alloys subjected to ECAP exhibited ultrafine grains at 8th pass because of random texture (Minárik et al. 2016). In contrast, relatively higher number of passes was required to achieve ultrafine grains in extruded ZK60 and ZM21 Mg alloys due to typical fibre texture (Mostaed et al. 2014b, Minárik et al. 2016). In the present study, fine grains were obtained by subjecting as received ZE41 Mg alloy upto 8th pass ECAP. This is because the as received ZE41 Mg alloy exhibited random texture after casting. Hence, it is reasonable to believe that the apart from processing temperature the initial texture or history of processing decides the number of ECAP passes to achieve grain refinement. In addition, the XRD peaks of ZE41 Mg alloy exhibits variation in intensity which indicates changes in texture as shown in figure 4.8. The texture evolution based EBSD also indicates the variation in texture with respect to each ECAP condition. Thus, the XRD peaks are also in line with the texture plots generated from EBSD. In addition, the XRD and texture plots obtained in the present study is in accordance with recent findings (Krajňák et al. 2017).

4.5 MECHANICAL PROPERTIES OF ZE41 MAGNESIUM ALLOY.

4.5.1 Influence of micro-texture and grain refinement on yield strength of ZE41Mg.

The mechanical properties of ZE41 Mg alloy viz., yield strength (YS), ultimate tensile strength (UTS) and % elongation are depicted in the figure 4.11 as a function of ECAP passes. It is well established that various mechanisms such as solid solution strengthening, precipitate strengthening and grain boundary strengthening influence the mechanical properties of ECAPed Mg samples. From XRD peaks represented in figure 4.8, it is observed that there are negligible changes in the lattice parameters of ZE41 Mg alloy. This indicates that solid solution strengthening did not contribute significantly for improvement in mechanical properties of ZE41 Mg alloy. It is also known that the dispersion strengthening mechanism is possible, only if the particle size is about 100 nm. Also, if precipitation hardening is the only reason for strengthening, the mechanical properties would have increased chronologically with increase in number of passes (Ding et al. 2010). From figure 4.11, it is evident that the mechanical properties did not increase chronologically with increase in number of passes. Indeed, during first step ECAP, the yield

strength of as received ZE41 Mg increased significantly till 4th pass ECAP. However, during second step ECAP, the yield strength decreased sharply. Hence, it is reasonable to conclude that precipitation strengthening did not occur during ECAP. The XRD peaks after ECAP are in accordance with previous findings. They also reported that solid solution strengthening and precipitate strengthening did not influence the mechanical properties of Mg alloy (Ding et al. 2010). In addition, other studies on ECAP of AE21, AE42, LAE442, ZK60, AX41 and ZM21 Mg alloys revealed that mechanical properties are dependent on grain boundary and texture (Mostaed et al. 2015a, Mostaed et al. 2014b, Minárik et al. 2016, Kim et al.2002,Minárik et al. 2016a, Minárik et al. 2016b ,Krajňák et al. 2017, Praveen et al.2019). Hence, in the present study the grain boundary strengthening and texture are taken into consideration for further analysis. The mechanical properties of ZE41 Mg alloy are quantified in the table 4.1. According to Hall- Petch relation, the yield strength of ZE41 Mg alloy should be improved due to grain refinement after ECAP. The yield strength of ZE41 Mg alloy was 158 MPa in as received condition and gradually

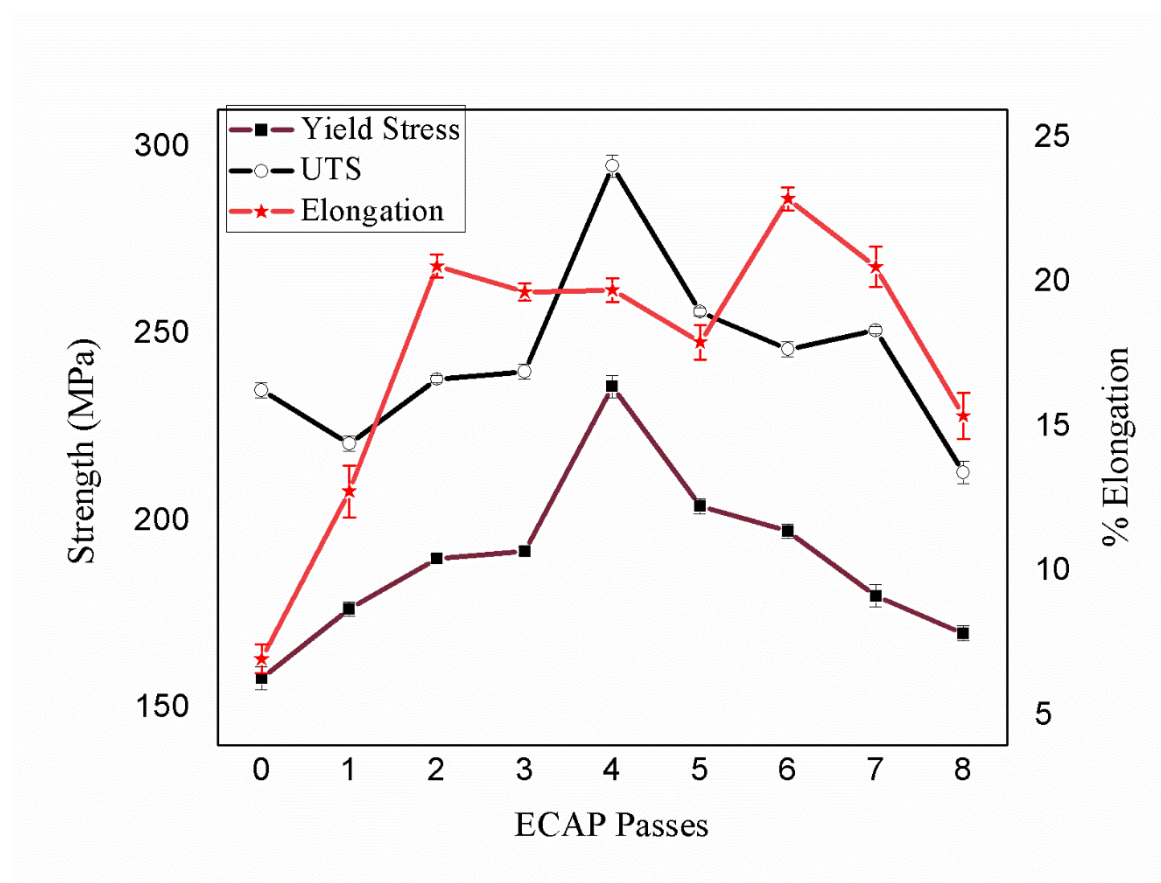


Fig 4.11 Mechanical properties of ZE41 Mg alloy as function of number of ECAP passes.

Table 4.1 Mechanical properties of ZE41 Mg alloy.

ECAP pass	Avg Grain Size (μm)	Yield Stress (MPa)	UTS (MPa)	% Elongation	Maximum Texture Intensity	Schmid factor
0	46 ± 3.7	158 ± 3	235 ± 2	7 ± 0.5	7.38	0.21
1 st	24 ± 1.9	177 ± 2	220 ± 2	12.8 ± 0.9	13.77	0.28
2 nd	13 ± 0.9	190 ± 1	238 ± 1	20.59 ± 0.4	10.07	0.29
3 rd	5.76 ± 0.5	192 ± 1	240 ± 2	19.69 ± 0.3	8.07	0.31
4 th	10 ± 0.8	236 ± 3	295 ± 3	19.76 ± 0.4	9.66	0.30
5 th	4.8 ± 0.8	204 ± 2	256 ± 1	17.95 ± 0.6	5.15	0.31
6 th	7.13 ± 0.8	197 ± 2	246 ± 2	22.92 ± 0.4	9.23	0.34
7 th	3.93 ± 0.6	181 ± 3	251 ± 1	20.56 ± 0.7	6.04	0.31
8 th	2.5 ± 0.9	172 ± 2	213 ± 3	15.41 ± 0.8	6.98	0.33

increased to 177 MPa, 190 MPa, 192 MPa and 236 MPa after 1st pass, 2nd pass, 3rd pass and 4th pass ECAP respectively. From figure 4.11 and table 4.1, it is evident that remarkable increase in yield tensile strength was observed with increasing ECAP passes during the first step of ECAP. This increase in yield strength resulted from the grain refinement after ECAP is observed from figure 4.1 (b-e). Ding et al. (2010) investigated the mechanical properties of ZE41 Mg before and after performing 6th pass ECAP at 320°C. The yield strength of ECAPed samples were greater than as received. However, the yield strength of 1st, 2nd and 6th pass ECAP samples were similar and measured to be 220 MPa (Ding et al. 2010). In single step process all ECAP passes are carried out at same temperature. In this procedure, fine grains undergo grain growth. This is because fine grains are not stable at higher temperature. To control the grain growth and further enhance the mechanical properties, recent studies performed ECAP at two steps (Mostaed et al. 2015a, Mostaed et al. 2014b). Hence, in the present study second step of ECAP was carried at a relatively lower temperature of 275°C. In contrast, the second step of ECAP witnessed a sharp decrease in yield strength (YS) values of 204 MPa, 197 MPa, 181 MPa and 172 MPa after 5th pass 6th pass 7th pass and 8th pass respectively. This decrease could be explained by the fact that other metallurgical factors like texture influence the yield strength of ZE41 Mg alloy (Ding et al. 2010). The formation of new texture element and their alignment with ECAP shear plane as represented in figure 4.10 (c) and (e) decreased the yield strength of ZE41 Mg alloy despite the grain refinement depicted in figure 4.2 (c) and (e). In conclusion, during the second step of ECAP processing, texture softening predominates the effect of grain

refinement. Similar drop in yield strength of ECAPed Mg alloys at the second step was also reported by various investigators (Mostaed et al. 2015a, Mostaed et al. 2014b, Kim et al.2002, Minárik et al. 2016a).

4.5.2 Modes of fractures and its effect on ductility of ZE41 Mg before and after ECAP.

The mechanical behaviour of Mg alloys at room temperature and relatively higher temperatures are typically affected by basal slip. Hence, the schmid factor values for basal slip (0001) <11-20> are generated from EBSD plots for ZE41 Mg samples. The Schmid

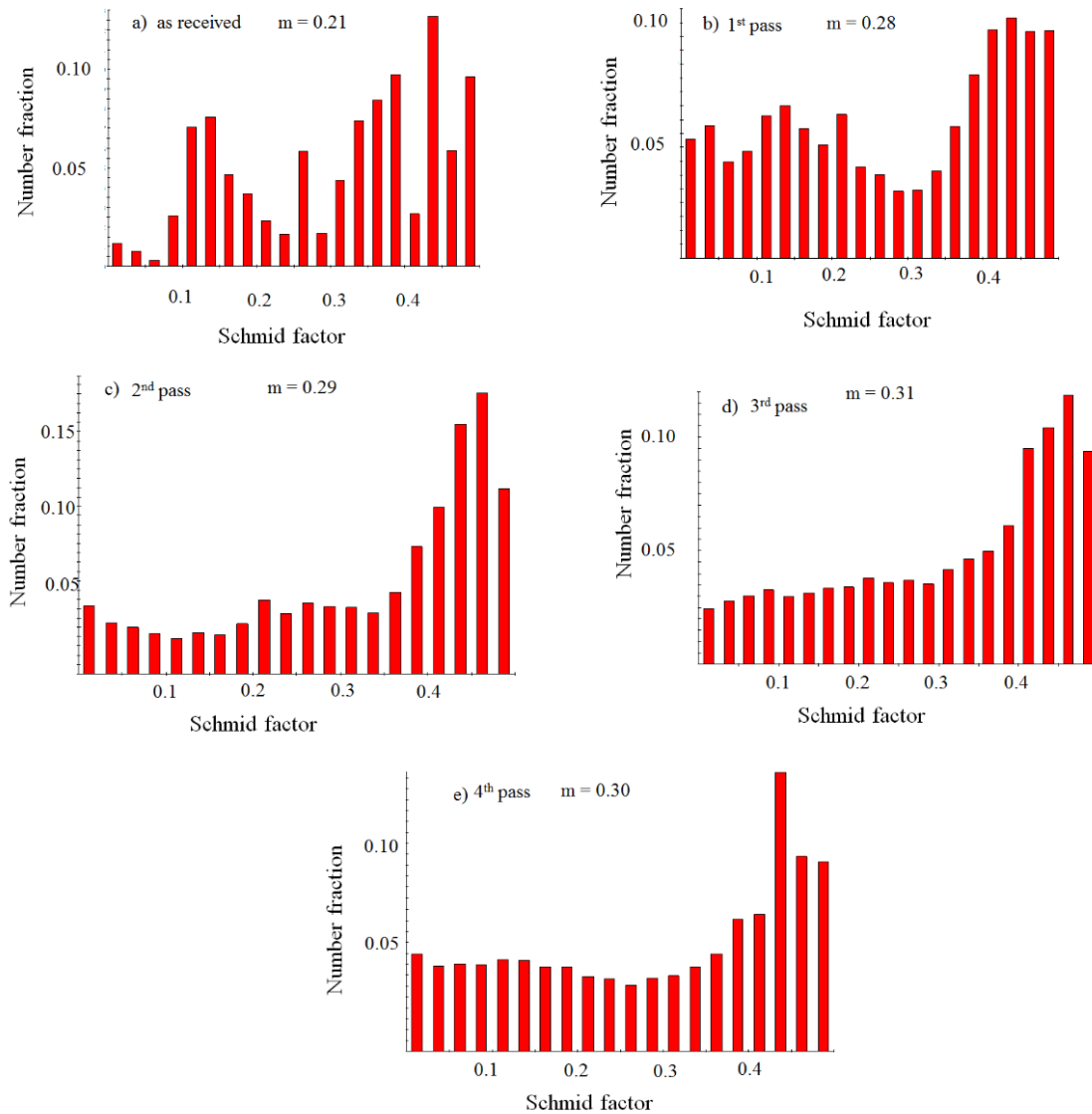


Fig 4.12 Schmid factor and corresponding number fraction of ZE41 Mg alloy in

(a) as received (b) 1st pass (c) 2nd pass (d) 3rd pass (e) 4th pass.

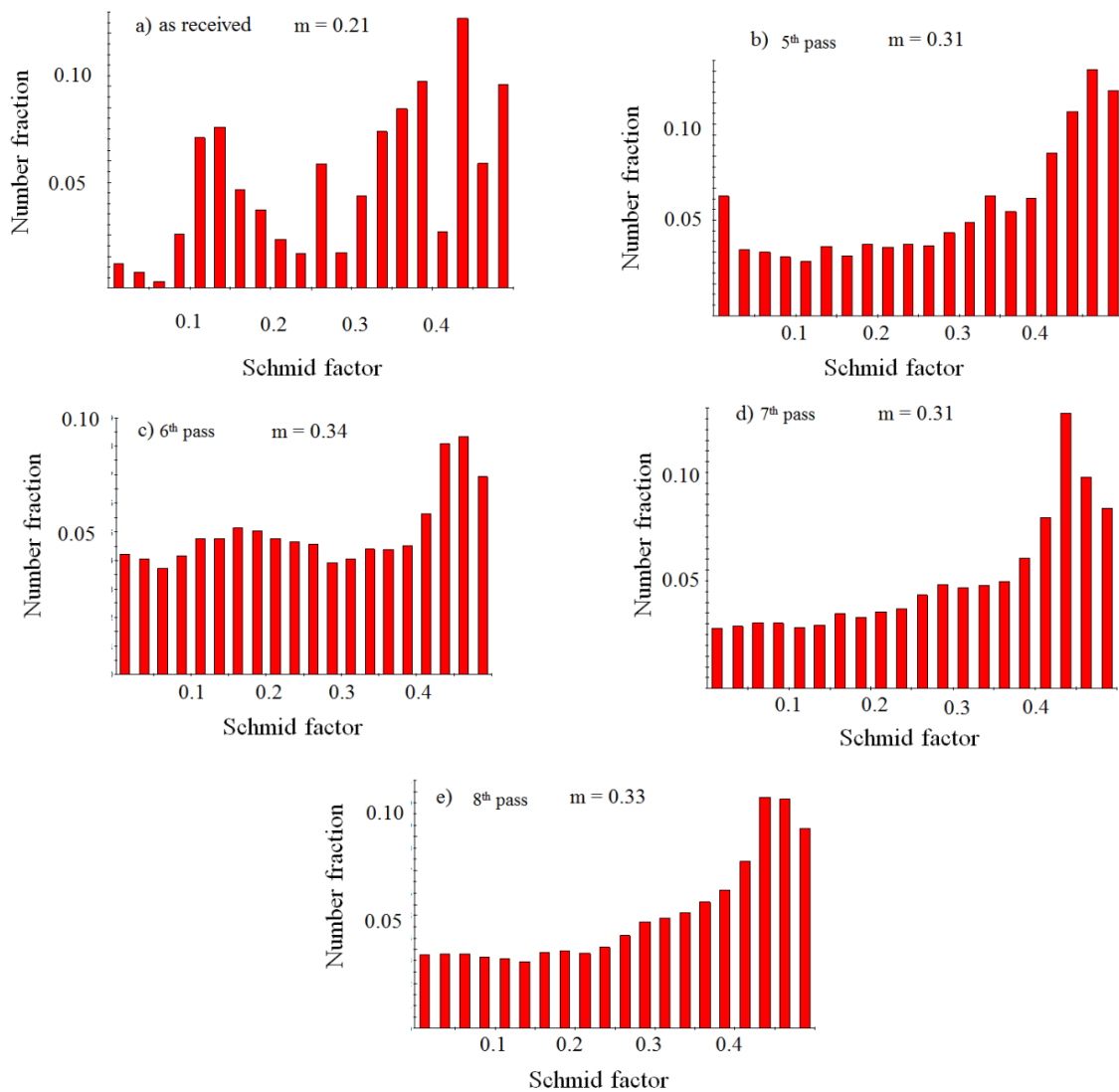


Fig 4.13 Schmid factor and corresponding number fraction of ZE41 Mg alloy in

(a) as received (b) 5th pass (c) 6th pass (d) 7th pass (e) 8th pass.

factor values for basal slip (0001) of ZE41 Mg alloy during first step ECAP is shown in the figure 4.12. The Schmid factor values of ZE41 Mg alloy is reported to be 0.21, 0.28, 0.29, 0.31 and 0.30 for as received, 1st pass, 2nd pass, 3rd pass and 4th pass respectively. It is interesting to note that the Schmid factor values of all first step ECAPed samples viz., 1st pass, 2nd pass, 3rd pass and 4th pass are relatively higher than the as received sample. Figure 4.13 depicts the Schmid factor values of ZE41 Mg alloy during second step ECAP as a function of their number fraction. The Schmid factor values during second step of ECAP is calculated to be 0.31, 0.34, 0.31 and 0.33 for 5th pass, 6th pass, 7th pass and 8th pass respectively. The similar trend continued during the second step of ECAP as well with 6th

pass sample exhibiting highest Schmid factor value of 0.34. The schmid factor values in the current study are also in good agreements with recent findings (Mostaed et al. 2015a, Mostaed et al. 2014b, Minárik et al. 2016a). During the first step of ECAP, elongation was 7% in as received condition which increased to ~20% after 4th ECAP pass. However, the maximum elongation of 23% was observed during second step after 6th pass ECAP. The basal texture orientation of 6th pass ECAP sample as shown in figure 4.10 (c) along with the maximum schmid factor value of 0.34 favours dislocation glide on slip plane thereby improving the ductility. The fractured SEM surface morphology of as received and 2nd pass, 4th pass, 6th pass, 8th pass ECAPed ZE41 Mg samples are depicted in figure 4.14 (a-e) respectively. Tear ridges and micro cracks were observed on the fractured surface of as received ZE41 Mg. This signifies brittle mode of fracture and hence the as received sample exhibited the lowest % elongation of 7% as depicted in figure 4.14 (a). The fractured SEM surface morphology of 2nd pass ECAP sample exhibited cleavages despite increase in % elongation as seen in figure 4.14 (b). This might be due to the bimodal grain distribution of 2nd pass ECAP in which fine grains contribute to increase in % elongation upto 21%. In the 4th pass ECAP sample dimples were observed as shown in figure 4.14 (c). But the % elongation declined relatively to value of 20%. This is attributed to grain growth

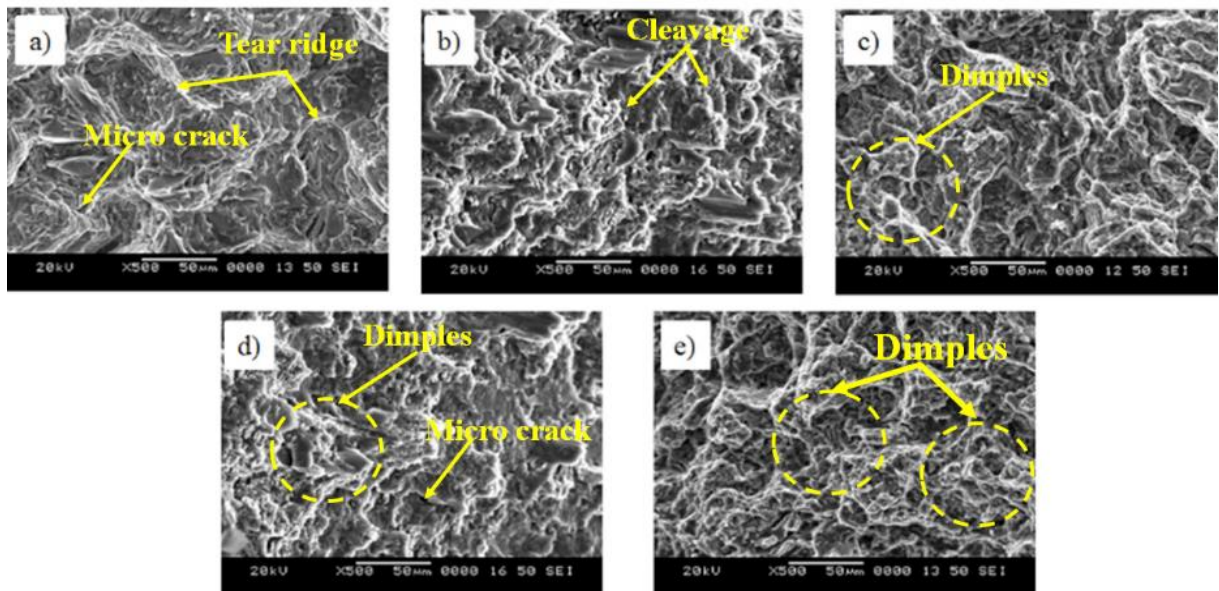


Fig 4.14 SEM fractured micrographs (a) as received (b) 2nd pass (c) 4th pass (d) 6th pass (e) 8th pass of ZE41 Mg alloy.

experienced during 4th pass of first step ECAP as represented in figure 4.1 (e). In 6th and 8th pass ECAPed samples dimples were observed and their size is relatively lower than 4th pass sample as depicted in figure 4.14 (d) and (e) respectively. Indeed, relatively smaller dimples contribute to increase in % elongation of Mg. However, in addition to dimples, micro-cracks were also observed in both 6th and 8th pass ECAP sample. The appearance of micro cracks is corroborated to processing ECAP at a relatively lower temperature of 275°C. Surprisingly, the attenuation in elongation upto 15% evinced after 8th pass. Probably, it is related to the incomplete dissolution of orthorhombic T-phase which is incompatible with hexagonal closed pack (HCP) structure of magnesium (Chen et al. 2008, Jin et al. 2005). In summary, the mechanical properties of ZE41 Mg alloy subject to ECAP has correlation to microstructure especially grain refinement, texture and processing temperature. In general, the bulk texture and micro texture of Mg alloys are obtained using XRD and EBSD analysis respectively. Indeed, the current study involves micro texture analysis of ECAPed ZE41 Mg samples generated from EBSD results. The global or bulk texture generated from XRD affected the mechanical properties of ZE41 Mg alloy (Ding et al. 2010). Minarik et al (2016) proved that global texture of magnesium alloys are in accordance with their micro texture (Minárik et al. 2016b). The present study also reveal that the mechanical behaviour of ZE41 Mg alloy are affected by both grain refinement and crystallographic orientation or texture.

4.6 SUMMARY

Equal channel angular pressing (ECAP) is carried out on as received ZE41 Mg alloy. First step of ECAP involves the 1st pass, 2nd pass, 3rd pass and 4th pass ZE41 Mg pressed at 300°C. While the second step involved additional 4 passes viz. 5th pass, 6th pass, 7th pass and 8th pass ECAPed at 275°C. The microstructure of ZE41 Mg alloy before and after two step ECAP processing is revealed by using EBSD technique. The pole figures, grain boundary characteristics, Schmid factor values generated from EBSD micrographs were correlated to mechanical properties. In addition, the strengthening mechanisms responsible for remarkable enhancement in mechanical properties of ZE41 Mg after ECAP are highlighted. The significant findings in the present chapter are summarized as follows.

- ❖ The as received ZE41 Mg sample exhibited a heterogeneous microstructure with average grain size of 46 μm . After 1st and 2nd pass of ECAP dynamic recrystallization occurred along grain boundaries resulting in bimodal grain distribution. A relatively uniform microstructure with grain refinement upto 5.7 μm was achieved by the end of 3rd pass ECAP. However, after 4th pass ECAP average grain diameter reached a value of 10 μm i.e the grain growth occurred due to unstable nature of fine grains. Comparing the grain sizes of as received and ECAPed ZE41 Mg samples it can be concluded that grain refinement effect was phenomenal during first step ECAP.
- ❖ During second step ECAP, the effect of grain refinement was marginal. Indeed, the average grain size of 5th pass, 6th pass and 7th pass ZE41 ECAP samples were 4.8 μm , 7.13 μm and 3.93 μm respectively. Interestingly, fine grains of 2.5 μm were achieved at the 8th pass of ECAP.
- ❖ The grain boundary maps revealed that during first step of ECAP the area fraction of low angle grain boundaries (LAGBs) are at least 50% greater than high angle grain boundaries (HAGBs) except 3rd pass sample. However, during second step of ECAP, the area fraction of both LAGBs and HAGBs are comparable. A relatively uniform microstructure might be achieved when the area fraction of LAGBs and HAGBs are comparable.
- ❖ Kernel average misorientation (KAM) maps constructed from EBSD micrographs revealed that local grain misorientation was in the range of 0° to 3° during first step of ECAP. The range of local grain misorientation increased relatively 2° to 4° during second step of ECAP. Interestingly, 8th pass ZE41 Mg sample evinced higher local grain misorientation among them.
- ❖ The as received ZE41 Mg sample evinced a random texture with a maximum texture intensity value of 7.3. The position and the value of the maximum texture intensity varied with increase in number of ECAP passes attributed to rotation of ECAP sample in route B_c. During first step of ECAP, there was relative increase in texture intensity from 7.38 in as received condition to 9.66 by end of 4th pass.
- ❖ In contrast, the texture intensity dropped relatively to 5.15 during 5th pass ECAP. This is followed by relative increase in texture intensity upto 6.04 and 6.98 during 7th pass and 8th pass ECAP respectively. The trend in texture intensity during first

step and second step ECAP performed on ZE41 Mg alloy signifies formation of new texture element.

- ❖ The yield strength of ZE41 Mg alloy increased significantly from 158 MPa in as received sample to 236 MPa by the end of first step ECAP. This signifies that during first step ECAP the ZE41 Mg samples were in line with Hall-Petch relation. In contrast, in the course of second step ECAP the samples evinced a sharp decrease in yield strength of 172 MPa during 8th pass. This is corroborated to texture softening effect that dominated the grain refinement phenomenon.
- ❖ The as received ZE41 Mg alloy exhibited a % elongation of 7% due to the presence of tear ridges and micro cracks. On the contrary, the 6th pass ECAP sample showed the highest % elongation of 23 % because of appearance of dimples in their fractured surface morphology. In addition, the highest Schmid factor value of 0.34 also contributed the improvement in % elongation of 6th pass ECAPed samples.

CHAPTER 5

INFLUENCE OF GRAIN REFINEMENT AND CRYSTALLOGRAPHIC ORIENTATION ON CORROSION BEHAVIOUR OF ZE41 MAGNESIUM ALLOY.

5.1 CORROSION BEHAVIOUR OF ZE41 MAGNESIUM ALLOY

ZE41 Mg samples were tested in three different concentrations of NaCl solution viz., 0 M, 0.1 M and 1 M NaCl to study the corrosion behaviour. These process parameters were chosen in order to analyse the combined effect of grain refinement and crystallographic orientation on corrosion behaviour of ZE41 Mg alloy. Chapter 4 highlighted the microstructure and mechanical properties of ZE41 Mg alloy after carrying out two step ECAP on as received ZE41 Mg. Mg alloys are known to exhibit relatively lower corrosion resistance. Indeed, the aim of the present study is to improve the corrosion resistance of ZE41 Mg alloy by ECAP. Hence, in this chapter, the influence of microstructure i.e grain size, secondary phase and crystallographic orientation on ZE41 Mg samples is explored. This assisted in proposing the possible corrosion mechanism of ZE41 Mg alloy in interaction with 0 M, 0.1 M and 1 M NaCl solution.

5.1.1 Open Circuit Potential (OCP) of ZE41 Mg alloy

The OCP curves of ZE41 Mg alloy studied in three different concentrations of sodium chloride (NaCl) is represented in figure 5.1 (a-c). The potential steadily increased for all ZE41 Mg samples in interaction with 0 M NaCl solution indicating a stable surface film formation as observed from figure 5.1(a). Similar stable surface film formation was reported by various investigators (Dinodi and Shetty 2014; Zhao et al. 2008). The as received ZE41 Mg sample exhibited the lowest potential value. In contrast, the potential of samples processed by ECAP moved towards nobler direction. However, the overall potential varied within the range of -1500 ± 60 mV in 0 M NaCl solution. In contrast, when tested in 0.1 M NaCl solution, ZE41 Mg samples attained a steady state at -1550 ± 10 mV electrode potential evident from figure 5.1 (b). The OCP curves of ZE41 Mg samples exhibited drastically different behaviour in interaction with 1 M NaCl solution, apparent

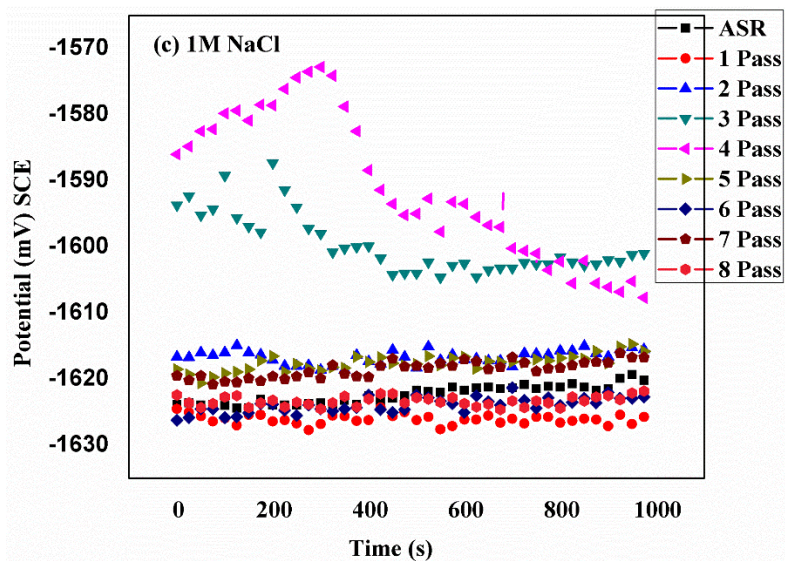
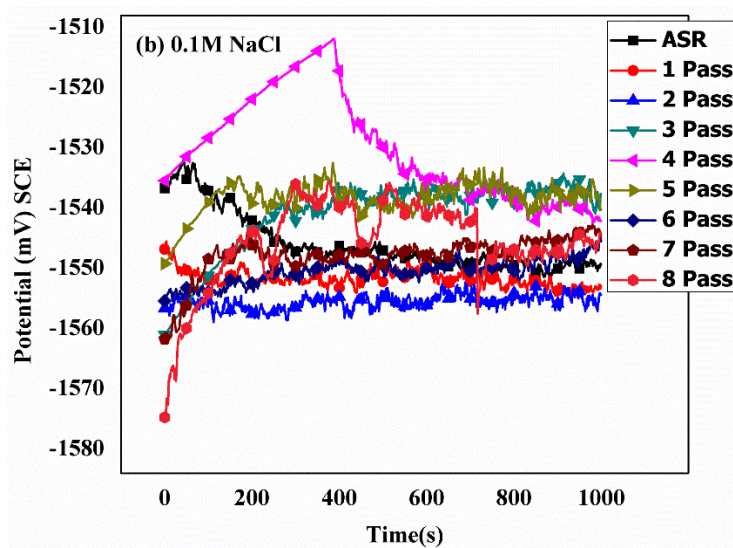
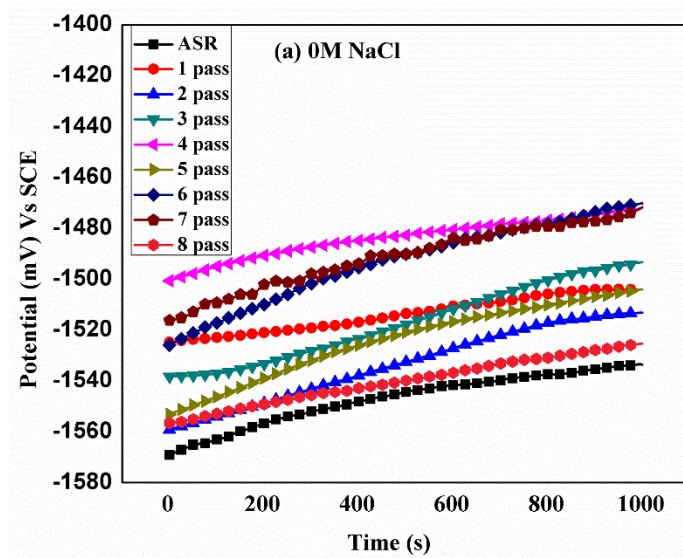


Fig 5.1 OCP curves of ZE41 Mg samples in (a) 0M NaCl (b) 0.1M NaCl (c) 1M NaCl.

from figure 5.1 (c). The 3rd pass and 4th pass ZE41 Mg sample showed initial increase in potential and attained steady state at -1600 mV. While the other ZE41 Mg samples did not show change in potential with respect to time. It is also interesting to note that the 4th pass ZE41 Mg sample exhibited the highest positive potential in chloride containing environments, 0.1 M and 1 M NaCl, which is evident from 5.1 (b) and (c). The changes in trends of OCP curves of ZE41 Mg samples in different environments viz., 0 M, 0.1 M and 1 M NaCl signifies the variation in corrosion behaviour. Indeed, the difference in corrosion behaviour of as received and ECAPed samples is attributed to changes in microstructure resulted from subsequent ECAP passes, evident from figures 4.1 and 4.2. Similar trends in OCP curves were observed by various researchers when ZE41Mg alloy was tested in the presence of inhibitors and chloride containing environments (Dinodi and Shetty 2014; Zhao et al. 2008). However, OCP curves describes only the thermodynamics of corrosion. Inorder to understand the corrosion kinetics of ZE41 Mg samples, electrochemical impedance spectroscopy (EIS) and potentiodynamic polarization (PDP) tests were carried out.

5.1.2 Realizing the nature of surface film formed on ZE41 Mg alloy using Electrochemical Impedance Spectroscopy (EIS).

Nyquist plot of ZE41 Mg samples ECAPed at first step 300°C and second step 275°C are depicted in figure 5.2 (a-c) and 5.3 (a-c) respectively. The characteristic features of Mg samples viz., High and intermediate frequency capacitive loops as well as low frequency inductive loop (LFID) were observed in all different environments. High and intermediate frequency capacitive loops are attributed to charge transfer resistance (R_{ct}) and ingress of testing medium into the corrosion product layer respectively. The occurrence of LFID is generally ascribed to adsorption of species like Mg^+ and $Mg(OH)^+$ on the surface film of Mg (Dinodi and Shetty 2014; King et al. 2014). From figures 5.2 (a) and 5.3 (a), it is observed that Nyquist plots of as received and ECAPed ZE41 Mg samples tested in 0 M NaCl is overlapping. In general, larger diameter of capacitive loop denotes better corrosion resistance of material under study. Interestingly, the diameter of high frequency capacitive loop of ECAPed ZE41 Mg samples are relatively larger than the as received ZE41 Mg. Despite the significant variation in microstructure of as received and ECAPed ZE41 Mg samples observed from figure 4.1 and 4.2, minimal variation in their corrosion behaviour is observed in figures 5.2 (a) and 5.3 (a). Certainly, this phenomenon is related to the extra

resistance offered by Mg phase and T Phase (Mg_7Zn_3RE) present in ZE41 Mg samples, especially when tested in 0 M NaCl solution. In contrast, when tested in 0.1 M and 1 M NaCl solution, all passes of ECAPed ZE41 Mg samples exhibited a significantly larger diameter capacitive loops when compared to the as received ZE41 Mg, observed from figures 5.2 (b-c) and 5.3 (b-c) respectively. This implies that corrosion resistance of ECAPed samples is significantly higher than as received ZE41 Mg in chloride containing environments, 0.1 M and 1 M NaCl. In summary, from figures 5.2 (a-c) and 5.3 (a-c), ECAP improved the corrosion resistance of ZE41 Mg alloy. However, the factors responsible for the enhancement in corrosion resistance should be evaluated to get better insights for proposing corrosion mechanism. Hence, the Nyquist plots of ZE41 Mg samples represented in figures 5.2 (a-c) and 5.3 (a-c) are fitted using simple Randle's circuit using V4 analysis software. Figure 5.4 (a-c) represents the parameters of simple Randle's circuit derived from Nyquist plots of ZE41 Mg samples as a function of number of ECAP passes. Charge transfer resistance (R_{ct}) is the most important parameter influencing the corrosion resistance of material. However, solution resistance (R_{sol}) and double layer capacitance (C_{dl}) also influence the corrosion process and are attributed to amount of corrosion products and thickness of Helmholtz double layer respectively. All ECAPed ZE41 Mg samples exhibited increased resistance to charge transfer when compared with as received ZE41 Mg sample in all three environments 0 M, 0.1 M and 1 M NaCl. From EBSD micrographs represented in figures 4.1 and 4.2, it is clear that equal channel angular pressing resulted in a remarkable grain refinement. But, the effect of grain refinement and crystallographic orientation was marginal on charge transfer resistance (R_{ct}) as shown in figure 5.4 (a). This is attributed to less aggressive nature of 0 M NaCl solution and its minimal influence on microstructure. Similar results were obtained by Zainal Abidin et al. 2011 when Mg alloys were tested in less aggressive corrosion medium. In 0M NaCl solution, the values of solution resistance (R_{sol}) varied apparently with respect to number of ECAP passes. In contrast, negligible variation of solution resistance (R_{sol}) values was observed when tested in 0.1M and 1M NaCl solution. Also the solution resistance (R_{sol}) decreased with increasing the chloride ion concentration which is apparent from figure 5.4 (b). This phenomenon is ascribed to the increasing corrosion products with increase in NaCl concentration. The thickness of surface film is inversely proportional to double layer capacitance (C_{dl}). Indeed, double layer capacitance (C_{dl}) did not have significant influence on the ECAP pass number in all the three environments 0 M, 0.1 M and 1 M NaCl, evident from figure 5.4 (c).

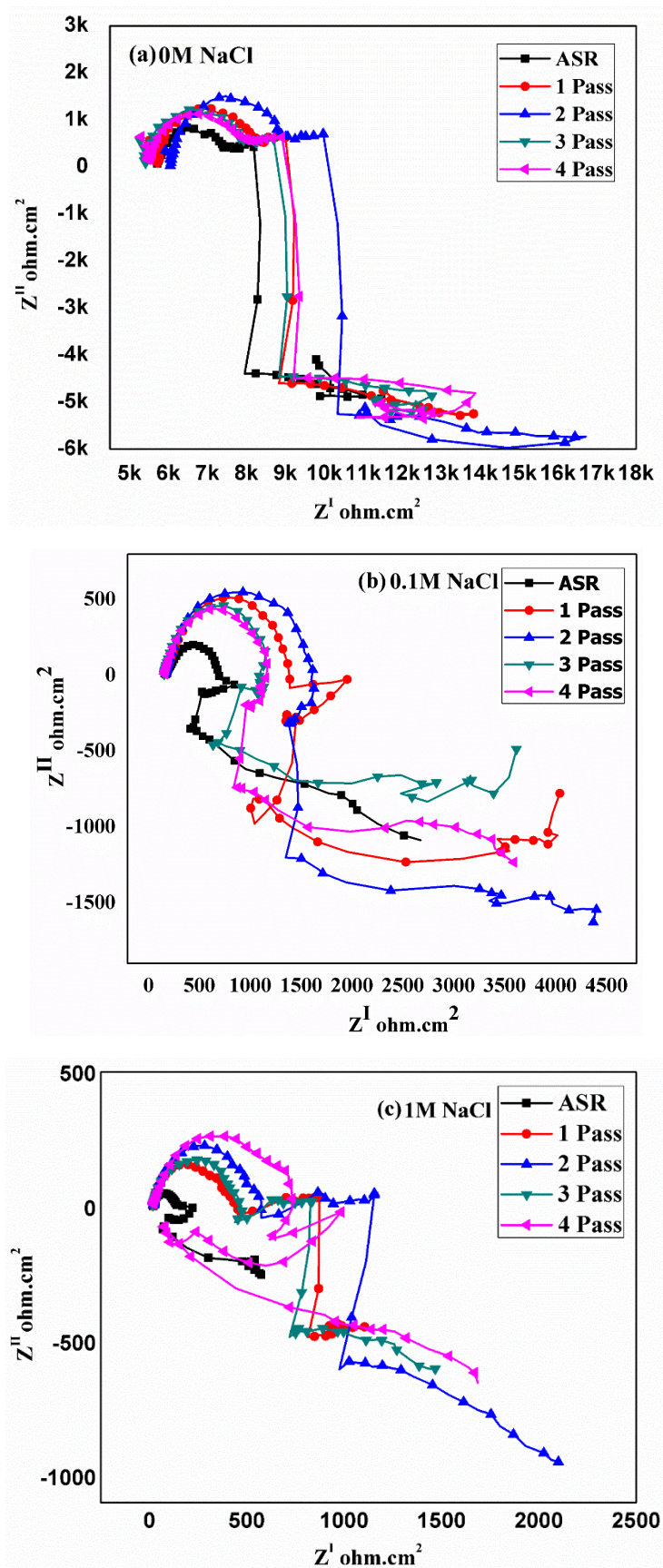


Fig 5.2 Nyquist Plot of first step ECAPed ZE41 Mg (a) 0 M (b) 0.1 M (c) 1 M NaCl.

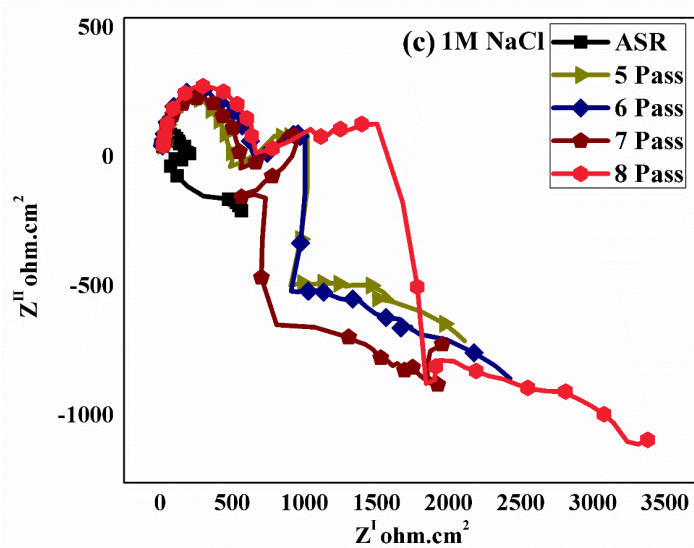
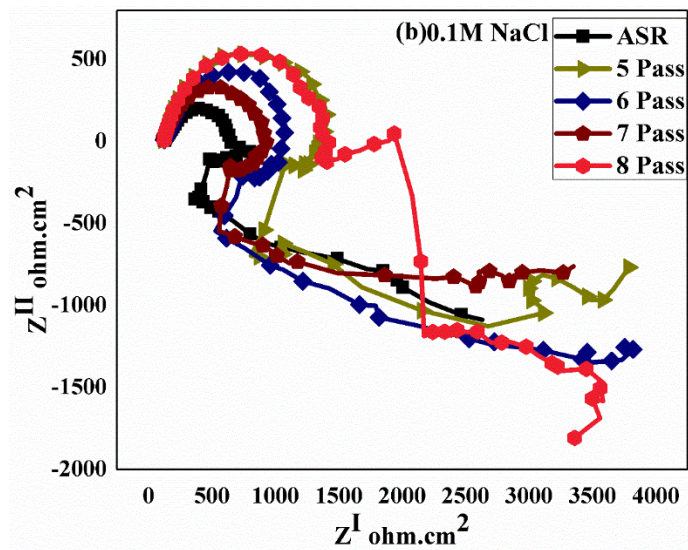
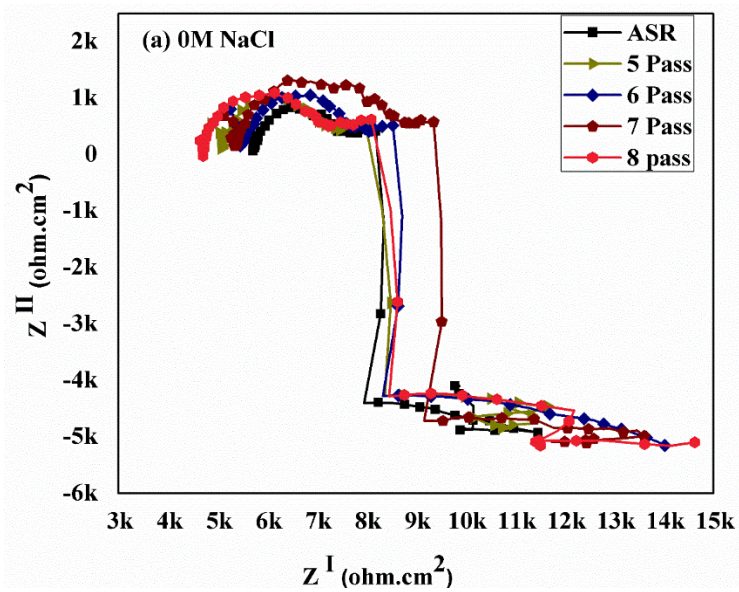


Fig 5.3 Nyquist Plot of second step ECAPed ZE41 Mg (a) 0 M (b) 0.1 M (c) 1 M NaCl.

Table 5.1 Corrosion parameters of ZE41 Mg alloy generated from Nyquist plot.

	NaCl	ASR	1 st Pass	2 nd Pass	3 rd Pass	4 th Pass	5 th Pass	6 th Pass	7 th Pass	8 th Pass
R_{ct} ($\Omega.cm^2$)	0 M	1991	3270	3015	2917	3000	2526	2788	4139	2891
	0.1 M	529	1705	1458	1051	1035	1356	978	811	1246
	1 M	124	379	496	450	706	448	613	520	633
R_{sol} ($\Omega.cm^2$)	0 M	5594	5447	6009	5193	5220	4887	5132	4974	4649
	0.1 M	127	123	124	109	115	118	124	118	124
	1 M	19	18	20	17	17	20	16	19	20
C_{dl} (μF)	0 M	15.1	30	8.1	12.1	14.8	14.9	11.9	20.7	25.4
	0.1 M	10.7	59.4	2.90	9.31	8.63	9.09	8.62	9.51	7.08
	1 M	23.7	22.1	16.4	9.52	14.7	11.6	12.4	15.8	15.6
Impedance ($\Omega.cm^2$)	0 M	10644	12477	12094	13594	12617	11872	15158	13439	15535
	0.1 M	2890	4092	4647	3694	3725	3758	3953	3495	3873
	1 M	611	1237	2315	1660	1680	2257	2398	2084	3611

Table 5.1 quantifies the corrosion parameters viz., charge transfer resistance (R_{ct}), solution resistance (R_{sol}), double layer capacitance (C_{dl}). In summary, the values of charge transfer resistance (R_{ct}), solution resistance (R_{sol}) and double layer capacitance (C_{dl}) neither increased nor decreased steadily with respect to ECAP pass number. This is clearly depicted and understood from figure 5.4 (a-c) and table 5.1. The diminution in values of charge transfer Resistance (R_{ct}) and solution resistance (R_{sol}) with increase in NaCl concentration is related to destructive nature of chloride ions on surface film of ZE41 Mg alloy which is evident from figure 5.4 (a) and (b). Similar kind of decrease in charge transfer resistance (R_{ct}) and solution resistance (R_{sol}) was reported earlier in case of Pure Mg and ZE41 Mg in interaction with chloride ions (King et al. 2014; Zhao et al. 2008). However, the impedance value is collectively influenced by summation of charge transfer resistance (R_{ct}), solution resistance (R_s) and double layer capacitance (C_{dl}) (Jüttner 1990). Higher value of impedance signifies good corrosion resistance of material with interacting environment. The Bode impedance plot of ZE41 Mg samples ECAPed during first step at 300°C and second step 275°C is depicted in figure 5.5 (a-c) and 5.6 (a-c) respectively. From the trend of figures 5.5 and 5.6, it is evident that at higher frequency (10 kHz -100 Hz) and moderate

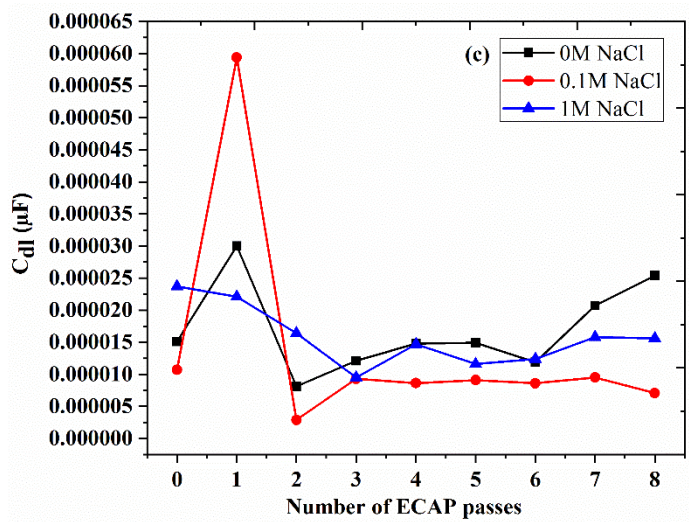
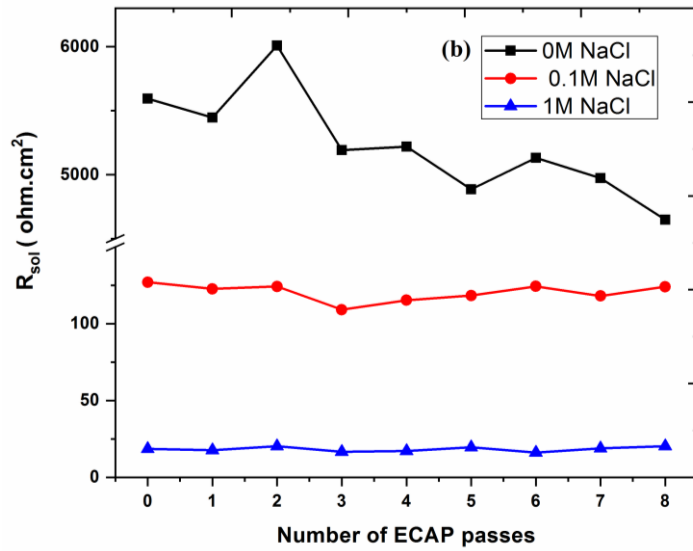
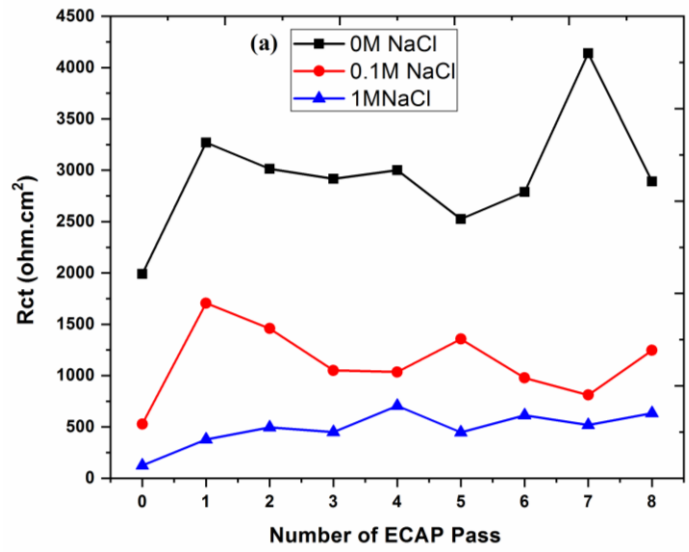


Fig 5.4 corrosion parameters as a function of number of ECAP Passes (a) R_{ct} (b) R_s (c) C_{dl}

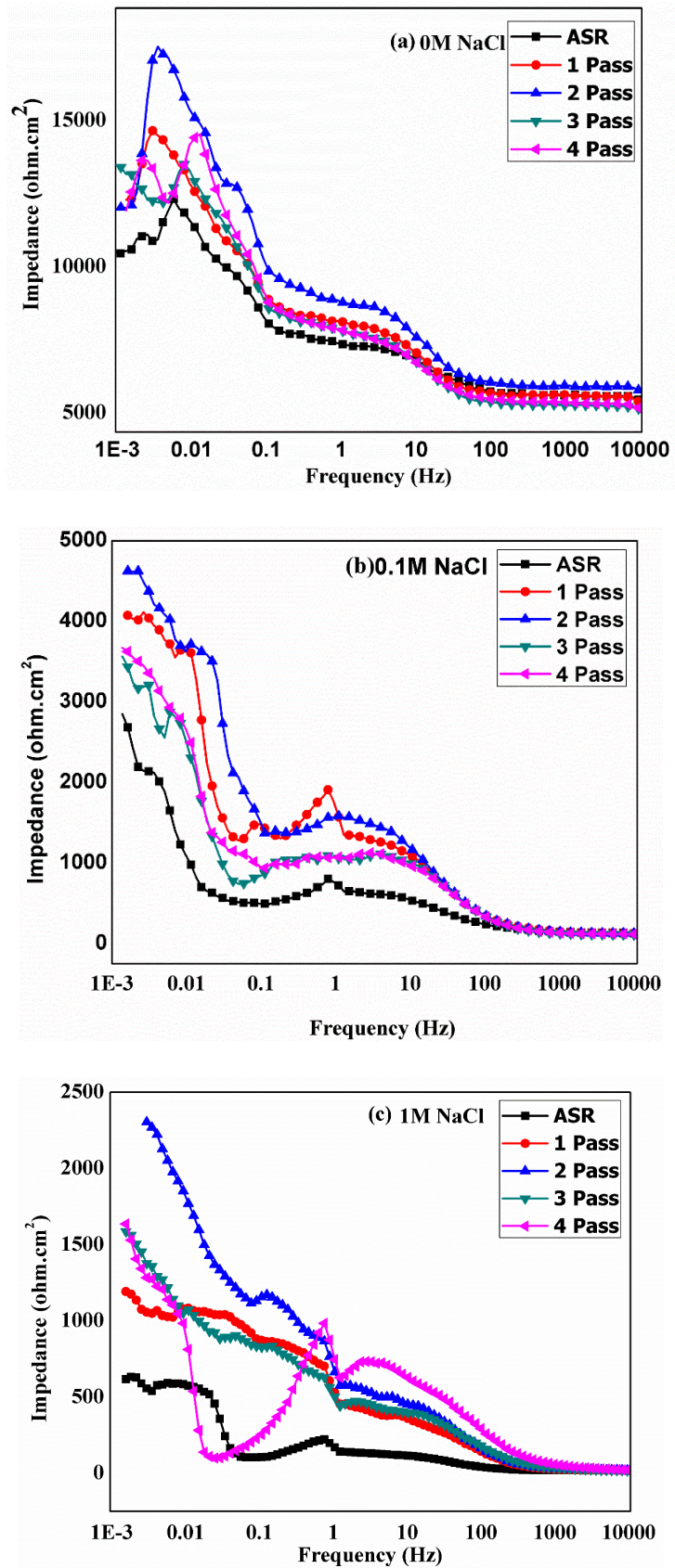


Fig 5.5 Bode Plot of first step ECAPed ZE41 Mg (a) 0 M (b) 0.1 M (c) 1 M NaCl.

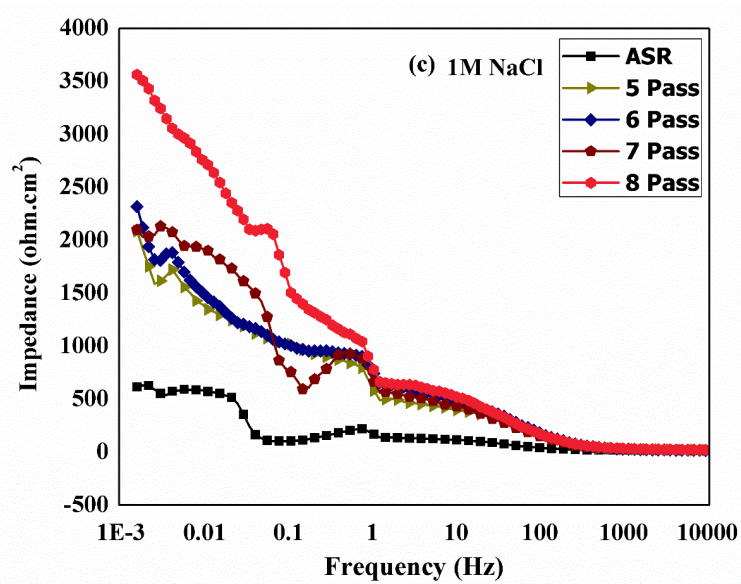
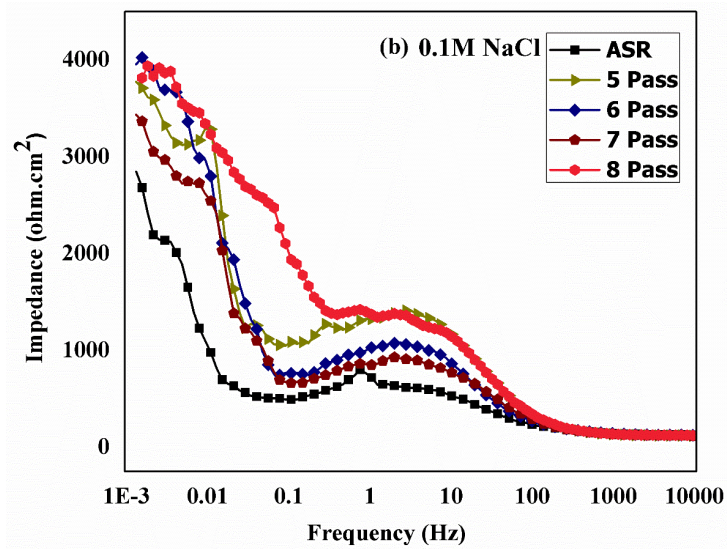
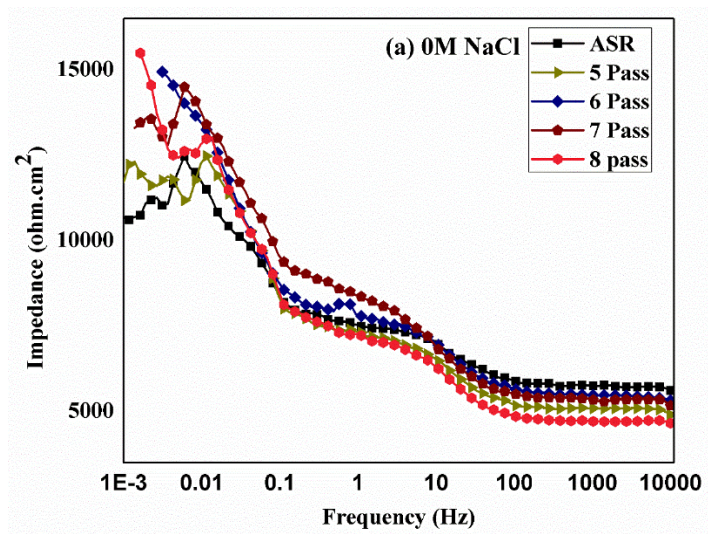


Fig 5.6 Bode Plot of second step ECAPed ZE41 Mg (a) 0 M (b) 0.1 M (c) 1 M NaCl.

frequency (100 Hz - 0.1Hz) minimal and moderate changes were observed on impedance values respectively. In contrast, the variation of impedance values became significant at very low frequency (0.1 Hz to 0.001 Hz). The inflection points on impedance curves corresponds to the time constants observed in the Nyquist plots, figures 5.2 and 5.3. The Bode plots obtained in the current study are in reasonable agreement with models proposed (Jüttner 1990) and recent findings (Dinodi and Shetty 2014; King et al. 2014). It is evident from figure 5.5 (a) that the decrease in impedance was observed at very low frequency of 0.01Hz which is attributed to occurrence of pitting in 0 M NaCl. The impedance values diminished due to the presence of chloride ions in 0.1 M and 1 M NaCl which is evident from figure 5.5 (b) and (c) respectively. The Bode impedance plots of ZE41 Mg samples ECAPed during second step at 275°C also show the same trends and is represented in figure 5.6 (a-c). The decrease in impedance values with increasing chloride ion concentration is accordance with the decrease in electrode potential observed in OCP curves depicted in figure 5.1 (a-c) as well as reduction in values of charge transfer resistance (R_{ct}) and solution resistance (R_s), figure 5.4 (a-b). From, figures 5.5 (a), 5.6 (a) and table 5.1, it is clear that the impedance values of ECAPed ZE41 Mg samples are relatively greater than the as received ZE41 Mg. In general, higher impedance values indicates better corrosion resistance of samples in interaction with corrosive environment. However, there is marginal change in values of impedance from 10644 $\Omega.cm^2$ in as received sample to the range of 11872 to 15535 $\Omega.cm^2$ in ECAPed ZE41 Mg samples. Therefore, it is reasonable to believe that ECAP improved the corrosion resistance of ZE41 Mg when tested in 0 M NaCl solution. When tested in 0.1 M NaCl, ECAPed ZE41 Mg samples exhibited impedance values in the range of 3495 $\Omega.cm^2$ to 4647 $\Omega.cm^2$. These values of impedance shown by ECAPed ZE41 Mg samples is significantly greater than impedance value of 2890 $\Omega.cm^2$ exhibited by as received ZE41 Mg. Similarly, when tested in 1 M NaCl solution, the impedance value of as received ZE41 Mg improved remarkably from 611 $\Omega.cm^2$ to range of 1237 to 3611 $\Omega.cm^2$. The impedance values of ZE41 Mg samples tested in 0 M, 0.1 M and 1 M NaCl is in complete agreement with values of charge transfer resistance (R_{ct}). Although, impedance is a function of charge transfer resistance (R_{ct}), solution resistance (R_s) and double layer capacitance (C_{dl}), charge transfer resistance (R_{ct}) is the dominant factors among them. In summary, the OCP values of ZE41 Mg samples are in line with the impedance values when interacted with 0 M, 0.1 M and 1 M NaCl solution. Similar kind

of results were reported when pure Magnesium was tested in 0.1 M, 1 M and 5 M NaCl solutions (King et al. 2014).

5.1.3 Evaluating corrosion rate of ZE41 Mg using Potentiodynamic polarisation plots

Figure 5.7 (a-c) illustrates the potentiodynamic polarization plots of ZE41 Mg samples ECAPed at first step tested in 0 M, 0.1 M and 1 M NaCl respectively. The potentiodynamic polarization plots of samples processed during the second step ECAP also evinced similar trends as first stage. They are presented in the figure 5.8 (a-c). From the figure 5.7 (a) and 5.8 (a), the following observations were made (i) the E_{corr} values are in good agreement with the OCP curves shown in figure 5.1(a) (ii) the anodic and the cathodic curves of Tafel plots of ZE41 Mg samples were overlapping (iii) the I_{corr} values calculated from extrapolation of cathodic slope evinced insignificant change with advancement of ECAP passes. Based on the I_{corr} values, the corrosion rates are calculated and tabulated in table 5.2. The as received sample exhibited a corrosion rate of 0.036 mm/yr, which is relatively higher when compared to the corrosion rate of ECAPed ZE41 Mg samples in the range of 0.027 to 0.034 mm/yr. In spite of significant changes in microstructure of ZE41 Mg samples seen in figures 4.1 and 4.2, a marginal change in their corrosion rate is observed when tested in 0 M NaCl. This is corroborated to extra resistance offered by Mg phase and T phase ($\text{Mg}_7\text{Zn}_3\text{RE}$) present in ZE41 Mg samples. These results are in good accordance with Nyquist plots obtained from EIS presented in figure 5.2 (a) and 5.3 (a). From figure 5.7 (b-c) and 5.8 (b-c), it is apparent that the I_{corr} values of all ECAPed ZE41 Mg samples are lesser than the as received ZE41 Mg alloy. It can also be observed that the 3rd and 4th pass ZE41 Mg samples exhibited significant shift of E_{corr} towards noble direction and less values of I_{corr} in both 0.1M and 1M NaCl solution. This is attributed to higher double layer film thickness of 3rd pass and 4th pass ZE41 Mg samples as represented in the figure 5.4 (c). In general, the Tafel plots in figures 5.7 (b-c) and 5.8 (b-c) shifted towards direction of increasing current density and lower potential values with increase in NaCl concentration due to aggressive nature of chloride ions. The corrosion rate reduced from 0.464 mm/yr in as received ZE41 Mg sample to the range of 0.041 to 0.342 mm/yr in ECAPed conditions when tested in 0.1 M NaCl solution. Similarly, corrosion rate evinced a remarkable reduction from 4.364 mm/yr in as received condition to range 0.758 to 2.901 mm/yr in ECAPed condition after interaction with 1 M NaCl solution. In summary, ECAP improved the corrosion resistance of ZE41 Mg alloy. However, analysing the combined effect of

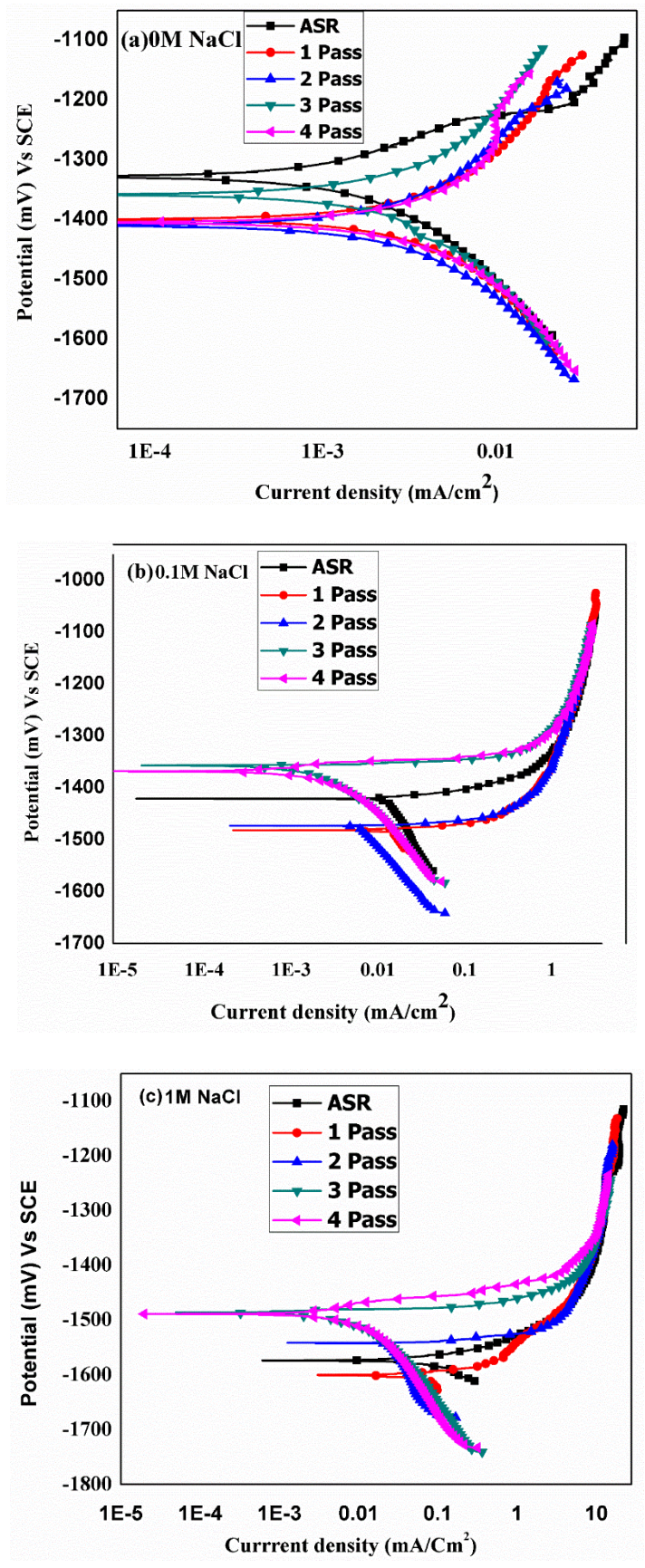


Fig 5.7 Tafel Plot of first step ECAPed ZE41 Mg (a) 0 M (b) 0.1 M (c) 1 M NaCl.

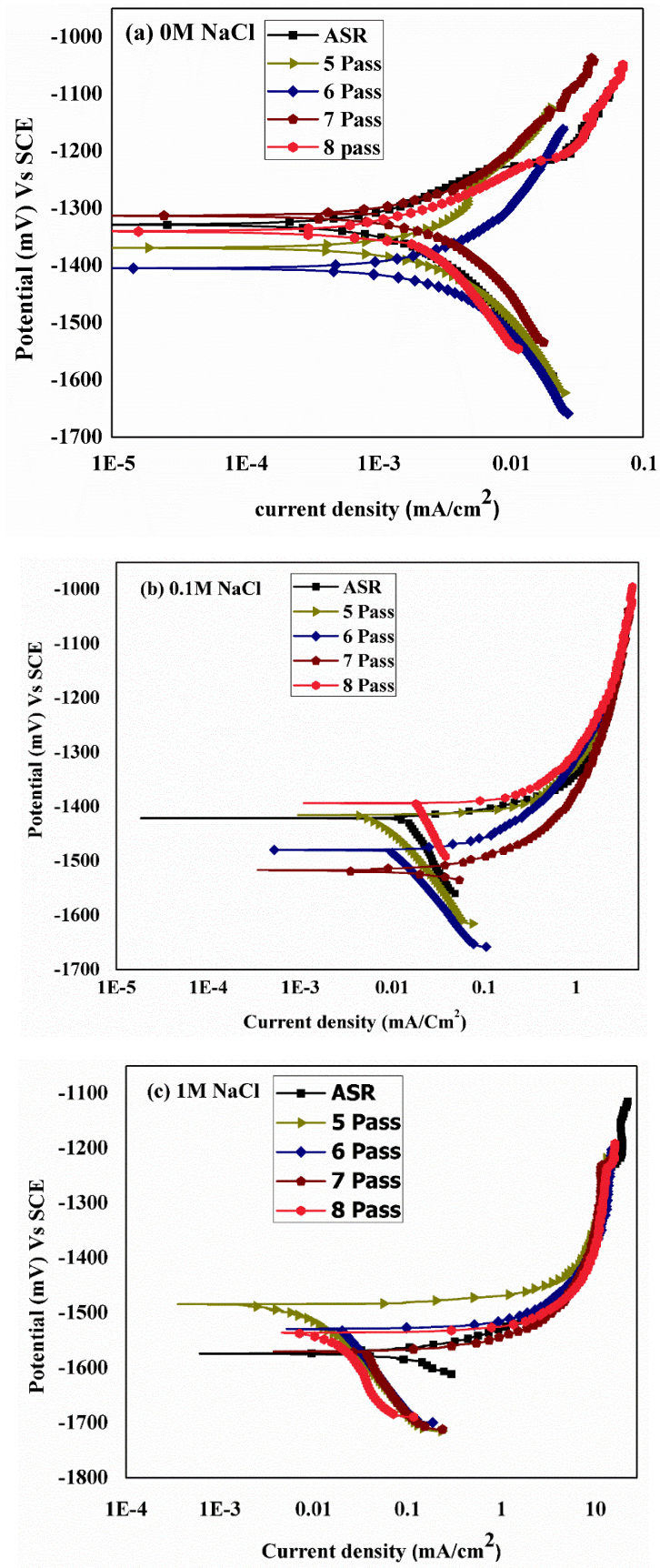


Fig 5.8 Tafel Plot of second step ECAPed ZE41 Mg (a) 0 M (b) 0.1 M (c) 1 M NaCl.

grain refinement and crystallographic orientation is necessary to thoroughly understand the corrosion mechanism of ZE41 Mg alloy.

5.2 COMBINED EFFECT OF GRAIN REFINEMENT AND CRYSTALLOGRAPHIC ORIENTATION ON ZE41 MAGNESIUM CORROSION.

The impedance values and corrosion rate of ZE41 Mg samples were obtained from Bode impedance plots and Tafel plots respectively. The corrosion rate of all ZE41 Mg samples is calculated from the equation 5.1 (Zhao et al. 2008).

$$\text{Corrosion Rate [CR] (mm/year)} = 22.85 i_{\text{corr}} \text{ (mA/Cm}^2\text{)} \dots \dots \dots (5.1).$$

Table 5.2 Impedance values and corrosion rate of ZE41 Mg alloy.

	NaCl	ASR	1 st Pass	2 nd Pass	3 rd Pass	4 th Pass	5 th Pass	6 th Pass	7 th Pass	8 th Pass
Grain size (μm)		46	24	13	5.7	10	4.8	7.13	3.9	2.5
Impedance ($\Omega\text{.cm}^2$)	0 M	10644	12477	12094	13594	12617	11872	15158	13439	15535
	0.1 M	2890	4092	4647	3694	3725	3758	3953	3495	3873
	1 M	611	1237	2315	1660	1680	2257	2398	2084	3611
Corrosion rate (mm/yr)	0 M	0.036	0.031	0.031	0.034	0.031	0.029	0.034	0.034	0.027
	0.1 M	0.434	0.342	0.182	0.041	0.041	0.148	0.274	0.2285	0.548
	1 M	4.364	2.901	1.590	0.763	0.758	0.795	1.05	1.59	0.735

The values of impedance and corrosion rate of ZE41 Mg samples are represented in the figure 5.9 (a) and (b) respectively. The grain size, impedance values and corrosion rate of ZE41 Mg alloy are tabulated in table 5.2. It is interesting to observe that the impedance values of ZE41 Mg samples are in the range of 10000 to 16000 $\Omega\text{.cm}^2$ in 0 M NaCl solution. In contrast, the impedance deteriorated to values between 600 to 4700 $\Omega\text{.cm}^2$ in chloride containing 0.1 M and 1 M NaCl. However, the corrosion rate of ZE41 Mg samples tested in 0.1 M NaCl are relatively higher than that of 0 M NaCl. Surprisingly, the corrosion rate of 3rd and 4th pass ZE41 Mg alloy tested in 0 M and 0.1 M NaCl are almost comparable as

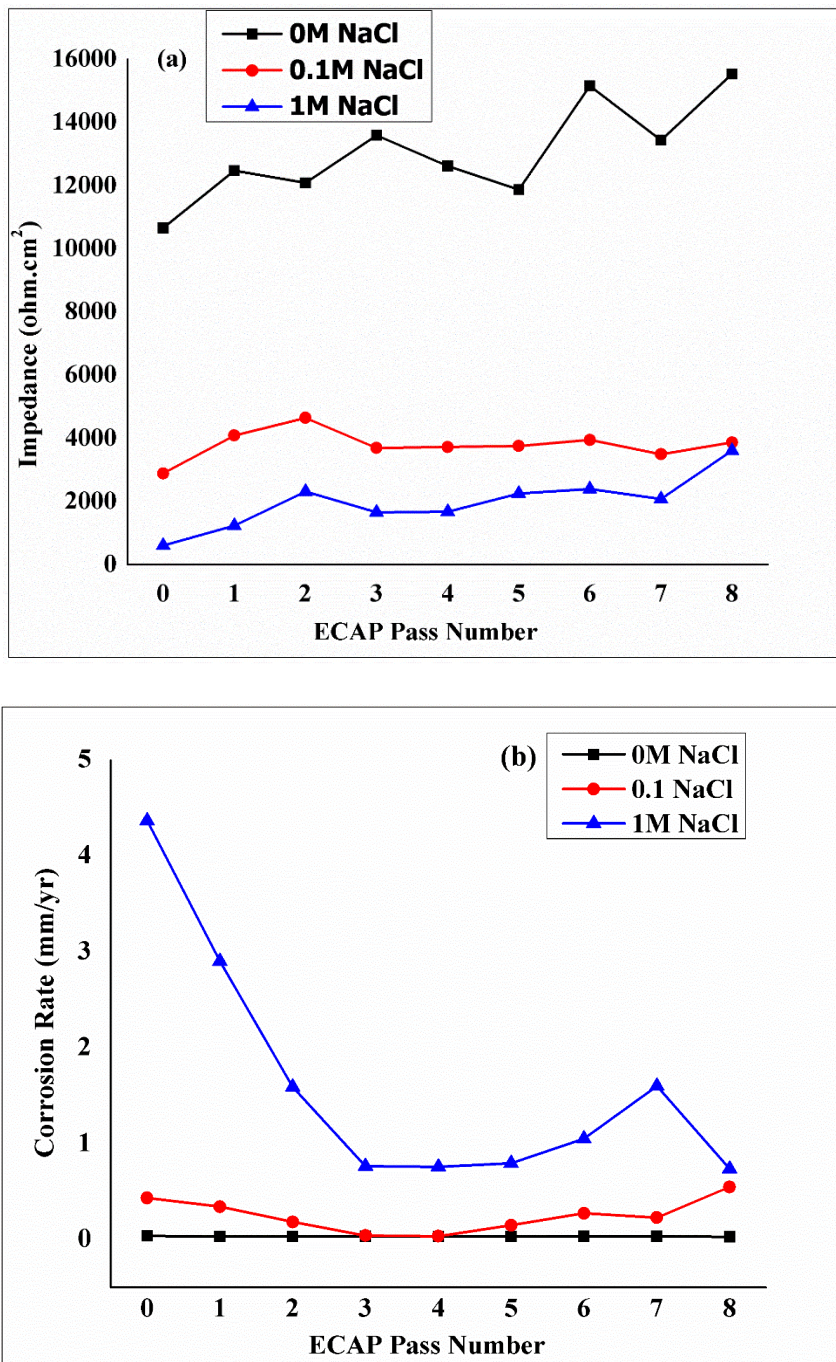


Fig 5.9 (a) Impedance (b) Corrosion rate as a function of number of ECAP Passes.

observed from figure 5.9 (b). This is related to the better surface film formation of ECAPed ZE41 Mg in 0.1M NaCl than 0M NaCl as shown in figure 5.4 (c). The double layer capacitance (C_{dl}) is directly proportional to local dielectric constant (ϵ) and inversely proportional to thickness of double layer film (d). This is given by Helmholtz relation and

represented in the equation 5.2. The lower the value of double layer capacitance (C_{dl}) higher will be the robustness of double layer film (d) (Dinodi and Shetty 2014).

$$C_{dl} = \frac{\epsilon}{4\pi d} \quad \dots (5.2)$$

Electrochemical impedance spectroscopy is non-destructive in nature and corrosion resistance is measured from impedance value of surface film. In contrast, Potentiodynamic polarisation calculates the corrosion rate by destruction of sample surface. However, similar trends in corrosion resistance is observed for ZE41 Mg samples which is evident from the figure 5.9 (a) and (b). The role of pH and chloride ion concentration (0 M, 0.1 M and 1 M NaCl) of ZE41 Mg alloy was reported earlier. The corrosion resistance obtained in the present study is relatively higher than previous study (Zhao et al. 2008). However, the present study cannot be compared to prior work because of the following difference in parameters (i) Zhao et al. 2008 added HCl and NaOH to adjust the pH (ii) their grain size was constant. Recent reports on corrosion of high purity Mg also conclude that corrosion resistance measured from both EIS and potentiodynamic polarization techniques exhibited same trends in results (King et al, 2014). All ECAPed ZE41 Mg samples exhibited better corrosion resistance than as received ZE41 Mg alloy. However, on careful observation one could note from figure 5.9 (a) and (b) that the corrosion resistance of ZE41 Mg samples neither increased nor decreased with chronological increase in ECAP pass number. If grain refinement is the only reason for increase in corrosion resistance, the corrosion resistance would have increased with respect to increase in number of ECAP passes in linear manner due to fine distribution of secondary phase particles. But in the present study such trend was not observed. Hence, other factors such as crystallographic orientation also influenced the corrosion behaviour of ZE41 Mg alloy. The corrosion behaviour of Mg alloys are influenced by microstructure i.e grain refinement (Baradarani et al. 2019; Minárik et al. 2013) and crystallographic orientation (Hoseini et al. 2009; Song and Xu 2012; Wang et al. 2016; Xin et al. 2011). Previous studies on ECAP of magnesium alloys reported that fine distribution of cathodic particle i.e secondary phases resulted in enhanced corrosion resistance (Zhang et al, 2013; Qiang et al. 2014 ; Naik et al.2019; Baradarani et al, 2019), while the adverse effects were attributed to crystalline defects (song et al.2011) without considering the role of crystallographic orientation. In this study, Inverse pole figures or

contours are generated from EBSD micrographs in order to enlighten the effect of crystallographic orientation on corrosion behaviour. The Inverse pole figures of all ZE41 Mg samples are illustrated in the figure 5.10 (a-i), with a sample plot denoting (0001), (10-10) and (2-1-10) plane orientation corresponding to figure 5.10 (a-i). It is worth mentioning that the basal plane in HCP crystals is the most closely packed plane than the prism planes. The higher planar atomic density of basal planes of Mg provides better corrosion resistance than the prism planes and their values are mentioned in table 5.3. When the samples are tested in less aggressive solutions like 0 M NaCl there is a minimal influence on microstructure. In other words, no significant change was observed from impedance value presented in figure 5.9 (a) and corrosion rate figure 5.9 (b) with respect the microstructural evolution depicted in figure 4.1 and 4.2. However, the as received ZE41 Mg sample and 8th pass ZE41 Mg sample exhibited majority of grain orientation towards (0001) and (2-1-10) plane respectively which is evident from figure 5.10 (a) and (i) respectively. Also, the 8th pass ZE41 Mg sample with a grain size of 2.5 μ m exhibited the highest corrosion resistance in 0 M NaCl solution. The corrosion morphology of as received, 4th pass and 8th pass of ECAPed ZE41 Mg samples in three different testing conditions are represented in figure 5.11 (a-c), (d-f) and (g-i) respectively. When tested in 0 M NaCl, the grain boundaries of as received ZE41 Mg sample were corroded due to micro galvanic corrosion between bulk Mg and T-Phase (Mg_7Zn_3RE). In contrast, the secondary phase particles are finely distributed after ECAP. Hence, for the 4th pass ZE41 Mg sample tested in 0 M condition the corrosion is less severe when compared to as received sample. However, in the 8th pass ZE41 Mg sample grain boundaries were not corroded. The observation clearly indicates that the corrosion resistance of ZE41 Mg alloy in 0 M NaCl solution is majorly influenced by grain refinement than crystallographic orientation. The corrosion morphology of as received, 4th pass and 8th pass ZE41 Mg samples represented in figure 5.11 (a, d, j), tested in 0 M NaCl solution is in accordance with corrosion rate tabulated in table 5.2. Majority of the grains were oriented in between (0001)/ (2-1-10) in 4th pass ZE41 Mg sample as observed in figure 5.10 (e). The 4th pass ZE41 Mg sample evinced highest corrosion resistance when tested in 0.1M and 1M NaCl solution. From figure 5.10 it is observed that all the ZE41 Mg samples viz., figure 5.10 (a-d, f-i) exhibited maximum intensity at two crystallographic orientations in exception to 4th pass ZE41 Mg represented in figure 5.10 (e). Interestingly, it is reported that micro-galvanic cells formed between planes with different crystallographic orientations deteriorate the corrosion resistance (Wang et al,

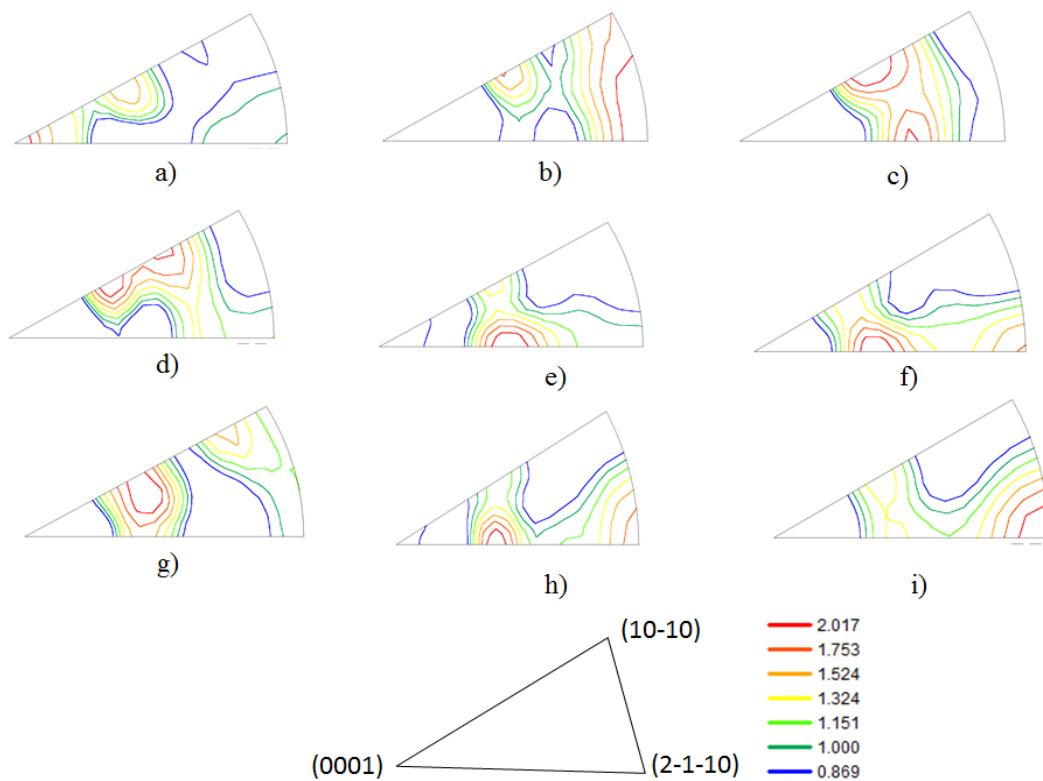


Fig 5.10 Inverse pole figures (contour) of ZE41 Mg alloys for different conditions (a) As received (b) 1st Pass (c) 2nd Pass (d) 3rd Pass (e) 4th Pass (f) 5th Pass (g) 6th Pass (h) 7th Pass (i) 8th Pass.

Table 5.3 Atomic densities of planes in different crystallographic orientation

Plane orientation	Atomic Density (atoms/m ²)
Basal Plane (0001)	1.13×10^{19}
Prism Plane (10-10)	6.94×10^{18}
Prism plane (2-1-10)	5.99×10^{18}

2016). In summary, the highest corrosion resistance was exhibited by the ZE41 Mg sample ECAPed at 4th pass on interaction with 0.1M NaCl and 1M NaCl rather than ultra-fine grain 8th pass ZE41 Mg sample. In 0.1 M condition, the corrosion morphology of as received and 8th pass ZE41 Mg sample evinced relatively severe corrosion when compared to the 4th pass ZE41 Mg sample. Indeed, from figure 5.11 (b), the grain and grain boundaries of as received ZE41 Mg samples were corroded. In addition, undermining of T Phase

(Mg₇Zn₃RE) occurred at triple junction of grain boundaries leading to formation of micro pits. In case of 4th pass samples tested in 0.1 M NaCl solution, a relatively uniform corrosion was observed from figure 5.11(e), resulting in a corrosion rate of 0.041 mm/yr. 8th pass ZE41 Mg samples tested in 0.1 M NaCl exhibited a corrosion rate of 0.548 mm/yr due to formation cleavage and macro-pits, seen from figure 5.11(h). In contrast, when tested in 1 M NaCl condition the surface appears to be severely corroded than 0.1 M condition. Indeed, the corrosion rate of as received, 4th pass and 8th pass were

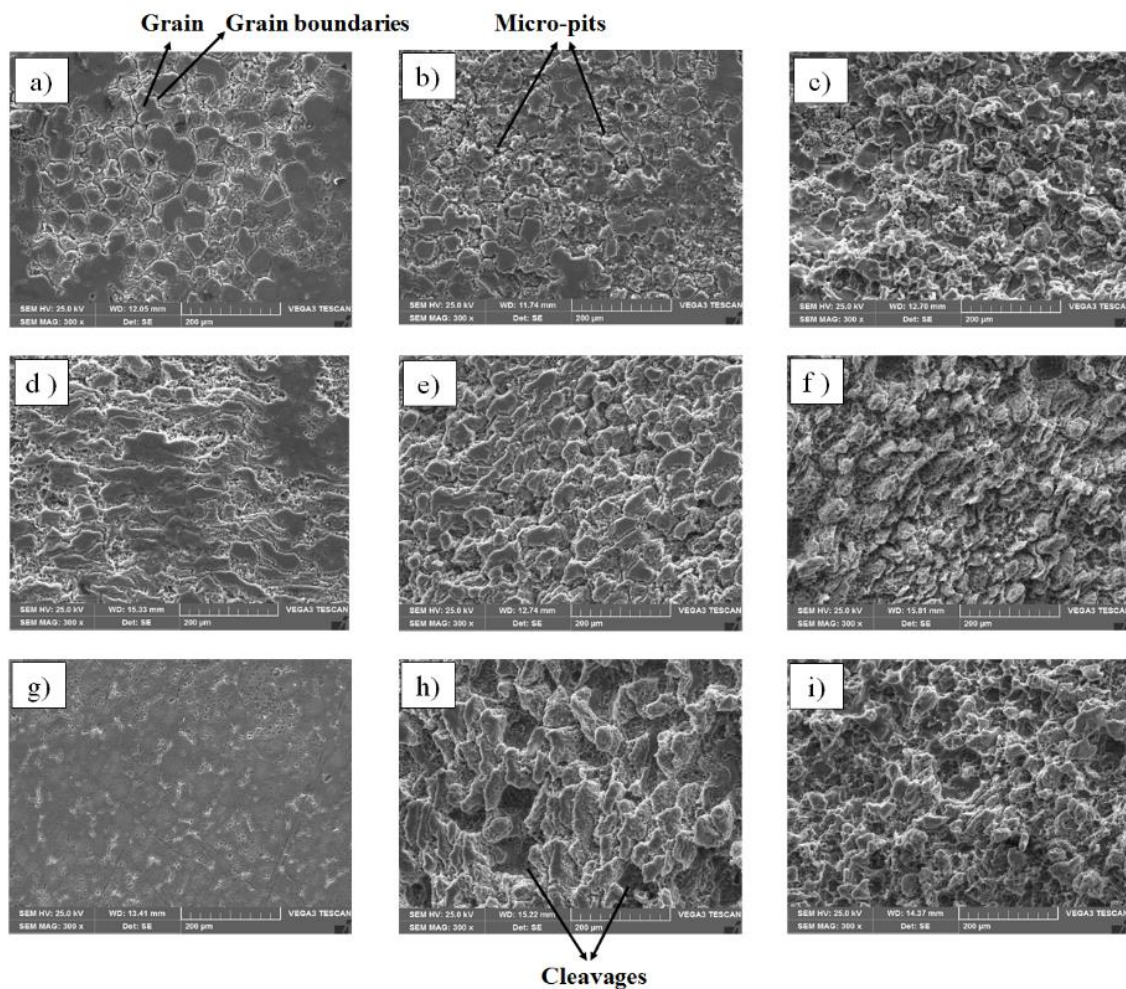


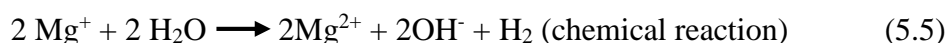
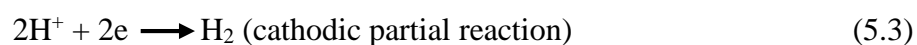
Fig 5.11 Corroded SEM images of [(a) 0 M, (b) 0.1 M, (c) 1 M of as received] [(d) 0 M, (e) 0.1 M, (f) 1 M of 4th pass] [(g) 0 M, (h) 0.1 M (i) 1M of 8th pass].

4.364 mm/yr, 0.758 mm/yr and 0.735 mm/yr for ZE41 Mg samples tested in 1 M NaCl. These values of corrosion rate for samples tested in 1 M NaCl is remarkably greater than the corrosion rates of ZE41 Mg samples in 0.1 M NaCl solution. Summarized, the corrosion

morphology depicted in figure 5.11 is in accordance with the corrosion rate presented in table 5.2. Thus, crystallographic orientation has predominated the effect of grain refinement during ZE41 Mg corrosion when tested in 0.1 M and 1 M NaCl which is clearly depicted in figure 4.1, 4.2 and 5.10 (a-i). In summary, the corrosion of ZE41 Mg alloy is influenced by microstructure i.e combined effect of both grain refinement and crystallographic orientation.

5.3 MECHANISM OF CORROSION IN ZE41 MAGNESIUM ALLOY

The corrosion mechanism of ZE41 Mg alloy is proposed based on the microstructure, impedance and corrosion rate obtained from EBSD, EIS and PDP plots respectively. The schematic of ZE41 Mg corrosion is represented in the figure 5.12. The anodic partial reaction at bulk magnesium occurs by the dissolution of magnesium and release of an electron as mentioned in equation (5.4). This electron is taken up at T phase (Mg_7Zn_3RE) acting as cathodes resulting in hydrogen evolution as shown in equation (5.3). In addition to electrochemical mode of corrosion, dissolution of magnesium occurs by chemical reaction which is referred as anodic hydrogen evolution mentioned in equation (5.5). This phenomenon of dissolution of Mg ions and release of hydrogen gas is clearly depicted in the stage 1 of figure 5.12. The overall corrosion reaction and product formation is represented in the equation (5.6) and (5.7) respectively. This occurs in the second stage during which the corrosion rate is accelerated by aggressive nature of chloride ions. It is well established that magnesium corrosion is dynamic in nature.





This is because, Mg forms a partially protective $\text{Mg}(\text{OH})_2$ layer in interaction with corrosive medium. The partially protective $\text{Mg}(\text{OH})_2$ layer prevents Mg from corrosion while the ions such as Cl^- accelerate corrosion. This process is clearly illustrated in the stage 3 of figure 5.12. Based on the above mentioned reaction, grain refinement, distribution of secondary phase particles and crystallographic orientation possible corrosion mechanism is proposed. In chloride containing environments (0.1 M and 1 M NaCl), the corrosion initially occurs by electrochemical reaction i.e micro galvanic corrosion between bulk Mg and T Phase. The process is then accompanied by occurrence

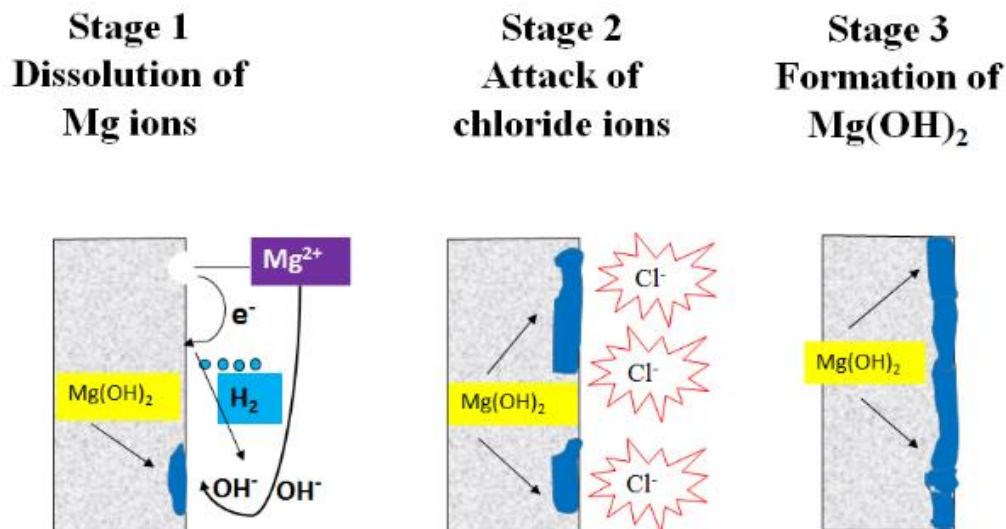


Fig 5.12 Mechanism of corrosion in ZE41 Mg alloy.

of corrosion due to chemical reaction from chloride ions. This combination of corrosion due electrochemical reaction and chemical reaction leads to undermining of secondary phase particles ($\text{Mg}_7\text{Zn}_3\text{RE}$), as observed from corrosion morphology in figure 5.11. The deviation from usual Tafel behaviour of magnesium alloys also signifies the occurrence of anodic hydrogen evolution due to chemical corrosion (5.5) as depicted in figure 5.7 and

5.8. In addition to corrosion reaction, the sample having fine grains and distribution of secondary phase particles with preferred orientation i.e 4th ZE41 Mg pass sample evinced the highest corrosion resistance. Hence, it is reasonable to conclude that Mg samples exhibiting fine grains, fine distribution of secondary phase particles (Mg_7Zn_3RE) along with preferred orientation (0001) is expected to show relatively better corrosion resistance. The theory of Mg corrosion, which suggests formation of univalent magnesium ions followed by a chemical redox step is employed in the present study. However, this theory was strongly confronted by number of recent works that suggest different potential explanations for the negative difference effects (Birbilis et al. 2014b). Moreover, the recent density functional theory (DFT) studies also contradict existence of stable uni positive magnesium intermediates (Würger et al, 2020). Therefore, it is advised that the future studies should consider the recent state of art on Mg in order thoroughly understand the corrosion mechanism.

5.4 SUMMARY

Two step equal channel angular pressing (ECAP) was carried out on as received ZE41 Mg alloy. Electron back scattered diffraction (EBSD) revealed the microstructural features especially grain size and crystallographic orientation. The corrosion behaviour of as received and ECAPed ZE41 Mg samples were tested in 0 M, 0.1 M and 1 M NaCl solution to simulate conditions encountered in automobile applications. The significance of the present study is highlighted and summarized below.

- ❖ The potential of ZE41 Mg samples increased significantly with respect to time, indicating formation of stable film in interaction with 0 M NaCl solution. ZE41 Mg samples evinced potential in the range of -1480 mV to -1560 mV. In contrast, when tested in chloride containing environments (0.1 M and 1 M NaCl), the increase in potential as function of time was marginal. In addition, the 4th pass ZE41 Mg samples exhibited highest potential values of -1540 mV and -1610 mV in 0.1 M and 1 M NaCl respectively.
- ❖ Two capacitive loops appeared in Nyquist plots at high (10 kHz -100 Hz) and medium frequency (100 Hz - 0.1Hz) respectively. In addition, an inductive loop was observed at the low frequency range of 0.1 to 0.001 Hz in all ZE41 Mg samples. The diameter of the capacitive loops were larger for ECAPed ZE41 Mg samples

when compared to the as received ZE41 Mg sample in 0 M, 0.1 M and 1 M NaCl solution.

- ❖ The impedance values of ZE41 Mg alloy were found to be between 10000 to 16000 ohm.cm² when tested in 0 M NaCl. The impedance values drastically decreased to values between 600 to 4700 ohm.cm² for ZE41 Mg samples in 0.1 M and 1 M NaCl solution due to the aggressive nature of chloride ions. The corrosion rate of 0.027 mm/yr – 0.036mm/yr, 0.041mm/yr – 0.548 and 0.758 mm/yr – 4.364 mm/yr ranges was obtained for ZE41 Mg samples tested in 0 M, 0.1 M and 1 M NaCl respectively. The potentiodynamic polarization plots were in line with the impedance values of ZE41 Mg samples.
- ❖ ZE41 Mg samples exhibited maximum intensity at two crystallographic orientations among (0001), (10-10) and (2-1-10) planes, except 4th pass ZE41 Mg sample which evinced texture intensity only in single crystallographic orientation corresponding to (0001) plane.
- ❖ In 0 M NaCl solution, the 8th pass ZE41 Mg sample with grain size of 2.5 µm exhibited the highest corrosion resistance. In contrast, 4th pass ZE41 Mg sample with grain size of 10 µm, evinced better corrosion resistance in chloride containing environments (0.1 M and 1 M NaCl). Hence, it can be concluded that the fine grains in the range of 2.5 µm to 10 µm along with favourable crystallographic orientation (0001) assists in increasing the corrosion resistance of ZE41 Mg alloy.
- ❖ The corrosion rate drastically decreased from 0.434 mm/yr and 4.364 mm/yr in as received condition to 0.041 mm/yr and 0.758 mm/yr for 4th pass ZE41 Mg samples when tested in 0.1 M and 1 M NaCl solution respectively. The 4th and 8th pass ZE41 Mg samples with fine grains in the range of 2.5 µm to 10 µm and favourable orientation (0001), evinced highest corrosion resistance in chloride containing environments (0.1 M and 1 M NaCl) respectively.
- ❖ A mechanism of corrosion occurring in ZE41 Mg alloy was proposed based on the EBSD micrographs, OCP, Nyquist, potentiodynamic polarization and corrosion morphology to get better insights into the corrosion behaviour. Based on the corrosion mechanism it can be concluded that in order to achieve better corrosion resistance in ZE41 Mg alloy the following parameters are favourable (i) fine grains upto 10µm (ii) fine distribution of secondary phase particles (iii) preferable crystallographic orientation (0001).

CHAPTER 6

EFFECT OF EQUAL CHANNEL ANGULAR PRESSING ON GALVANIC CORROSION OF ZE41 MAGNESIUM ALLOY.

6.1 INTRODUCTION

Chapter 1 outlined the importance of magnesium and its alloys in automobile industry. It also emphasized the weight reduction obtained in automobiles components after replacing magnesium in place of aluminium and steel. However, not all components in automobile can be made of magnesium alloys. Hence, magnesium alloys should be coupled with aluminium and steel components in real time applications. When coupled with other metals, magnesium forms a galvanic couple that results in galvanic corrosion. One of the objectives of the present study is to improve galvanic corrosion resistance of ZE41 Mg using ECAP. In this chapter, an effort has been made to explore the galvanic corrosion behaviour of as received (ASR) and equal channel angular pressed (ECAPed) ZE41 magnesium alloy when coupled with Al7075 aluminium alloy. The nature of oxide/hydroxide film formed, change in physical properties of film due to corrosion products (Al^{3+} ion) were investigated using electrochemical tests. Zero resistance ammeter (ZRA) was used to quantify the galvanic corrosion rate in three different environments to mimic a practical environment encountered in application of ZE41 magnesium alloy.

6.2 MICROSTRUCTURAL EVOLUTION OF ZE41 MAGNESIUM ALLOY BEFORE AND AFTER ECAP

The microstructural evolution of ZE41 magnesium alloy observed from ZEISS optical microscope before and after equal channel angular pressing is shown in figure 6.1 (a-g). The average grain size of as received ZE41 magnesium alloy is 48 μm . This was measured by using linear intercept method and is apparent from figure 6.1(a). After 2nd pass of equal channel angular pressing at 300°C, a bimodal distribution of grain size is observed in the microstructure with grains ranging in the size of 30 and 20 μm . However average grain size is of 26 μm as shown in the figure 6.1(b). Figure 6.1(c) depicts the 4th pass ZE41 Mg alloy

equal channel angular pressed at 300 °C. Grain growth was observed and the average grain size measured was 28 μm. The grain growth occurs in magnesium and its alloys because of carrying out ECAP at relatively higher temperatures between the range of 200 to 320°C. This is due to the fact that, the fine grains obtained after severe plastic deformation are not in equilibrium state. The activation energy of fine grain alloy is lesser than the coarse grain alloy. This forces the fine grains to attain equilibrium state resulting in grain growth (Mostaed et al. 2014a, 2015). The 5th pass and 6th pass equal channel angular pressing of

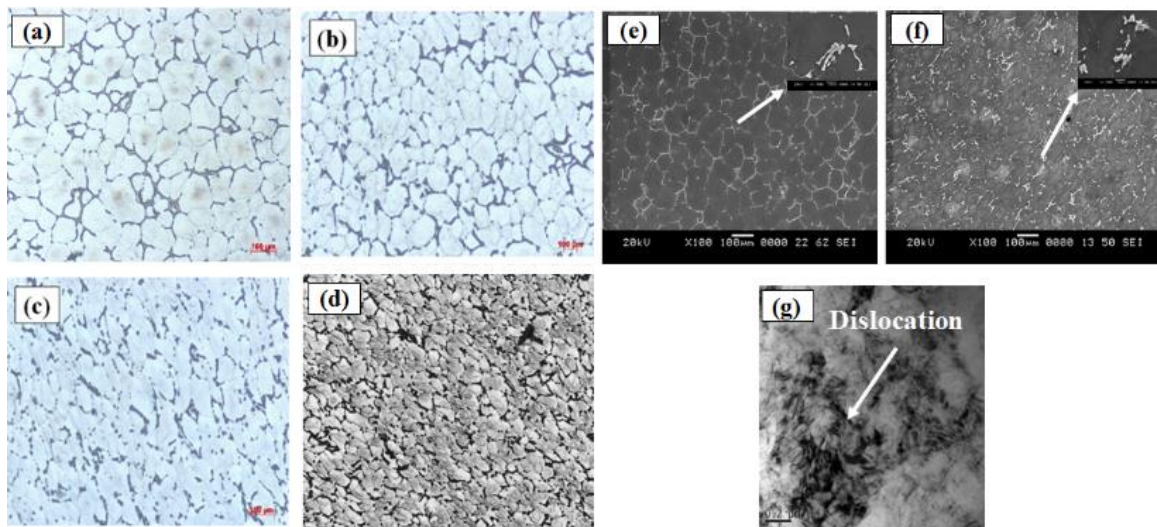


Fig 6.1 Optical images showing microstructural evolution (a) As Received (b) 2nd Pass (c) 4th Pass (d) 6th Pass, SEM images of (e) As Received (f) 6th Pass and (g) TEM image of 6th Pass.

ZE41 magnesium alloy were carried out relatively at a lower temperature of 275°C to suppress the grain growth encountered during first stage. The equi-axed ultrafine grain microstructure with average grain size of 15 μm resulted from dynamic recrystallization which is seen from the optical image of 6th pass equal channel angular pressing represented in the figure 6.1(d). Similar kind of ultrafine grain refinement has been reported by different researchers (Chen et al. 2008a; Jin et al. 2005; Mostaed et al. 2015). The grain refinement obtained is in good agreement with one of the grain refinement models proposed by Figueiredo and Langdon 2010. Two step equal channel angular pressing strategy was adapted in this study in-order to achieve enhanced improvement in mechanical properties viz., yield strength, % elongation as well as ultimate tensile strength suggested by various researchers (Chen et al. 2008a; He et al. 2010; Jin et al. 2005; Mostaed et al. 2014a; b,

2015; Qiang et al. 2014). The SEM images of as received and 6th pass equal channel angular pressed samples are represented in the figure 6.1 (e) and (f) respectively. The inset marked by white arrow in figure 6.1 (e) shows the distribution of T phase (Mg_7Zn_3RE) at the triple junction of grain boundaries. After 6th pass ECAP the T-Phase (Mg_7Zn_3RE) is broken into fine particles which is evident from the inset of figure 6.1 (f) marked by white arrow. Also the dislocation induced after 6th pass ECAP are presented in the figure 6.1 (g). In general, these dislocation resulting from severe plastic deformation process deteriorate the corrosion resistance of material under study. Indeed, similar kind of T phase (Mg_7Zn_3RE) distribution (Song et al. 2011b) and dislocations were observed by various researchers during equal channel angular pressing. In summary, equal channel angular pressing has resulted in refined microstructure along with distribution of T Phase (Mg_7Zn_3RE) into finer ones.

6.3 GALVANIC CORROSION BEHAVIOUR OF AS RECEIVED (ASR) AND EQUAL CHANNEL ANGULAR PRESSED ZE41 Mg-Al7075 COUPLE

Three types of corrosion tests viz., open circuit potential (OCP), electrochemical impedance spectroscopy (EIS) and potentiodynamic polarization were carried out on galvanic couples in the chronological order.

6.3.1 Open circuit potential (OCP) of ZE41 Mg-Al7075 couple

The open circuit potential of the ZE41 Mg-Al7075 galvanic couple tested in 0 M NaCl, 0.1 M NaCl and 1 M NaCl concentration are shown in the figure 6.2 (a-c) respectively. From figure 6.2 (a) it is apparent that 4th pass galvanic sample showed more positive potential measuring up to -1320 mV. While, the as received sample attained stable open circuit potential at the value of -1480 mV in 0 M NaCl solution. The trend of as received and equal channel angular pressed galvanic samples are similar when tested in 0 M NaCl solution. The gradual increase in potential with respect to time observed from figure 6.2 (a-c) indicates the formation of surface film on surface of metal due to its interaction with environment. On the other hand, decrease in potential as a function of time signifies the breakdown of surface film (Dinodi and Shetty 2014; Zhao et al. 2008). Figure 6.2 (b) represents the open circuit potential of as received and equal channel angular pressed galvanic couple in interaction with 0.1 M NaCl solution. One can observe that the trend of as received sample shows initial increase in potential till 400 seconds and then decreases gradually till 2000 seconds. But, all the equal channel angular pressed galvanic samples exhibited a decrease in potential up to 400 seconds and then increased gradually.

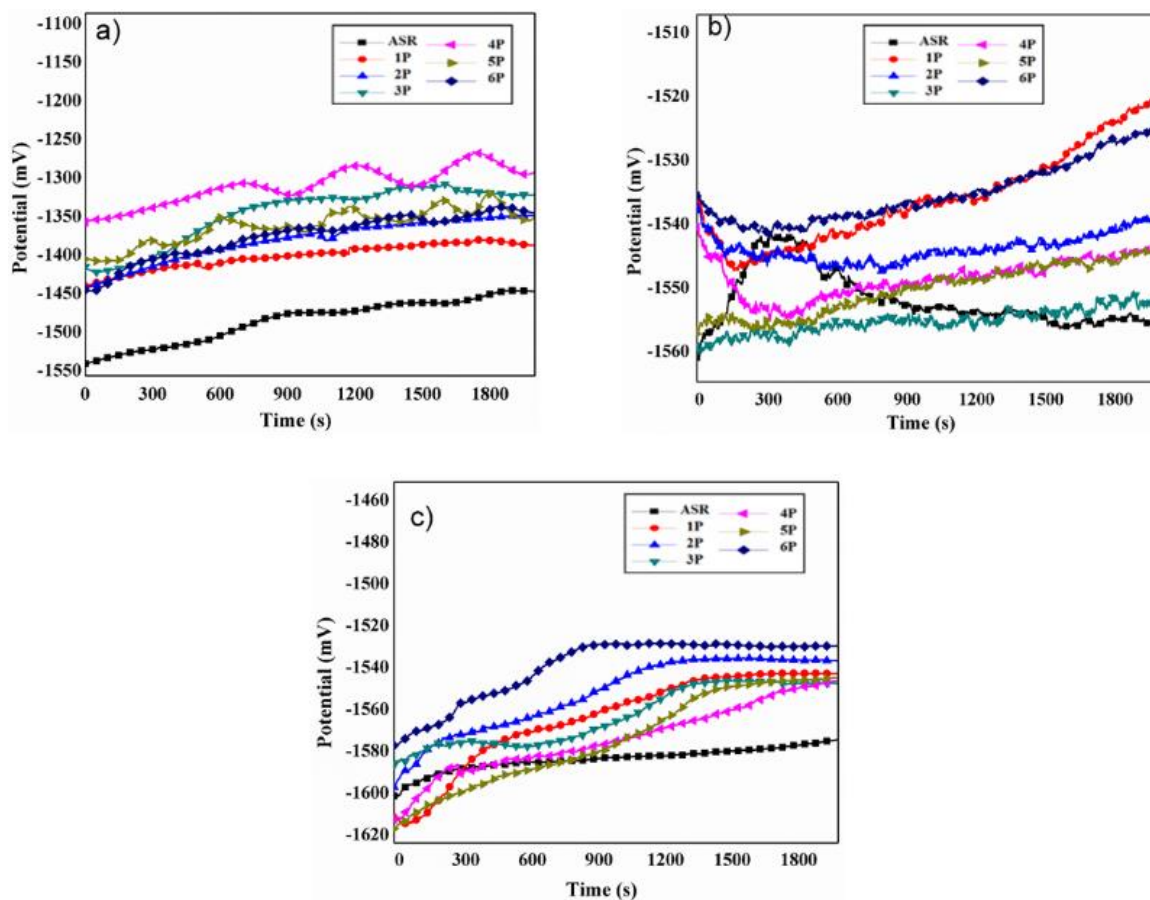


Fig 6.2 OCP curves of ZE41 Mg- Al7075 galvanic couple for ASR and ECAPed sample in three different concentration of NaCl (a) 0M NaCl solution (b) 0.1 M NaCl solution and (c) 1M NaCl solution.

This noticeable contrast in trend of as received and equal channel angular pressed ZE41 Mg- Al7075 galvanic couple hints different corrosion behaviour in 0.1 M NaCl solution. In 0.1 M NaCl solution both as received and the equal channel angular pressed galvanic samples attained stable open circuit potential value in the range of -1565 mV to -1520 mV above 1800 seconds duration. The galvanic samples tested in 1 M NaCl solution evinced same trend in case of as received as well as equal channel angular pressed galvanic samples. All the equal channel angular pressed galvanic samples attained open circuit potential at more noble potential than as received samples. These OCP curves obtained from our experiments are in good agreement with the previous findings (Zhao et al. 2008). These researchers also tested the corrosion behaviour of ZE41 Mg alloy in three different corrosive environments (Zhao et al. 2008). In contrast, the current study involves a galvanic scenario. However, from figure 6.2 (a-c) it is observed that the presence of Al7075 did not

alter open circuit potential of ZE41 Mg. This indicates that only stable surface film is formed on both ZE41 Mg-Al7075 couple and there is no significant role of corrosion products from Al7075 on galvanic corrosion during open circuit potential duration of 2000 seconds.

6.3.2 Electrochemical impedance spectroscopy (EIS) of ZE41 Mg-Al7075 couple

Nyquist and Bode impedance plots obtained from EIS studies give detailed information about the characteristics of surface film formed on the test specimen. The figure 6.3 (a-c) depicts the Nyquist plot for galvanic corrosion of ZE41 Mg-Al7075 couple in three different corrosive environments. Figure 6.3 (a) represents the Nyquist plot for galvanic couples in 0 M NaCl solution. The plot consists of a two capacitive loops at high frequency (hf) and medium frequency (mf) respectively. In addition, two inductive loops appeared at low frequency (lf). The capacitive loop at higher and medium frequency is attributed to charge transfer resistance (R_{ct}). The occurrence of inductive loop might be attributed to adsorption of species such as Mg^+ , $Mg(OH)^+$ and formation of precipitates (Dinodi and Shetty 2014; King et al. 2014). In the present investigation galvanic scenario is involved. Hence, there is a possibility that due to the presence of Al7075 aluminium alloy in the galvanic couple, adsorption of species from $Al_2(OH)_6$ precipitate may have occurred. The occurrence of inductive loop also confirm the adsorption of Al^{3+} ions and occurrence of passivation. Similar observations were obtained for AZ31 Mg alloy when tested after 24 hours immersion in 0.05M Na_2SO_4 added with DBS anionic surfactants (Ardelean et al. 2012). Figures 6.3 (b) and (c) represent the Nyquist plot for galvanic couples tested in 0.1 M NaCl and 1 M NaCl respectively. The spectra evinced one capacitive loop at higher frequency and other at middle frequency. The occurrence of inductive loop at low frequency was also observed. The trend of spectra of samples tested in 0.1 M NaCl was observed to be similar to those tested in 1 M NaCl. However, there is a diminution in the imaginary impedance values for samples tested in 1 M NaCl which is due to the known aggressive nature of chloride ions. The trend of plot for samples tested in chloride containing environments (0.1 M and 1 M NaCl) is significantly different from those tested in 0 M NaCl solution. When tested in 0.1 M and 1 M NaCl corrosive medium, the middle frequency inductive loop was not observed which clearly indicates that effect of passivation offered by Al7075 is predominated by aggressive nature of chloride ions. The spectra obtained in the current investigation for galvanic couples tested in 0.1 M and 1 M NaCl is in good agreement with research findings (Dinodi and Shetty 2014; King et al. 2014).

ACM v4 analysis software was used to fit the Nyquist plots. Equivalent electrical circuit represented in figure 6.3 (d) quantifies the values of circuit elements viz., charge transfer resistance (R_{ct}), solution resistance (R_{sol}) and double layer capacitance (C_{dl}). Figure 6.4 (a) represents the charge transfer resistance (R_{ct}) of all galvanic samples as a function of ECAP pass number tested in three different corrosive environments. From figure 6.4 (a) it is clear that in case of galvanic samples tested under 0 M NaCl environment the 3rd pass sample showed highest value of R_{ct} 4963 ohm.cm² when compared with as received sample having lowest R_{ct} value of 2501 Ohm.cm². It is also interesting to note that the R_{ct} values of 5th pass and 6th pass sample were less than 3rd pass, 4th pass samples, but greater than 1st pass, 2nd pass and as received galvanic samples. In summary, the values of charge transfer resistance (R_{ct}) in 0 M NaCl were categorized in the descending order as follows 3rd pass > 4th pass > 5th pass > 6th pass > 1st pass > as received > 2nd pass. Similarly, for the galvanic

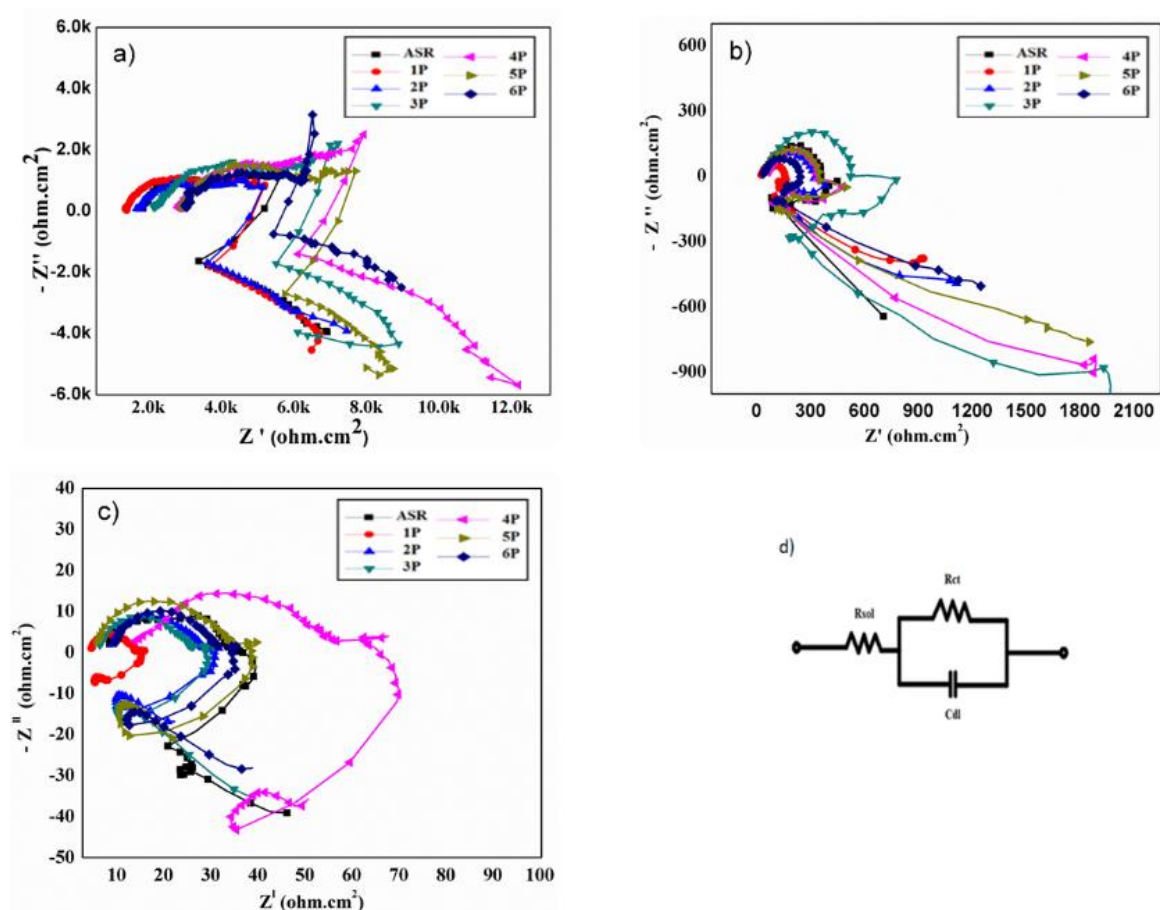


Fig 6.3 Nyquist plot for galvanic corrosion of ZE41 Mg- Al7075 galvanic couple for ASR and ECAPed sample in three different concentration of NaCl (a) 0M NaCl solution (b) 0.1 M NaCl solution and (c) 1M NaCl solution (d) Electrical Equivalent Circuit

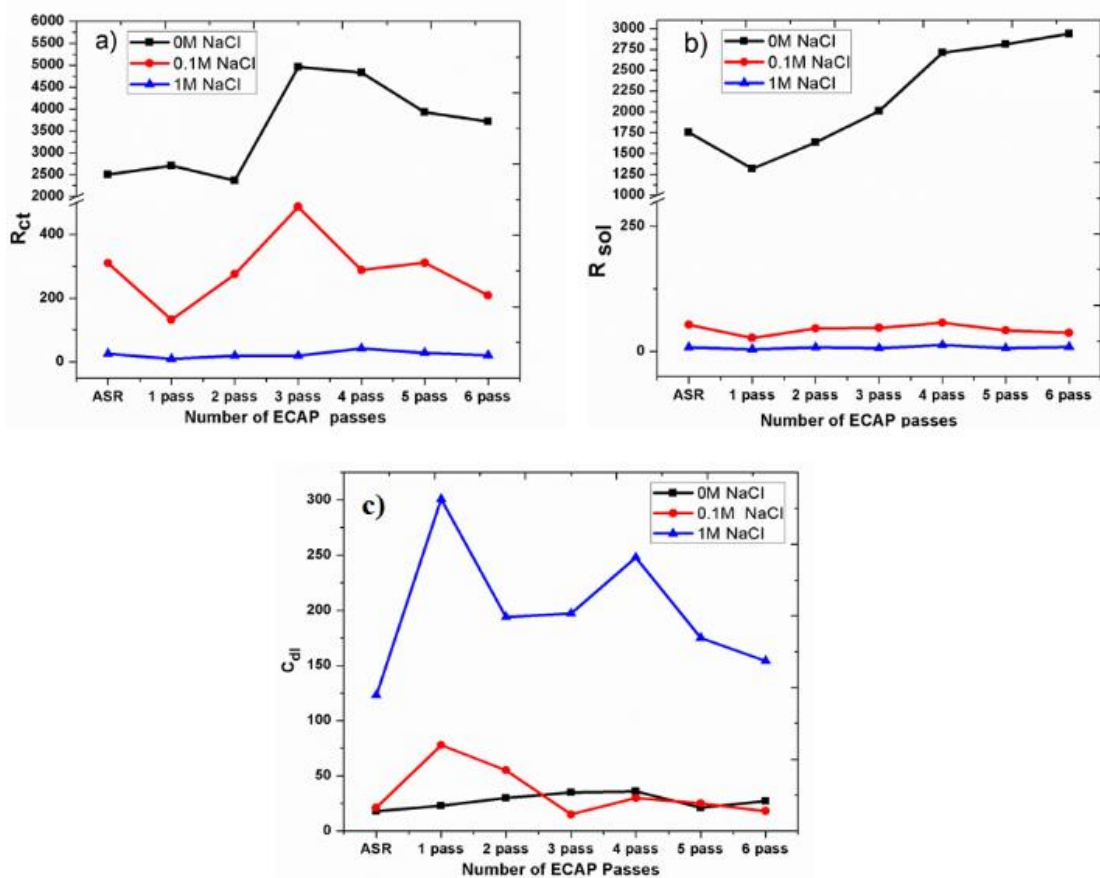


Figure 6.4 (a) Charge Transfer function (R_{ct}) and (b) Solution resistance (R_s) as a function of number ECAP passes in three different corrosive medium (c) Double layer capacitance C_{dl} as a function of number of ECAP passes.

samples tested in 0.1 M NaCl corrosive environment the values of charge transfer resistance (R_{ct}) were ranked as follows 3rd pass > 5th pass > as received > 4th pass > 2nd pass > 6th pass > 1st pass in descending order. When tested in 1 M NaCl, the values of charge transfer resistance (R_{ct}) were rated according to their descending order as follows 4th pass > 5th pass > as received > 6th pass > 2nd pass > 3rd pass > 1st pass. The drastic diminution in the values of charge transfer resistance with increase in NaCl concentration is due to aggressive nature of chloride ions preventing the formation of surface film. From the figure 6.4 (b) it is apparent that the values of solution resistance for galvanic samples in 0 M NaCl are much higher 2938 ohm.cm² to 1316 ohm.cm² when compared to those tested in 0.1 M NaCl: values ranging between 25 ohm.cm² to 60 ohm.cm² and 1M NaCl solution having values in the range of 3 ohm.cm² to 15 ohm.cm². The decrease in solution resistance (R_{sol}) with increase in NaCl concentration was attributed to the shortcut effect that occurred due to the

accumulation of corrosion products in between the ZE41 magnesium alloy (anode) and Al7075 Al alloy (cathode). The findings in the current research is authenticated with results reported from other researchers (Deshpande 2010a; Song et al. 2004). In summary, with increasing the ECAP pass number upto 4th pass the values of charge transfer resistance and solution resistance increased due to fine distribution of secondary phase particles achieved by equal channel angular pressing as presented in figure 6.1 (f). The double layer capacitance (C_{dl}) is corroborated to local dielectric constant (ϵ) and thickness of double layer film (d) by Helmholtz relation (Dinodi and Shetty 2014). The higher the thickness of double layer film and lesser the value of dielectric constant, the lower will be the C_{dl} value. The lesser value of C_{dl} indicates better corrosion resistance. Increasing the concentration of NaCl from 0 M NaCl to 0.1 M NaCl and 1 M NaCl in the corrosive medium is expected to increase the double layer capacitance (C_{dl}). Figure 6.4 (c) represents the double layer capacitance values obtained in three different concentration of NaCl corrosive medium as a function of number of ECAP passes. The double layer capacitance values of galvanic samples tested in 1M NaCl are higher up to more than 10 times when compared to those tested in less aggressive solutions such as 0 M and 0.1 M NaCl. Interestingly, the double layer capacitance values of 3rd pass, 4th pass and 6th pass galvanic samples tested in 0.1 M NaCl were relatively lesser than samples tested in 0 M NaCl solution. In order to better understand the mechanism of galvanic corrosion, corrosion products obtained after galvanic corrosion of ZE41 Mg-Al7075 couple is analysed using EDS and XRD. This behaviour might be related to the passivation offered by corrosion products from aluminium (Song et al. 2004).

6.3.3 EDS and XRD analysis of ZE41 Magnesium alloy after galvanic corrosion.

The selected area and EDS spectrum of the sample after 4th pass of equal channel angular pressing is represented in figures 6.5 (b) and (c) respectively. The surface of corroded samples were analysed using EDS and the results for the sample after 4th pass ECAP is shown in inset of figure 6.5 (c). With increasing NaCl concentration, Wt % of Magnesium reduced and the Wt% of Aluminium was increased. This may be due to chloride ions causing dissolution in magnesium as well as Aluminium alloy and the precipitates from Al7075 alloy deposited on ZE41 Mg alloy. From the EDS analysis on corroded surfaces of ZE41 Magnesium alloy presented in inset of figure 6.5 (c), the possibility of $Mg(OH)_2$ as well as $Al_2(OH)_6$ formation can be inferred. X-ray diffraction analysis was carried out on

the 4th pass equal channel angular pressed samples after galvanic corrosion in three different corrosive medium to further elaborate the presence of corresponding phases and the same is represented in the figure 6.5 (a). Mg, Mg₇Zn₃RE (Ternary Phase), Mg(OH)₂ and Al₂(OH)₆ phases were found in all three corroded samples. The spectra of 4th pass samples tested in 0 M and 0.1 M NaCl were similar due to their less aggressive nature. Strikingly, the samples tested in 1 M NaCl exhibited diminished peaks which might be correlated to undermining and fallout of ternary phase as well as bulk grain and in accordance with values of Wt% obtained from EDS analysis.

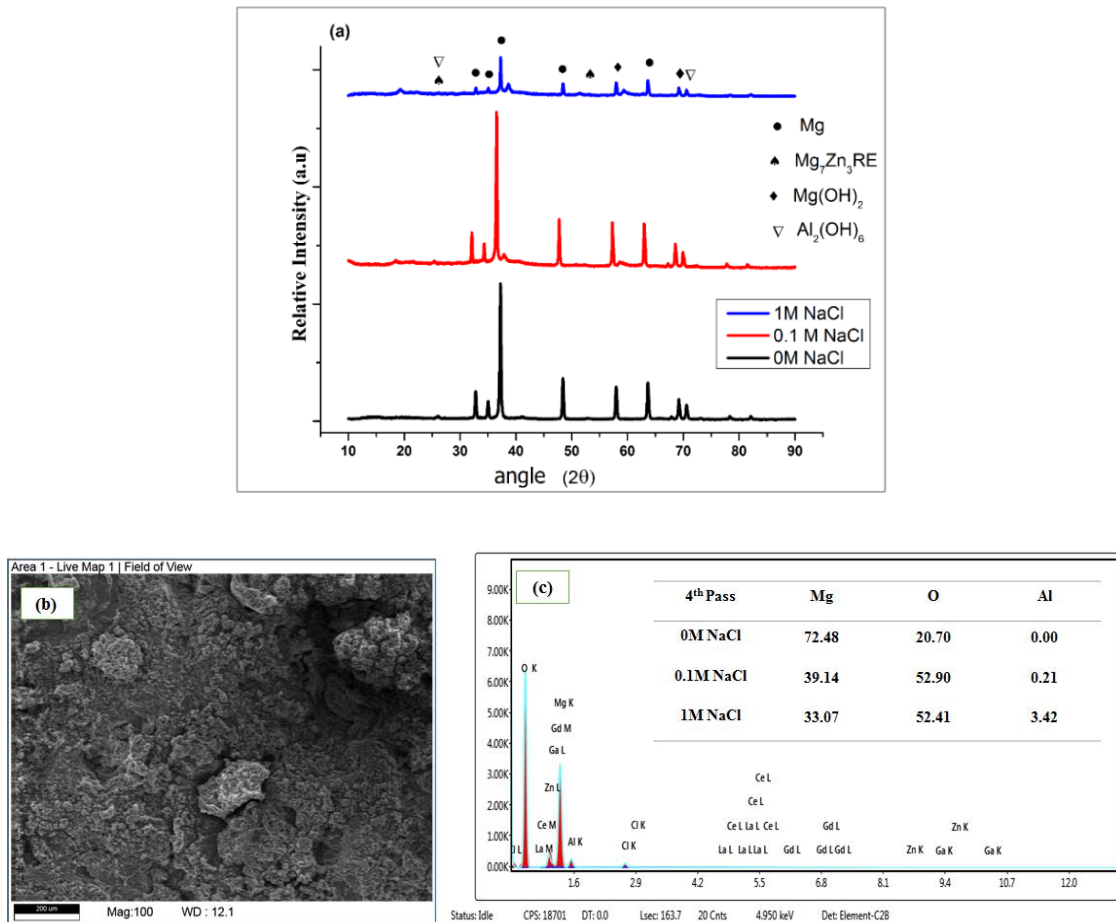


Figure 6.5 (a) XRD plot of 4th Pass ZE41 Mg alloy (b) selected area for EDS analysis on 4th pass sample (c) EDS spectra 4th Pass galvanic sample tested in 1M NaCl solution.

Al₂(OH)₆ phases were found in all three corroded samples. The spectra of 4th pass samples tested in 0 M and 0.1 M NaCl were similar due to their less aggressive nature. Strikingly, the samples tested in 1 M NaCl exhibited diminished peaks which might be correlated to undermining and fallout of ternary phase as well as bulk grain and in accordance with values of Wt% obtained from EDS analysis.

6.3.4 Influence of microstructure on resistance to galvanic corrosion in three different environments.

The value of impedance is collectively influenced by all the circuit elements present in the simple Randle's circuit viz. charge transfer resistance (R_{ct}), solution resistance (R_s) and double layer capacitance (C_{dl}) (Jüttner 1990). It is established that higher the value of

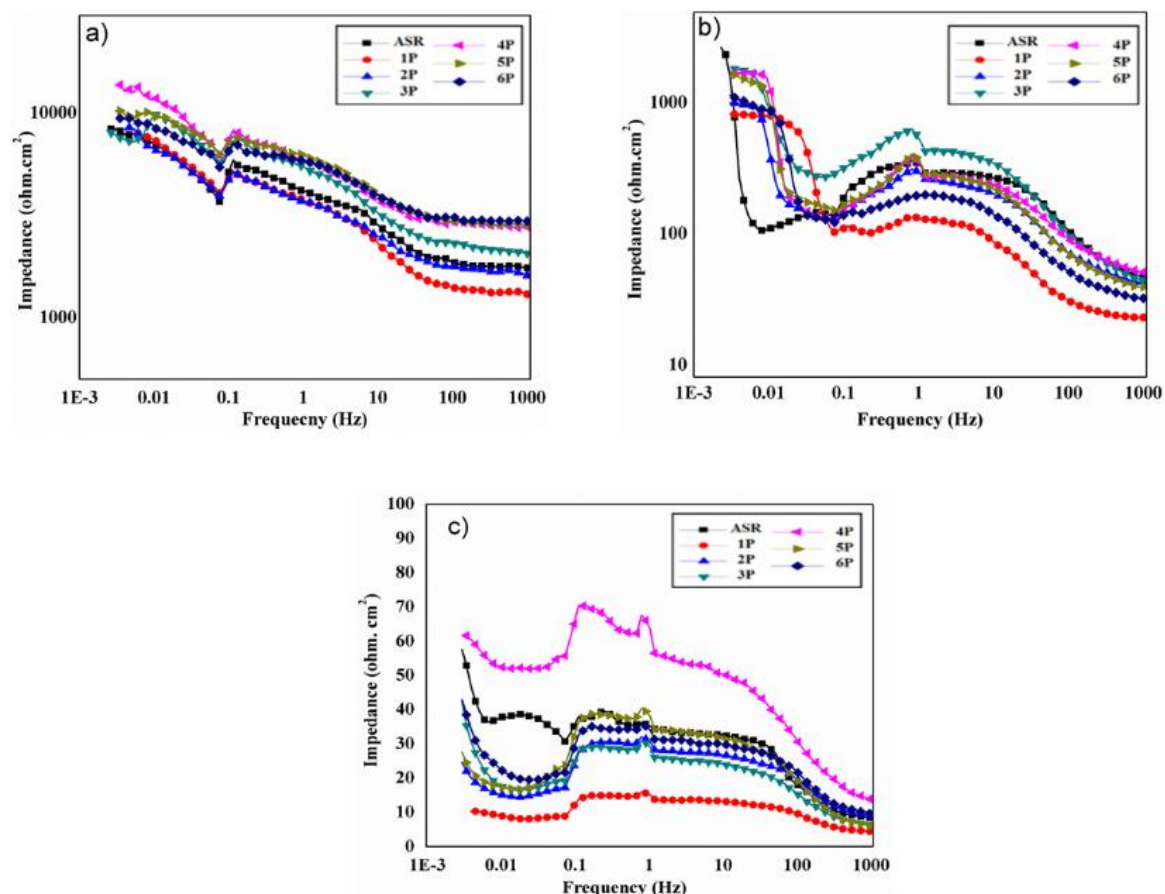


Figure 6.6 Bode impedance plot for galvanic corrosion of ZE41 Mg – Al7075 for three different concentration of NaCl solution (a) 0M NaCl (b) 0.1M NaCl (c) 1M NaCl.

impedance, higher is the corrosion resistance of the material under study. Bode impedance plot for galvanic corrosion of ZE41 Mg–Al7075 in 0 M NaCl is represented in the figure 6.6 (a). The trend of bode impedance spectrum is in reasonable agreement with one of the models proposed (Jüttner 1990). The 4th pass ECAP sample showed highest impedance value while 1st pass and 2nd pass galvanic sample exhibited lowest impedance value in 0 M NaCl solution. The impedance value increased with increase in number of passes from 1st

pass, 2nd pass, 3rd pass and 4th pass due to fine distribution of T Phase (Mg_7Zn_3RE) depicted in figure 6.1 (f). Similar kind of second phase distribution and improvement in corrosion resistance was also observed by various investigators (JIANG et al. 2009; Minárik et al. 2013; Naik et al. 2018, 2019; Shen et al. 2012). For the 5th pass and 6th pass Mg sample in the galvanic couple, the impedance value were lesser compared to 4th pass but greater than 1st pass, 2nd pass and 3rd pass galvanic sample in 0 M NaCl solution. It should be borne in mind that for 5th pass and 6th pass sample the ECAP was carried out at 275°C, while the 1st pass, 2nd pass, 3rd pass and 4th pass were ECAPed at 300°C. This reduction in impedance values during 5th and 6th pass is related to the dislocation induced after equal channel angular pressing as presented in the figure 6.1(g). Various investigators also observed crystalline defects such as dislocation density and reported decrement in corrosion resistance when carrying out equal channel angular pressing on Mg alloys at relatively lower temperature (Song et al. 2011b). Figure. 6.6 (b) depicts the Bode impedance plot for galvanic corrosion of ZE41 Mg–Al7075 in 0.1 M NaCl. Surprisingly, the as received galvanic sample showed highest impedance value whilst the 1st pass galvanic sample evinced lowest impedance in 0.1 M NaCl. This deviation from usual trend is reflected on the OCP curves presented in figure 6.2 (b) conforming difference in corrosion behaviour which is expected to be revealed in corrosion morphology. The trends of impedance spectra obtained for 1 M NaCl were similar to 0 M NaCl for both as received and equal channel angular pressed galvanic samples. But drastic reduction in impedance values occurred due to aggressive nature of chloride ions which is inferred from figure 6.6 (c). This is also in accordance with open circuit potential curves of same the condition shown in figure 6.2 (c).

6.3.5 Potentiodynamic polarization of galvanic couple

The corrosion rate calculated from Tafel plots for three different NaCl concentration is tabulated in the table 6.1. Tafel plots for galvanic corrosion behaviour of ZE41 Mg–Al7075 galvanic couple in 0 M NaCl, 0.1 M NaCl and 1 M NaCl solution is represented in figures 6.7 (a-c) respectively. From figure 6.7 (a) the following inferences can be drawn (i) the as received and equal channel angular pressed galvanic samples evinced similar Tafel behaviour which is in accordance with their open circuit potential trends shown in figure 6.2 (a). (ii) Equal channel angular pressed samples exhibited nobler potential than as received sample but there is no remarkable difference in their corrosion rates. This is attributed to the fact that testing in less aggressive environments such as deionized water

might suppress the micro-galvanic corrosion occurring between the bulk grain Mg and T-phase (Mg_7Zn_3RE) due to extra resistance (Ishida et al. 2011). Also there might be negligible influence of corrosion products on galvanic corrosion behaviour of galvanic samples tested in 0 M NaCl solution which is evident from the EDS results of the same tabulated in the inset of figure 6.5 (c). The corrosion rate tabulated in table 6.1 and Bode impedance plot tested in 0 M NaCl figure 6.6 (a), clearly shows that 4th pass galvanic sample exhibited highest corrosion resistance in 0 M NaCl solution. Similarly, on examining figure 6.7 (b) the following observations are noted (i) the trends of as received

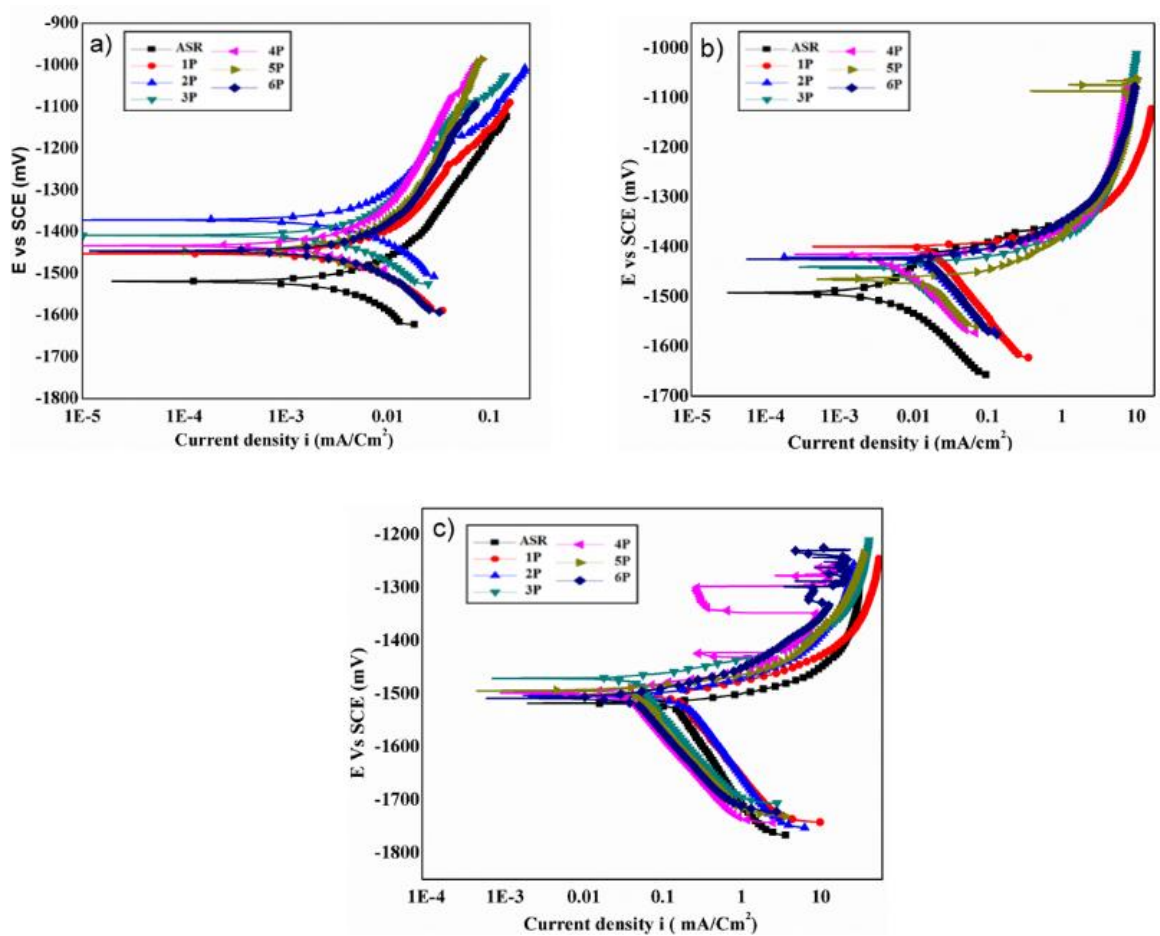


Figure 6.7 Tafel plot for galvanic corrosion of ZE41 Mg – Al7075 in (a) 0M NaCl (b) 0.1M NaCl (c) 1M NaCl solution.

and equal channel angular pressed samples are noticeably different in terms of their anodic behaviour which is in complete agreement with trends of their OCP curve represented in figure 6.2 (b) (ii) Ennoblement in the value of potential occurred after equal channel angular

pressing (iii) as received sample exhibited lower potential when compared with equal channel angular pressed samples but the corrosion rate of as received sample was measured to be the lowest among all samples. Strikingly, the corrosion rate tabulated in the table 6.1 and Bode impedance plot depicted in figure 6.6 (b) indicated that as received sample evinced highest corrosion resistance in 0.1 M NaCl followed by 4th pass galvanic sample. The reason for same is elucidated by comparing their corrosion morphology. From figure 6.7 (c), one can observe that (i) as received and equal channel angular pressed galvanic samples showed similar trends which is in accordance with their open circuit potential curves presented in figure 6.2 (c) (ii) as received sample exhibited the lowest corrosion

Table 6.1 Corrosion rate of galvanic couple in 0M NaCl, 0.1M NaCl and 1M NaCl solutions.

CR (mm/yr)	ASR	1 st pass	2 nd pass	3 rd pass	4 th pass	5 th pass	6 th pass
0M NaCl	0.12	0.15	0.22	0.13	0.05	0.07	0.08
0.1 M NaCl	3	6.16	4.7	5	4.1	5.1	5
1M NaCl	24.7	28.6	15.4	27.4	11.171	18.7	12.2

potential while all ECAPed galvanic samples attained nobler values. (iii) 4th pass sample exhibited relatively better resistance to corrosion. The corrosion rate for galvanic couples increased with increase in chloride ion concentration. Similar kind of trend in corrosion rate was observed when ZE41 magnesium alloy was tested in 0 M, 0.1 M and 1 M NaCl (Song et al. 2004) and for Pure Mg tested in 0.1 M, 1 M and 5 M NaCl (King et al. 2014). However, the current investigation enlighten the galvanic corrosion behaviour of equal channel angular pressed ZE41 Mg alloy that is influenced by microstructure and corrosion products from Al alloy. In summary, equal channel angular pressing improved the resistance to galvanic corrosion which is evident from the corrosion rate of galvanic couples presented in table 6.1 and also in complete agreement with trends of Bode impedance plots presented in figure 6.6.

6.3.6 Corrosion morphology of ZE41 Magnesium alloy after galvanic corrosion in 0 M, 0.1 M and 1 M NaCl solution.

The corrosion morphology of as received and 4th pass Mg samples in galvanic couple are shown in the figure 6.8 (a-f). In 0M NaCl corrosive medium, the as received sample evinced minute patches of pits inside the bulk grain presented and marked (circle) in figure 6.8 (a),

while the grain boundaries remain un-attacked. However, in the corroded surface of 4th pass galvanic sample pits were not observed as shown and marked (rectangle) in figure 6.8 (d) exhibiting uniform corrosion. In case of galvanic samples tested in 0.1 M NaCl, the as received sample depicted in figure 6.8 (b), exhibited pitting corrosion (marked in ellipse) in relatively lesser areas due to micro-galvanic corrosion between Mg and T Phase (Mg_7Zn_3RE). In contrast, on observing the 4th pass galvanic sample pits were not found, it is rather uniformly corroded all over the sample surface as represented and marked in figure 6.8 (e). The higher corrosion rate of 4.1 mm/yr observed in 4th Pass sample is due to the corrosion occurring uniformly covering more areas on sample surface. The as received sample exhibited relatively lesser corrosion rate of 3 mm/yr due to the occurrence of

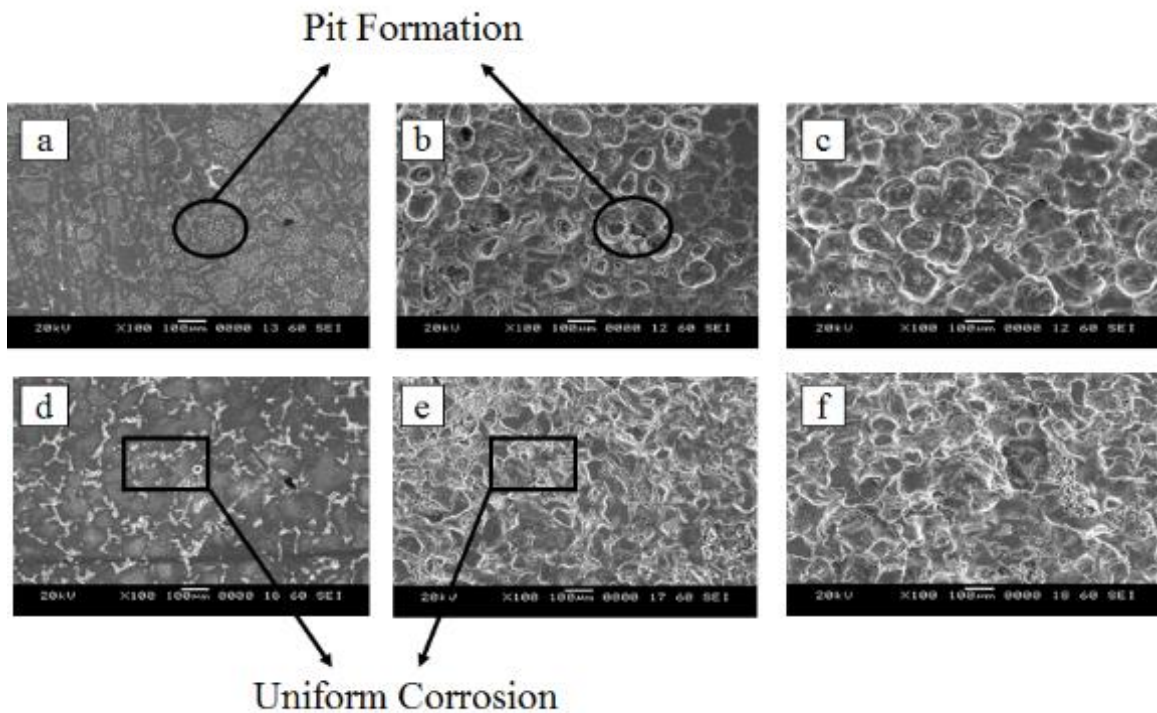


Figure 6.8 Corrosion morphology of ASR (a) (b) (c) and 4th pass galvanic samples (d) (e) (f) in 0M NaCl, 0.1 M NaCl and 1M NaCl respectively.

pitting corrosion in selective areas when tested in 0.1M NaCl. Equal channel angular pressing converted the form of corrosion from pitting to uniform corrosion due to the fine distribution of secondary phase particles as observed from figure 6.1 (f). This phenomenon was also observed by various investigators (JIANG et al. 2009; Mostaed et al. 2014a; b; Qiang et al. 2014; Shen et al. 2012). The corrosion morphology of as received and 4th pass samples tested in 1 M NaCl are shown in figure 6.8 (c) and (f) respectively. The grains and

grain boundaries were not observed on the corroded surface of as received and 4th pass samples. Hence, the entire surface of both as received and 4th pass samples were severely corroded. However, from the corrosion rate tabulated in the table 6.1 and XRD results represented in the figure 6.5 (a), it is clear that a layer of magnesium is removed from the surface due to aggressive nature of chloride ions when tested in 1 M NaCl solution.

6.3.7 Mechanism of galvanic corrosion in ZE41 Mg–Al7075 galvanic couple.

In order to study the influence of species on corrosion process, XPS analysis was carried out on the corroded surface of galvanic samples. The high resolution spectra of Mg 1s, Al 2p and O 1s signals for ZE41 Mg sample tested in 0 M NaCl is depicted in the figure 6.9 (a-c) respectively. The binding energy values 1301.1, 1302.5, 1303.8 and 1304.7 eV corresponds to magnesium, magnesium hydroxide, magnesium oxide and magnesium di-aluminium tetroxide respectively as represented in high resolution spectra of Mg 1s signal, figure 6.9 (a). Al 2p signal depicted in figure 6.9 (b) evinced peak at binding energy value of 75 eV indicating aluminium oxide. Similarly, from figure 6.9 (c), the peaks formed at binding energy values 529.8, 531.2 and 533.3 eV signifies the formation of aluminium oxide, magnesium oxide and magnesium hydroxide. Similar kind of spectra was observed when XPS analysis was carried out for ZE41 Mg samples tested in 0.1 M and 1 M NaCl as observed from figure 6.9 (d). The striking difference was reduction in intensity of the signals corroborated to aggressive nature of chloride ions. The binding energy values measured in the present investigation is in line with previous findings (Wang et al. 2010). The phenomenon of galvanic corrosion in three different environments is clearly understood from the EIS, SEM, EDS, XRD, TEM and XPS analysis. A schematic representation of galvanic corrosion occurring in ZE41 Mg–Al7075 couple is elucidated in the figure 6.10. The first stage commences with dissolution of both ZE41 Mg and Al7075 alloy in interaction with corrosive environment. This phenomenon is referred as macro-galvanic corrosion and occurs when active metals such as Mg is coupled with relatively noble metals such as aluminium and steel (Song and Atrens 2003). The second stage involves the formation of precipitates such as magnesium hydroxide and aluminium hydroxide. XPS spectra presented in figure 6.9 and XRD analysis depicted in figure 6.5 (a) validate the precipitate formation. Table 6.2 presents the percentage of atomic concentration quantified from XPS analysis performed on corroded ZE41 Mg samples in three different corrosive environments. From the values of atomic concentration percentage

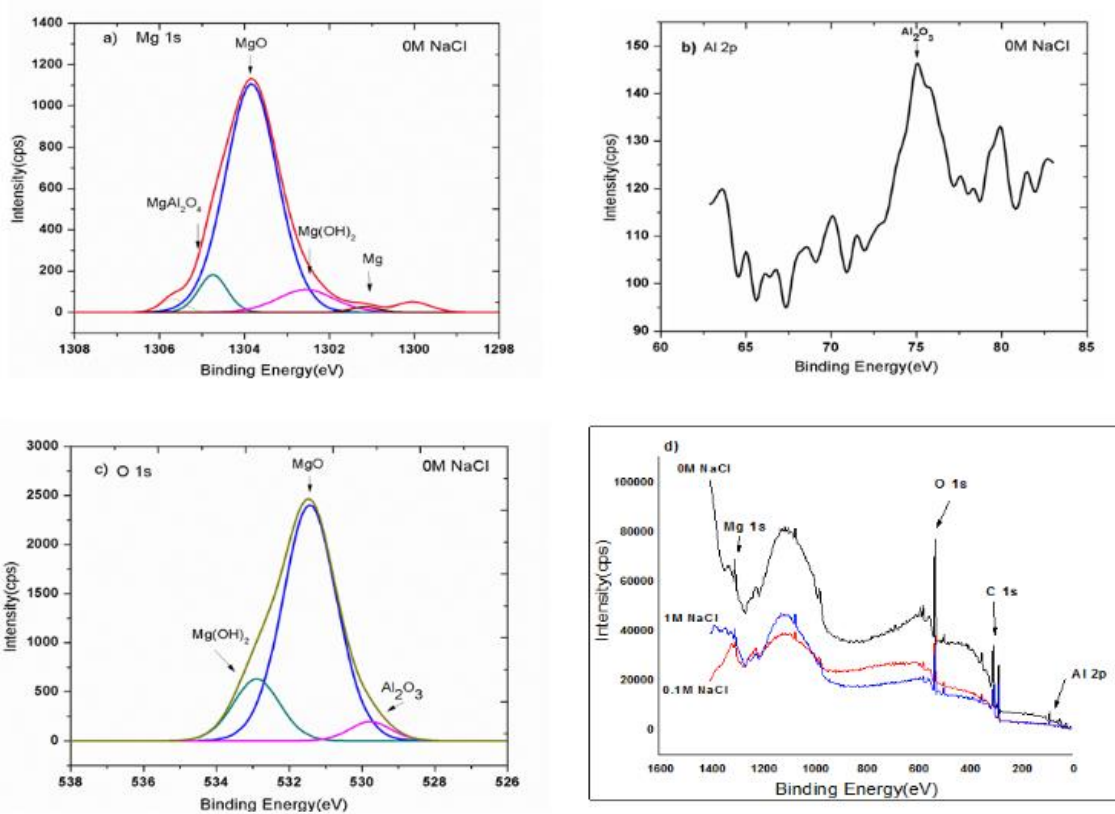


Figure 6.9 XPS analysis of ZE41 Magnesium alloy after galvanic corrosion in 0M NaCl (a) Mg 1s (b) Al 2p and (c) O 1s spectra (d) XPS survey spectra for ZE41 Mg samples tested 0M,0.1M and 1M NaCl solution.

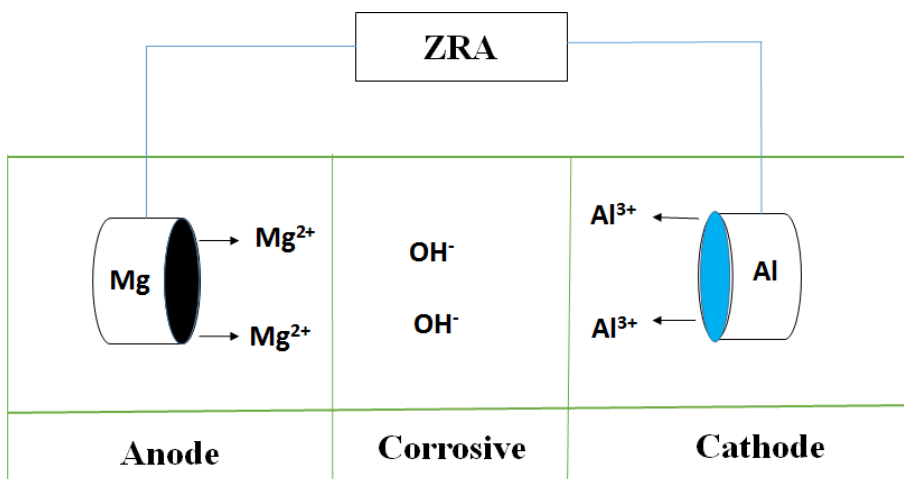


Figure 6.10 Schematic representation of ZE41 Magnesium alloy and Al7075 Aluminium alloy couple in interaction with corrosive medium.

Table 6.2 Atomic concentration from XPS analysis.

Atomic concentration %	0M NaCl	0.1M NaCl	1M NaCl
Mg 1s	6.51	7.23	5.73
Al 2p	0.10	0.00	0.00
O 1s	37.64	29.63	29.83
Mg / O	0.170	0.244	0.192
Al / O	0.002	0	0
Al / Mg	0.015	0	0

Surface film models

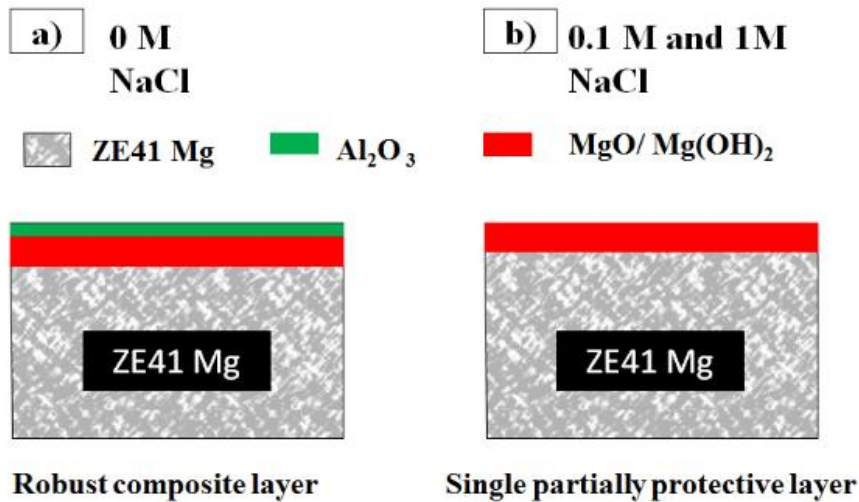


Fig 6.11 surface film models developed on ZE41 Mg after galvanic corrosion.

obtained from each signal and their corresponding spectra the surface film model formed during galvanic corrosion is proposed. The schematic representation of surface film models are shown in the figure 6.11. In 0 M NaCl solution, the surface film consists of magnesium hydroxide in the outermost layer, magnesium oxide in the middle followed by a thin film of aluminium oxide layer on ZE41 magnesium alloy. The atomic concentration percentage ratio of [Mg/O], [Al/O] and [Al/Mg] of 0 M NaCl (measured to be non –zero values)

tabulated in table 6.2 and peaks corresponding to binding energies marked in figure 6.9 (a-c) validate surface film model. In deionized water or 0 M NaCl solution a robust and composite oxide/hydroxide layer is formed due to passivation offered by Al^{3+} ions in addition to partially protective magnesium oxide/hydroxide layer. The formation of inductive loop at low frequency is common trait of magnesium and its alloys observed from Nyquist plots represented in figure 6.3 (a-c). The significance of low frequency inductive loop is believed to be adsorption of species without throwing light on the species. While the recent research reports suggested that $\text{Mg}(\text{OH})_{\text{ads}}^+$ and Mg_{ads}^+ are the species responsible for loop formation (Dinodi and Shetty 2014; King et al. 2014). Fairman and Bray postulated that two Al^{3+} ions could be incorporated into $\text{Mg}(\text{OH})_2$ surface film by replacing three Mg^{2+} ions electrically and physically (Fairman and Bray, 1971). Thus, previous studies also supports our conclusion that corrosion products from aluminium alloy offers passivation during galvanic corrosion (Song et al. 2004). In contrast to samples tested in 0 M NaCl solution, the percentage of atomic concentration obtained from Al 2p signal is Zero in both 0.1 M and 1 M NaCl corrosive medium. This clearly depicts that their surface film does not consist of aluminium oxide/hydroxide layer. Hence, the surface film of ZE41 Mg alloy consists only magnesium oxide/hydroxide layer in 0.1 M and 1 M NaCl solution which is apparent from Fig.6.9 (d). This clearly indicates that the passivation offered by corrosion products from aluminium alloy is predominated by the aggressive nature of chloride ions. This is also apparent from Nyquist Plot represented in figure 6.3 and the corrosion rate tabulated in table 6.1. Similar kind of surface film model for AZ magnesium alloys tested in sodium chloride solution was proposed (Song et al. 1998). The current investigation is also in good agreement with findings (Wang et al. 2010). In summary, galvanic corrosion is dynamic in nature accompanied by formation of partially protective magnesium oxide/ hydroxide layer, passivation offered by Al^{3+} ions from corrosion products and aggressive nature of corrosive medium destroying protective film formation. Equal channel Angular Pressing of ZE41 Mg improved the resistance to galvanic corrosion due to fine distribution of secondary phase particles as presented in figure 6.1 (f) and passivation offered by Al7075 Al alloy.

6.4 COMPARISON OF CORROSION AND GALVANIC CORROSION BEHAVIOUR OF ZE41 MAGNESIUM ALLOY.

The thermodynamic nature of corrosion is generally obtained from open circuit potential. The open circuit potential of Al7075 alloy, ZE41 Mg and coupled ZE41 Mg– Al7075 alloy is represented in the figure 6.12. The OCP value at the end of 2000 seconds time duration is found to be -789 mV and -1621mV for Al7075 alloy and ZE41 Mg respectively. It is also interesting to observe that the OCP value of ZE41 Mg–Al7075 galvanic couple (G) is -1548 mV which is relatively higher than that of ZE41 Mg alloy. The OCP values of Al7075

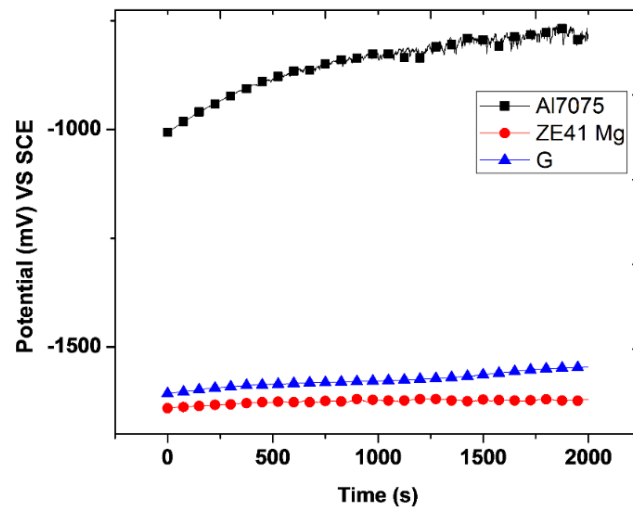


Fig 6.12 Open Circuit potential of Al7075, ZE41 Mg and coupled ZE41 Mg–Al7075.

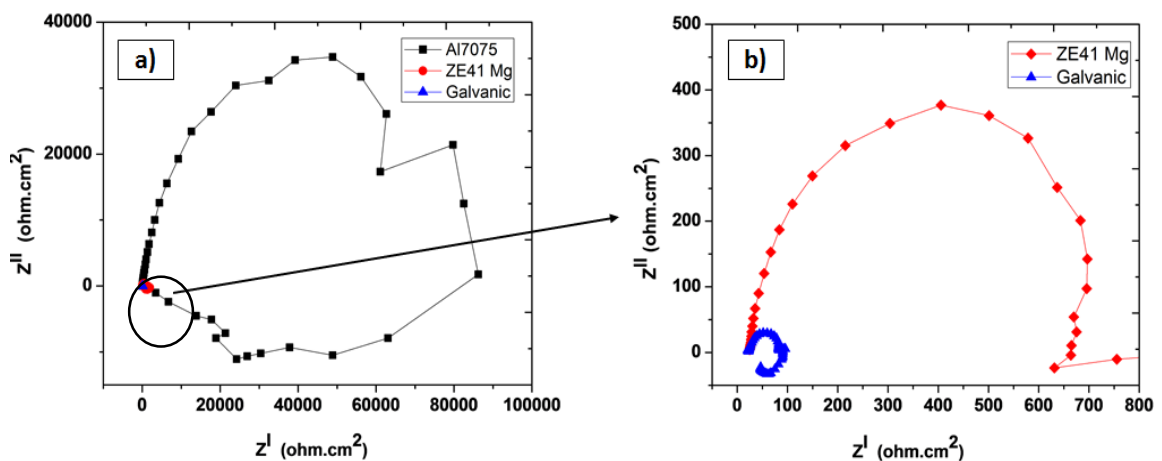


Fig.6.13 (a) Nyquist plot of Al7075, ZE41 Mg and coupled ZE41 Mg–Al7075
(b) Expanded view of Figure (a).

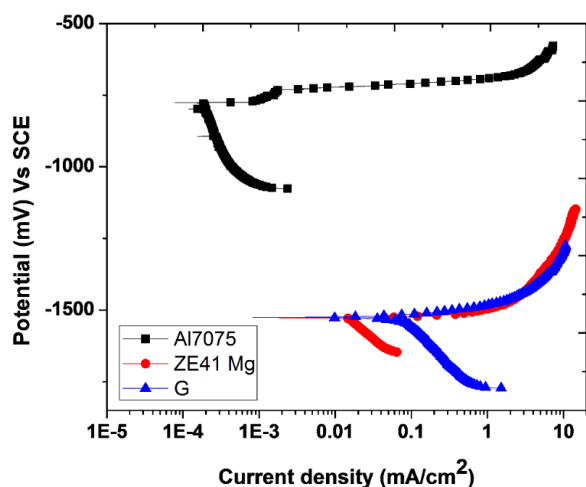
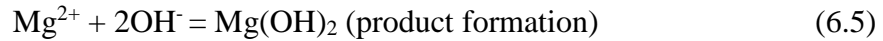
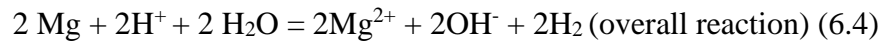
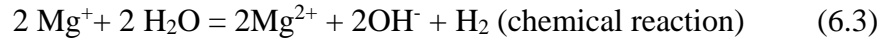
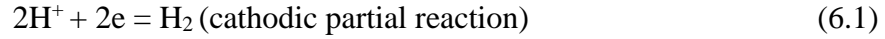


Fig 6.14 Potentiodynamic polarization curve of Al7075, ZE41 Mg and coupled ZE41 Mg-Al7075.

and ZE41 Mg are in line with the galvanic series and research findings (Atrens et al, 2008). Noble potential in OCP curve signifies better corrosion resistance. Hence, the corrosion resistance of materials considered in this study is ranked in order as follows Al7075 alloy > coupled ZE41 Mg–Al7075 > ZE41 Mg. But this order of corrosion resistance cannot be concluded from OCP curves because it does not give any information about corrosion rate. In general, Nyquist plot gives detailed information about the formation of surface film and its nature. Nyquist plot of Al7075 alloy, ZE41 Mg and coupled ZE41 Mg–Al7075 alloy tested in 3.5 Wt% NaCl is represented in the figure 6.13 (a). It is apparent that the diameter of Al7075 alloy is significantly higher in the range of 35000 ohm.cm². Figure 6.13 (b) depicts the expanded view of figure 6.13 (a). It is observed that the diameter of semi-circle reaches maximum at imaginary impedance value of 376 ohm.cm² and 39 ohm.cm² for ZE41 Mg and couple ZE41 Mg - Al7075 alloy. Figure 6.14 depicts the potentiodynamic polarisation plot of Al7075 alloy, ZE41 Mg and coupled ZE41 Mg – Al7075 alloy tested in 3.5 Wt% NaCl. The Potentiodynamic polarization curve of Al7075 alloy is at the most noble potential of -800mV. It is interesting to observe that the potential of both ZE41 Mg and coupled ZE41 Mg–Al7075 alloy is -1500mV approximately. The significant difference between them is the position of cathodic slope. This is due to the fact that when ZE41 Mg is tested in 3.5Wt% NaCl, micro galvanic corrosion occurs due to potential difference between magnesium acting as anode and Mg₇Zn₃RE acting as cathode as represented in figure 6.15 (a). The anodic partial reaction at bulk magnesium occurs by the dissolution of

magnesium and release of an electron as mentioned in equation (6.2). This electron is taken up at Mg_7Zn_3RE cathodes resulting in hydrogen evolution as shown in equation (6.1). In addition to electrochemical mode of corrosion, dissolution of magnesium occurs by chemical reaction which is referred as anodic hydrogen evolution mentioned in equation (6.3). This is the main reason for deviation from Tafel behaviour which is apparent



from figure 6.14. The overall reaction represented in the equation (6.4) includes corrosion of magnesium by electrochemical and chemical mode (Song and Atrens, 2003). In contrast when tested as couple i.e ZE41 Mg–Al7075 alloy the magnesium in ZE41 Mg possessing lower or active potential becomes anode while Al7075 alloy having a relatively higher potential becomes cathode. Higher the area of cathode higher is the hydrogen evolution at cathode. Eventually, higher hydrogen evolution will result in higher anodic dissolution. This is the reason for shift in the cathodic slope towards a region of higher corrosion current density when Al7075 alloy is galvanically coupled to ZE41 Mg alloy. The corrosion rate is calculated from the equation (6.6) mentioned below.

$$\text{Corrosion Rate [CR]} \text{ (mm/year)} = 22.85 i_{\text{corr}} \text{ (mA/cm}^2\text{)} \quad (6.6)$$

The corrosion rate of ZE41 Mg and coupled ZE41 Mg – Al7075 is calculated to be 0.83 mm/yr and 6.21 mm/yr. The microstructure of as received ZE41 Mg revealed the presence of T-phase (Mg_7Zn_3RE) along the grain boundaries as shown in the figure 6.15 (a). During corrosion of ZE41 Mg in 3.5 Wt% NaCl, electrochemical corrosion occurs between Mg phase and T phase. Mg phase acts as an anode and T phase (Mg_7Zn_3RE) acts a micro cathode (Mg_7Zn_3RE). Due to the presence of micro cathodes the corrosion in ZE41 Mg

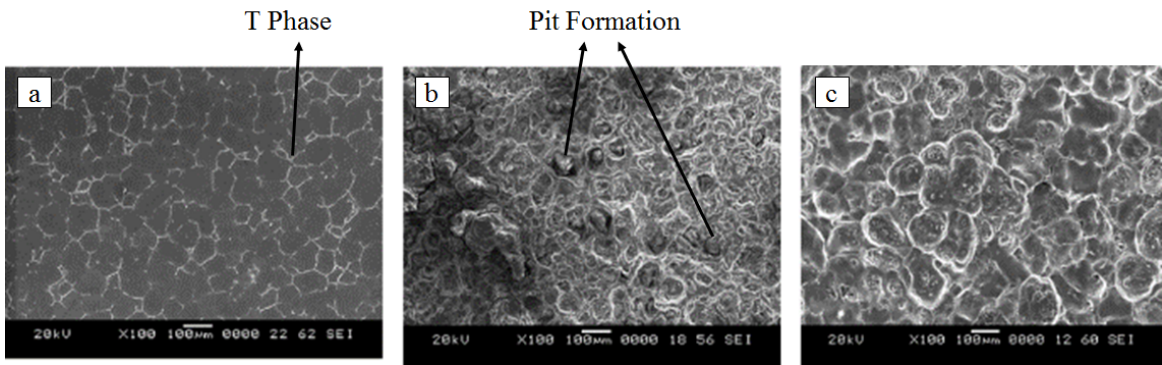


Fig 6.15 SEM images of (a) ZE41 Mg (b) corroded ZE41 Mg (c) corroded galvanic ZE41 Mg

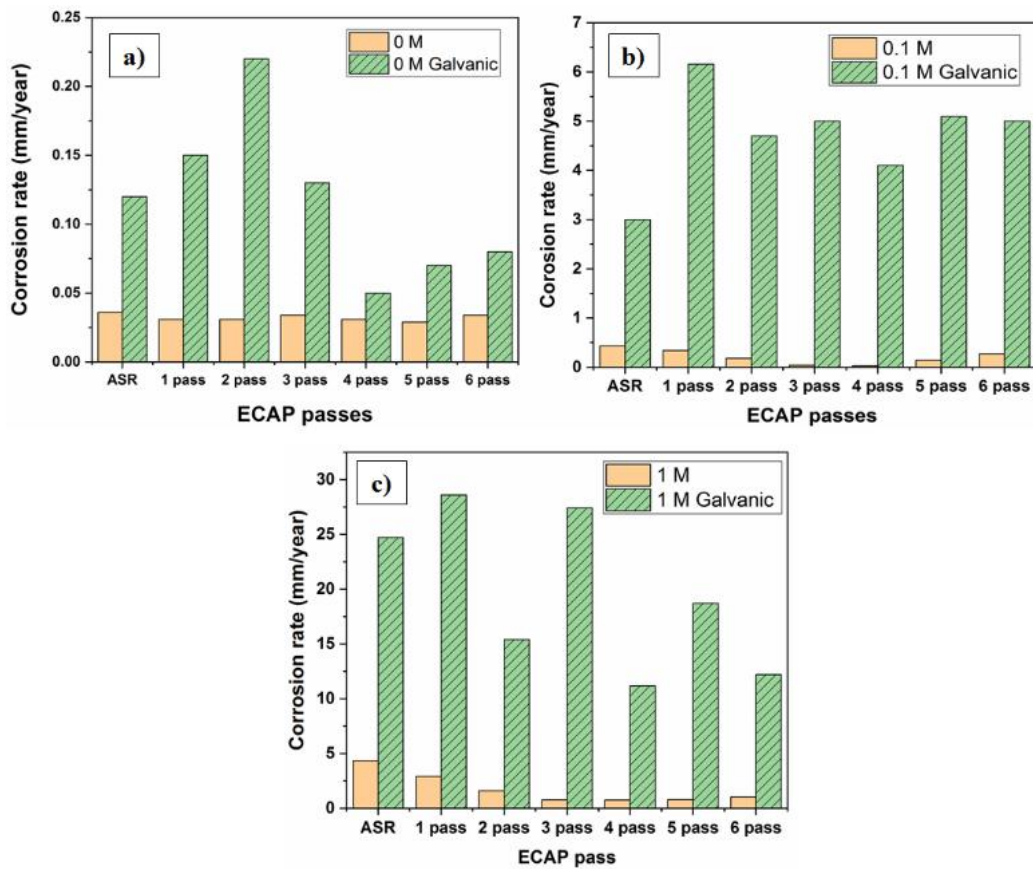


Fig 6.16 Comparing the corrosion rate obtained from ZE41 Mg corrosion and galvanic corrosion of ZE41 Mg- Al7075 couple.

occurs mainly along grain boundaries. This leads to formation of inter-granular corrosion attack along with undermining of T phase (Mg_7Zn_3RE) resulting in pit formation as seen from figure 6.15 (b). In contrast, during galvanic scenario, two materials viz., ZE41 Mg and Al7075 Al alloy are involved. Hence, electrochemical reaction occurs between Mg phase, T phase (Mg_7Zn_3RE) and Al7075 Al alloy. Indeed, Mg phase acts as anode, while T phase (Mg_7Zn_3RE) and Al7075 Al alloy acts as micro cathodes and macro cathodes respectively. Due to the presence of macro cathode a significantly higher corrosion rate of 6.21 mm/yr was observed in galvanic scenario. As a result of this higher corrosion rate, the grain boundaries were not visible in figure 6.15 (c). Therefore, the corroded SEM images depicted in figure 6.15 (a-c) are in accordance with their corresponding corrosion rates. Also during galvanic corrosion, ZE41 Mg corrosion leads to product $Mg(OH)_2$ formation as shown in equation (6.5). Similarly, Al7075 alloy corrosion results in $Al_2(OH)_6$ precipitate formation which offers passivation MC Zhao et.al (2008). But, the corrosion rate of ZE41 Mg- Al7075 couple is approximately five times that of ZE41 Mg. So, it can be concluded that the destructive nature of chloride ions in 3.5 Wt% NaCl is predominated by passivation effect offered by corrosion products from Al7075 alloy. This is a preliminary test carried out using 3.5 Wt% NaCl. This laid the foundation to understand the difference between corrosion behaviour of individual Al7075 aluminium alloy, ZE41 Mg alloy and ZE41 Mg – Al7075 Al couple. The chapter 5 elucidated the corrosion behaviour of ZE41 Mg alloy. In contrast, the chapter 6 highlights the galvanic corrosion behaviour of ZE41 Mg – Al7075 Al couple. Comparing the corrosion rate obtained from ZE41 Mg corrosion and galvanic corrosion of ZE41 Mg – Al7075 Al couple will enlighten the role of ECAP on their corrosion behaviour. The corrosion of ZE41 Mg and galvanic corrosion of ZE41 Mg – Al7075 Al couple is compared in the figure 6.16 (a-c). In general, the corrosion rate of ZE41 Mg – Al7075 Al couple is significantly higher than that of ZE41 Mg. This is attributed to the difference in cathode areas involved in ZE41 Mg and ZE41 Mg – Al7075 Al couple. The schematic of corrosion and galvanic corrosion of ZE41 Mg is represented in the figure 6.17. It is observed that the ZE41 Mg contains Mg in the bulk grains and ternary phase (Mg_7Zn_3RE) decorated along the grain boundaries, seen from figure 6.15 (a). The bulk Mg acts as anode and the ternary phase acts as cathode. During corrosion of ZE41 Mg, micro galvanic cells are formed between bulk Mg and ternary phase. In contrast, during the galvanic corrosion scenario, two materials ZE41 Mg and Al7075 Al alloy are involved.

Table 6.3 corrosion rate obtained from ZE41 Mg and ZE41 Mg- Al7075 Al couple and the % change in corrosion rate after ECAP.

Corrosion rate CR (mm/yr)	ASR	1 st pass	2 nd pass	3 rd pass	4 th pass	5 th pass	6 th pass
0M	0.036	0.031	0.031	0.034	0.031	0.029	0.034
% change in CR		16.12	16.12	5.88	16.12	24.13	5.88
0.1 M	0.43	0.34	0.18	0.04	0.03	0.14	0.27
% change in CR		26.47	138.88	975	1333	207	59.25
1M	4.36	2.9	1.59	0.76	0.75	0.79	1.05
% change in CR		50.33	174.21	473.68	481.33	451.89	315.23
0M Gal	0.12	0.15	0.22	0.13	0.05	0.07	0.08
% change in CR		20	45.45	7.69	140	71.42	50
0.1 M Gal	3	6.16	4.7	5	4.1	5.1	5
% change in CR		51.28	36.17	40	26.82	41.17	26.82
1M NaCl Gal	24.7	28.6	15.4	27.4	11.17	18.7	12.2
% change in CR		13.63	60.38	9.85	121.12	32.08	102.45

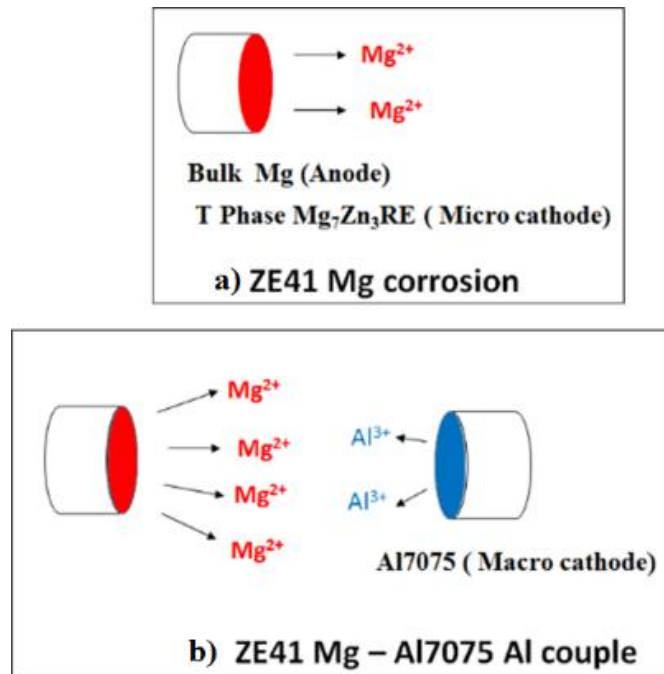


Fig 6.17 Schematic of (a) ZE41 Mg corrosion and (b) galvanic corrosion of ZE41 Mg- Al7075 couple.

Al7075 acts as macro cathode while ZE41 Mg becomes the anode. The presence of macro cathode of 15mm² area is exposed to corrosive medium. This larger area of cathode results in higher hydrogen evolution as mentioned in the equation 6.1. In addition it results in accelerating the dissolution of Mg²⁺ ions thereby increasing the corrosion rate in the galvanic scenario. However, from figure 6.16 it is interesting to observe that (i) in general the corrosion rate of 4th pass ECAP sample was found to be relatively lower when compared to other samples in 0 M, 0.1 M and 1 M NaCl solutions. (ii) the decrement in corrosion rate is more pronounced in 0.1 M and 1 M NaCl. The corrosion rate obtained from ZE41 Mg and ZE41 Mg- Al7075 Al couple and their corresponding change in corrosion rate as a result of ECAP is quantified in the table 6.3. From table 6.3 it is apparent that the corrosion rate of 4th pass sample decreased by a percentage of 16.12, 1333 and 481.3 in 0 M, 0.1 M and 1 M respectively. Hence, in case of ZE41 Mg corrosion it is reasonable to conclude that ECAP improved the corrosion resistance of ZE41 Mg alloy due to fine grains, fine distribution of secondary phase particles and preferred crystallographic orientation. In case of galvanic scenario, 4th pass ECAPed sample evinced lower corrosion rate when tested in 0 M and 1 M NaCl solution. The percentage decrement in corrosion rate of galvanic couple is calculated to be 140 and 121.12 in 0 M and 1 M NaCl. In contrast, the corrosion rate of galvanic couple for 4th pass sample increased by 26.82% compared to the as received condition when tested in 0.1 M NaCl. The corrosion morphology of as received and 4th pass sample after galvanic corrosion in figure 6.8, clearly indicated the reason behind the deviation from general trend. The as received sample evinced pitting corrosion while the 4th pass sample evinced uniform corrosion. Pitting occurred on the as received sample surface in relatively lesser areas. Although, 4th pass ZE41 Mg exhibited uniform mode of corrosion, the corroding area was relatively higher when compared to the as received condition in galvanic scenario. This resulted in relatively higher corrosion rate of ECAPed samples when compared to the as received condition. In general, the galvanic corrosion resistance of ZE41 Mg is improved significantly due to ECAP. In addition the ECAP converted the regime of corrosion from pitting to uniform mode of corrosion. It is well established that there is a pressing need to improve the corrosion resistance and ductility of magnesium and its alloys to extend their applications in automobile industries. From the present study, it is very apparent that the ECAP improved the corrosion and galvanic corrosion of ZE41 Mg alloy. In addition, ECAP improved the mechanical properties of ZE41 Mg alloy significantly. In summary, ECAP proved to be a promising method to

improve mechanical properties and corrosion resistance of ZE41 Mg simultaneously. Hence, ultrafine grains Mg alloys obtained as a result of ECAP is a promising solution to extend the application of Mg and its alloys in automobile industries.

6.5 SUMMARY

The galvanic corrosion behaviour of as received and equal channel angular pressed ZE41 Mg samples in interaction with Al7075 Al alloy was investigated in three different corrosive environments 0 M NaCl, 0.1 M NaCl and 1 M NaCl to mimic the conditions experienced in engineering applications. Equal channel angular pressing improved the resistance to galvanic corrosion in ZE41 Mg–Al7075 aluminum alloy galvanic couple in combination with passivation effect offered by corrosion products from Al7075 aluminum alloy.

- ❖ The as received ZE41 magnesium alloy having average grain size of 48 μm was subjected to equal channel angular pressing. The grain refinement of 15 μm was achieved after 6th pass ECAP.
- ❖ The open circuit potential (OCP) of ZE41 Mg – Al7075 Al couple evinced relative increase in corrosion potential with respect to time indicating stable film formation. In addition, the corrosion potential of the ECAPed samples were at least 20 mV relatively greater than the as received samples in 0 M, 0.1 M and 1 M NaCl conditions.
- ❖ Nyquist plot of galvanic couple tested in 0 M NaCl exhibited two capacitive loops; one at high (10 kHz – 100 Hz) and medium frequency (100 Hz – 0.1 Hz) in addition to appearance of two inductive loops at low frequency (0.1 Hz– 0.001 Hz). In contrast, in chloride containing environments viz., 0.1 M and 1 M NaCl two capacitive loops and one inductive loop appeared in higher (10 kHz – 100 Hz), medium (100 Hz – 0.1 Hz) and low frequency (0.1 Hz– 0.001 Hz) respectively.
- ❖ The impedance values were in the range of 10,000, 1000 and 60 ohm.cm^2 for galvanic couples tested in 0 M, 0.1 M and 1 M NaCl. The impedance values decreased drastically with increase in chloride content due to aggressive nature of chloride ions. The impedance value of 10,578 ohm.cm^2 and 64 ohm.cm^2 corresponding to 4th pass samples was found to be the highest in 0 M and 1 M NaCl

solutions. In contrast, when tested in 0.1 M NaCl the impedance values of 4th pass and as received galvanic samples were comparable in the range of 1500 ohm.cm².

- ❖ Resistance to galvanic corrosion evinced a remarkable improvement of 58% and 54% after 4th pass equal channel angular pressing due to fine distribution of T Phase (Mg₇Zn₃RE) in interaction with 0 M and 1 M NaCl respectively.
- ❖ Galvanic corrosion resistance diminished by 26% after 4th pass equal channel angular pressing in comparison with as received counterparts when tested in 0.1 M NaCl solution. However, in as cast sample pits were observed while the 4th pass sample exhibited uniform corrosion which is preferred in engineering applications.
- ❖ Galvanic corrosion is dynamic in nature accompanied by formation of partially protective magnesium oxide/ hydroxide layer, passivation offered by Al³⁺ ions from corrosion products and aggressive nature of corrosive medium destroying protective film formation.
- ❖ In 0 M NaCl solution a composite oxide/hydroxide layer of magnesium and aluminum is formed with atomic concentration % of 0.170 %, 0.002 %, 0.015% corresponding to Mg/O, Al/O and Al/Mg respectively. In contrast, the surface film consist only a layer of magnesium oxide/hydroxide layer corresponding to 0.244 % and 0.192 % atomic concentration ratio % for Mg/O when tested in 0.1 M and 1 M NaCl respectively. The Al/O and Al/Mg atomic concentration ratios were measured to be zero due to aggressive nature of chloride ions.

CHAPTER 7

CONCLUSION

In this research work, the mechanical properties and corrosion behaviour of ZE41 Mg alloy before and after two step ECAP processing were studied using EBSD technique. First stage of ECAP involves the 1st 2nd 3rd and 4th pass ZE41 Mg pressed at 300°C while the second stage involved additional passes viz., 5th 6th 7th and 8th ECAPed at 275°C. The corrosion behaviour of all ZE41 Mg samples were tested in 0 M, 0.1 M and 1 M NaCl solution to simulate conditions encountered in automobile applications. In addition, the galvanic corrosion behaviour of the as-received and ECAPed ZE41 Mg samples in interaction with Al7075 Al alloy was also investigated in three different corrosive environments, 0 M, 0.1M and 1M NaCl, to mimic the conditions experienced in engineering applications. The following conclusion were drawn from this study.

- ❖ The as received ZE41 Mg sample exhibited a heterogeneous microstructure with average grain size of 46 μm . After 1st and 2nd pass of ECAP dynamic recrystallization occurred along grain boundaries resulting in bimodal grain distribution. A relatively uniform microstructure with grain refinement upto 5.7 μm was achieved by the end of 3rd pass ECAP. However, after 4th pass ECAP average grain diameter reached a value of 10 μm i.e the grain growth occurred due to unstable nature of fine grains. Comparing the grain sizes of as received and ECAPed ZE41 Mg samples it can be concluded that grain refinement effect was phenomenal during first step ECAP.

- ❖ During second step ECAP, the effect of grain refinement was marginal. Indeed, the average grain size of 5th pass, 6th pass and 7th pass ZE41 ECAP samples were 4.8 μm , 7.13 μm and 3.93 μm respectively. Interestingly, fine grains of 2.5 μm were achieved at the 8th pass of ECAP.

- ❖ The yield strength of ZE41 Mg alloy increased significantly from 158 MPa in as received sample to 236 MPa by the end of first step ECAP. This signifies that during first step ECAP the ZE41 Mg samples were in line with Hall-Petch relation. In contrast, in the course of second step ECAP the samples evinced a sharp decrease in yield strength of 172 MPa during 8th pass. This is corroborated to texture softening effect that dominated the grain refinement phenomenon.
- ❖ The as received ZE41 Mg alloy exhibited a % elongation of 7% due to the presence of tear ridges and micro cracks. On the contrary, the 6th pass ECAP sample showed the highest % elongation of 23 % because of appearance of dimples in their fractured surface morphology. In addition, the highest Schmid factor value of 0.34 also contributed the improvement in % elongation of 6th pass ECAPed samples.
- ❖ The corrosion rate of 0.0036 mm/yr in as received condition decreased to a value of 0.027 mm/yr at 8th pass ECAP when tested in 0M NaCl. This marginal improvement in corrosion resistance signified the minimal influence of ZE41 Mg on microstructure which is also evident from EIS and Potentiodynamic polarisation results.
- ❖ 4th pass ECAP sample with 10 μ m average grain diameter exhibited the corrosion rate of 0.034 and 0.708 mm/yr when tested in 0.1M and 1M NaCl respectively. These values of corrosion rate were found to be relatively lower than of 8th pass ECAP sample with grain size of 2.5 μ m i.e 0.548 and 0.735 mm/yr. Thus, the effect of grain refinement on corrosion of ZE41 Mg alloy is predominated by crystallographic orientation.
- ❖ Galvanic corrosion is dynamic in nature accompanied by the formation of partially protective magnesium oxide/hydroxide layer, passivation offered by Al³⁺ ions from corrosion products and aggressive nature of corrosive medium destroying protective film formation. In 0 M NaCl solution a composite oxide/hydroxide layer of magnesium and Aluminum is formed with atomic concentration % of 0.170 %,

0.002 %, 0.015% corresponding to Mg/O, Al/O and Al/Mg respectively. In contrast, the surface film consist only a layer of magnesium oxide/hydroxide layer corresponding to 0.244 % and 0.192 % atomic concentration ratio % for Mg/O when tested in 0.1 M and 1 M NaCl respectively. The Al/O and Al/Mg atomic concentration ratios were measured to be zero due to aggressive nature of chloride ions.

- ❖ Resistance to galvanic corrosion evinced a remarkable improvement of 58% and 54% after 4th pass in interaction with 0 M and 1M NaCl respectively due to fine distribution of T-phase (Mg_7Zn_3RE) resulted from ECAP.
- ❖ Galvanic corrosion resistance diminished by 26% after 4th pass ECAP in comparison with as-received sample when tested in 0.1M NaCl solution. However, in as received sample pits were observed while the 4th pass sample exhibited uniform corrosion which is preferred in engineering applications.
- ❖ The corrosion rate of Al7075 alloy, ZE41 Mg and coupled ZE41 Mg – Al7075 is calculated to be 0.02 mm/yr, 0.83 mm/yr and 6.21 mm/yr when tested in 3.5 Wt% NaCl. ECAP improved the resistance to galvanic corrosion of ZE41 Mg–Al7075 Al alloy galvanic couple upto 140 %, 26.82 % and 121.12 % when tested in 0 M, 0.1 M and 1 M NaCl solution respectively. Indeed, the grain refinement upto 15 μm and fine distribution of T phase (Mg_7ZN_3RE) were responsible for such enhancement in corrosion resistance after ECAP.

SCOPE FOR FUTURE WORK

In the present work, ZE41 Mg alloy was subjected to ECAP. The mechanical properties of ECAPed samples improved significantly due to effect of grain refinement. However, crystallographic orientation after ECAP also dictated the mechanical properties of ZE41 Mg alloys. The corrosion resistance of ECAPed ZE41 Mg samples were relatively higher than the as received samples. The corrosion behaviour of ZE41 Mg alloy was dependant on grain refinement, size and distribution of secondary phases and effect of crystallographic orientation. In addition, the galvanic corrosion resistance of ZE41 Mg alloy also improved after ECAP. Apart from these studies, the following research areas very much significant and interesting as well. Therefore, exploring these areas of research are of great importance. Indeed, these scope for future work is recommended based on the knowledge and experience gained over the years, after investigating the mechanical properties and corrosion behaviour of various ECAPed Mg alloys.

- ❖ The combined influence of grain refinement and effect of crystallographic orientation could be studied after subjecting Mg alloys to ECAP using R route. This is because, our research group proved that Mg samples processed through R route exhibited relatively higher mechanical properties than those processed by route Bc.
- ❖ Mg and its alloys are subjected to a combination of stress and corrosion in real-time applications, especially in automobile application. Hence, it is mandatory to investigate the stress corrosion cracking behaviour of Mg alloys using constant and varying loading conditions to mimic the same.
- ❖ Recently, Mg alloys are potentially researched as biodegradable implants in fracture fixative application in humans. Till date, MAGNEZIX and RESOMET are the only Mg based implants that are commercially available in the market. Thus, the performance of ECAPed Mg samples *in vivo* models may perhaps be studied to develop commercial bio-degradable implants.

- ❖ It is well known that Mg and its alloys tend to catch fire during casting and high speed machining. Therefore processing Mg alloys and achieving near net shape in final products is highly challenging. Additive manufacturing of Mg alloys could possibly revolutionize the processing and application of Mg based alloys. Therefore, it is of prime importance to process Mg alloys using additive manufacturing technology and thoroughly understand the mechanical properties and corrosion behaviour of the same.

REFERENCES

- Agnew, S. R., Horton, J. A., Lillo, T. M., and Brown, D. W. (2004). "Enhanced ductility in strongly textured magnesium produced by equal channel angular processing." *Scr. Mater.*, 50(3), 377–381.
- Argade, G. R., Panigrahi, S. K., & Mishra, R. S. (2012). Effects of grain size on the corrosion resistance of wrought magnesium alloys containing neodymium. *Corrosion Science*, 58, 145-151.
- Atrens, B. A., Winzer, N., and Dietzel, W. (2011). "Stress Corrosion Cracking of Magnesium Alloys **." (1), 11–18.
- Avvari, M., & Narendranath, S. (2014). Influence of Route-R on wrought magnesium AZ61 alloy mechanical properties through equal channel angular pressing. *Journal of Magnesium and Alloys*, 2(2), 159-164.
- Avvari, M., Narendranath, S., & Nayaka, H. S. (2015). A review on wrought magnesium alloys processed by equal channel angular pressing. *Int J Mater Prod Tec*, 51, 139-164.
- Avvari, M., & Narendranath, S. (2018). Effect of secondary Mg 17 Al 12 phase on AZ80 alloy processed by equal channel angular pressing (ECAP). *Silicon*, 10(1), 39-47.
- Azushima, A., Kopp, R., Korhonen, A., Yang, D. Y., Micari, F., Lahoti, G. D., ... & Yanagida, A. (2008). Severe plastic deformation (SPD) processes for metals. *CIRP annals*, 57(2), 716-735.
- Bazhenov, V. E., Kolygin, A. V., Sung, M. C., Park, S. H., Titov, A. Y., Bautin, V. A., ... & Malyutin, K. V. (2020). Design of MgZnSiCa casting magnesium alloy with high thermal conductivity. *Journal of Magnesium and Alloys*, 8(1), 184-191.
- Banjade, D. R., Porter, S. D., McMullan, B. M., and Harb, J. N. (2016). "Hydrogen Evolution during the Corrosion of Galvanically Coupled Magnesium." *J. Electrochem. Soc.*, 163(3), C116–C123.
- Birbilis, N., Ralston, K. D., Virtanen, S., Fraser, H. L., & Davies, C. H. J. (2010). Grain character influences on corrosion of ECAPed pure magnesium. *Corrosion Engineering, Science and Technology*, 45(3), 224-230.

Biswas, S., Dhinwal, S. S., & Suwas, S. (2010). Room-temperature equal channel angular extrusion of pure magnesium. *Acta materialia*, 58(9), 3247-3261.

Coy, A. E., Viejo, F., Skeldon, P., and Thompson, G. E. (2010). "Susceptibility of rare-earth-magnesium alloys to micro-galvanic corrosion." *Corros. Sci.*, 52(12), 3896–3906.

Copyrights: Diary Number: 14668/2018-CO/L., Reg. No: L-79923/2018).

Chen, B., Lin, D.-L., Jin, L., Zeng, X.-Q., and Lu, C. (2008a). "Equal-channel angular pressing of magnesium alloy AZ91 and its effects on microstructure and mechanical properties." *Mater. Sci. Eng. A*, 483–484, 113–116.

Dargusch, M. S., Shi, Z., Zhu, H., Atrens, A., & Song, G. L. (2020). Microstructure modification and corrosion resistance enhancement of die-cast Mg-Al-Re alloy by Sr alloying. *Journal of Magnesium and Alloys*.

Deshpande, K. B. (2010a). "Experimental investigation of galvanic corrosion: Comparison between SVET and immersion techniques." *Corros. Sci.*, 52(9), 2819–2826.

Deshpande, K. B. (2010b). "Validated numerical modelling of galvanic corrosion for couples: Magnesium alloy (AE44)-mild steel and AE44-aluminium alloy (AA6063) in brine solution." *Corros. Sci.*, 52(10), 3514–3522.

Deshpande, K. B. (2012). "Effect of aluminium spacer on galvanic corrosion between magnesium and mild steel using numerical model and SVET experiments." *Corros. Sci.*, 62, 184–191.

Ding, R., Chung, C., Chiu, Y., & Lyon, P. (2010). Effect of ECAP on microstructure and mechanical properties of ZE41 magnesium alloy. *Materials Science and Engineering: A*, 527(16-17), 3777-3784.

Dinodi, N., and Shetty, A. N. (2014). "Alkyl carboxylates as efficient and green inhibitors of magnesium alloy ze41 corrosion in aqueous salt solution." *Corros. Sci.*, 85, 411–427.

Dumitru, F. D., Higuera-Cobos, O. F., & Cabrera, J. M. (2014). ZK60 alloy processed by ECAP: Microstructural, physical and mechanical characterization. *Materials Science and Engineering: A*, 594, 32-39.

Figueiredo, R. B., and Langdon, T. G. (2010). "Grain refinement and mechanical behavior of a magnesium alloy processed by ECAP." *J. Mater. Sci.*, 45(17), 4827–4836.

- Gopi, K. R., Nayaka, H. S., & Sahu, S. (2016). Investigation of microstructure and mechanical properties of ECAP-processed AM series magnesium alloy. *Journal of Materials Engineering and Performance*, 25(9), 3737-3745.
- He, Y., Pan, Q., Qin, Y., Liu, X., Li, W., Chiu, Y., and Chen, J. J. J. (2010). "Microstructure and mechanical properties of ZK60 alloy processed by two-step equal channel angular pressing." *J. Alloys Compd.*, 492(1–2), 605–610.
- Hou, R., Victoria-Hernandez, J., Jiang, P., Willumeit-Römer, R., Luthringer-Feyerabend, B., Yi, S., ... & Feyerabend, F. (2019). In vitro evaluation of the ZX11 magnesium alloy as potential bone plate: Degradability and mechanical integrity. *Acta biomaterialia*, 97, 608-622.
- Janeček, M., Yi, S., Král, R., Vratna, J., & Kainer, K. U. (2010). Texture and microstructure evolution in ultrafine-grained AZ31 processed by EX-ECAP. *Journal of materials science*, 45(17), 4665-4671.
- Jiang, J., Ma, A., Saito, N., Shen, Z., Song, D., Lu, F., Nishida, Y., Yang, D., and Lin, P. (2009). "Improving corrosion resistance of RE-containing magnesium alloy ZE41A through ECAP." *J. Rare Earths*, 27(5), 848–852.
- Jin, L., Lin, D., Mao, D., Zeng, X., and Ding, W. (2005). "Mechanical properties and microstructure of AZ31 Mg alloy processed by two-step equal channel angular extrusion." *Mater. Lett.*, 59(18), 2267–2270.
- Kang, Z., Zhou, L., & Zhang, J. (2015). Achieving high strain rate superplasticity in Mg–Y–Nd–Zr alloy processed by homogenization treatment and equal channel angular pressing. *Materials Science and Engineering: A*, 633, 59-62.
- Kulekci, M. K. (2008). Magnesium and its alloys applications in automotive industry. *The International Journal of Advanced Manufacturing Technology*, 39(9-10), 851-865.
- Kim, W. J., An, C. W., Kim, Y. S., & Hong, S. I. (2002). Mechanical properties and microstructures of an AZ61 Mg Alloy produced by equal channel angular pressing. *Scripta materialia*, 47(1), 39-44.
- Kim, W. J., Hong, S. I., Kim, Y. S., Min, S. H., Jeong, H. T., & Lee, J. D. (2003). Texture development and its effect on mechanical properties of an AZ61 Mg alloy fabricated by equal channel angular pressing. *Acta materialia*, 51(11), 3293-3307.

- King, A. D., Birbilis, N., and Scully, J. R. (2014). “Accurate electrochemical measurement of magnesium corrosion rates; A combined impedance, mass-loss and hydrogen collection study.” *Electrochim. Acta*, 121, 394–406.
- Krajňák, T., Minárik, P., Stráská, J., Gubicza, J., Máthis, K., & Janeček, M. (2017). Influence of equal channel angular pressing temperature on texture, microstructure and mechanical properties of extruded AX41 magnesium. *Journal of Alloys and Compounds*, 705, 273-282.
- Krajňák, T., Minárik, P., Stráská, J., Gubicza, J., Máthis, K., & Janeček, M. (2019). Influence of the initial state on the microstructure and mechanical properties of AX41 alloy processed by ECAP. *Journal of Materials Science*, 54(4), 3469-3484.
- Liu, M., Qiu, D., Zhao, M. C., Song, G., and Atrens, A. (2008). “The effect of crystallographic orientation on the active corrosion of pure magnesium.” *Scr. Mater.*, 58(5), 421–424.
- Lin, H. K., Huang, J. C., & Langdon, T. G. (2005). Relationship between texture and low temperature superplasticity in an extruded AZ31 Mg alloy processed by ECAP. *Materials Science and Engineering: A*, 402(1-2), 250-257.
- Mcadam, G., Talevski, J., Trueman, a R., Danek, S., and Hinton, B. R. W. (2005). “Evaluation of anodised coatings applied to magnesium alloy ZE41A-T5 for potential use in RAN Seahawk helicopters.” *Corros. Mater.*, 30(6), 12–20.
- Mei, D., Lamaka, S. V., Lu, X., & Zheludkevich, M. L. (2020). Selecting medium for corrosion testing of bioabsorbable magnesium and other metals—a critical review. *Corrosion Science*, 108722.
- Minárik, P., Král, R., and Janeček, M. (2013). “Effect of ECAP processing on corrosion resistance of AE21 and AE42 magnesium alloys.” *Appl. Surf. Sci.*, 281, 44–48.
- Minárik, P., Král, R., Pešička, J., & Chmelík, F. (2015). Evolution of mechanical properties of LAE442 magnesium alloy processed by extrusion and ECAP. *Journal of materials Research and Technology*, 4(1), 75-78.
- Minárik, P., Král, R., Čížek, J., and Chmelík, F. (2016a). “Effect of different c/a ratio on the microstructure and mechanical properties in magnesium alloys processed by ECAP.” *Acta Mater.*, 107, 83–95.

- Minárik, P., Král, R., Pešička, J., Daniš, S., and Janeček, M. (2016b). “Microstructure characterization of LAE442 magnesium alloy processed by extrusion and ECAP.” *Mater. Charact.*, 112, 1–10.
- Minárik, P., Veselý, J., Král, R., Bohlen, J., Kubásek, J., Janeček, M., & Stráská, J. (2017a). Exceptional mechanical properties of ultra-fine grain Mg-4Y-3RE alloy processed by ECAP. *Materials Science and Engineering: A*, 708, 193-198.
- Minárik, P., Jablonská, E., Král, R., Lipov, J., Ruml, T., Blawert, C., ... & Chmelík, F. (2017b). Effect of equal channel angular pressing on in vitro degradation of LAE442 magnesium alloy. *Materials Science and Engineering: C*, 73, 736-742.
- Mostaed, E., Hashempour, M., Fabrizi, A., Dellasega, D., Bestetti, M., Bonollo, F., & Vedani, M. (2014). Microstructure, texture evolution, mechanical properties and corrosion behavior of ECAP processed ZK60 magnesium alloy for biodegradable applications. *Journal of the Mechanical Behavior of Biomedical Materials*, 37, 307-322.
- Mostaed, E., Fabrizi, A., Dellasega, D., Bonollo, F., and Vedani, M. (2015). “Microstructure, mechanical behavior and low temperature superplasticity of ECAP processed ZM21 Mg alloy.” *J. Alloys Compd.*, 638, 267–276.
- Mukai, T., Yamanoi, M., Watanabe, H., & Higashi, K. (2001). Ductility enhancement in AZ31 magnesium alloy by controlling its grain structure. *Scripta materialia*, 45(1), 89-94.
- Muralidhar, A., Narendranath, S., & Nayaka, H. S. (2013). Effect of equal channel angular pressing on AZ31 wrought magnesium alloys. *Journal of Magnesium and Alloys*, 1(4), 336-340.
- Naik, G. M., Narendranath, S., & Kumar, S. S. (2019). Effect of ECAP Die Angles on Microstructure Mechanical Properties and Corrosion Behavior of AZ80 Mg Alloy. *Journal of Materials Engineering and Performance*, 28(5), 2610-2619.
- Neil, W. C., Forsyth, M., Howlett, P. C., Hutchinson, C. R., and Hinton, B. R. W. (2009). “Corrosion of magnesium alloy ZE41 - The role of microstructural features.” *Corros. Sci.*, 51(2), 387–394.
- Neil, W. C., Forsyth, M., Howlett, P. C., Hutchinson, C. R., and Hinton, B. R. W. (2011). “Corrosion of heat treated magnesium alloy ZE41.” *Corros. Sci.*, 53(10), 3299–3308.

- Pan, F., Yang, M., & Chen, X. (2016). A review on casting magnesium alloys: modification of commercial alloys and development of new alloys. *Journal of Materials Science & Technology*, 32(12), 1211-1221.
- Pan, Y., Wu, G., Cheng, X., Zhang, Z., Li, M., Ji, S., & Huang, Z. (2015). Galvanic corrosion behaviour of carbon fibre reinforced polymer/magnesium alloys coupling. *Corrosion Science*, 98, 672-677.
- Qiang, G., Mostaed, E., Zanella, C., Zhentao, Y., & Vedani, M. (2014). Ultra-fine grained degradable magnesium for biomedical applications. *Rare Metal Materials and Engineering*, 43(11), 2561-2566.
- Ruanli, Z., Jin, Z., and Wen, G. (2015). "Effect of Silane on Galvanic Corrosion between EW75 Magnesium Alloy and TC4 Alloy." *Rare Met. Mater. Eng.*, 44(8), 1838–1844.
- Savguira, Y., North, T. H., & Thorpe, S. J. (2017). Effect of grain orientation on the corrosion resistance of FSSW joints made in AZ31B. *Corrosion Engineering, Science and Technology*, 52(3), 195-200.
- Song, G., Atrens, A., Wu, X., & Zhang, B. (1998). Corrosion behaviour of AZ21, AZ501 and AZ91 in sodium chloride. *Corrosion science*, 40(10), 1769-1791.
- Song, G. L., & Atrens, A. (1999). Corrosion mechanisms of magnesium alloys. *Advanced engineering materials*, 1(1), 11-33.
- Song, G., & Atrens, A. (2003). Understanding magnesium corrosion—a framework for improved alloy performance. *Advanced engineering materials*, 5(12), 837-858.
- Song, G., Johannesson, B., Hapugoda, S., & StJohn, D. (2004). Galvanic corrosion of magnesium alloy AZ91D in contact with an aluminium alloy, steel and zinc. *Corrosion Science*, 46(4), 955-977.
- Song, G. L., Mishra, R., & Xu, Z. (2010). Crystallographic orientation and electrochemical activity of AZ31 Mg alloy. *Electrochemistry Communications*, 12(8), 1009-1012.
- Song, G. L., & Xu, Z. (2012). Crystal orientation and electrochemical corrosion of polycrystalline Mg. *Corrosion Science*, 63, 100-112.

- Song, D., Ma, A., Jiang, J., Lin, P., Yang, D., & Fan, J. (2010). Corrosion behavior of equal-channel-angular-pressed pure magnesium in NaCl aqueous solution. *Corrosion Science*, 52(2), 481-490.
- Song, D., Ma, A. B., Jiang, J. H., Lin, P. H., Yang, D. H., & Fan, J. F. (2011). Corrosion behaviour of bulk ultra-fine grained AZ91D magnesium alloy fabricated by equal-channel angular pressing. *Corrosion Science*, 53(1), 362-373.
- Suh, J., Victoria-Hernandez, J., Letzig, D., Golle, R., Yi, S., Bohlen, J., & Volk, W. (2015). Improvement in cold formability of AZ31 magnesium alloy sheets processed by equal channel angular pressing. *Journal of Materials Processing Technology*, 217, 286-293.
- Suh, J., Victoria-Hernández, J., Letzig, D., Golle, R., & Volk, W. (2016). Enhanced mechanical behavior and reduced mechanical anisotropy of AZ31 Mg alloy sheet processed by ECAP. *Materials Science and Engineering: A*, 650, 523-529.
- Sun, W., Liu, G., Wang, L., Wu, T., & Liu, Y. (2013). An arbitrary Lagrangian–Eulerian model for studying the influences of corrosion product deposition on bimetallic corrosion. *Journal of Solid State Electrochemistry*, 17(3), 829-840.
- Victoria-Hernández, J., Suh, J., Yi, S., Bohlen, J., Volk, W., & Letzig, D. (2016). Strain-induced selective grain growth in AZ31 Mg alloy sheet deformed by equal channel angular pressing. *Materials Characterization*, 113, 98-107.
- Walker, J., Shadanbaz, S., Kirkland, N. T., Stace, E., Woodfield, T., Staiger, M. P., & Dias, G. J. (2012). Magnesium alloys: predicting in vivo corrosion with in vitro immersion testing. *Journal of Biomedical Materials Research Part B: Applied Biomaterials*, 100(4), 1134-1141.
- Wang, B. J., Xu, D. K., Dong, J. H., & Ke, W. (2014). Effect of the crystallographic orientation and twinning on the corrosion resistance of an as-extruded Mg–3Al–1Zn (wt.%) bar. *Scripta Materialia*, 88, 5-8.
- Wang, C. J., Kang, J. W., Deng, K. K., Nie, K. B., Liang, W., & Li, W. G. (2020). Microstructure and mechanical properties of Mg-4Zn-xGd (x= 0, 0.5, 1, 2) alloys. *Journal of Magnesium and Alloys*, 8(2), 441-451.

- Wang, B., Xu, D., Dong, J., & Ke, W. (2016). Effect of texture on biodegradable behavior of an as-extruded Mg–3% Al–1% Zn alloy in phosphate buffer saline medium. *Journal of Materials Science & Technology*, 32(7), 646-652.
- Wang, K., Li, C., Li, Y., Lu, J., Wang, Y., & Luo, X. (2021). Multi-physics analysis of the galvanic corrosion of Mg-steel couple under the influence of time-dependent anisotropic deposition film. *Journal of Magnesium and Alloys*.
- Xin, R., Li, B., Li, L., and Liu, Q. (2011). “Influence of texture on corrosion rate of AZ31 Mg alloy in 3.5wt.% NaCl.” *Mater. Des.*, 32(8–9), 4548–4552.
- Yamashita, A., Horita, Z., & Langdon, T. G. (2001). Improving the mechanical properties of magnesium and a magnesium alloy through severe plastic deformation. *Materials Science and Engineering: A*, 300(1-2), 142-147.
- Yang, M. B., Pan, F. S., Zhang, J., & Zhang, J. (2005). An analysis of the development and applications of current and new Mg-Al based elevated temperature magnesium alloys. In *Materials Science Forum* (Vol. 488, pp. 923-926). Trans Tech Publications Ltd.
- Yuan, Y., Ma, A., Gou, X., Jiang, J., Arhin, G., Song, D., & Liu, H. (2016). Effect of heat treatment and deformation temperature on the mechanical properties of ECAP processed ZK60 magnesium alloy. *Materials Science and Engineering: A*, 677, 125-132.
- Yuan, W., Panigrahi, S. K., & Mishra, R. S. (2013). Achieving high strength and high ductility in friction stir-processed cast magnesium alloy. *Metallurgical and Materials Transactions A*, 44(8), 3675-3684.
- Zong, Y., Yuan, G., Zhang, X., Mao, L., Niu, J., & Ding, W. (2012). Comparison of biodegradable behaviors of AZ31 and Mg–Nd–Zn–Zr alloys in Hank's physiological solution. *Materials Science and Engineering: B*, 177(5), 395-401.
- Zheng, Y. F., Gu, X. N., & Witte, F. (2014). “Biodegradable metals.” *Mater. Sci. Engg.: R: Reports*, 77, 1-34.
- Zhang, F., Ma, A., Jiang, J., Xu, H., Song, D., Lu, F., and Nishida, Y. (2013). “Enhanced biodegradation behavior of ultrafine-grained ZE41A magnesium alloy in Hank's solution.” *Prog. Nat. Sci. Mater. Int.*, 23(4), 420–424.

Zhang, J., Kang, Z., & Zhou, L. (2015). Microstructure evolution and mechanical properties of Mg–Gd–Nd–Zn–Zr alloy processed by equal channel angular pressing. *Materials Science and Engineering: A*, 647, 184-190.

Zhang, Z., Wu, G., Atrens, A., & Ding, W. (2020). Influence of trace As content on the microstructure and corrosion behavior of the AZ91 alloy in different metallurgical conditions. *Journal of Magnesium and Alloys*, 8(1), 301-317.

Zhao, M. C., Liu, M., Song, G. L., & Atrens, A. (2008). Influence of pH and chloride ion concentration on the corrosion of Mg alloy ZE41. *Corrosion Science*, 50(11), 3168-3178.

Zhou, M., Morisada, Y., & Fujii, H. (2020). Effect of Ca addition on the microstructure and the mechanical properties of asymmetric double-sided friction stir welded AZ61 magnesium alloy. *Journal of Magnesium and Alloys*, 8(1), 91-102.

Zhao, W., Wang, J., Weiyang, J., Qiao, B., Wang, Y., Li, Y., & Jiang, D. (2020). A novel biodegradable Mg-1Zn-0.5 Sn alloy: Mechanical properties, corrosion behavior, biocompatibility, and antibacterial activity. *Journal of Magnesium and Alloys*, 8(2), 374-386.

Zhang, J., Kang, Z., & Zhou, L. (2015). Microstructure evolution and mechanical properties of Mg–Gd–Nd–Zn–Zr alloy processed by equal channel angular pressing. *Materials Science and Engineering: A*, 647, 184-190.

Zhang, J., Kang, Z., & Wang, F. (2016). Mechanical properties and biocorrosion resistance of the Mg-Gd-Nd-Zn-Zr alloy processed by equal channel angular pressing. *Materials Science and Engineering: C*, 68, 194-197.

List of Publications based on PhD Research Work

Sl. No.	Title of the paper	Authors	Name of the Journal/ Conference/ Symposium,	Month & Year of Publication	Category *
1	Enhancement of resistance to galvanic corrosion of ZE41 Mg alloy by equal channel angular pressing.	Prithivirajan S Narendranath S Vijay Desai	Materials and Corrosion (John Wiley) IF:1.458	Published Dec-2019	1
2	Analyzing the combined effect of crystallographic orientation and grain refinement on mechanical properties and corrosion behavior of ECAPed ZE41 Mg alloy by EBSD	Prithivirajan S Narendranath S Vijay Desai	Journal of Magnesium and Alloys (Elsevier) IF: 7.1	Published Aug-2020	1
3	Recent developments in <i>in vivo</i> studies and clinical applications of magnesium based biodegradable implants – a review.	Prithivirajan S Narendranath S Vijay Desai	Journal of Magnesium and Alloys (Elsevier) IF: 7.1	Published March 2021	1
4	Bio corrosion impacts on mechanical integrity of ZM21 Mg for orthopaedic implants processed by equal channel angular pressing.	Prithivirajan S Mayur Bapu Nyahale Gajanan M Naik Narendranath S Aswini Prabhu Rekha PD	Journal of Materials Science: Materials in Medicine. (Springer) IF: 2.4	Published July 2021	1

5	Galvanic corrosion behaviour of coupled ZE41Mg – Al7075 Al alloy in 3.5 Wt% NaCl	Prithivirajan S Mayur Babu Nyahale Narendranath S Vijay Desai	9 th International Engineering Symposium- IES 2020 Kumamoto university Japan	Published March-2020	3
6	Recent progress in equal channel angular pressing of magnesium alloys starting from Segal's idea to advancements till date – A review.	Prithivirajan S Narendranath S Vijay Desai	Journal of Magnesium and Alloys	Under review	2

* Category: 1 : Journal paper, full paper accepted

2: Journal paper, under review

3: Conference/Symposium paper, full

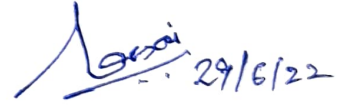
4: Conference/Symposium paper, abstract reviewed



Research Scholar: **Prithivirajan S**



Research Supervisor(s): **Prof. Narendranath S.**



29/6/22
Prof. Vijay Desai.

PRITHIVIRAJAN SEKAR

Research Scholar, (Thesis submission in progress)

Department of Mechanical Engineering,

National Institute of Technology Karnataka (NITK), Surathkal.

Mangalore, Karnataka, India - 575025.

Contact No : +91 8861090324.

Alternate contact No : +91 8056247911.

Email : sekarprithviraj@gmail.com.



Degree	Institution / University	Year	Specialization	% of marks	Class
Ph.D	National Institute of Technology Karnataka NITK Surathkal.	2017 – 2021	Mechanical Engineering	-	Ph.D pursuing
M.E	Madras Institute of Technology / Anna University, Chennai	2015 – 2017	Manufacturing Engineering	89	First class with distinction
B.E	St. Joseph's college of Engg/ Anna University, Chennai.	2011 – 2015	Mechanical Engineering	81	First Class
H.S.C.	Sri Ramakrishna Vidyalaya Gurukulam, Ulundurpet.	2011	State Board	94	First class
S.S.L.C	Sri Ramakrishna Vidyalaya Gurukulam, Ulundurpet.	2009	Matriculation	91	First class

KEY PROJECTS

PhD Thesis: Studies on mechanical properties and corrosion behaviour of ZE41 Mg alloy subject to equal channel angular pressing (ECAP). Guided by **Prof. Narendranath S** and **Prof. Vijay Desai**, Dept of Mechanical Engineering, NITK Surathkal.

Involvement in other auxiliary projects during PhD

Project 1: “Bio-corrosion impacts on mechanical integrity of ZM21 Mg for orthopaedic implant application processed by equal channel angular pressing (ECAP)”.

Project 2: “Effect of Zinc on mechanical properties and corrosion behaviour of Magnesium based composites for orthopaedic application – a preliminary study”.

M.E Thesis: “Integration and vibration testing of 2U cube satellite”.

B.E Thesis: “Investigating the machinability of austenite 316L and super Duplex stainless steel”.

LEADERSHIP SKILLS

- 1. Teaching Assistant:** Engineering Drawing, Dept. of Mechanical Engineering, NITK Surathkal.
- 2. Class representative:** M.E Manufacturing, Dept of Production Technology, MIT, Anna University.
- 3. Cultural minister:** School Parliament, Sri Ramakrishna Vidyalaya Gurukulam.
- 4. Organizer:** Drawing Forum, Sri Ramakrishna Vidyalaya Gurukulam.

ACHIEVEMENTS

1. Recipient of Scholarship for H.S.C in SRKVG [June 2009- May 2011]
2. Won second place for football in Tamilnadu inter engineering sports [TIES-2013]

PUBLICATIONS

International Journals based on PhD work.

- 1. Prithvirajan, S., Narendranath, S., & Desai, V. (2020).** Enhancement of resistance to galvanic corrosion of ZE41 Mg alloy by equal channel angular pressing. *Materials and Corrosion*, 71(4), 571-584. (Wiley, IF: 1.5).
- 2. Prithvirajan, S., Narendranath, S., & Desai, V. (2020).** Analysing the combined effect of crystallographic orientation and grain refinement on mechanical properties and corrosion behaviour of ECAPed ZE41 Mg alloy. *Journal of Magnesium and Alloys*, 8(4), 1128-1143. (Elsevier, IF: 7.1)
- 3. Prithvirajan S, Narendranath S, Vijay Desai, (2021).** Recent progress in in vivo studies and clinical applications of magnesium based biodegradable implants – A review, *Journal of Magnesium and Alloys*. In press. (Elsevier, IF: 7.1)

International Journals based on auxiliary work.

4. Prithvirajan S, Mayur Babu Nyahale, Gajanan M Naik, Narendranath S, Aswini Prabhu, Rekha PD,(2021). Bio-corrosion impacts on mechanical integrity of ZM21 Mg for orthopaedic implant application processed by equal channel angular pressing. *Journal of Material Science: Materials in medicine*. Accepted. (*Springer, IF: 2.4*)

5. Sandeep Moudgalya K V, Prithvirajan S, Suresh Hebbar, H, M R Rahman, (2021). Effect of Zinc on mechanical properties and corrosion behaviour of Magnesium based composites for orthopaedic application – a preliminary study. *Journal of Magnesium and Alloys* (Under review)

International Conferences/ Symposium/ Poster.

6. Prithvirajan S, Mayur Babu Nyahale, Narendranath S, Vijay Desai, (2021) Galvanic corrosion behaviour of coupled ZE41 Mg –Al7075 Al alloy in 3.5 Wt% NaCl. 9th International Engineering Conference- **IES 2020, Kumamoto University Japan.**

PERSONAL PROFILE

Father's name : Mr. Sekar V.
Languages known : Tamil, Kannada, English and German.
Nationality : Indian.
Marital status : Single.
Permanent address : 2/2 mettu street, Perani village, Villupuram, District,
Tamilnadu-605651.
Mobile number : +91 8861090324, +91 8056247911.
Email Id : sekarprithviraj@gmail.com

DECLARATION

I hereby assure that the above mentioned information is true to best of my knowledge.



Prithvirajan Sekar.